

The nature and origins of warm absorbers in Active Galactic Nuclei

Alexander Joseph Blustin

Mullard Space Science Laboratory
Department of Space and Climate Physics
University College London

A thesis submitted to the University of London
for the degree of Doctor of Philosophy

Ben Zoma said, Who is wise? He who learns from all men, as it is said, From all my teachers I have gotten understanding.

Ethics of the Fathers, Chapter IV

To all my teachers

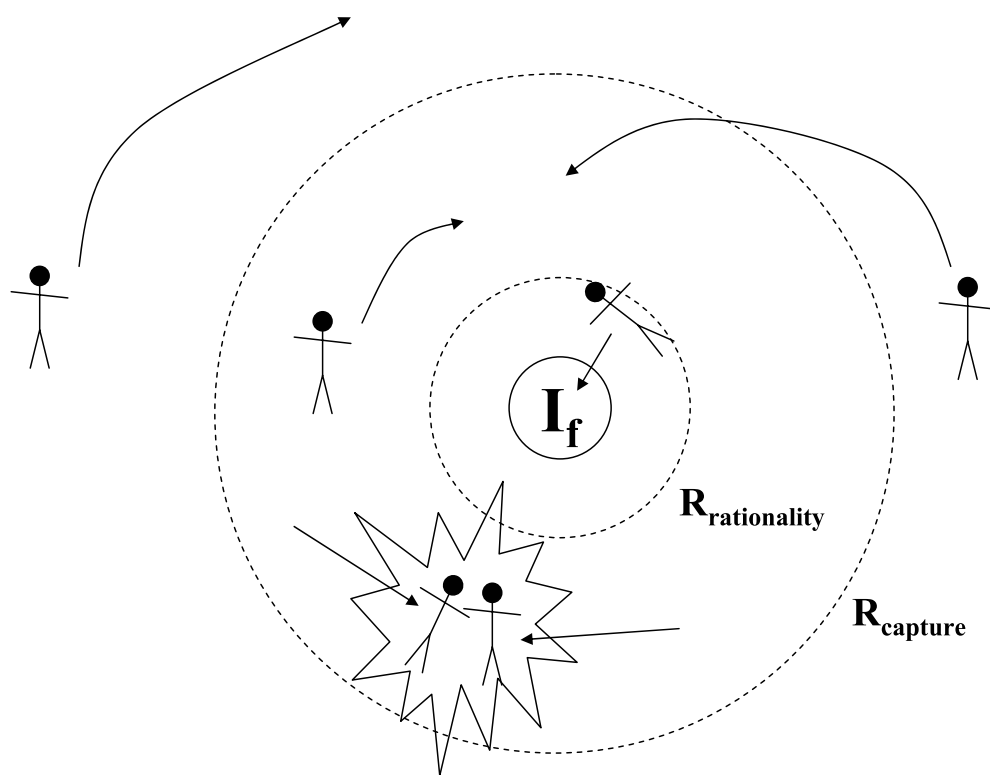
ABSTRACT

This dissertation describes my analysis of XMM-Newton observations of six Active Galactic Nuclei (AGN), concentrating on the high resolution spectroscopy of soft X-ray absorption features, and discusses the results in the context of the origins and astrophysical implications of ionised outflows in AGN. I studied two Seyfert galaxies (NGC 3783 and NGC 7469) and four BL Lac objects (1H1219+301, H1426+428, Markarian 501 and PKS 0548-322), all of which have shown evidence in previous work of soft X-ray ionised absorption.

NGC 3783 has very deep soft X-ray absorption. I find that there are at least two main ionisation phases. The low ionisation phase appears to be fairly well concentrated around a single ionisation parameter, whilst the high ionisation phase probably contains a range of ionisation levels. NGC 7469 has a warm absorber with a much lower overall column in our line of sight. Despite this, the detected ions from its absorber span a range of four orders of magnitude in ionisation parameter. In the BL Lac objects, neither the RGS nor the EPIC spectra show any evidence of intrinsic ionised absorption. By looking back over the history of observations of ionised X-ray absorption in these sources, I am able to show that the existence of such features can be ruled out at 93% confidence.

I compare the results of these analyses with findings from high resolution X-ray spectroscopic observations of other AGN, in order to come to some conclusions about the origins and importance of the warm absorber phenomenon. I find that Seyfert, NLSy1 and certain QSO absorbers are most consistent with an origin in the dusty torus, whilst the outflows in two QSOs are more likely to be accretion disc winds. I show that the kinetic luminosities of the torus outflows must account for less than 1% of the bolometric luminosities of the AGN.

Astrophysicists accreting onto a fashionable idea, I_f



After R. McCray, as presented by Krolik (1999)

ACKNOWLEDGEMENTS

First of all I wish to acknowledge my supervisor, Dr. Graziella Branduardi-Raymont, for the significant effort she has put into supervising me in trying times, but most of all for being an interesting person. I am also indebted to my secondary supervisor, Dr. Mat Page, for being endlessly generous with his time and expertise. I thank both of them for their uncompromising attitude to excellence.

I am also very grateful for the many fruitful interactions I have had with my collaborators within the RGS consortium and elsewhere, especially Dr. Jelle Kaastra, Dr. Ehud Behar, and Dr. Gerard Kriss. Much technical help - and suspension of disbelief - was forthcoming from staff, postdocs and students within MSSL. Special thanks go to Steven von Fuerst (for being singular) and Rhaana Starling (for being informative). I acknowledge the financial support of a PPARC studentship, which has kept me in a style to which I have been pleased to become accustomed.

Thanks, too, to the 'league of nations' for continually confounding my cynicism, which may have reached a state of perfection, and to all those others who make existence possible and enjoyable.

Finally, I thank my parents for bringing me up to be a scientist, and my sister for continually reminding me that I am really just a great big turkey.

Contents

Abstract	3
Acknowledgements	5
1 Introduction	21
1.1 XMM-Newton observations of active galaxies	21
1.2 Active galaxies	22
1.2.1 Seyfert galaxies	27
1.2.2 BL Lac objects	30
1.3 Spectroscopy	33
1.3.1 Continuum processes	34
1.3.2 Atomic spectroscopy	37
1.3.3 Observational relevance to Seyfert 1s and BL Lac objects . . .	49
1.3.4 Spectral modelling	51
2 Observations and data analysis	53
2.1 Introduction	53
2.2 The XMM-Newton Observatory	53
2.2.1 EPIC-MOS and EPIC-pn	54
2.2.2 RGS	57
2.2.3 OM	59
2.3 Observations	60
2.4 Data processing	64
2.4.1 EPIC-MOS	65

2.4.2	EPIC-pn	66
2.4.3	RGS	67
2.4.4	OM	70
2.5	Data analysis	71
3	NGC 3783	76
3.1	Introduction	76
3.2	Lightcurves, 2–10 keV continuum and Fe K α line	78
3.3	RGS spectrum	86
3.4	Warm absorber modelling	89
3.4.1	Two-phase model	90
3.4.2	Detailed model	94
3.5	Discussion	94
3.5.1	Broadband X-ray and UV variability	94
3.5.2	Emission and absorption in the Fe K α region.	94
3.5.3	The soft X-ray warm absorber	99
3.5.4	The structure of the warm absorber in NGC 3783	102
3.6	Some recent results	102
3.6.1	Behar et al. (2003)	103
3.6.2	Krongold et al. (2003)	104
3.6.3	Netzer et al. (2003)	105
3.6.4	Reeves et al. (2004)	107
3.7	Conclusions	109
4	NGC 7469	112
4.1	Introduction	112
4.2	X-ray results from XMM-Newton	112
4.2.1	X-ray and UV Variability	113
4.2.2	0.2–10 keV continuum and Fe K α line	113
4.2.3	RGS spectrum	119
4.3	Discussion and conclusions	131

4.3.1	XMM-Newton observation	131
4.3.2	UV results from FUSE and the X-ray/UV connection	133
5	BL Lac objects	138
5.1	Introduction	138
5.2	Lightcurves	141
5.3	EPIC spectra	143
5.4	RGS spectra	143
5.5	Discussion and conclusions	150
6	Conclusions and new perspectives	156
6.1	Introduction	156
6.2	Phenomenology of X-ray warm absorbers	157
6.3	The nature of warm absorbers	167
6.3.1	The energetics of warm absorbers	172
6.3.2	Where do warm absorbers come from?	178
6.3.3	Where do warm absorbers end up?	186
6.3.4	Are warm absorbers important?	189
6.4	Future work	190
	Bibliography	192

List of Figures

1.1	Schematic representation of the ‘Unified Model’ of AGN. In the centre is the black hole and accretion disc. Surrounding this is the Broad Line Region (BLR); both the black hole and accretion disc, and the BLR, are enclosed within the optically thick dusty torus. Further out, the Narrow Line Region (NLR) forms an ionisation cone. The jet, which is usually only present in radio-loud AGN, travels along the axis of the system.	25
1.2	Broad absorption feature (at ~ 0.65 keV) in the Einstein OGS spectrum of PKS 2155-304 (Canizares and Kruper, 1984).	32

- 1.3 Part of the emission line spectrum of O VII, created by recombination of electrons onto O VIII ions; the plot shows how the shape of the Radiative Recombination Continuum (RRC) feature changes according to the temperature of the thermal distribution of recombining electrons (from Kahn et al., 2002). In each of the three cases (with electron temperatures of 2 eV, 8 eV and 32 eV respectively) the recombination rate is assumed to be the same, so the heights of the emission lines are constant. The inset graph (top right) shows the whole range of O VII soft X-ray emission features at a recombining electron temperature of 2 eV, including the triplet of resonance (r), intercombination (i) and forbidden (f) emission lines whose intensity ratios are sensitive to density and temperature. These plots demonstrate clearly that the O VII RRC will only be easily observable when it arises in low temperature, photoionised gas. 40
- 1.4 Variation of relative ionic abundance with ionisation parameter ξ of different oxygen states within a photoionised plasma. The ionisation states go in order of increasing ionisation from left to right, from neutral (O I) to fully stripped (O IX). The relative abundance is given in terms of the log of the ionic column density for solar abundances (Anders and Grevesse, 1989), where hydrogen is 10 by definition (so that a log column of 4 for any ion means that the column of that ion with respect to hydrogen is $10^{4-10} = 1 \times 10^{-6} \text{ cm}^{-2}$). The data were generated by J. Kaastra using Xstar, with the NGC 5548 SED used in Kaastra et al. (2002b) and a gas density of 10^8 cm^{-3} . The temperature of the gas in the model is a function of the ionisation parameter. 41

- 1.5 Variation of relative ionic abundance with ionisation parameter ξ of different iron states within a photoionised plasma. The ionisation states go in order of increasing ionisation from left to right, from neutral (Fe I) to fully stripped (Fe XXVII). The relative abundance is given in terms of the log of the ionic column density for solar abundances (Anders and Grevesse, 1989), where hydrogen is 10 by definition (so that a log column of 4 for any ion means that the column of that ion with respect to hydrogen is $10^{4-10} = 1 \times 10^{-6} \text{ cm}^{-2}$). The data were generated by J. Kaastra using Xstar, with the NGC 5548 SED used in Kaastra et al. (2002b) and a gas density of 10^8 cm^{-3} . The temperature of the gas in the model is a function of the ionisation parameter. 42
- 1.6 Simplified energy level diagram for a He-like ion (based on Fig. 1, Dubau and Porquet, 2002). Solid lines are collisional transitions and dotted lines are radiative transitions. The lines denoted w, x, y and z are the resonance (w), intercombination (x+y) and forbidden (z) lines of the triplet respectively. 44
- 1.7 The effect of photoexcitation on the relative strengths of the soft X-ray emission lines of O VII. PI = photoionisation, PE = photoexcitation, CIE = collisional ionisation. The combination of photoexcitation and photoionisation can produce the triplet ratios expected from the combination of photoionisation and collisional ionisation (expected in an AGN with a nuclear starburst); the two cases can only be differentiated by looking at the higher order transitions (from Kinkhabwala et al., 2002). 47
- 1.8 A Voigt profile plotted at a range of optical depths; $x' = \lambda - \lambda_0$ in units of $2g/\sqrt{\ln 2}$, where g is the Half Width Half Maximum (HWHM) of the Gaussian part of the line (from Tatum, 2003). 49

1.9	The curve of growth of a Voigt profile, plotted for different values of the ‘gaussianity’ k_G of the line, where $k_G = g/(l + g)$ and g and l are the HWHMs of the Gaussian and Lorentzian parts of the lines respectively. W' is the equivalent width of the line in units of $2g/\sqrt{\ln 2}$, and $\tau(0)$ is the optical depth at the central wavelength of the line (from Tatum, 2003).	50
2.1	Layout of the instruments on XMM-Newton (not to scale); the three mirror modules are co-aligned with the Optical Monitor (OM). Two of the mirror modules have Reflection Grating Arrays (RGAs) attached to them, which disperse about 40% of the X-rays onto the RGS Focal Cameras (RFCs). The EPIC-MOS CCD cameras are at the prime foci of these two telescopes, and the EPIC-pn is at the prime focus of the telescope without an RGA. The dotted lines indicate the paths of the X-ray photons.	55
2.2	Total effective area of XMM-Newton mirrors, alongside those of AXAF (i.e. Chandra), ASCA and ROSAT (from Ehle et al., 2003).	56
2.3	Effective areas of the individual instruments on XMM-Newton (from Ehle et al., 2003).	56
2.4	Energy resolution of the EPIC-MOS cameras (from Ehle et al., 2003). The datapoints show the gradual degradation of the MOS resolution over the course of the mission so far due to a gradual increase in Charge Transfer Inefficiency (CTI).	57
2.5	Energy resolution of the EPIC-pn cameras (from Ehle et al., 2003). The red lines show the resolutions for single and double events at CCD line 190 (the focus position); the double events have a much poorer resolution due to a currently insufficient correction for Charge Transfer Inefficiency (CTI). The green line is for events occurring at CCD line 10, near a read-out node.	58
2.6	Comparison of the effective areas of the grating spectrometers on XMM-Newton and Chandra (from Ehle et al. 2003).	60

2.7	Comparison of the resolving powers, in the first dispersion order ($m=1$) of the grating spectrometers on XMM-Newton and Chandra (from Dewey, 2002); the resolving powers of the Chandra ACIS detectors are also plotted for the Front-Illuminated (FI) CCDs pre-launch (before the degradation in CTI; roughly comparable to EPIC resolving power), and one of the Back-Illuminated (BI) CCDs (S3).	61
2.8	The bandpasses of the lenticular filters of the OM (from Ehle et al., 2003).	64
2.9	The effective area of RGS1 + RGS2 (first order), from response matrices generated with SAS V5.2 (black), SAS V5.3.3 (red) and SAS V5.4 (blue).	69
3.1	UVW2 image of NGC 3783, with the entire series of images co-added; North is up, East to the left, and the image is about 50" x 40" in size with 0.5" pixels. The nuclear image is saturated so that the the spiral arms are visible.	80
3.2	Multiwavelength background-subtracted lightcurves of NGC 3783: top, UV (140–270 nm) lightcurve from the OM, in 1000 s time bins; middle three, PN lightcurves in the bands 0.2–2, 2–6 and 6–10 keV, in 300 s time bins; bottom, the hardness ratio (2–10 keV / 0.2–2 keV flux) in 300 s time bins. The error bars are slightly overestimated in these plots: from top to bottom the errors on the points should be ± 0.08 , 0.2, 0.1 and 0.05 counts s^{-1} respectively, and the error on the hardness ratio should be ± 0.01	81
3.3	Hardness – intensity plot of NGC 3783 in 30 minute time bins. The error bars are slightly overestimated: the error on the total flux should be ± 0.08 counts s^{-1} , and the error on the hardness ratio should be ± 0.003	82
3.4	Continuum power-law fit to the 3.5–5.5 and 7.5–10 keV ranges of the pn spectrum of NGC 3783, extrapolated over 0.2–10 keV. The ratio of the data to the continuum model is shown in the bottom panel.	83

3.5	Fit to the iron emission lines in the pn spectrum of NGC 3783 (left, lines 1 and 2 (Fe K α); right, line 3). Top panel: data (black) and model (red). Bottom panel: overall model (solid line) and model components (dotted line).	85
3.6	Combined RGS1 and RGS2 rest frame spectrum of NGC 3783 (black), with the power-law continuum (blue) and the power-law plus two-phase warm absorber model (red) superimposed, plotted over the range 6–38 Å. Species absorbing or emitting in various spectral ranges are indicated.	92
3.7	The two phases of the NGC 3783 warm absorber model applied separately to the continuum (high-ionisation phase in red, low-ionisation phase in blue, and power-law continuum in black) plotted over the range 6–38 Å (rest frame). The absorption edges in the continuum are due to neutral gas in our Galaxy.	93
3.8	Combined RGS1 and RGS2 rest frame spectrum of NGC 3783 (black), binned into groups of two channels, with detailed warm absorber model superimposed (red), plotted over the range 6–22 Å. The most important spectral features in the data and model are labelled. . . .	96
3.9	Combined RGS1 and RGS2 rest frame spectrum of NGC 3783 (black), binned into groups of two channels, with detailed warm absorber model superimposed (red), plotted over the range 22–38 Å. The most important spectral features in the data and model are labelled. . . .	97
3.10	Ionic column plotted against ionisation parameter of maximum abundance for the iron states VI–XXIV (except Fe xv, for which only an upper limit could be obtained) listed in Table 3.6.	98

- 3.11 The result of constructing a two-phase warm absorber model using *xabs* with the columns and ionisation parameters of Krongold et al. (2003) (red line), compared to the 40 ks RGS spectrum of NGC 3783 (black points; plotted in the observed frame). Their power-law plus blackbody spectral continuum is used with re-fitted normalisations. The blue line shows what happens when $\log \xi$ of the low ionisation phase is set to 0.3 so that the UTA appears in the correct place for the *xabs* ionisation balance. In both cases, significant absorption from O VI, which was not included in the Krongold et al. (2003) model, is present. 106
- 4.1 Multiwavelength background-subtracted lightcurves: top, UV (140–270 nm) lightcurve from the OM, in 1000 s time bins; middle four, pn lightcurves in the bands 0.2–10, 0.2–2, 2–6 and 6–10 keV, in 300 s time bins; bottom, the hardness ratio (2–10 keV / 0.2–2 keV flux) in 300 s time bins. 114
- 4.2 Hardness – intensity plot in 30 minute time bins. 115
- 4.3 UVW2 filter image (combined from all exposures) of NGC 7469 (bottom right) and IC 5283 (top left). North is up, East to the left; image size approx. 140" x 110". NGC 7469 is within an imaging window with 0.5" pixels, whereas IC 5283 is in a 1" pixel region. The nuclear image of NGC 7469 is saturated so that the wider UV structure of the galaxy is visible. 116
- 4.4 The soft (blue) and hard (black) PN spectra plotted with the best fit model for the total pn spectrum (red), with the two blackbodies, power-law and Fe K α line model components (all in grey). 117
- 4.5 The ratio of the soft pn spectrum (blue) and the hard pn spectrum (black) to the best fit model for the total pn spectrum. 117
- 4.6 The (observer's frame) Fe K α emission line (combined MOS1, MOS2 and pn data) with the model including both Fe K α and Fe K β 119

- 4.7 Combined RGS1 and RGS2 rest frame spectrum of NGC 7469 (black), binned into groups of three channels, with power-law plus two blackbody continuum model superimposed (red) including all lines listed in Table 4.3 and Table 4.4, plotted over the range 6–22 Å. The positions of other possible spectral features are labelled. The G subscript refers to features originating in our galaxy, and F_{inst} is an instrumental Fluorine feature. 121
- 4.8 As for Fig. 4.7, plotted in the range 22–38 Å. 122
- 4.9 Top: combined RGS1 and RGS2 rest frame spectrum of NGC 7469 (6–38 Å) with power-law plus two blackbody continuum superimposed, and the positions of important features marked. Bottom: plot of the statistical significance of the narrow absorption and emission lines. This plot shows the absolute value of the change in χ^2 when a narrow Gaussian of variable width (up to 1000 km s⁻¹) is added to an underlying continuum which has been smoothed with a 70 channel boxcar function (see Section 2.5). Positive and negative values of $|\Delta\chi^2|$ refer to emission and absorption features respectively. The number of σ indicates the confidence level at which the spectral feature, as fitted by the Gaussian, is significant. Since the fit involves one interesting parameter, namely the equivalent width of the Gaussian, the number of σ represented by a given percentage confidence level is the square root of $|\Delta\chi^2|$ 123
- 4.10 Velocity shift plotted against $\log \xi$ of maximum abundance for ions observed in the RGS spectrum of NGC 7469. 126
- 4.11 The O VII emission line triplet region with model overposed (continuum plus fitted columns of O VII and O VIII; the other absorption and emission lines are included with the parameters given in Table 4.3 and Table 4.4). Positions of other transitions not significantly detected are also shown. 130

- 4.12 Part of the FUSE UV spectrum of NGC 7469 (Kriss et al., 2003), showing the multiple intrinsic absorption components (red), the absorption due to our Galaxy (dark blue), the continuum level (black dotted line), and the continuum plus broad and narrow emission lines (green). The light blue lines represent two extreme models, tried by Kriss et al. (2003), in which there are either no narrow emission lines, or the narrow emission lines are not obscured at all by the intrinsic absorber. 134
- 4.13 The overall picture of the circumnuclear region of NGC 7469 as inferred from X-ray and UV absorption and emission measurements. . . 137
- 5.1 The 0.4–10 keV pn lightcurves of 1H1219+301, H1426+428 and Markarian 501 (from orbits 474 and 475), all in 300 s time bins, and the RGS lightcurve of PKS 0548-322 (0.35–2.5 keV; 600 s time bins). 142
- 5.2 Left panels: ratios of the pn spectra of 1H1219+301, H1426+428 and Markarian 501 to fitted power-laws with fixed Galactic neutral absorption (plotted in the observed frame). Right panels: the pn spectra of 1H1219+301, H1426+428 and Markarian 501 with superimposed best-fit broken power-law models (with fixed Galactic neutral absorption; plotted in the observed frame). In all plots, the spectra are grouped to a minimum of 40, 350 and 100 counts per bin respectively. 145
- 5.3 The statistical significance of narrow absorption and emission features in the RGS spectra of 1H1219+301 (top; as in Fig 4.9), and the RGS spectrum itself with best-fit broken power-law model (red) superimposed (bottom), plotted in the source rest frame. 146
- 5.4 The statistical significance of narrow absorption and emission features in the RGS spectra of H1426+428 (top; as in Fig 4.9), and the RGS spectrum itself with best-fit broken power-law model (red) superimposed (bottom), plotted in the source rest frame. 147

5.5	The statistical significance of narrow absorption and emission features in the RGS spectra of Markarian 501 (top; as in Fig 4.9), and the RGS spectrum itself with best-fit broken power-law model (red) superimposed (bottom), plotted in the source rest frame.	148
5.6	The statistical significance of narrow absorption and emission features in the RGS spectra of PKS 0548-322 (top; as in Fig 4.9), and the RGS spectrum itself with best-fit broken power-law model (red) superimposed (bottom), plotted in the source rest frame.	149
5.7	2–10 keV fluxes of 1H1219+301, H1426+428, Markarian 501 and PKS 0548-322 observed with Einstein, ROSAT, BBXRT, ASCA, BeppoSAX and XMM-Newton. Observations where intrinsic absorption was reported are circled.	154
6.1	The distribution in redshift and bolometric luminosity of Seyfert 1 type AGN observed with the high-resolution spectrometers on XMM-Newton and Chandra: filled shapes indicate that the presence of a warm absorber has been reported.	160
6.2	Log ξ_{avg} versus log L_{bol} for the objects in Table 6.4.	165
6.3	Log N_{Htot} versus log L_{bol} for the objects in Table 6.4.	166
6.4	Average outflow velocity, v_{avg} , versus log L_{bol} for the objects in Table 6.4, excluding PG0844+349 and PG1211+143.	168
6.5	Average outflow velocity, v_{avg} , versus log N_{Htot} for the objects in Table 6.4, excluding PG0844+349 and PG1211+143.	169
6.6	Average outflow velocity, v_{avg} , versus log ξ_{avg} for the objects in Table 6.4, excluding PG0844+349 and PG1211+143.	170

List of Tables

2.1	62
2.2	63
2.3	65
2.4	67
3.1	79
3.2	80
3.3	84
3.4	88
3.5	91
3.6	95
3.7	110
4.1	113
4.2	118
4.3	124
4.4	125
4.5	129
5.1	139
5.2	144
5.3	152
5.4	153
6.1	158

6.2	159
6.3	161
6.4	163
6.5	176
6.6	179
6.7	181
6.8	182

Chapter 1

Introduction

1.1 XMM-Newton observations of active galaxies

The launch of the XMM-Newton and Chandra X-ray observatories at the end of the 1990s was the beginning of a new era in X-ray astronomy. Higher spectral and spatial resolution, and a huge increase in collecting area, brought a new impetus to the study of many classes of celestial objects. Active Galactic Nuclei (AGN), popular targets for observation right across the electromagnetic spectrum, have been a particularly fruitful area of investigation. In this thesis, I present the results of my work on XMM-Newton observations of various active galaxies, concentrating on the X-ray spectroscopy of ionised gas in their active nuclei, and I discuss the conclusions these analyses bring me to about the nature, structure and origins of ionised outflows in AGN.

This chapter begins with a general introduction to active galaxies. I then introduce the two classes of AGN that I deal with in this thesis - Seyfert galaxies and BL Lac objects - and finally I describe the physical basis of X-ray spectroscopy. Chapter 2 contains a description of the data analysis methods I have used, and a discussion of the challenges in modelling the high resolution X-ray spectra which come from Chandra and XMM-Newton.

Chapters 3 to 6 contain the results that my work has generated. Chapters 3 and 4 deal with two Seyfert galaxies, NGC 3783 and NGC 7469, and Chapter 5

moves on to BL Lac objects. These three chapters use results from both the grating spectrometers (RGS) and the CCD spectrometers (EPIC), but concentrate mostly on understanding the high resolution grating spectra. Chapter 6 brings together the results from the previous chapters and discusses what they - and other recent XMM-Newton and Chandra spectral results - mean for our understanding of the ionised absorbers.

1.2 Active galaxies

An active galaxy is one which contains a compact site of powerful non-stellar energy release at its core, known as an Active Galactic Nucleus (AGN). AGN have bolometric luminosities of 10^{42} – 10^{48} erg s⁻¹. The lowest luminosity AGN, Low Ionisation Nuclear Emission Region galaxies (LINERs), may be hard to distinguish from the surrounding star formation activity. The highest luminosity AGN, the quasars, may outshine their entire host galaxy.

The AGN energy can be released right across the electromagnetic spectrum, from radio waves to gamma rays, and different processes inside and outside the active nucleus are manifested in different wavebands. The exact combination of phenomena observed from a particular AGN depends upon which of the various classes of active nucleus it is; I discuss this in more detail below. Generally speaking, there are a set of characteristic spectral features which can be observed in these objects. The most spectacular AGN phenomena are the radio jets which blast their way out of the host galaxy into space. These jets often have a much greater extent than the host galaxy itself. Moving closer in, the infra-red band contains re-emission from hot dust in the close vicinity of the active nucleus, which has been heated by high-energy radiation from the central engine. The optical band shows emission lines from clouds illuminated by the AGN. These emission lines arise from regions at different distances from the central engine, the broadest lines originating closest to the nucleus. Within the nucleus itself, UV continuum emission comes from thermal plasma at a range of temperatures, which generates a superposition of blackbody

spectra forming the ‘Big Blue Bump’. The X-ray continuum, probably produced by the inverse-Compton process, comes from the very centre of the nucleus and extends over much smaller scales than the UV emission. Coming full circle, in AGN with radio jets which are aligned along our line of sight, gamma rays are often observed. In fact, AGN jets can be sources of radiation in all wavebands. Variability in these different bands is, broadly speaking, a function of the size of the emission region; the X-ray flux can vary on a timescale of seconds, whereas the extended radio structures might only change over a timescale of millions of years (e.g. Krolik, 1999).

The model most popularly invoked to explain all of these phenomena involves matter accreting onto a supermassive black hole, which might have a mass of up to 10^9 times that of our Sun. The accreting matter forms a disc around the black hole, since it must lose its angular momentum before accreting. This accretion disc emits thermal blackbody radiation in the UV band. The blackbody temperature of the emission decreases with distance from the centre, with the outer parts of the disc - which is a few light days across - emitting in the optical regime (e.g. Rees, 1984).

Immediately above the disc is thought to lie a ‘corona’ of highly energetic electrons, possibly heated by magnetic phenomena. These electrons interact with UV photons from the disc below, boosting the photons up to X-ray energies through the Inverse Compton process (Haardt and Maraschi, 1991, 1993). The resulting upscattered spectrum has the power-law form which is characteristic of AGN X-ray spectra. Variation of the conditions in the corona is a possible cause for the observed X-ray continuum variability.

Some of these X-rays escape outwards, away from the central engine, and some of them are reflected back off the accretion disc. This reflection can potentially give rise to the ‘reflection hump’ (which peaks at $\sim 20\text{--}50$ keV), and also a strong broad fluorescence emission line from neutral iron. Relativistic effects due to the strong gravitational field of the black hole can cause this emission line to be distorted in a characteristic way, with a stretched out red wing (e.g. Nandra et al., 1997).

The central black hole and accretion disc exist in a wider environment. The distance scales within this environment are dependent upon the mass of the black hole;

the more massive the black hole, the larger the distances. In the description of the AGN environment which follows, I give values which would be typically appropriate to a $M \sim 10^7 M_{\odot}$ black hole. The overall scenario which I describe - the Unified Model of AGN - is shown in Fig. 1.1.

Moving away from the black hole by a few light days, one comes to the Broad Line Region (BLR). This consists of fast-moving clouds, illuminated by the radiation from the central engine, which give off highly broadened optical and UV emission lines. The velocity widths of these lines are of the order of several thousand km s^{-1} , and the gas has a density of $\sim 10^{10} \text{ cm}^{-3}$ (e.g. Davidson and Netzer, 1979).

These broad lines are only visible in certain AGN though, and the detection of the broad lines in *polarised* light from AGN which had previously been thought not to have them (e.g. in the case of NGC 1068, Antonucci and Miller 1985) was the first indication that the broad lines could be present but obscured from view, only visible in light scattered into our line of sight (and therefore polarised). There is also evidence of this obscuring matter in X-rays, as the soft X-ray band in such sources is absorbed away by columns of around $10^{23} - 10^{24} \text{ cm}^{-2}$ (e.g. Bassani et al., 1999). A narrow iron $K\alpha$ (6.39 keV) fluorescence line is often visible, with a width compatible with an origin in material of the order of a parsec away from the central engine; the recent observation of a Compton shoulder associated with such a line (Reeves et al., 2004) in NGC 3783 implies reflection from Compton-thick, high column density material of the type that causes the X-ray absorption. The obscuring material is heated by the high energy radiation from the central engine, and re-emits the energy in the infra-red band; the large IR bump in AGN spectra can be well modelled by thermal emission from relatively cool, dusty material heated by the central continuum (Barvainis, 1987). These facts are together taken as evidence for the existence of a dusty torus of material, with a diameter of about a hundred light years, which encloses the central engine and BLR within its central void. There have been attempts to directly image tori in nearby AGN; the first such image to be published was that of a 125 pc diameter torus around the nucleus of the radio galaxy NGC 4261 observed with HST (Jaffe et al., 1993), although this is much larger than

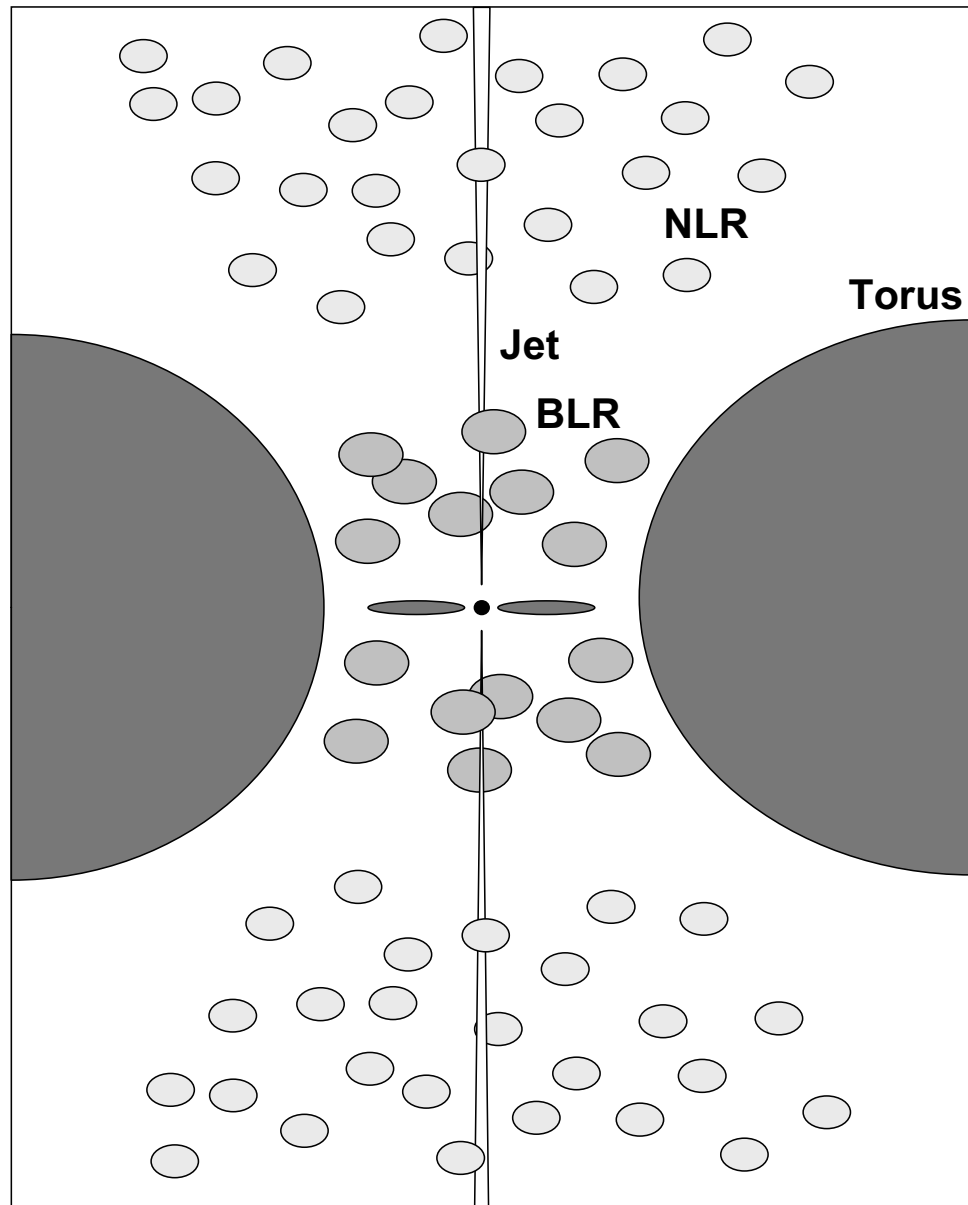


Figure 1.1: Schematic representation of the ‘Unified Model’ of AGN. In the centre is the black hole and accretion disc. Surrounding this is the Broad Line Region (BLR); both the black hole and accretion disc, and the BLR, are enclosed within the optically thick dusty torus. Further out, the Narrow Line Region (NLR) forms an ionisation cone. The jet, which is usually only present in radio-loud AGN, travels along the axis of the system.

we would expect the torus obscuring the BLR to be. More recently, Very Long Baseline Array (VLBA) radio observations at 8.6 GHz have revealed a torus-like structure in the nucleus of NGC 1068, about 0.6 pc across (Gallimore et al., 1997), whose existence had previously been indicated by a study of water masers in this object (Greenhill et al., 1996). Hydroxyl (OH) maser emission has since been found to be a powerful probe of the structure and kinematics of the obscuring torus in Markarian 231 (Klöckner et al., 2003).

Outside the dusty torus, and illuminated by the cone of radiation that emanates from within it, are the Narrow Line Region (NLR) clouds. The observation that the NLR clouds do actually form ionisation cones (Pogge, 1988) is further evidence for the existence of the torus. These clouds give off narrow optical and UV emission lines with a velocity width of perhaps 1000 km s^{-1} , and contain material with a range of densities, from less than 10^3 cm^{-3} up to perhaps 10^6 cm^{-3} (e.g. Krolik, 1999). The NLR is hundreds of light years from the central engine.

The optically thick torus ensures that the radiation one observes from an AGN will be orientation dependent. Observing an AGN face-on, we will see both broad and narrow optical emission lines, as well as the direct X-ray and UV radiation from the central engine. If, on the other hand, the torus is obstructing our line of sight to the central engine, we will only see the narrow optical and UV emission lines, alongside nuclear X-rays reflected off the torus, and the very hard X-rays which the torus does not absorb.

The radio jet only appears to be present (or at least observable) in $\sim 10\%$ of AGN. It is thought to arise from magnetohydrodynamic processes in the accretion disc, and generates synchrotron radiation from the charged particles, probably electrons (and perhaps positrons) spiralling along the magnetic field lines defining the jet axis. Nearby radio-loud AGN occur almost exclusively in elliptical galaxies, whereas radio-quiet AGN (those lacking significant radio structures) are hosted by spiral galaxies. Dunlop et al. (2003) have found that more distant and luminous AGN, namely the quasars, reside in elliptical galaxies whether they are radio-loud or radio-quiet; they find the radio-loudness of an AGN to be dependent upon the mass of the central

black hole, with radio-loud objects always having a black hole mass greater than 10^9 solar masses. This restriction of radio phenomena to the extreme end of the black hole mass range provides a straightforward explanation of why only a small fraction of AGN are radio-loud.

Somewhere within the AGN structure - and there is no consensus about the location - lies the ‘warm absorber’. This consists of a highly-ionised gaseous outflow which leaves its imprint on the soft X-ray and UV spectra by way of distinctive absorption features. Understanding the warm absorber is crucial in building up a picture of the physical structure of the nuclear environment, the energy transport within it, and the interactions of the active nucleus with the host galaxy. The class of AGN with the best studied and best understood warm absorbers is the Seyfert galaxies.

1.2.1 Seyfert galaxies

As knowledge of AGN increases, with technological improvements in instrumentation, the ‘boundaries’ between different classes of AGN become ever more vague. The basic characteristic of a Seyfert galaxy is the presence of a radio-quiet active nucleus - i.e. no extended radio structure. Nearby Seyfert nuclei are found in spiral galaxies; at higher redshifts and luminosities, they can also appear in ellipticals. The subject of higher redshift Seyferts then begs the question of how Seyferts differ from radio-quiet quasars. An approximate distinction is whether a host galaxy is visible; Seyferts have a readily observable host, whereas quasars do not. Of course, improving instrumentation inevitably shifts this boundary to ever more distant objects, and so the following general criterion is used: for quasars, the B-band magnitude M_B is less than -23, whereas for Seyferts, M_B is greater than -23 (Véron-Cetty and Véron, 2003). In the X-ray band, the very approximate dividing line is that quasars have a 2–10 keV luminosity L_x greater than about 10^{44} erg s^{-1} , whereas Seyferts have luminosities lower than this. The dividing line in both X-rays and optical corresponds to the break in the respective luminosity function between numerous, nearby, low luminosity AGN (Seyferts) and rare, distant and highly luminous AGN

(quasars).

Seyfert galaxies are subdivided into the Seyfert 1 and Seyfert 2 categories according to their optical emission line properties. In Seyfert 1 galaxies we see both broad and narrow optical emission lines, as well as the high energy radiation direct from the nucleus. Seyfert 2 galaxies only have narrow optical emission lines. The existence of the two classes of Seyfert galaxies is thought to be an orientation effect due to the obscuring effect of the dusty torus, as described above. Of course, there are objects with intermediate properties between the two classes, and these are designated Seyfert 1.2, 1.5 and so on. NGC 3783 and NGC 7469, which I investigate in this thesis, are designated Seyfert 1 and Seyfert 1.2 respectively.

Seyfert 1 galaxies have a typical set of observational properties in the X-ray band. Their X-ray spectral slope Γ was initially found to be ~ 1.7 in data from the Einstein observatory (Mushotzky, 1984) and EXOSAT (Turner and Pounds, 1989); later work revealed, using data from GINGA (Nandra and Pounds, 1994) and ASCA (Nandra et al., 1997), that the average spectral index is ~ 1.9 if the effects of the soft X-ray warm absorber and hard X-ray reflection (see below) are taken into account. In the hard X-ray band, the spectrum often contains evidence of reflection from either neutral or ionised matter in the form of the $\sim 20\text{--}50$ keV ‘reflection hump’ (which can affect the form of the spectrum down to below 10 keV), a neutral iron absorption edge at 7.1 keV, and an iron $K\alpha$ emission line. Prior to XMM-Newton and Chandra, it was thought that relativistic broadening of these lines was very common, due to an origin in the inner regions of an accretion disc (Nandra et al., 1997); however, with the better signal-to-noise and better spectral resolution of current observations, many lines previously thought to be broadened have been shown to be narrow, for example in NGC 3783 (Kaspi et al., 2001), NGC 4151 (Schurch et al., 2003), and NGC 5548 (Pounds et al., 2003c). The new data have, though, strongly supported the existence of relativistic disclines in MCG-6-30-15 (e.g. Vaughan and Fabian, 2004), Markarian 766 (Mason et al., 2003a) and probably also NGC 4051 (Salvi, 2003).

There is often an excess over the extrapolation of the hard X-ray continuum

(generally below ~ 2 keV), which can be modelled as a combination of blackbodies (Shields, 1978; Malkan and Sargent, 1982) - emission from the innermost parts of an accretion disc - or a blackbody spectrum modified by inverse compton scattering in a hot disc corona (Haardt and Maraschi, 1991, 1993). The soft excess - or underlying power-law, where a soft excess is not present - is cut into by absorption features due to the warm absorber. X-ray warm absorption was first identified in the spectrum of the radio-quiet quasar MR2251-178 by Halpern (1984).

Prior to Chandra and XMM-Newton, these soft X-ray features were modelled as absorption edges due to O VII and O VIII (e.g. Reynolds, 1997). Since that time, it has been known that the situation is more complicated: the main (and diagnostically most useful) manifestation of X-ray warm absorbers is narrow absorption lines (Kaastra et al., 2000), similar to those seen for many years in the UV; the feature which looked at CCD resolution like an O VII absorption edge now turns out to be partially or entirely due to an Unresolved Transition Array (UTA) of M-shell iron transitions (Sako et al., 2001), and there is even (contested) evidence for soft X-ray relativistically broadened emission lines (Branduardi-Raymont et al., 2001; Sako et al., 2003), analogous to those seen from Fe $K\alpha$. We now have firm evidence that warm absorbers are outflowing and have multiple ionisation phases (e.g. Kaspi et al., 2001).

Our knowledge of Seyfert 2 galaxies has also moved on since the launch of Chandra and XMM-Newton. In the past, the soft X-ray band (below ~ 2 keV) was seen to be completely absorbed away by the torus; we now know that this band contains many narrow emission lines from photoionised gas. The high angular resolution ($\sim 0.5''$) of the Chandra mirrors has been used to show that this gas takes the form of extended ionisation cones, which - at least in the case of NGC 1068 - were found to coincide with the spatial extent of the optical NLR (Young et al., 2001; Ogle et al., 2003). Kinkhabwala et al. (2002) find that the properties of this gas are consistent with those derived for the warm absorbers seen in Seyfert 1s, and claim that warm absorbers originate, indeed, in the gas of these ionisation cones seen in our direct line of sight to the central source (and thus in absorption) rather than from the side

(in emission).

Another area of interest is those objects which are intermediate between Seyfert 1 and 2. One such object, the Seyfert 1.9 galaxy NGC 7314, has been shown to exhibit evidence of lowly ionised material which probably comes from outer layers of the intervening torus (Branduardi-Raymont et al., 2002). This is of particular interest as one of the possible sources of warm absorber material is the outer layers of the torus (e.g. Krolik and Kriss, 2001), which could be photoionised by the intense radiation of the AGN and then propelled outwards by radiation pressure.

In Chapters 3 and 4, I describe my work on NGC 3783 and NGC 7469. These are Seyferts with very different kinds of warm absorber. NGC 3783 has very deep soft X-ray absorption, whereas NGC 7469 has very shallow absorption and a prominent soft excess.

1.2.2 BL Lac objects

The defining feature of BL Lac objects is their featureless continuum emission which stretches right across the electromagnetic spectrum, from radio waves to gamma rays. The overall spectral distribution of these objects generally has two peaks; the low energy peak is interpreted as synchrotron emission from a jet oriented along our line of sight, whilst the high energy peak is thought to be the result of Inverse Comptonisation of the synchrotron photons by the energetic electrons in the jet (e.g. Maraschi et al., 1992; Ghisellini et al., 1998). The synchrotron peak can be located anywhere from the far-IR to the hard X-ray band, and the high energy (Inverse Compton) peak appears at gamma-ray energies. The wide energy range across which the synchrotron peak can be generated has given rise to two main observationally-biased categories of BL Lacs (e.g. Padovani and Giommi, 1995); those which were first detected in radio surveys (RBLs or LBLs - Low-energy peaked BL Lacs) and those which were found by X-ray missions (XBLs or HBLs - High-energy peaked BL Lacs).

Probably all BL Lac objects reside in elliptical host galaxies (Urry et al., 2000). This, combined with the well-observed radio morphology of these sources and the

presence of the powerful jet, is evidence that BL Lacs are the active nuclei of radio galaxies oriented so that we are looking straight down the jet towards the nucleus. Because their spectra are dominated by the jet emission, obtaining any spectral information about the conditions in and around the nucleus itself is difficult.

In the early 1980s, the Objective Grating Spectrometer (OGS) on board the Einstein X-ray observatory detected the first indication of an X-ray spectral feature in a BL Lac. Canizares and Kruper (1984) found a broad absorption feature in the soft X-ray spectrum of PKS 2155-304 (Fig 1.2); this feature, at an energy of around 600 eV, was interpreted as either a K-shell absorption edge of O VIII or a resonance absorption trough of O VIII Ly α . Since then, similar features have been reported in other BL Lac objects: 1H1219+301, Markarian 501, PKS 0548-322, Markarian 421 (Madejski et al., 1991) and H1426+428 (Madejski et al., 1992). This is of great importance, as this absorption feature is our only spectroscopic clue as to the nature of the immediate environment of these objects.

XMM-Newton and Chandra have made many calibration observations of Markarian 421 and PKS 2155-304, with no sign as yet of the deep broad absorption features (e.g. den Herder, 2002). Chandra spectra of Markarian 421 have, however, shown evidence of weak intrinsic narrow absorption lines of O VII He α (Nicastrò et al., 2000, 2003), and narrow absorption lines from the intervening Warm-Hot Intergalactic Medium (WHIM) have been found in Chandra spectra of PKS 2155-304 (Nicastrò et al., 2002) and Markarian 421 (Nicastrò et al., 2003), as well as in XMM-Newton RGS spectra of Markarian 421, PKS 2155-304 and 3C 273 (Rasmussen et al., 2003). In Chapter 5 of this thesis, I present my work on four BL Lac objects (1H1219+301, H1426+428, Markarian 501 and PKS 0548-322) which were observed in XMM-Newton RGS Guaranteed Time in order to investigate the broad absorption features observed in the past.

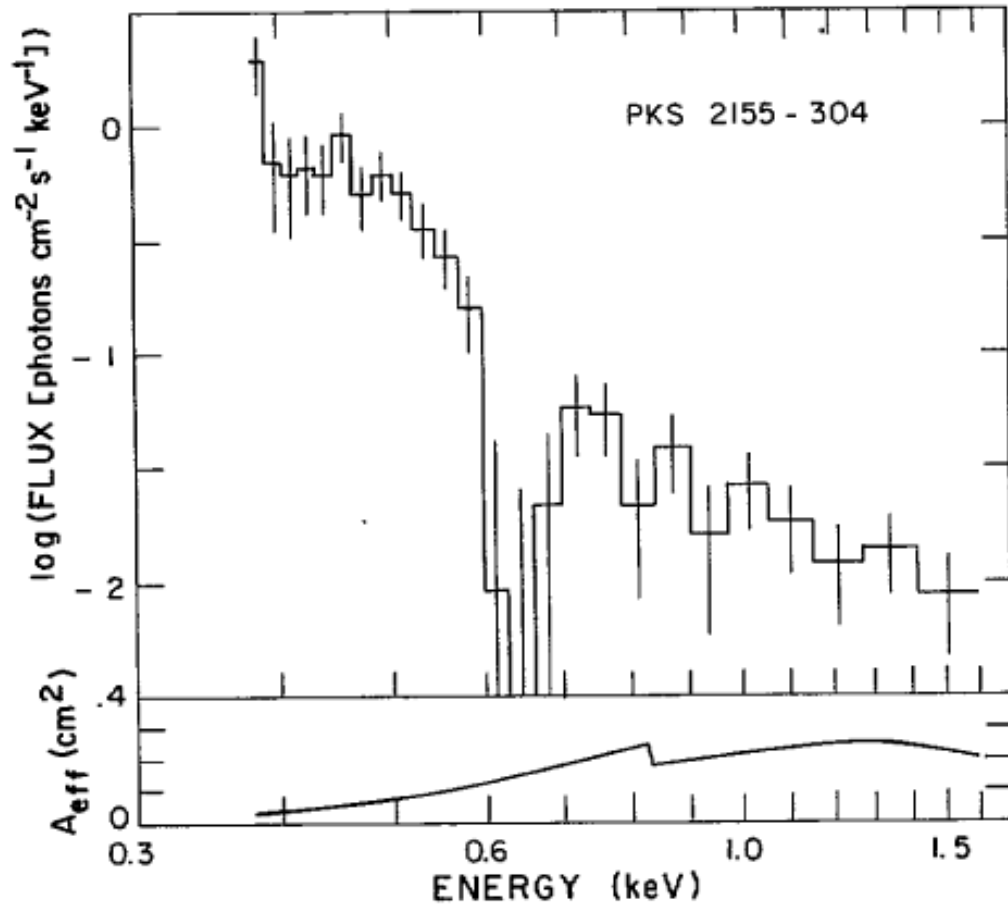


Figure 1.2: Broad absorption feature (at ~ 0.65 keV) in the Einstein OGS spectrum of PKS 2155-304 (Canizares and Kruper, 1984).

1.3 Spectroscopy

This thesis concentrates on the X-ray spectroscopy of AGN. In this section, I introduce the scientific background and practical usage of X-ray spectroscopy as it applies to AGN.

Astronomical X-ray spectroscopy has become a very different field since the launch of Chandra and XMM-Newton. Prior to these missions, the relatively low spectral resolution (and statistical quality) of the data precluded almost all spectroscopy of individual atomic transitions, with the scope of analysis largely limited to continuum processes. Certain classes of objects - including stars, supernovae and galaxy clusters - did have spectra good enough to fit low resolution models of emission lines from thermal plasmas, but it was still a very long way from the kind of direct measurements which could be made at optical wavelengths. Solar physics was the major exception as it has been possible to do high resolution X-ray spectroscopy of the Sun for many years; this difference in the quality of data, and in the type of science that could be done, must surely be a major contributor to the way that X-ray solar studies have diverged from ‘mainstream’ X-ray astronomy. As far as Active Galactic Nuclei were concerned, atomic spectroscopy was almost entirely limited to the prominent Fe $K\alpha$ emission line at 6.39 keV. Absorption edges of O VII and O VIII were fitted in the soft X-ray band (e.g. Reynolds, 1997), where there were signs of absorption by ionised gas, and as time went by some groups began fitting this absorption with self-consistent photoionised absorption models (e.g. George et al., 1998) based on codes such as Cloudy (Ferland et al., 1998), Xstar (Kallman and McCray, 1982) and ION (Netzer, 1996). Even so, it was not necessary for most X-ray astronomers to have a detailed physical understanding of atomic spectroscopy.

It is no longer possible to get away with this. The high spectral resolution, high signal-to-noise X-ray spectra being returned on a daily basis from Chandra and XMM-Newton have finally put atomic physics into X-ray astronomy. It goes without saying that this has greatly increased the scientific reach of the discipline, and has

brought the X-ray spectroscopic techniques developed in solar X-ray spectroscopy (and plasma physics) to a much wider community. In this section I will begin by describing the processes which generate X-ray continuum spectra, and move on to discuss atomic spectroscopy and the uses to which it can now be put in the study of AGN.

1.3.1 Continuum processes

The mathematical function forever linked with AGN is the power-law. This describes the basic shape of the spectral continuum in the X-ray band, and is expressed algebraically as:

$$F_p = AE^{-\Gamma}, \quad (1.1)$$

where $F_p(E)$ is the X-ray photon flux per unit energy E , and Γ is the photon index or slope of the power law. Multiplying through by E , one gets the energy flux F_E :

$$EF_p = F_E = AE^{-\Gamma+1} = AE^{-\alpha}, \quad (1.2)$$

where α is known as the energy index, and multiplying by E a second time yields

$$EF_E = \nu F_\nu, \quad (1.3)$$

where ν is frequency. $\log \nu F_\nu$ is commonly plotted against $\log \nu$ in plots of the overall Spectral Energy Distribution (SED) of AGN. Such plots are useful because a totally flat spectrum, with the same energy output all the way from radio waves to gamma rays, would appear as a horizontal line. The energy output per unit logarithmic frequency interval is therefore directly comparable between different parts of the spectrum, and it is immediately obvious where the majority of the energy output is taking place.

What, though, is the physics behind the power-law continuum? This continuum emission shape is formed by the Inverse Compton process, whereby relatively low

energy photons interact with very fast-moving electrons (with kinetic energies of up to a few hundred keV), gaining energy from them. The probability of multiple interactions decreases exponentially with the number of scatterings, whilst the energy increase per scattering is also exponential - the balance of these two effects produces the power-law shape (e.g. Reynolds and Nowak, 2003). In the AGN context, the inner parts of the accretion disc radiate in the ultraviolet, and these UV photons encounter high energy electrons within a ‘corona’ above the accretion disc. The photons are then upscattered to X-ray energies. Changes in the populations and distributions of the UV photons and relativistic electrons then provide a natural explanation for the variability of the power-law continuum.

The UV emission from the accretion disc is thought to be thermal in origin. Generally, thermal plasma at a high enough temperature gives off X-ray emission lines and bremsstrahlung radiation as it cools. At relatively lower gas temperatures - below ~ 2 keV - the emission lines dominate, but at temperatures of a few keV the bremsstrahlung continuum becomes much more important than the lines. I discuss emission lines in detail below; bremsstrahlung is literally ‘braking radiation’ given off by electrons as they interact electromagnetically with the ions in the plasma and are decelerated onto a different trajectory. In an accretion disc, the plasma has a very high optical depth; it therefore radiates as a blackbody rather than emitting a bremsstrahlung continuum or emission lines. It is actually unusual to see an X-ray bremsstrahlung spectrum in AGN; the only situations where it is important are regions of significant star formation - the nuclei of starburst galaxies, which may host LINERs - and also in cases where there is extended X-ray emitting plasma around the nucleus, and in the ISM, of a radio galaxy.

The blackbody spectrum used in xspec (see chapter 2) has the form

$$F(E) = \frac{8.0525 L_{39} E^2 dE}{D_{10}^2 (kT)^4 (e^{E/kT} - 1)}. \quad (1.4)$$

where $F(E)$ is the flux at energy E , L_{39} is the source luminosity in units of 10^{39} erg s^{-1} , D_{10}^2 is the distance to the source in units of 10 kpc, and kT is the temperature of the emitter in keV. Although the accretion discs of AGN are thought to be too cool to give rise to blackbody radiation at X-ray wavelengths, the X-ray soft excess is often

modelled with one or more blackbody components as a convenient fitting strategy. It could be more physically realistic to use an Inverse Comptonisation model, such as *compTT* in *xspec*, but such models have a large number of parameters which are hard to constrain.

As well as Inverse Comptonisation of accretion disc photons, power-law spectra can also be generated by synchrotron emission from electrons spiralling at relativistic speeds along the magnetic field of AGN jets. In AGN, synchrotron emission is generally most important in the radio band, but certain BL Lacs have a synchrotron peak in the X-rays or at even higher energies (e.g. Costamante et al., 2001). These photons can then interact again with the relativistic electrons, being boosted to higher energies (X-rays and γ -rays) by Inverse Comptonisation. This is known as the Synchrotron Self-Compton process, which is most important in jet dominated sources: this predominantly means BL Lac objects and their high luminosity, high redshift versions (radio quasars), but jets can also be important in Seyfert type objects like III Zw II (Salvi et al., 2002).

Another important process influencing the X-ray spectrum is reflection. The spectral effects of reflection depend upon the ionisation state of the material the X-rays are being reflected from. If the reflector is highly ionised (e.g. Nayakshin et al., 2000), the reflected and incident spectra are very similar below 30 keV, because the scattering is independent of energy, but the reflected spectrum begins to roll over above that energy and has gone down to almost zero by 100 keV. This is due to high energy photons losing energy from multiple scatterings in the medium. If, at the other extreme, the reflector is neutral (Lightman and White, 1988; George and Fabian, 1991), the reflected spectrum begins to fall off below around 20 keV (due mostly to iron opacity) and above about 50 keV due to Compton recoil (the higher the photon energy, the greater the fraction of its energy it loses per collision). Neutral reflectors also give rise to fluorescent emission lines (see below). This reflection hump between ~ 20 – 50 keV is observed in many AGN, and can be interpreted as originating from reflection off a neutral (or lowly ionised) accretion disc, or alternatively as reflection off the dusty torus. Although the reflected flux begins to decrease

below about 20 keV, the reflected component of the continuum can have enough flux in it to enable the low energy tail of the reflection hump to be observable down to around 8 keV.

1.3.2 Atomic spectroscopy

The major emission line produced in X-ray reflection, Fe $K\alpha$, was generally the only atomic line transition directly measurable in AGN spectra prior to Chandra and XMM-Newton. Now, with soft X-ray spectra showing a huge range of spectral features, one has to understand the atomic processes which produce them. In this section, I describe some of these processes and their practical relevance for X-ray spectroscopy of AGN. The following discussion owes much to Reynolds (1996), Dubau and Porquet (2002), Kinkhabwala et al. (2002) and Tatum (2003).

There are two ionisation mechanisms which govern the behaviour of astrophysical X-ray emitting and absorbing plasma. In collisional ionisation, free electrons collide with the ions in the plasma and the resulting energy transfer liberates further electrons from the outer shells of the ions. In the intense radiation field of an AGN, however, photoionisation is the most important process.

Photoionisation is defined as the removal of an electron from an ion due to energy transfer from an incident photon. That part of the photon energy over and above the energy threshold needed to remove the electron (the ionisation energy) becomes the kinetic energy of the liberated electron. The energy level an electron can be removed from is therefore determined by the energy of the incoming photon; UV photons could be sufficient to remove outer-shell electrons, whereas relatively hard X-rays are required to remove the inner-shell electrons of a medium-Z element like iron.

If an inner shell (K-shell) electron is removed by an incoming high-energy photon, an electron from another energy level - for example the L-shell - can then drop down to fill the space in the K-shell, with the emission of a fluorescent line photon. Alternatively, if there is another L-shell electron available, the energy released from this electron transition can go into removing it from the ion. This is known as

the Auger effect or autoionisation. The fluorescent yield is the probability that photoionisation will be followed by fluorescent line photon emission rather than autoionisation. Fluorescent yields have $\sim Z^3$ dependence (e.g. Krolik, 1999), so although inner-shell emission lines from higher Z elements (especially Fe, but also Si, S, Ar and Ca) can be observed, such lines in low- Z elements like O, N and C, will be much weaker.

The broad range of photon energies emitted by an AGN implies that all ionisation states can potentially be observed. In this thesis, I adopt the terminology which labels an ion according to which neutral atom would have the same electronic configuration. For example, if an atom had only one or two of its electrons left, its electronic configuration resembles that of hydrogen or helium. Such an ion is then termed hydrogen-like (H-like) and helium-like (He-like); this notation is also extended to configurations involving larger numbers of electrons with the use of the appropriate term for the number of electrons remaining: Li-like, Be-like, and so on.

Of course, an incident photon may not have enough energy to remove an electron from an ion. In this case, it might still be able to transfer enough energy to a bound electron to enable it to move to a higher energy level, which is called photoexcitation. This is known as a bound-bound transition as the electron remains bound to the ion. Since there is only one energy at which a transition between a particular pair of levels can take place, this leads to the formation of an absorption line in a narrow, well-defined energy range. In photoionisation, when an electron is removed from an atom altogether - a bound-free transition - the electron can be removed by any photon with an energy greater than the threshold for removing the electron from the atom. The absorption feature produced by a bound-free transition is therefore very spread out; it is deepest at the ionisation energy, and extends to higher energies, becoming weaker with increasing energy. The absorption at energies above the threshold can be expressed as a function of energy E as

$$Q_E = e^{-d(\frac{E}{E_t})^{-3}}, \quad (1.5)$$

where Q_E is the multiplicative factor, d is the absorption depth at the threshold and E_t is the threshold energy.

These processes also work in the opposite direction. The recombination of a free electron onto an ion, emitting a photon, is called radiative recombination. Another possible mechanism for this is dielectronic recombination; this is the recombination of a free electron onto an ion, in which the energy of recombination is not emitted as a photon but instead goes into promoting a bound electron to an excited state. This then leads either to autoionisation - the electron leaving the atom - or to the electron moving down to a lower energy level and emitting a photon.

Recombination of free electrons onto the ground state of ions leads to the generation of photons with a range of energies, since the free electrons will have a particular energy distribution. If the free electrons have a thermal (Maxwellian) energy distribution, the shape of the resulting Radiative Recombination Continua (RRC) is determined by the electron temperature T ; the RRC width is of order $\sim kT$. In a collisional plasma, the electrons are at a high temperature with a wide range of energies, so the RRCs will be broad, shallow, and difficult to distinguish from the underlying bremsstrahlung continuum. In photoionised plasma, the electrons are at a lower temperature for the same level of ionisation, with a narrower distribution of energies, and so the RRCs are narrow and appear as clearly visible triangular emission features at the ionisation energy (i.e. absorption edge position) of a given ion. Fig. 1.3 shows how the shape of an RRC changes with temperature.

For a body of photoionised gas, the ionisation state can be quantified in terms of the ionisation parameter ξ , defined as the ratio of ionising flux to the gas density:

$$\xi = \frac{L}{nr^2} \quad (1.6)$$

where L is the 1–1000 Rydberg source luminosity (in erg s^{-1}), n the gas density (in cm^{-3}) and r the source distance in cm, so ξ has the units erg cm s^{-1} (Tarter et al., 1969). Fig. 1.4 and Fig. 1.5 are plots of the relative ionic abundances of oxygen and iron states, respectively, in plasma at a range of ionisation parameters; these two astronomically abundant elements are particularly important in modelling AGN warm absorbers.

ξ is the ionisation parameter that I use throughout this thesis; other definitions of ionisation parameter are also used by AGN spectroscopists. The main alternative

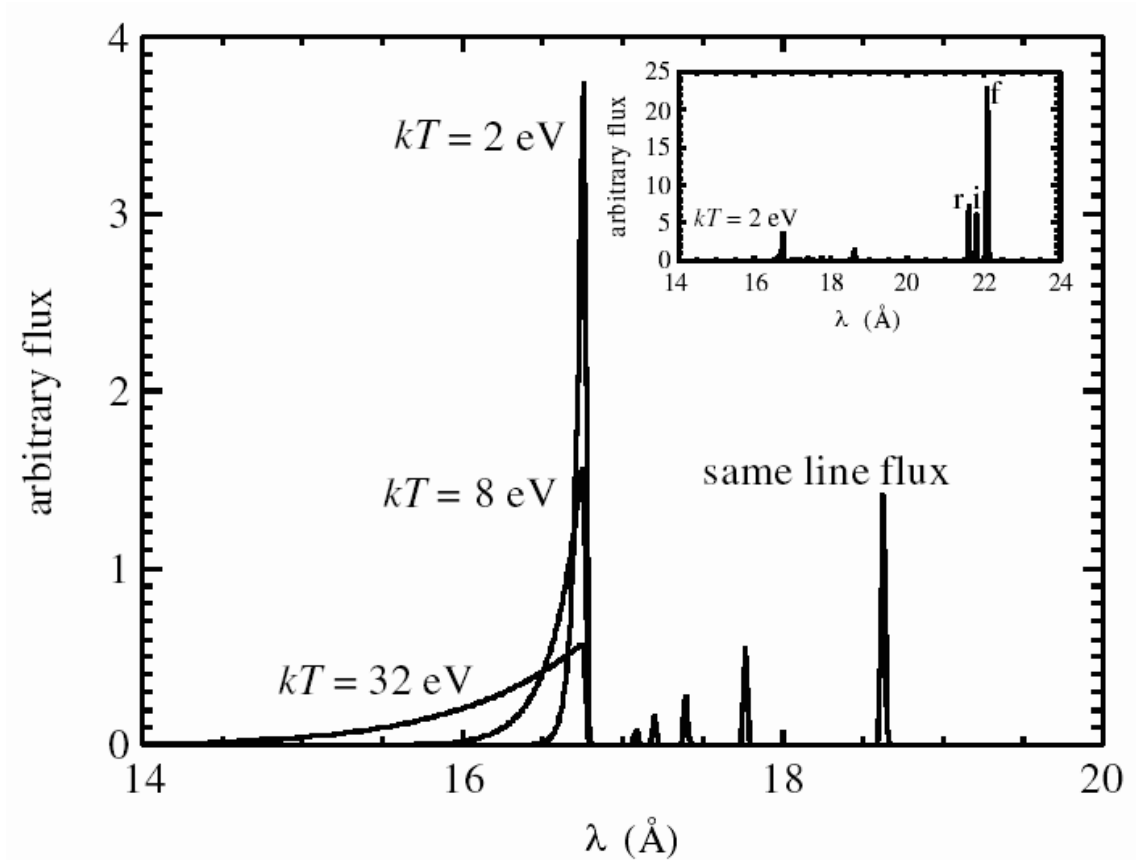


Figure 1.3: Part of the emission line spectrum of O VII, created by recombination of electrons onto O VIII ions; the plot shows how the shape of the Radiative Recombination Continuum (RRC) feature changes according to the temperature of the thermal distribution of recombining electrons (from Kahn et al., 2002). In each of the three cases (with electron temperatures of 2 eV, 8 eV and 32 eV respectively) the recombination rate is assumed to be the same, so the heights of the emission lines are constant. The inset graph (top right) shows the whole range of O VII soft X-ray emission features at a recombining electron temperature of 2 eV, including the triplet of resonance (r), intercombination (i) and forbidden (f) emission lines whose intensity ratios are sensitive to density and temperature. These plots demonstrate clearly that the O VII RRC will only be easily observable when it arises in low temperature, photoionised gas.

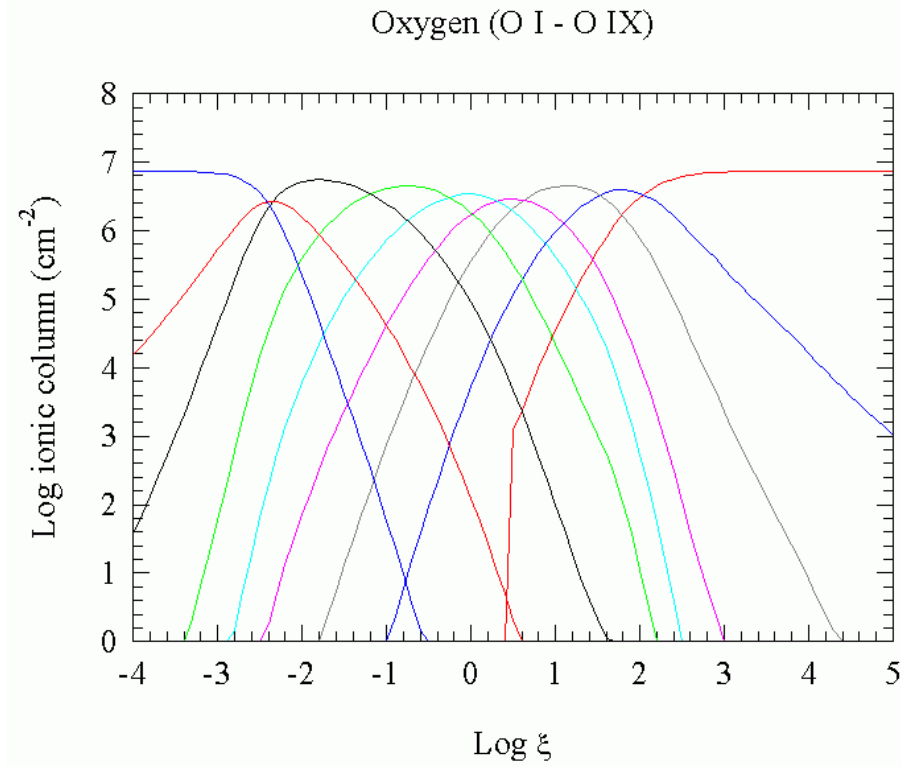


Figure 1.4: Variation of relative ionic abundance with ionisation parameter ξ of different oxygen states within a photoionised plasma. The ionisation states go in order of increasing ionisation from left to right, from neutral (O I) to fully stripped (O IX). The relative abundance is given in terms of the log of the ionic column density for solar abundances (Anders and Grevesse, 1989), where hydrogen is 10 by definition (so that a log column of 4 for any ion means that the column of that ion with respect to hydrogen is $10^{4-10} = 1 \times 10^{-6} \text{ cm}^{-2}$). The data were generated by J. Kaastra using Xstar, with the NGC 5548 SED used in Kaastra et al. (2002b) and a gas density of 10^8 cm^{-3} . The temperature of the gas in the model is a function of the ionisation parameter.

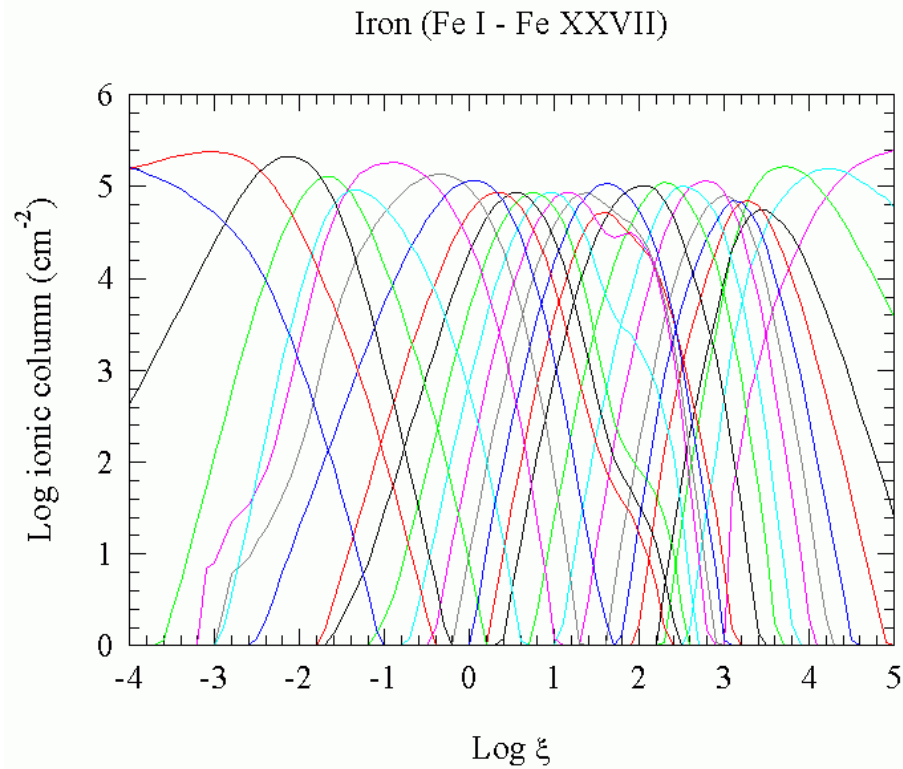


Figure 1.5: Variation of relative ionic abundance with ionisation parameter ξ of different iron states within a photoionised plasma. The ionisation states go in order of increasing ionisation from left to right, from neutral (Fe I) to fully stripped (Fe XXVII). The relative abundance is given in terms of the log of the ionic column density for solar abundances (Anders and Grevesse, 1989), where hydrogen is 10 by definition (so that a log column of 4 for any ion means that the column of that ion with respect to hydrogen is $10^{4-10} = 1 \times 10^{-6} \text{ cm}^{-2}$). The data were generated by J. Kaastra using Xstar, with the NGC 5548 SED used in Kaastra et al. (2002b) and a gas density of 10^8 cm^{-3} . The temperature of the gas in the model is a function of the ionisation parameter.

to ξ is U (see e.g. Netzer, 1996), which is the ratio of the number density of ionising photons to the electron density:

$$U = \int_{\nu} \frac{L_{\nu}/h\nu}{4\pi nr^2c} d\nu \quad (1.7)$$

U can be integrated over the entire Lyman continuum (generally taken as 1–1000 Ryd, or ~ 13.6 eV–13.6 keV), over the 0.1–10 keV range where most of the actual X-ray absorption takes place (U_x), or over the energy range most relevant for oxygen absorption, namely 0.54–10 keV (the ‘oxygen ionisation parameter’ U_{ox}). The relationship between ξ and U is

$$\xi = U \frac{Lhc}{D_L^2 \int_{\nu} \frac{f_{\nu}}{\nu} d\nu} \quad (1.8)$$

where L is the 1–1000 Rydberg source luminosity (in erg s^{-1}) as before, D_L is the luminosity distance from us to the source (in cm), and f_{ν} is the source flux as a function of frequency. This last factor is generally assumed, for convenience, to have a power-law form;

$$f_{\nu} = k\nu^{-\alpha} \quad (1.9)$$

where k is a normalisation constant and α is the energy index of the power-law. An AGN SED will usually be parameterised by a series of adjoining power-laws with different slopes, and the flux has therefore to be integrated over all of these.

The spectral features formed can be sensitive to the physical conditions in the gas. An important example of this are the He-like triplets. These are triplets of emission lines from He-like ions whose ratios are sensitive to the density, temperature and ionisation mechanism of the plasma. These lines are known as the forbidden ($1s2s \ ^3S_1 - 1s^2 \ ^1S_0$; termed z), intercombination ($1s2p \ ^3P_{1,2} - 1s^2 \ ^1S_0$; x+y) and resonance ($1s2p \ ^1P_1 - 1s^2 \ ^1S_0$; w) lines respectively. The origins of this effect are best described with reference to the energy level diagram (Fig. 1.6).

The populations of the different energy levels depend upon the rates of collisional excitation and ionisation, photoexcitation and photoionisation, and radiative and dielectronic recombination. In a low density plasma, collisional excitation and ionisation will generally be unimportant. As the density increases, however, the

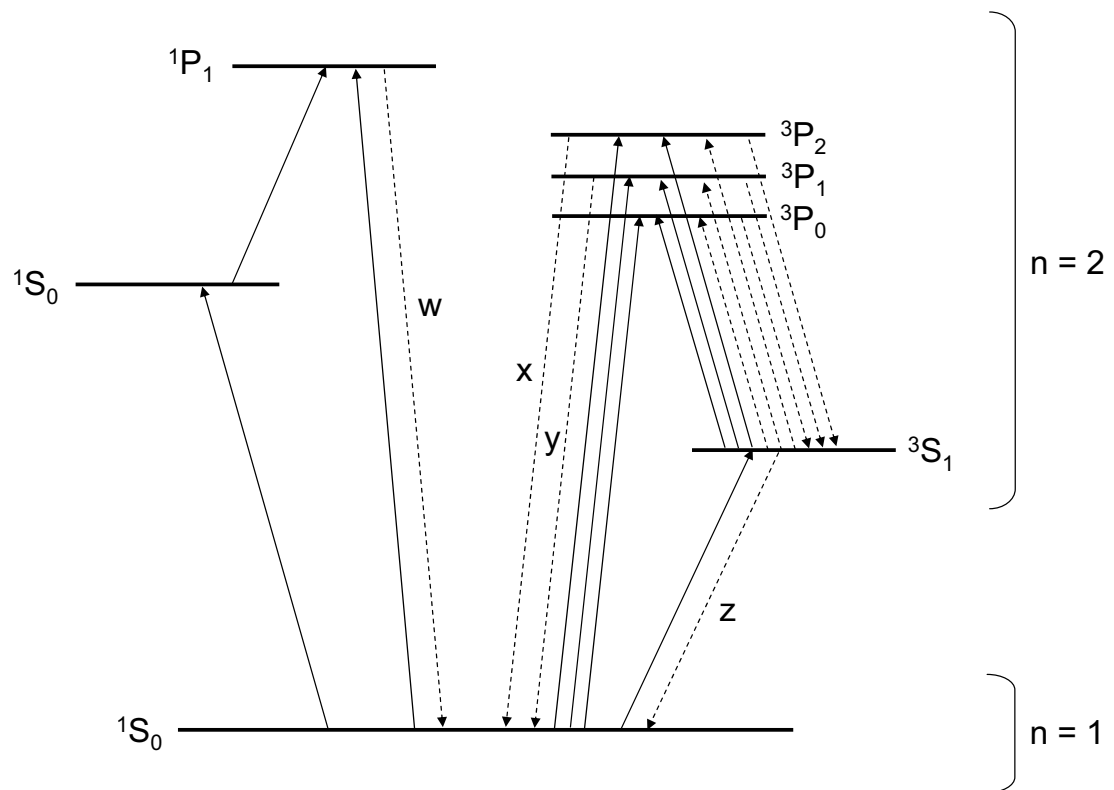


Figure 1.6: Simplified energy level diagram for a He-like ion (based on Fig. 1, Dubau and Porquet, 2002). Solid lines are collisional transitions and dotted lines are radiative transitions. The lines denoted w, x, y and z are the resonance (w), intercombination (x+y) and forbidden (z) lines of the triplet respectively.

probability of collisions increases, and an electron in the $2s\ ^3S_1$ level becomes more liable to be collisionally excited to $2p\ ^3P_{1,2}$. Instead of making the radiative transition associated with the forbidden line, then, the electron is collisionally excited to the upper levels of the intercombination lines. Therefore, as the density increases, the intercombination line blend ($x+y$) gains strength at the expense of the forbidden line. The ratio of the forbidden to intercombination line,

$$R = \frac{z}{x + y}, \quad (1.10)$$

can therefore be used as a density diagnostic. At higher densities, electrons in the $2s\ ^1S_0$ level become collisionally excited to $2p\ ^1P_1$, the upper level of the resonance line, so the resonance line also gains in strength at high densities. The rate of collisional excitation also increases with increasing temperature, and so the effects described here are also temperature sensitive. The temperature sensitivity for the resonance line is, however, different to that for the forbidden and intercombination lines. The ratio therefore used as a temperature diagnostic is

$$G = \frac{z + (x + y)}{w}. \quad (1.11)$$

Values for R and G were calculated by Porquet and Dubau (2000) for the He-like ions of C, N, O, Ne, Mg and Si over a wide range of densities and temperatures. G can also be used as an indicator of the ionisation process, since the resonance line dominates the other two lines of the triplet in a collisional plasma, whereas the forbidden line is the most prominent in a photoionised plasma. Porquet and Dubau (2000) put numbers to this as follows: $G \sim 1$ corresponds to a collisional plasma, whereas G greater than 4 implies a purely photoionised medium. Any number in between the two could be an indication of a mixture of the two processes.

Another ratio defined by Porquet and Dubau (2000) is

$$X_{ion} = \frac{u}{w}, \quad (1.12)$$

where u is the flux of the H-like $Ly\alpha$ emission line and w is the flux of the resonance line (which is $He\alpha$) as before. The ratio of these two line strengths is used to

determine the ionisation state of the gas which is emitting the He-like triplet. It is important to note that this ratio does not correspond directly to the relative proportion of the H-like and He-like species in the gas; rather, since these lines are driven by recombination from the next states up, it corresponds to a ratio of the fully-stripped to the H-like populations (Behar et al., 2003). The ratio can be compared to a plot such as Fig. 1.4 in order to find the corresponding ionisation parameter.

It turns out that the diagnostics involving R and G have to be treated quite carefully (Kinkhabwala et al., 2002; Dubau and Porquet, 2002). The original problem was posed in terms of electron collision rates having the major influence on the line ratios; it turns out that, in any scenario where intense UV radiation is present, electrons will move from the $2s\ ^3S_1$ level up to $2p\ ^3P_{1,2}$ by photoexcitation. This mimics the effect of collisional excitation on the relative populations of the levels and therefore on the density diagnostic $R=z/(x+y)$ ratio. The influence of photoexcitation on the strengths of the z and $(x+y)$ lines also has an effect on the temperature diagnostic G ratio, and on its use in determining the dominant ionisation mechanism. An apparent hybrid plasma (both collisionally ionised and photoionised) could simply be a photoionised plasma in which photoexcitation is important. The practical implication of this is that these quantitative diagnostics have to be treated with some care for UV-bright systems like AGN or starbursts, although they retain their validity in collisional plasmas such as stellar coronae.

As shown by Kinkhabwala et al. (2002), He-like triplets have to be considered alongside other spectral features, such as the higher order emission transitions ($\text{He}\beta$, $\text{He}\gamma$ etc., which are also enhanced by photoexcitation) and the He-like RRC, to gain a more reliable picture of the physical conditions within the plasma (see Fig. 1.7).

The shape of the absorption and emission lines themselves is the most basic diagnostic of the state of the plasma. The standard measure of the strength or depth of a line is its *equivalent width*: this is the ‘area’ of the spectral continuum that a line takes up. Emission and absorption lines have a shape following the Voigt profile, which is a convolution of the Gaussian and Lorentzian profiles; a Gaussian

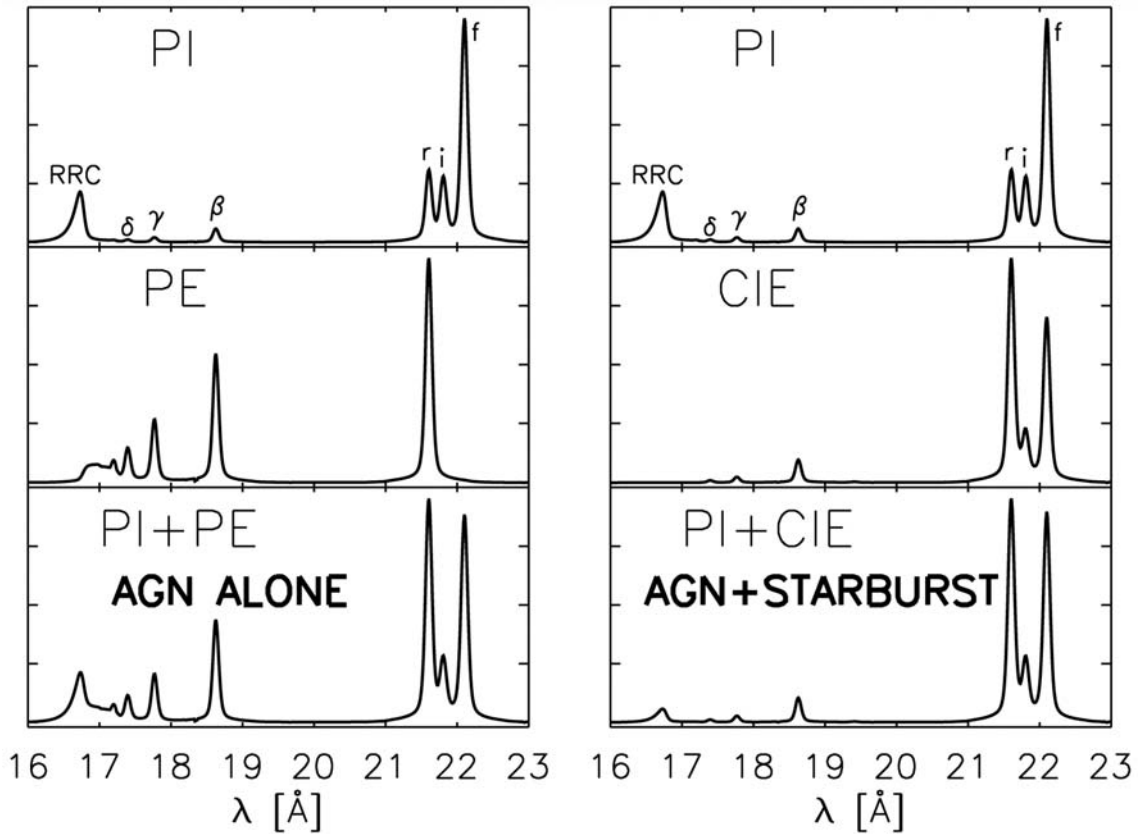


Figure 1.7: The effect of photoexcitation on the relative strengths of the soft X-ray emission lines of O VII. PI = photoionisation, PE = photoexcitation, CIE = collisional ionisation. The combination of photoexcitation and photoionisation can produce the triplet ratios expected from the combination of photoionisation and collisional ionisation (expected in an AGN with a nuclear starburst); the two cases can only be differentiated by looking at the higher order transitions (from Kinkhabwala et al., 2002).

profile is well concentrated around its central value, falling off quickly either side of it, whereas a Lorentzian has a narrow core and extended wings. The Gaussian part is contributed by thermal broadening, microturbulence and bulk motions, whilst the Lorentzian part originates from the natural width of the line (i.e. the intrinsic quantum mechanical uncertainty in the transition energy; the longer the lifetime of the state, the smaller the uncertainty in its energy) and pressure broadening. This last factor is partly due to the effects of Heisenberg's uncertainty principle: if the lifetimes of the energy states are reduced due to frequent collisions in a dense gas, the uncertainty in their energy levels is increased, and therefore any given transition can occur over a wider spread of frequencies, broadening the observed spectral lines. Pressure broadening is also partly due to electrostatic interactions between atoms, ions and electrons becoming more important at higher densities. These interactions include the Stark effect splitting bound electron energy levels in the presence of the electric field of a colliding charged particle, and the van der Waals induced dipole attractions between neutral atoms.

Fig. 1.8 shows how a Voigt profile changes with increasing optical depth. At low optical depth (and low absorbing column), the equivalent width of a Voigt profile absorption line increases linearly with the number of absorbing ions in the column. This is the optically thin regime, where the depth of the line can be used to directly infer the column density. Once the line becomes deep enough to absorb away all the continuum flux at its central wavelength, it is considered to be *saturated*; increasing the number of absorbers cannot increase the depth of the line. The curve of equivalent width against optical depth - the curve of growth (see Fig 1.9) - will be almost horizontal in this regime. In this optically thick limit, the equivalent width is entirely dependent upon the intrinsic width of the Gaussian component (i.e. the width due to thermal or velocity broadening). Because the absorption line has a Voigt profile, though, an increasing absorbing column will eventually lead to the Lorentzian wings of the line becoming significant, and the equivalent width increasing again (but more slowly than in the first phase). The picture is similar for an emission line, except for the fact that the upper limit to the initial phase

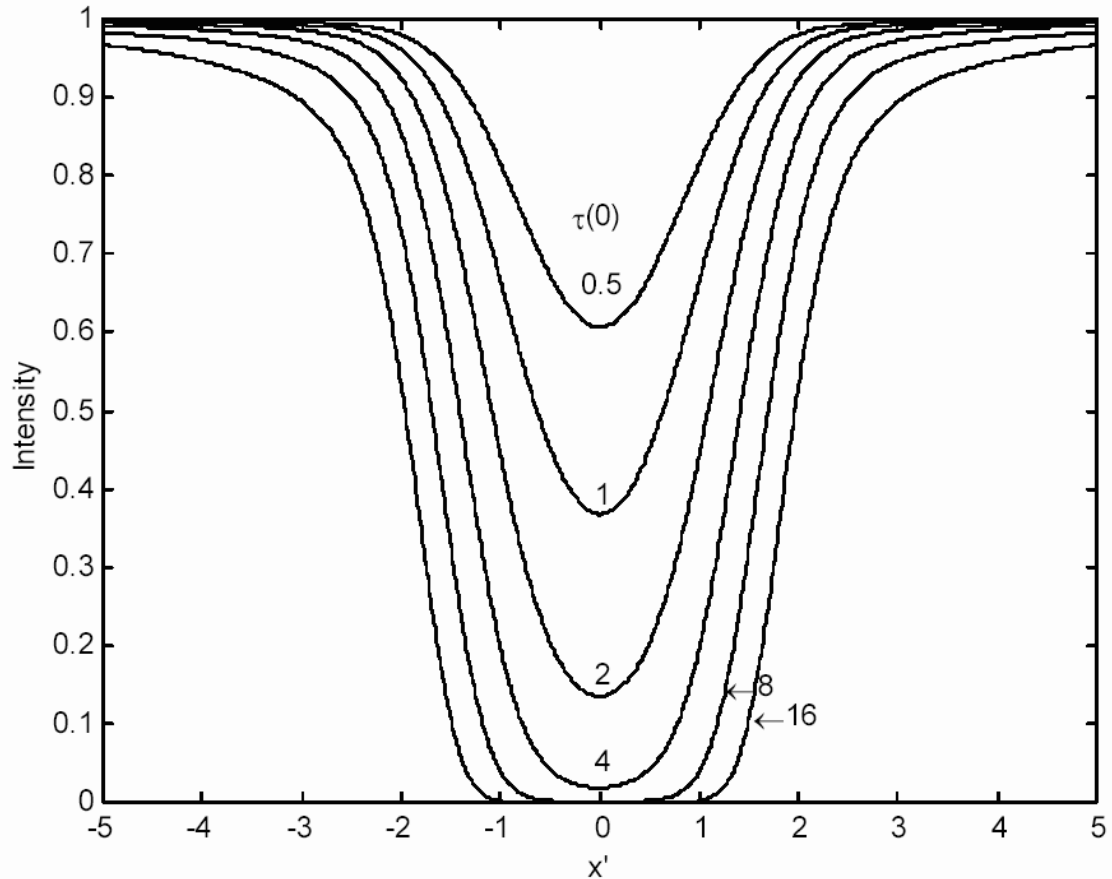


Figure 1.8: A Voigt profile plotted at a range of optical depths; $x' = \lambda - \lambda_0$ in units of $2g/\sqrt{\ln 2}$, where g is the Half Width Half Maximum (HWHM) of the Gaussian part of the line (from Tatum, 2003).

of the curve of growth is defined by the flux reaching the maximum defined by the blackbody curve at the appropriate temperature. In practice, it is very common for AGN narrow X-ray absorption lines to be saturated, but this limit is not reached by the emission lines.

1.3.3 Observational relevance to Seyfert 1s and BL Lac objects

In an XMM-Newton RGS or Chandra HETGS/LETGS soft X-ray spectrum of an AGN, the two biggest limitations are signal-to-noise (less of a problem for XMM-

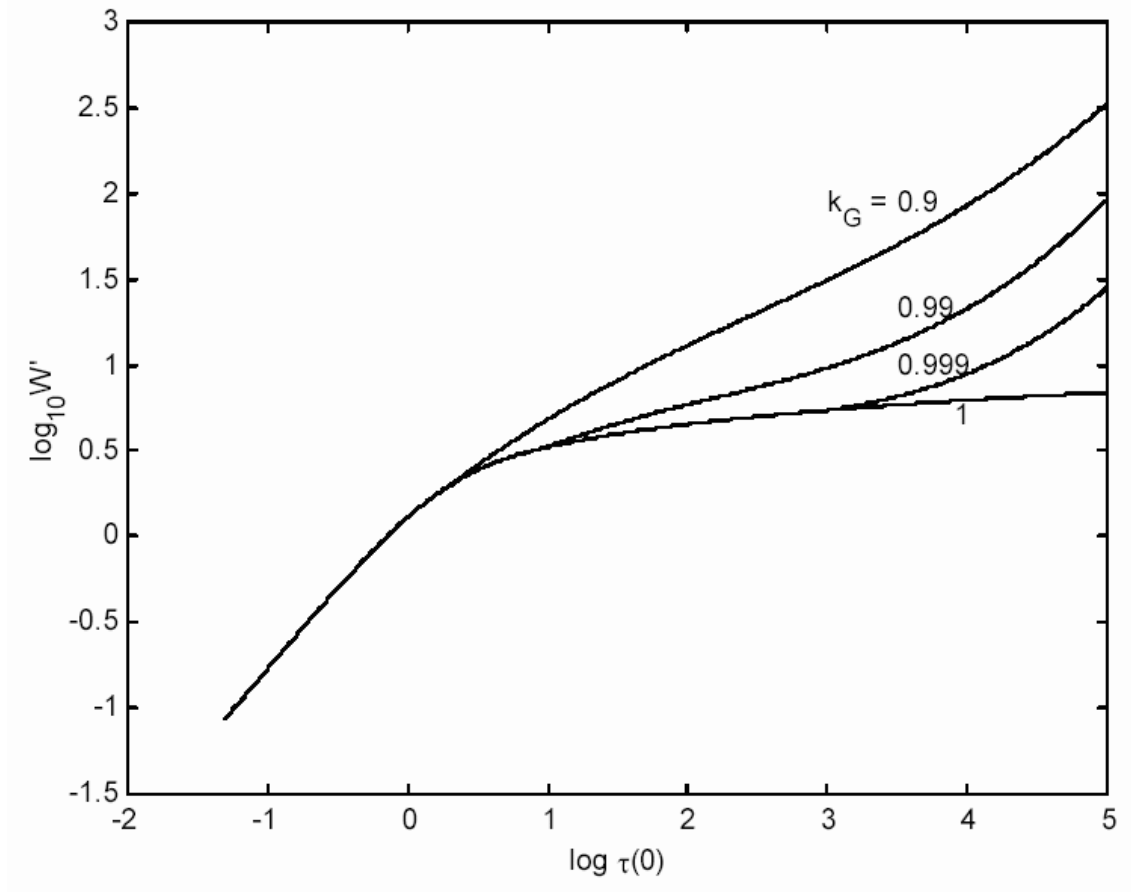


Figure 1.9: The curve of growth of a Voigt profile, plotted for different values of the ‘gaussianity’ k_G of the line, where $k_G = g/(l + g)$ and g and l are the HWHMs of the Gaussian and Lorentzian parts of the lines respectively. W' is the equivalent width of the line in units of $2g/\sqrt{\ln 2}$, and $\tau(0)$ is the optical depth at the central wavelength of the line (from Tatum, 2003).

Newton) and spectral resolution (less of a problem for Chandra). Taking those into account, one can start to attempt some spectroscopy. The first thing to look for is obviously whether there are any narrow spectral lines present (or indeed intrinsic absorption edges), and whether the features that could be lines are actually statistically significant, and not instrumental artifacts. I discuss this further in Chapter 2.

Having found and identified some believable features, one can then measure their Doppler shifted velocities, looking for the presence of outflows and inflows (redshifted emission and blueshifted absorption are the sign of a spherical or perhaps biconical outflow). There may be more than one blueshift component, and at the RGS resolution these may simply appear as a single broad absorption line. Curve of growth analysis can be used to determine the column densities of the different ions. Model fitting is another convenient way of doing this, and is helped by the presence of absorption edges at high column densities. At the RGS resolution it is generally not possible to resolve the widths of absorption lines directly, and so one has to either use model fitting, curve of growth analysis, or a value measured by Chandra or a UV spectrometer on FUSE or HST - if one assumes that the intrinsic UV absorption originates from the same gas as the X-ray absorption.

Knowing the ionic columns then allows one to derive the ionisation structure of the medium and the relative elemental abundances. Any emission lines in the spectrum are also useful; even given the limited applicability of He-like triplet ratios in AGN, the O VII triplet gives a strong indication of its origins in photoionised gas by virtue of the dominance of the forbidden line (this can be the most prominent spectral feature). If the signal-to-noise is great enough, RRCs can be used to determine the temperature of the emitting gas.

1.3.4 Spectral modelling

For the practical purposes of fitting an X-ray spectrum with some kind of global spectral model, it is desirable to have a tool which calculates the output spectrum from a cloud of photoionised gas. One such code is Xstar (Kallman and McCray,

1982), which takes an input spectrum of a given shape and luminosity and propagates it through a plasma at a given ionisation parameter. The output includes absorption, emission and continuum spectra. In this thesis, I concentrate on the modelling of photoionised absorption using SPEX (Kaastra et al., 2002a) models constructed from Xstar output, which are described in more detail in the next chapter.

Chapter 2

Observations and data analysis

2.1 Introduction

This chapter describes the observations and data analysis methods for the AGN discussed in this thesis. I begin by providing a brief description of the XMM-Newton instrumentation and compare some of its parameters with those of other X-ray missions. The work described in this thesis was carried out over three years relatively early on in the mission, whilst instrument calibration and dedicated analysis software were continuously improving, and I took advantage of such improvements as they became available. There has also, inevitably, been some evolution in certain aspects of data pre-processing methods over this time; I discuss the probable effects of this upon my data analysis in cases where it occurs.

2.2 The XMM-Newton Observatory

The XMM-Newton observatory (Jansen et al., 2001; Ehle et al., 2003) was launched in December 1999. It carries three grazing incidence Wolter type 1 X-ray telescopes, each with 58 concentric mirror shells and a focal length of 7.5 m. Two X-ray instruments are at the foci of the three telescopes: the European Photon Imaging Camera (EPIC), for imaging and spectroscopy, and the Reflection Grating Spectrometer (RGS) for high resolution spectroscopy. There are three EPIC cameras,

one per telescope, and two RGS chains. The overall layout of the instrumentation on XMM-Newton is shown in Fig 2.1.

The combined geometric effective area of the mirrors is 4650 cm^2 at 1.5 keV and $\sim 3000 \text{ cm}^2$ at 6 keV, the highest of any X-ray mission so far; Fig 2.2 shows the total effective area of the XMM-Newton mirrors alongside those of Chandra, ROSAT and ASCA, and the effective areas of the individual X-ray instruments on XMM-Newton are plotted in Fig. 2.3. The FWHM of the Point Spread Function (PSF) of the telescopes is about $6''$, as opposed to the $\sim 0.5''$ (FWHM) achieved with the Chandra mirrors (Chandra Team, 2003). Co-aligned with the X-ray telescopes is the Optical Monitor, an optical/UV telescope. I describe some of the relevant features of the scientific instruments on board XMM-Newton below.

2.2.1 EPIC-MOS and EPIC-pn

There are two EPIC-MOS (Turner et al., 2001) units on XMM-Newton. These are front-illuminated CCD cameras situated at the prime foci of two of the mirror assemblies. Each MOS camera has a $\sim 30'$ FOV, with a source PSF that is largely determined by the angular resolution of the telescopes ($\sim 6''$ FWHM), and an energy range of 0.15–15 keV. The intrinsic energy resolution of the CCD chips enables the detectors to perform non-dispersive spectroscopy on all the sources in the field of view. The FWHM energy resolution of MOS is $\sim 140 \text{ eV}$ at 6 keV, as compared with a FWHM resolution of $\sim 140 \text{ eV}$ at this energy for the Chandra ACIS CCDs (pre-launch; this has since degraded to $\sim 150\text{--}340 \text{ eV}$, dependent upon detector position, due to proton damage early in the mission (Chandra Team, 2003)), $\sim 120 \text{ eV}$ for the ASCA CCD detector (Solid State Imaging Spectrometer; HEASARC website (2004)), $\sim 30 \text{ eV}$ for the Chandra High Energy Grating (Chandra Team, 2003), and $\sim 6.5 \text{ eV}$ for the microcalorimeter on the forthcoming Astro-E2 mission (HEASARC website, 2004). Fig. 2.4 shows how the MOS resolution changes over the energy range of the instrument.

The EPIC-pn (Strüder et al., 2001) is a back-illuminated CCD camera at the prime focus of the third X-ray telescope. Like the EPIC-MOS, it has a $30'$ FOV,

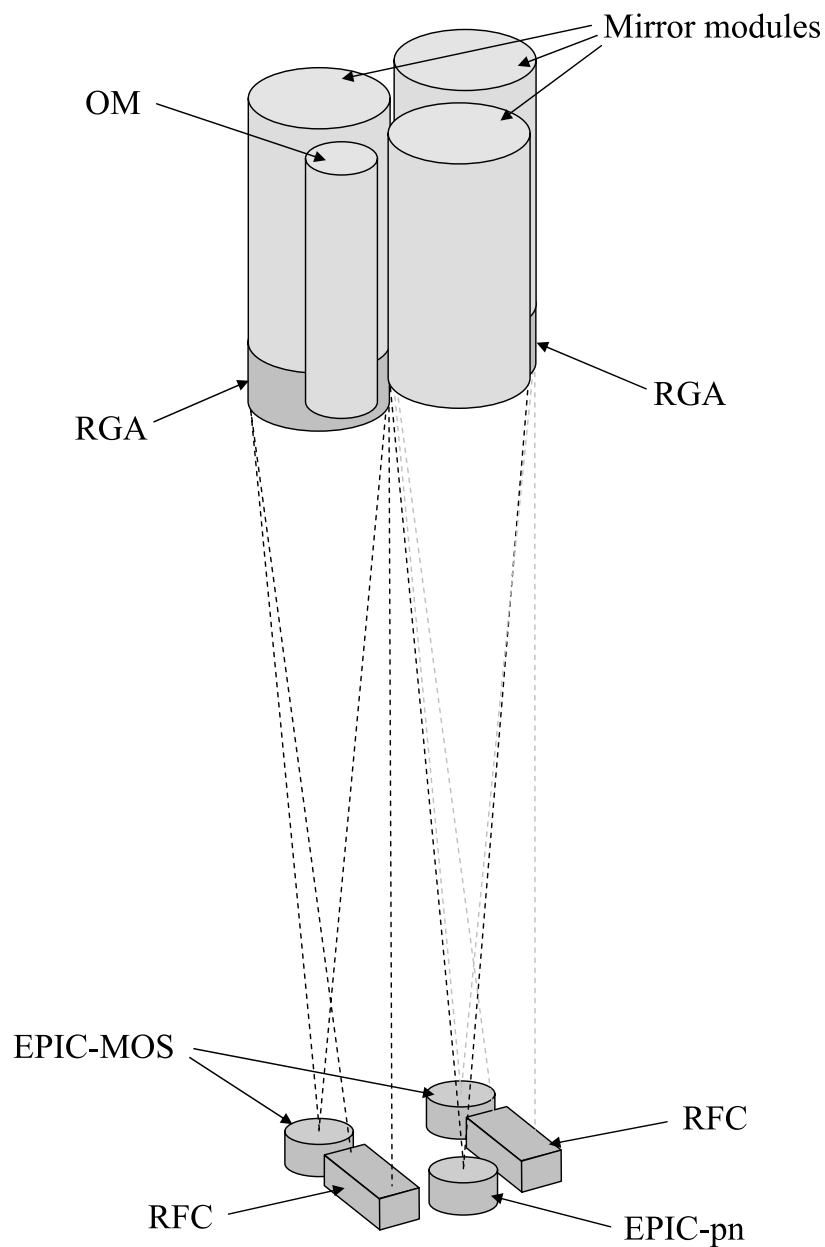


Figure 2.1: Layout of the instruments on XMM-Newton (not to scale); the three mirror modules are co-aligned with the Optical Monitor (OM). Two of the mirror modules have Reflection Grating Arrays (RGAs) attached to them, which disperse about 40% of the X-rays onto the RGS Focal Cameras (RFCs). The EPIC-MOS CCD cameras are at the prime foci of these two telescopes, and the EPIC-pn is at the prime focus of the telescope without an RGA. The dotted lines indicate the paths of the X-ray photons.

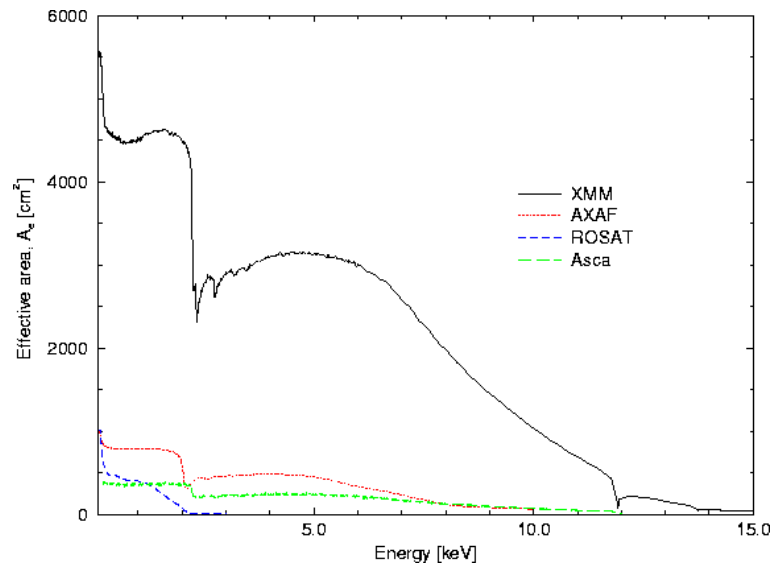


Figure 2.2: Total effective area of XMM-Newton mirrors, alongside those of AXAF (i.e. Chandra), ASCA and ROSAT (from Ehle et al., 2003).

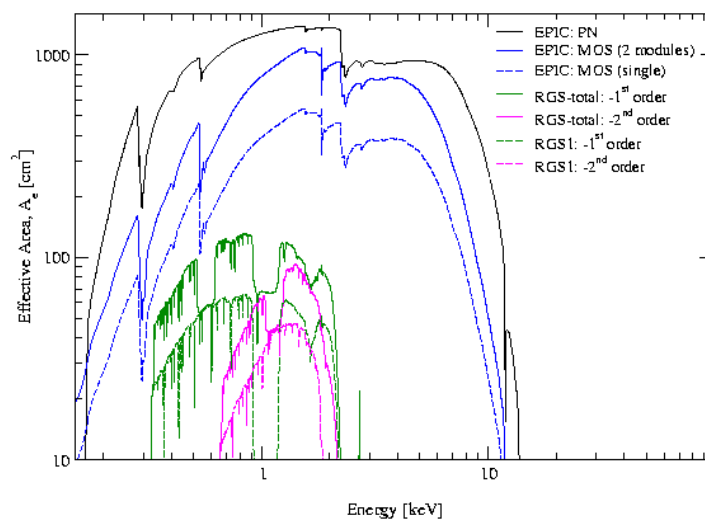


Figure 2.3: Effective areas of the individual instruments on XMM-Newton (from Ehle et al., 2003).

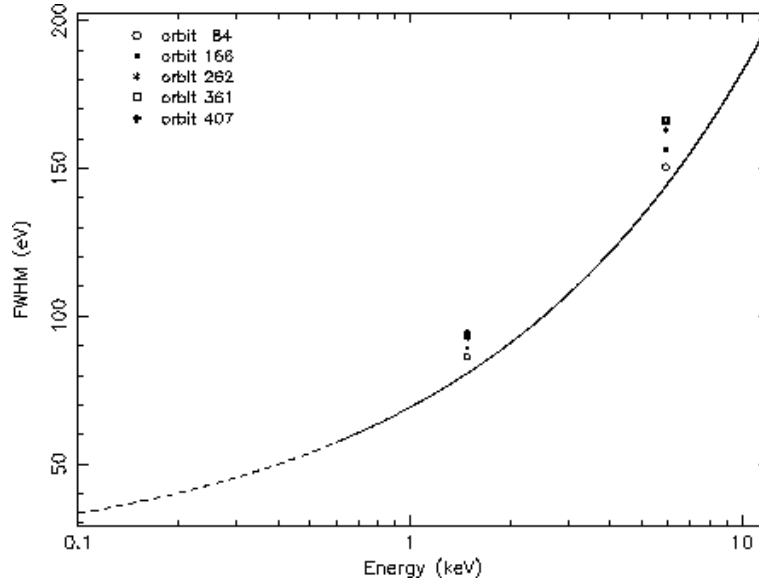


Figure 2.4: Energy resolution of the EPIC-MOS cameras (from Ehle et al., 2003). The datapoints show the gradual degradation of the MOS resolution over the course of the mission so far due to a gradual increase in Charge Transfer Inefficiency (CTI).

a source PSF of $\sim 6''$ FWHM, and an energy range of 0.15–15 keV. The energy resolution of pn is ~ 150 eV FWHM at 6 keV, if only single-pixel events are used. The energy resolution is lower for a spectrum selected solely from double events (instances where an incoming photon has deposited its energy across two neighbouring pixels), as the reconstruction of the energy of the original event currently uses an insufficient correction for Charge Transfer Inefficiency (CTI) - the loss of electrons into ‘traps’ in the silicon as charge is transferred across the CCD to be read out. The closer an event occurs to the readout node, therefore, the less degraded the energy resolution will become during charge transfer. A plot of the energy resolution of pn across its energy range is given in Fig. 2.5.

2.2.2 RGS

The Reflection Grating Spectrometer (RGS; den Herder et al. 2001) provides the high-resolution spectroscopic capability of XMM-Newton. Behind the two X-ray telescopes which focus onto the EPIC-MOS cameras are Reflection Grating Arrays,

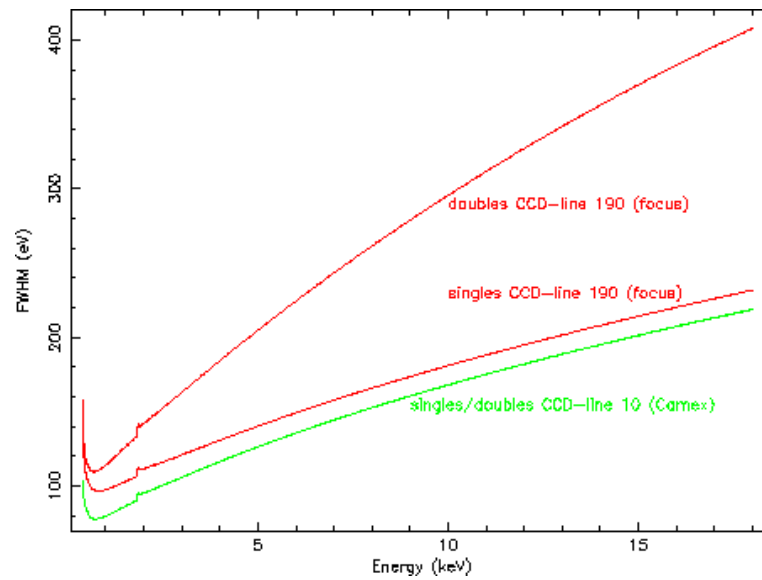


Figure 2.5: Energy resolution of the EPIC-pn cameras (from Ehle et al., 2003). The red lines show the resolutions for single and double events at CCD line 190 (the focus position); the double events have a much poorer resolution due to a currently insufficient correction for Charge Transfer Inefficiency (CTI). The green line is for events occurring at CCD line 10, near a read-out node.

which disperse about 40% of the incident X-rays from each telescope onto two CCD strips (the RGS Focal Cameras; RFCs) located at secondary foci offset by ~ 56 cm from the prime foci. Although the different order spectra overlap on the detector, they can be separated due to the intrinsic energy resolution of the CCDs.

The RGS wavelength range is 5–38 Å (0.33–2.5 keV in energy). The FWHM resolution in the first dispersion order is roughly constant across this range at ~ 0.06 Å, and about half this value in the second order. The effective areas of the two RGS instruments, for the two orders, are plotted in Fig. 2.3. The wavelength ranges 10.5–14.0 Å in RGS1 and 20.1–23.9 Å in RGS2 are unavailable due to failure of RGS1 CCD7 and RGS CCD4 (each RFC has 9 CCD chips in total). The systematic uncertainty in the wavelength scale is ± 8 mÅ.

The only other high spectral resolution astronomical X-ray instruments currently flying are the High Energy Transmission Grating Spectrometer (HETGS; Chandra Team 2003) and Low Energy Transmission Grating Spectrometer (LETGS; Chandra Team 2003) on the Chandra X-ray Observatory. Apart from the different technologies used in the spectrometers on XMM-Newton and Chandra (reflection gratings and transmission gratings respectively), the major differences between the two, from an observer’s point of view, relate to effective area and spectral resolution. In the soft X-ray band where the spectrometers of both missions are sensitive, the RGS has a much higher effective area: Fig. 2.6 compares the effective areas of the XMM-Newton and Chandra grating spectrometers. The spectral resolutions of the Chandra spectrometers are, however, higher than for the RGS (0.06 Å), at 0.012 Å (HETGS/HEG), 0.024 Å (HETGS/MEG) and 0.05 Å (LETGS) respectively, basically due to the higher angular resolution of the Chandra X-ray optics (Paerels and Kahn, 2003); see Fig 2.7.

2.2.3 OM

The Optical Monitor (OM; Mason et al. 2001) is a 30 cm optical/UV telescope, sensitive over the range 180–600 nm, with a $\sim 17'$ field of view. The camera is based on a Microchannel Plate intensified solid state detector which, unusually for

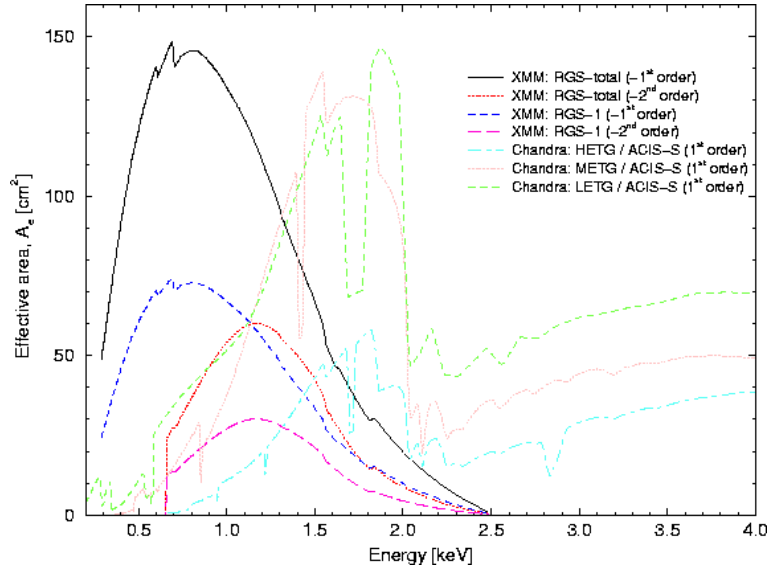


Figure 2.6: Comparison of the effective areas of the grating spectrometers on XMM-Newton and Chandra (from Ehle et al. 2003).

an instrument in this waveband, operates as a photon-counting device. Its ability to record the position and time of arrival of each photon allows it to generate high time resolution lightcurves (down to 0.5 s) as well as more standard images. The OM image pixels are $0.5''$ in size (although they are often binned up to $1''$ pixels). The OM has 7 optical and UV filters, as well as an optical and a UV grism; their bandpasses (excluding those of the grisms) are plotted in Fig. 2.8. The filter I have made the most use of in this work is UVW2, which is sensitive over the range 180–250 nm with a peak wavelength of ~ 210 nm. The source PSF of this filter is $\sim 1.85''$ FWHM.

2.3 Observations

Table 2.1 and Table 2.2 give the dates, observing modes and instrument exposure times for the Seyfert galaxies and BL Lac objects, respectively, that I investigate.

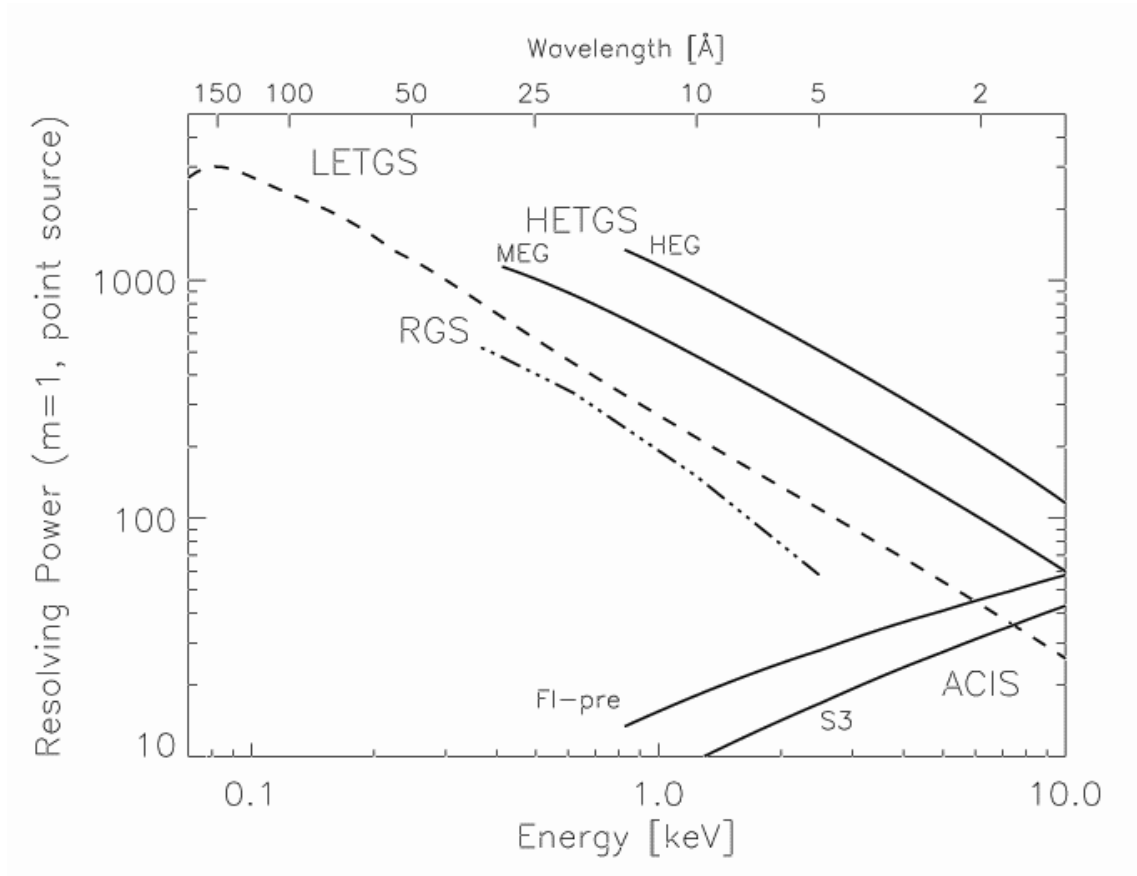


Figure 2.7: Comparison of the resolving powers, in the first dispersion order ($m=1$) of the grating spectrometers on XMM-Newton and Chandra (from Dewey, 2002); the resolving powers of the Chandra ACIS detectors are also plotted for the Front-Illuminated (FI) CCDs pre-launch (before the degradation in CTI; roughly comparable to EPIC resolving power), and one of the Back-Illuminated (BI) CCDs (S3).

Table 2.1: Dates, instrument modes and exposure times for the Seyfert observations described in this thesis.

Object	observation date	EPIC-MOS1 ^a	EPIC-MOS2 ^a	EPIC-pn ^a	RGS1 ^b	RGS2 ^b	OM ^c
NGC 3783	2000-12-28	37724 (LW M)	37724 (LW M)	37263 (SW M)	40456	40456	40016 (UVW2 I)
NGC 7469	2000-12-26	41388 (LW M)	41388 (FF M)	40698 (SW M)	41467	41464	28500 (UVW2 I)

^a Exposure time in seconds for the EPIC instruments. The operating mode and filter are given in brackets (SW = Small Window, LW = Large Window, FF = Full Frame, TU = Timing Uncompressed; M = Medium filter, T = Thick filter).

^b Exposure time in seconds for the RGS units; all exposures were in Spectroscopy mode.

^c Exposure time in seconds for the OM (I = Image mode, F = Fast mode, SUD = Science User Defined mode).

Table 2.2: Dates, instrument modes and exposure times for the BL Lac observations described in this thesis.

Object	observation date	EPIC-MOS1 ^a	EPIC-MOS2 ^a	EPIC-pn ^a	RGS1 ^b	RGS2 ^b	OM ^c
1H1219+301	2001-06-11	29304 (SW M)	29304 (FF M)	28523 (SW M)	29854	29854	20000 (UVW2 I)
H1426+428	2001-06-16	4044 (TU M) 60407 (LW M)	4044 (TU M) 60357 (FF M)	66239 (SW M)	67442	67454	6000 (V F) 6000 (U F) 24000 (UVW1 F) 6000 (UVM2 F) 12000 (UVW2 F)
Markarian 501	2002-07-12	6802 (TU T) 1012 (TU M)	8699 (FF M)	6910 (SW T) 1720 (SW M)	10232	10227	6000 (UVM2 F) 4940 (UVG SUD)
	2002-07-14	7177 (TU M) 3857 (TU T)	11877 (FF M)	6910 (SW T) 4201 (SW M)	12654	12647	6000 (UVM2 F) 5000 (UVG SUD)
PKS0548-322	2001-09-25	0 (LW M)	0 (FF M)	0 (SW M)	0	0	35000 (UVW2 I)
	2001-10-03	47303 (LW M)	47277 (FF M)	0 (SW M)	48152	48161	39000 (UVW2 I)

^a Exposure time in seconds for the EPIC instruments. The operating mode and filter are given in brackets (SW = Small Window, LW = Large Window, FF = Full Frame, TU = Timing Uncompressed; M = Medium filter, T = Thick filter).

^b Exposure time in seconds for the RGS units; all exposures were in Spectroscopy mode.

^c Exposure time in seconds for the OM (I = Image mode, F = Fast mode, SUD = Science User Defined mode).

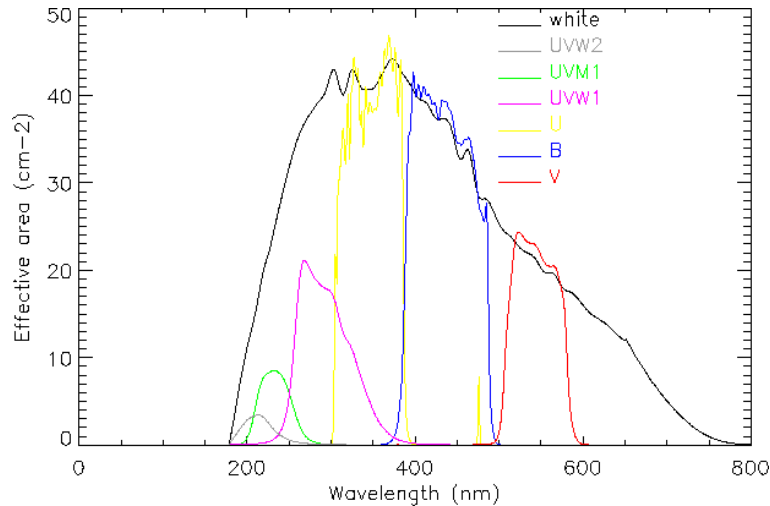


Figure 2.8: The bandpasses of the lenticular filters of the OM (from Ehle et al., 2003).

2.4 Data processing

All data were processed with the XMM-Newton Science Analysis Software (SAS). This compiles event lists from the raw data and extracts spectra and lightcurves. Processing the OM grism exposures currently requires the use of separate IDL routines developed at MSSL. The SAS preprocessors are `emproc` and `emchain` (for EPIC-MOS), `epproc` and `epchain` (EPIC-pn), `rgsproc` (RGS), `omichain` (OM imaging mode) and `omfchain` (OM fast mode). For the EPIC-MOS data, `emproc` and `emchain` are equivalent means of producing combined event lists from all CCD chips. Another task, `evselect`, is used to extract the spectra and lightcurves. EPIC-pn processing takes the same form. `Rgsproc` likewise combines the event lists from all RGS CCD chips, extracts source and background spectra using standardised extraction regions, generates background-subtracted source spectra and constructs response matrices. `Omichain` combines individual OM imaging exposures and applies the celestial co-ordinate system to the resulting images, whereas `omfchain` produces background subtracted lightcurves of sources observed in fast mode.

The versions of SAS used for each dataset are given in Table 2.3, and details of the analysis are given in the following sections.

Table 2.3: SAS Versions used in processing the data from each object.

Object	EPIC-pn	EPIC-MOS	RGS	OM
NGC 3783	5.2	5.2	5.2	devsas ^a
NGC 7469	5.3.3	5.3.3	5.3.3	5.3
1H1219+301	5.4.1	5.4.1	5.4.1	5.3.3
H1426+428	5.4.1	5.4.1	5.4.1	5.3.3
Markarian 501	5.4.1	5.4.1	5.4.1	5.3.3
PKS 0548-322	–	5.4.1	5.4.1	5.3.3

^a Development version of the SAS xmm-sas_20020107_1901-no-aka

2.4.1 EPIC-MOS

The EPIC-MOS data from all Small Window, Large Window and Full Frame exposures were found to be piled-up, since the count rates were above the limits given in the XMM-Newton User Handbook (Ehle et al., 2003) (5, 1.8, and 0.7 counts s⁻¹ for the three modes respectively) above which pile-up becomes a problem. These data were therefore not used further in the analysis, except in the case of NGC 7469 where the MOS and pn spectra were coadded to gain better statistics in the Fe K α region (see Chapter 4). In these cases, the standard pre-made distributed response matrices were used, and only single pixel events (pattern=0) were selected, to minimise the effects of pile-up. Only H1426+428 and Markarian 501 had MOS data which did not suffer from pile-up: these were taken in Timing Uncompressed mode, which was first satisfactorily reduced by SAS V5.4. In this mode, the central CCD chip images in one dimension only (so the resulting rows can be read out quickly) and the outer chips record photons in normal imaging mode. The background spectrum can thus be estimated from the outer CCDs; a spectrum for this purpose was obtained, in each case, using a circular extraction region of 90" radius. Unfortunately, I found that the TU response matrices had an incorrect energy scale in the region of the

oxygen K-edge at ~ 0.5 keV, which biased spectral fitting. I therefore decided not to use the TU mode MOS spectra in the analysis, especially given the existence of better signal-to-noise spectra from the EPIC-pn.

2.4.2 EPIC-pn

EPIC-pn data were available for each object except PKS 0548-322. In each case, the pn had been operated in Small Window mode (which has a high readout frequency) and so none of the data suffered from pile-up; the observed count rates were all well below $130 \text{ counts s}^{-1}$, where pile-up becomes a problem in this mode (Ehle et al., 2003). The circular region used for extracting the background spectra and lightcurves was kept the same size as that used for the source. The size of this region was determined by the need to avoid going over the edge of the data window (SAS V5.3.3 and V5.4.1) or by the requirements of the early Small Window mode response matrices to have a source extraction region of $60''$ or greater, due to the fraction of the source PSF that the region was expected to contain (SAS V5.2). The radius of the extraction region for each object is given in Table 2.4. Pre-made and publically distributed response matrices were used for NGC 3783 and NGC 7469; by the time I began working on the BL Lacs, the response matrix generating SAS task `rmfgen` had improved to the extent that it could achieve results consistent with the distributed official response matrices. I therefore used `rmfgen` to generate the response matrices for these latter observations. I used the SAS task `epatplot` to find the usable energy range of the BL Lac pn spectra, which was 0.4–10 keV. `Epatplot` plots the fractions of different event patterns as a function of energy; the observed events may deviate from the expected distributions due to detector noise (dark current; at low energies) or pile-up (at medium energies). I was unaware of the possibility of finding the lower useful energy bound of the spectrum during the analysis of NGC 7469 and the first NGC 3783 dataset, and used the standard 0.2–10 keV range in both cases. Nevertheless, it would have made no difference to the NGC 3783 work; the pn spectrum was not used for fitting below 3 keV. In the case of NGC 7469, where the pn continuum was actually fitted down to 0.2 keV, a

Table 2.4: Source extraction region radii (in arcseconds) for the pn exposures.

NGC 3783	NGC 7469	1H1219+301	H1426+428	Markarian 501
60	45	40	40	40

difference in the soft energy extent of the spectral range of perhaps 0.1 or 0.2 keV would have made little difference to the nature of the continuum model, whose main purpose was to demonstrate the basic shape of the continuum to be re-fitted separately to the RGS. All the pn spectra prior to SAS V5.4 were extracted using `pattern=0` and `flag=0`. ‘Pattern’ refers to the way the charge from an X-ray event is distributed over the CCD pixels; `pattern=0` refers to events involving single CCD pixels, which have the best energy resolution. ‘Flag’ is a measure of the quality of an X-ray event, where `flag=0` means that detections occurring in pixels bordering the CCD edges or next to bad pixels are ignored, since part of the charge can be lost into the undefined region thus giving an incorrect energy for the event. For the BL Lac spectra `pattern=0` was used and the standard flag selection (`((FLAG & 0xfb0000) == 0)`) which accepts `flag=0` events and excludes events on chip boundaries. Intervals affected by soft proton contamination were identified from a lightcurve of the entire background area (i.e. a lightcurve of data from the whole small window excluding the circle containing the source) and then filtered out of the event list before spectral extraction. NGC 7469 and NGC 3783 was not seriously affected by this, although 1H1219+301, H1426+428 and Markarian 501 lost $\sim 80\%$, $\sim 50\%$ and $\sim 40\%$ of the pn exposure time respectively.

2.4.3 RGS

`Rgsproc` produces separate spectra and response matrices for RGS1 and RGS2. The spectra are background-subtracted by `rgsproc` using background spectra extracted from regions spatially adjacent to the source in the CCD field of view. The standard source region includes events occurring within 90% of the cross-dispersion Point Spread Function (PSF), whilst the standard background region contains events out-

side 95% of the cross-dispersion PSF. To improve the overall signal-to-noise of the RGS data and facilitate spectroscopy, it is desirable to combine the RGS1 and RGS2 spectra. From SAS V5.3 onwards, `rgsproc` adjusts the RGS1 and RGS2 response matrices for the systematic effective area differences between the two, so the spectra and response matrices can be co-added without introducing significant error due to calibration differences. For spectra reduced by earlier SAS versions, though (NGC 3783 in this case), it was necessary to correct the response matrices for calibration differences before co-adding. This was done using the residuals of a power-law fit to the continuum source Markarian 421, which also corrected the spectra for an instrumental absorption feature due to neutral oxygen. The calibration files account for this feature in more recent versions of SAS. For the BL Lac RGS data, I also combined the first and second order RGS spectra to maximise statistical quality. The co-adding and correction of response matrices was done using dedicated software written by M. J. Page on the same principle described for the co-adding of EPIC spectra in Page et al. (2003). Fig 2.9 shows a comparison of the effective areas of the combined RGS1 and RGS2 (first order) response matrices generated for NGC 3783 by SAS V5.2 (with the Markarian 421 continuum correction), SAS V5.3.3 and SAS V5.4. There is no discernable difference between the SAS V5.3.3 and SAS V5.4 effective areas, and the SAS V5.2 curve follows the others very closely over most of the spectrum. The greatest discrepancy is in the range $\sim 12\text{--}19 \text{ \AA}$, where the effective area of the V5.2 curve can be up to $\sim 10\%$ higher than the other two. In general, although I have progressed to different SAS versions over the course of the work described in this thesis, the use of these different versions does not give rise to a significant difference in the overall RGS spectral shape.

Data affected by proton flaring were filtered out of the RGS event lists; time intervals which were badly affected by contamination were identified using a background lightcurve from RGS CCD9, which is closest to the optical axis and therefore suffers most from proton flaring. NGC 3783 and NGC 7469 were not significantly affected by this, although proton contamination was a much bigger problem with the BL Lac objects and $\sim 70\%$, $\sim 30\%$, $\sim 50\%$ and $\sim 30\%$ of the RGS data were

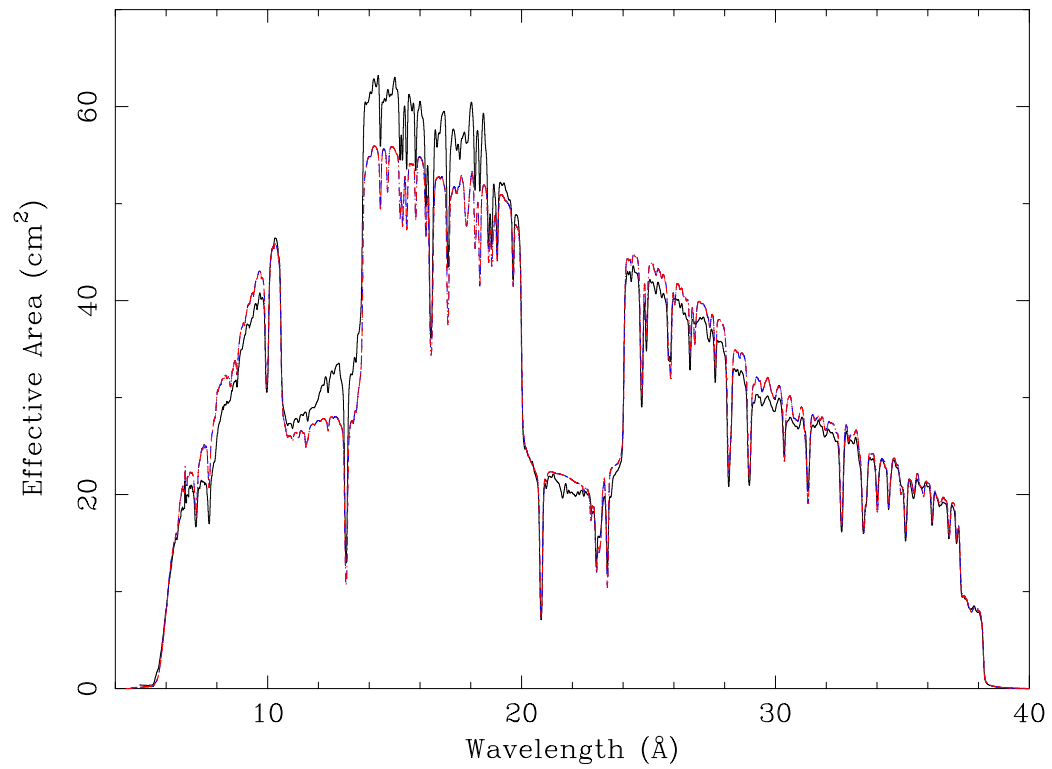


Figure 2.9: The effective area of RGS1 + RGS2 (first order), from response matrices generated with SAS V5.2 (black), SAS V5.3.3 (red) and SAS V5.4 (blue).

filtered out for 1H1219+301, H1426+428, Markarian 501 and PKS 0548-322 respectively. About 10% of the RGS data for NGC 7469 were lost as SAS was unable to process one of the data files due to a calibration problem.

2.4.4 OM

The SAS software for processing OM data is at an earlier stage of development than that for the X-ray instruments, so different data reduction processes need to be used depending upon what one requires from the data. During the observations reported here, the OM was operated in either Imaging, Fast or Science User Defined mode.

Imaging mode involves the production of a set of so-called ‘Rudi-5’ images, where different regions of the Field of View (FOV) are imaged sequentially at 1” resolution, with a high resolution (0.5”) image of the centre of the FOV taken simultaneously with every exposure. These images can be mosaiced together to produce an image of the full FOV, using `omichain`, and the series of high resolution central images can be used to produce a time series (usually in ~ 1000 s time bins) of the source by aperture photometry. I have used GAIA (the Graphical Astronomy and Image Analysis tool produced by the Central Laboratory of the Research Councils, UK) for aperture photometry. Background subtraction is performed using counts from an annular region surrounding the source. These OM count rates can be used to calculate flux points for the AGN in the different filter wavebands, using a recipe provided by the XMM-Newton Users’ Handbook (UHB; Ehle et al., 2003). Before converting to flux, though, the count rates must be corrected for coincidence losses, deadtime and reddening due to dust in our Galaxy. The coincidence loss and deadtime correction uses the formula

$$c_{\text{corr}} = -\ln(1 - (c \times t)) / t / (1 - d) \quad (2.1)$$

where c_{corr} is the corrected count rate, c is the raw count rate, t is the frametime in seconds and d is the ‘deadfraction’, the fraction of CCD time which is lost due to readout. The resulting count rate is dereddened using the method of Savage and Mathis (1979). For the three UV filters, this count rate needs only to be multiplied

by a conversion factor (provided in the SAS UHB) to obtain a flux value. For sources imaged with the optical filters, no straightforward flux conversion is given, so the count rate has to be converted firstly to magnitude (again using the recipe in the UHB), and then to flux using the standard flux conversion values for the Johnson UBV filters. Note that the OM optical filters are not exactly the same as the standard Johnson filters; the OM calibration team estimates an error on OM fluxes (UV and optical) of the order of 10% (A. Breeveld, priv. comm.).

Fast mode uses the Rudi-5 cycle too, but also has a data window - on the source at the centre of the FOV - which records the photons individually as they come into the detector and assigns a time-tag, at a given time resolution, to each one. This produces high time resolution lightcurves (generally 10 s time bins) of the source. `Omfchain` compiles these lightcurves from the instrument event lists. The accompanying Rudi-5 images are compiled by `omichain`.

Science User Defined mode requires the user to specify the size, resolution and position of the required imaging and timing windows, thus offering the greatest flexibility. It is used, in particular, for observations with the grism filters. OM grism data cannot be reduced by current versions of the SAS, but a set of dedicated IDL routines, developed for this purpose for use in instrument calibration by James (2003), are available.

2.5 Data analysis

The Optical and UV data from the OM were handled with standard software such as GAIA and FTOOLS, the X-ray and UV lightcurves were analysed with the Xronos packages in FTOOLS, and the broad-band CCD X-ray spectra from EPIC were fitted using Xspec, the standard X-ray spectral analysis package (Arnaud, 1996). The analysis of high-resolution RGS spectra, however, presents new problems.

In terms of resolution and signal-to-noise, the RGS is somewhere between traditional low resolution, low signal-to-noise X-ray spectra and high-resolution, high signal-to-noise optical spectra. In astronomy, X-ray spectroscopy has long been

characterised by model fitting, whereas optical spectroscopy has involved the identification and measurement of well defined spectral features. Both these approaches can run into trouble with the RGS.

The low signal-to-noise, and relatively low (by optical standards) resolving power of the RGS can make direct measurement of features difficult, especially as it can be hard to tell what is a genuine ‘feature’ and what is just noise. The reality of any given spectral feature can be measured by its statistical significance; another useful test is to see whether the feature is present in the spectra from both RGS1 and RGS2 independently. If the feature fits into a consistent pattern of atomic transitions with other features in the spectrum, the likelihood that it has been produced randomly is decreased. χ^2 fitting retains its statistical validity; it is, however, complicated by the fact that the number of bins containing the spectral features of interest is far smaller than the number of continuum bins: in this case, model fitting - of the type that is popular with CCD continuum spectra - can easily produce incorrect results, especially when dealing with complicated models, and a mixture of continuum absorption, line absorption and line emission as in many AGN spectra. The fitting software has no understanding of whether the model that it is fitting has any physical meaning. The ambiguities of RGS spectra of AGN thus require a sentient user to guide the fitting process.

Another complicating factor is the question of where the continuum level lies - in some cases, it is hard to establish whether a particular spectral pattern is due to emission or absorption without knowledge of the position of the underlying continuum. For this reason, the first stage in analysing the RGS spectrum of an AGN should be to work out the form and level of the underlying continuum. In cases where the ionised absorber column is very low, so there is little or no continuum absorption (as in NGC 7469), this will be very straightforward. In those cases where the warm absorption is very deep, however (as in NGC 3783), there is a need to disentangle the effects of continuum and blended line absorption from the basic shape of the continuum. There have been attempts to do this using Line Free Zones (LFZs) - spectral ranges unaffected by line absorption - to fix the level of the

continuum (e.g. Kaspi et al., 2001), but the results of this are entirely dependent upon having the correct model for the continuum absorption. I have, instead, taken the approach of fitting a continuum to a range of the spectrum which is known to be almost entirely unaffected by absorption (ranging between approximately 3–5 keV and 8–10 keV, depending upon the position of any iron lines), in the AGN I have worked on, and extrapolating this down over the RGS band. This requires that the continuum is established using spectra from the EPIC instruments, which has the potential for introducing error through cross-calibration uncertainties, although our knowledge of these is improving (den Herder et al., 2003). The assumption that the intrinsic soft X-ray continuum of any given Seyfert is actually an extrapolation of a simple power-law is also open to question, given the prevalence of soft excess components in these objects. In a deep warm absorber object such as NGC 3783, it is possible that a soft excess is being concealed by the presence of the absorber, and the intrinsic continuum is actually higher than we assume. The soft excess in NGC 7469 is not, however, concealed by the warm absorber and it was therefore possible to fit a model for it (see Chapter 4).

Once the continuum level has been established, the next step is to identify any statistically significant narrow spectral features. In a very high signal-to-noise spectrum, or one with particularly prominent features, it can be fairly obvious that the observed features are real, especially if they are easily identifiable with a known pattern of absorption and emission. In spectra with poorer signal-to-noise, or with features that appear in a novel pattern which is hard to interpret (or requires a controversial interpretation), there needs to be a way of quantifying the statistical significance of the observed features and of then determining whether they are likely to be real. In cases where I have needed to do this (the RGS spectra of NGC 7469 and the BL Lac objects) I have used a routine written by M. J. Page which fits a sliding Gaussian against a local continuum across an RGS spectrum, outputting a plot of σ (statistical significance) against wavelength. In an RGS spectrum of ~ 1000 bins, assuming statistical noise to follow the Poisson distribution, one would expect on average three bins to deviate by 3σ from the continuum level. Any

features at a higher level of significance, or a greater number of 3σ features than expected, are indications that the features are likely to be real. The width (Gaussian σ) of the fitted line is free to vary up to a maximum specified by the user; in the cases described in this thesis, a maximum width of 1000 km s^{-1} is used. With this value, the software took a week to run, so using a width much greater than this would have been impractical (the run-time scales approximately linearly with the maximum width of the Gaussian).

Knowing which features are significant, absorption models are applied and emission models added to the continuum until the spectral data are reproduced by the model. This has to be done with a full understanding of the properties the ionised absorber models used, and is thus a process of trial and error, changing model parameters until the spectrum is reproduced in a physically meaningful way. Only then is χ^2 fitting used, as a final optimisation of the model parameters once a reasonable answer has been reached via conscious 'measurement' of the features. This method is an attempt to deal with the intermediate nature of RGS spectroscopy - requiring some hybrid of the analytical philosophies used in the X-ray and optical regimes. χ^2 fitting is valid where the errors on the data points follow a Gaussian distribution; this is the case where there are more than about 20 counts per bin. The approximation to Gaussian errors is progressively less accurate for a smaller number of counts per bin, where the errors become better explained by Poisson statistics. In the cases I analyse, the average counts per spectral bin integrated over the whole observation are well above this level for the BL Lac objects (about 46, 86, 55 and 2000 counts per bin for 1H1219+301, H1426+428, Markarian 501 and PKS 0548-322 respectively). The NGC 7469 RGS spectrum has ~ 27 counts per bin, which is still in the Gaussian error regime, and the NGC 3783 spectrum has ~ 10 counts per bin where the approximation to Gaussian errors is not as good.

I used SPEX version 2.00 (Kaastra et al., 2002a) to analyse the RGS spectra. This software was written specifically with high resolution X-ray and UV spectroscopy in mind, and contains two ionised absorber models that are particularly useful for AGN spectra: *slab*, which applies absorption by specified columns of in-

dividual ions to a continuum, and *xabs* which models absorption by a given column of gas, at a given ionisation parameter and elemental composition. Both models allow the user to specify a blueshift or redshift for the absorber and the turbulent velocity of the gas, and benefit from the inclusion of recently calculated atomic data (derived from the Hebrew University Lawrence Livermore Atomic Code, HULLAC: Bar-Shalom et al. 2001), particularly for the inner shell transitions of oxygen and iron. These two models apply line and continuum absorption self-consistently, using Voigt profiles for the absorption lines. *Slab* is ideal for identifying the narrow absorption features in a spectrum, whilst *xabs*, which is based upon Xstar output, is used to construct self-consistent warm absorber models. Throughout this thesis, the *xabs* model I use is one which has been calculated assuming the SED of NGC 5548 as published by Kaastra et al. (2002b); this is a fairly typical Seyfert 1 continuum, with a hard X-ray power-law and a thermal soft excess.

Where a parameter value is obtained by χ^2 fitting, its error is determined by changing the value of the parameter until the value of χ^2 has changed by a specified amount which corresponds to a given confidence level (other free parameters in the model are allowed to change during this fitting); in the case of SPEX, the default bounds are the root mean square errors (rms; 1σ , approximately 68% confidence), which corresponds to a change in χ^2 ($\Delta\chi^2$) of 2. This value of $\Delta\chi^2$ is chosen because the variance of the χ^2 distribution is $2N$, where N is the number of degrees of freedom of the distribution (i.e. number of fitted parameters), and so where there is one interesting parameter, the variance corresponds to a $\Delta\chi^2$ of 2.

Chapter 3

NGC 3783

3.1 Introduction

Of the bright, nearby Seyfert galaxies, NGC 3783 has probably the deepest and best studied warm absorber. This chapter describes my work on the first 40 ks XMM-Newton observation of NGC 3783, as published in Blustin et al. (2002a). Since that paper, there have been four other publications on the warm absorber in this object, so at the end of this chapter I discuss the results of these and how they compare with my own findings. Some basic properties of this source are given in Table 3.1.

Many observers have studied the warm absorber of NGC 3783. Prior to the launch of Chandra, the state-of-the-art was represented by George et al. (1998); these authors, using ASCA data, fitted photoionised absorber models in which deep absorption edges of O VII and O VIII were the most prominent spectral features. It has also been claimed that NGC 3783 has a soft excess. Ghosh et al. (1992) were the first to suggest this, using very low resolution EXOSAT data, and the idea has since been resurrected by De Rosa et al. (2002b) whose much better quality BeppoSAX spectrum suggested the presence of a soft excess underlying the warm absorber.

The Chandra observatory was the first to obtain a high resolution soft X-ray spectrum of NGC 3783; a 56 ks HETGS spectrum was obtained in January 2000. By the time that my work on the XMM-Newton data appeared in print, there had been three papers on the Chandra datasets. The primary function of Kaspi et al.

(2000a) was to report that Chandra had indeed obtained the first high resolution soft X-ray spectrum of the source, and had detected many narrow absorption lines from the warm absorber, and also a few narrow emission lines; Kaspi et al. (2001) focussed mainly on the modelling of this initial dataset. Finally, Kaspi et al. (2002) presented a spectrum derived from the addition of data from several Chandra observations, totalling about 900 ksec, and used this exceptionally high signal-to-noise dataset to make detailed measurements of the individual absorption and emission lines in the spectrum.

Kaspi et al. (2001) made the first attempt at modelling a high-resolution spectrum of the NGC 3783 warm absorber. Using the original 56 ks spectrum, they fitted a continuum absorption model to Line Free Zones (spectral ranges where no absorption lines are present; see Chapter 2), and then modelled the narrow absorption and emission lines with photoionisation calculations. They found evidence for two ionisation phases in the absorber, with an order of magnitude difference between their ionisation parameters, and different covering factors. The model involved deep O VII and O VIII absorption edges and did not yet include the UTA. There has been much interest in trying to connect the UV absorption observed in NGC 3783 (Maran et al., 1996) with the X-ray absorber (see e.g. Shields and Hamann, 1997); Kaspi et al. (2001) noted that the lower ionisation phase in their model could potentially give rise to the observed UV absorption, but that this is highly dependent on the unobservable X-ray to UV continuum.

A later paper by Behar and Netzer (2002) showed that the depths of inner-shell Si absorption lines are consistent with the warm absorber having a continuous distribution of ionisation phases, rather than two well-defined ones.

The final list of atomic transitions detected in the 900 ks spectrum - as reported by Kaspi et al. (2002) - included absorption lines from the H and He-like ions of O, Ne, Mg, Si, S, Ar and Ca, H-like C, and various more lowly ionised states of S and Si. Iron L-shell transitions of Fe XVII–Fe XXIV are also present, alongside an M-shell iron UTA (first reported by Kaspi et al. 2001 in this source). There was evidence of a few emission lines, originating from O and Ne. A set of 42 strong

unblended absorption lines were used to find an average blueshift, relative to the systemic velocity, of $590 \pm 150 \text{ km s}^{-1}$, and a mean FWHM of $820 \pm 280 \text{ km s}^{-1}$. The line profiles are asymmetric, which - in the case of O VII - was shown to result from the combination of two absorbing systems whose velocity shift and FWHM are consistent with those observed in the UV. Certain lines have P-Cygni profiles due to the superposition of absorption and emission components; the narrow emission lines were at the systemic velocity of the source.

The Chandra spectra also provided the highest resolution view of the Fe $K\alpha$ line. This was found to be narrow, and was actually resolved by the HETGS to have a width of $1720 \pm 360 \text{ km s}^{-1}$ (Kaspi et al., 2002). There was evidence for a Compton shoulder redwards of the line itself, although there was no sign of a relativistically broadened component which was previously suggested by Nandra et al. (1997) on the basis of ASCA data, or the broad Gaussian line seen by De Rosa et al. (2002b) in BeppoSAX data.

The main focus of my work on the 40 ks XMM-Newton observation of NGC 3783 is the spectral modelling of the warm absorber. This was driven to some extent by the relatively poor signal-to-noise of the RGS data (at least compared to the 900 ks Chandra dataset), which made it more difficult to make accurate measurements of individual features. In this chapter I start off by describing the source variability in X-rays and UV, continue onto an analysis of the EPIC-pn data and particularly the Fe $K\alpha$ region, and then set out my method, and the results, of constructing a spectral model of the complex warm absorber of NGC 3783. I finish with a comparison of my conclusions with those of subsequent studies.

3.2 Lightcurves, 2–10 keV continuum and Fe $K\alpha$ line

The EPIC-pn data show that NGC 3783 was quite variable in X-rays during the observation (Fig 3.2), with a 30% difference between the highest and lowest flux levels, although the UV flux as measured from the series of OM UVW2 images

Table 3.1: Some basic information on NGC 3783 (coordinates are J2000)

Right Ascension	Declination	Redshift	Galactic column ^a
11h 39m 1.72s	-37d 44m 18.9s	0.00973 ^b	8.7

^a Galactic absorbing column in 10^{20} cm^{-2} (Alloin et al., 1995)

^b Theureau et al. (1998)

(Fig. 3.1) is constant within the 10% errors. A hardness-intensity plot (Fig. 3.3), using the 0.2–2 and 2–10 keV ranges as the soft and hard bands respectively, shows a slight tendency for the source to get softer as it gets brighter; the linear correlation coefficient for this trend is 0.35, with a $\sim 3\%$ probability of getting this value or higher from a random sample, giving a weak correlation significant at 2 sigma. If the final point on the plot is disregarded (it originates from the sudden spectral hardening at the end of the observation), the significance of the correlation increases to 3 sigma. Variability in the different energy bands has the same form, implying the existence of one dominant spectral component.

The deep warm absorber complicates the modelling of the continuum below it. Whilst it is quite possible to fit a power-law to the higher energies, it is hard to know what kind of continuum underlies the soft band. The softness-intensity relation hinted at by the lightcurves could imply the existence of a variable soft excess. Fitting a power-law with neutral absorption fixed at the Galactic value (see Table 3.1) to the 3.5–5.5 and 7.5–10 keV ranges, which avoid both the warm absorption and the iron $K\alpha$ line region, provides a continuum which goes over the soft band without any sign of an extra soft excess being required. This continuum is shown superimposed on the whole 0.2–10 keV pn spectrum in Fig. 3.4, along with the ratio of the data to the model, and the best fit continuum parameters are given in Table 3.2.

From Fig. 3.4 we can see that there appears to be two components to the Fe $K\alpha$ line, one broad and one narrow, as well as a weaker line at the position of Fe $K\beta$

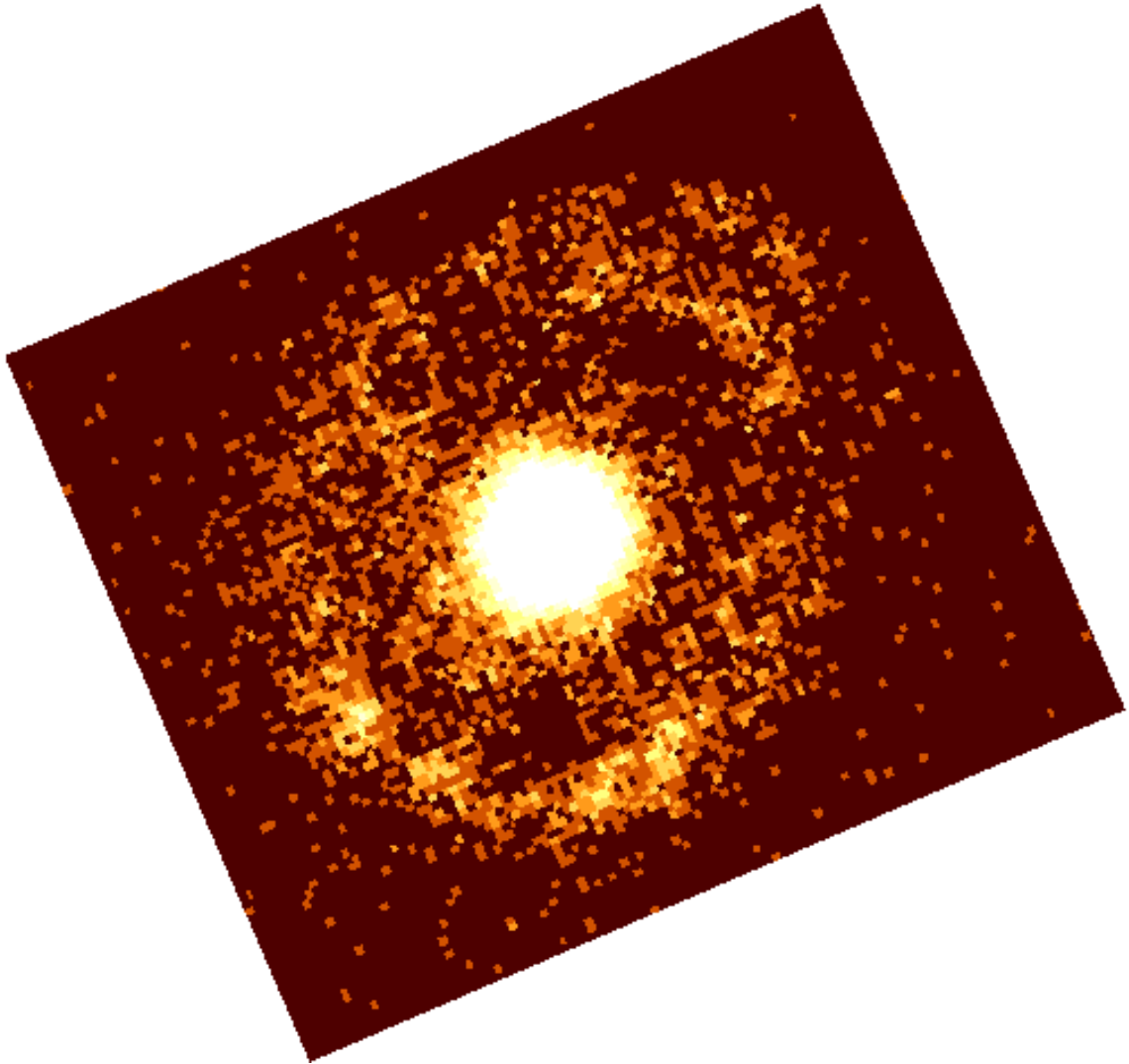


Figure 3.1: UVW2 image of NGC 3783, with the entire series of images co-added; North is up, East to the left, and the image is about $50'' \times 40''$ in size with $0.5''$ pixels. The nuclear image is saturated so that the the spiral arms are visible.

Table 3.2: The best fit power-law continuum parameters, fitted to the ranges 3.5–5.5 and 7.5–10 keV.

Photon index (Γ)	Normalisation ^a	N_{HGal} ^b	F_{2-10} ^c	χ^2_{reduced}
1.60 ± 0.02	0.0180 ± 0.0007	8.7	8.5	1.4 ^d

^a in photons $\text{keV}^{-1} \text{cm}^{-2} \text{s}^{-1}$ at 1 keV; ^b in 10^{20}cm^{-2} , fixed; ^c 2–10 keV model flux in $10^{-11} \text{erg cm}^{-2} \text{s}^{-1}$; ^d for 168 degrees of freedom.

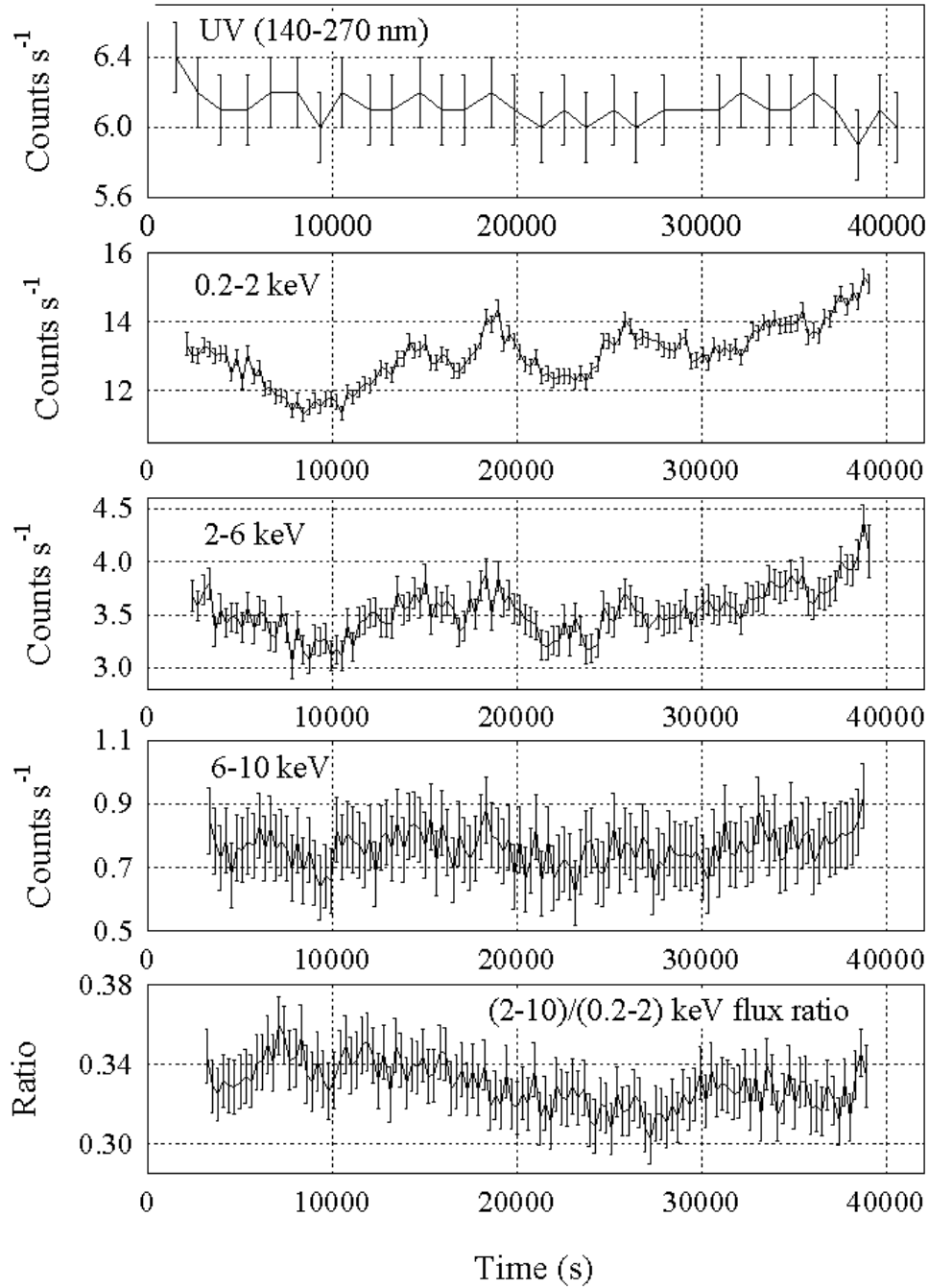


Figure 3.2: Multiwavelength background-subtracted lightcurves of NGC 3783: top, UV (140–270 nm) lightcurve from the OM, in 1000 s time bins; middle three, PN lightcurves in the bands 0.2–2, 2–6 and 6–10 keV, in 300 s time bins; bottom, the hardness ratio (2–10 keV / 0.2–2 keV flux) in 300 s time bins. The error bars are slightly overestimated in these plots: from top to bottom the errors on the points should be ± 0.08 , 0.2, 0.1 and 0.05 counts s^{-1} respectively, and the error on the hardness ratio should be ± 0.01 .

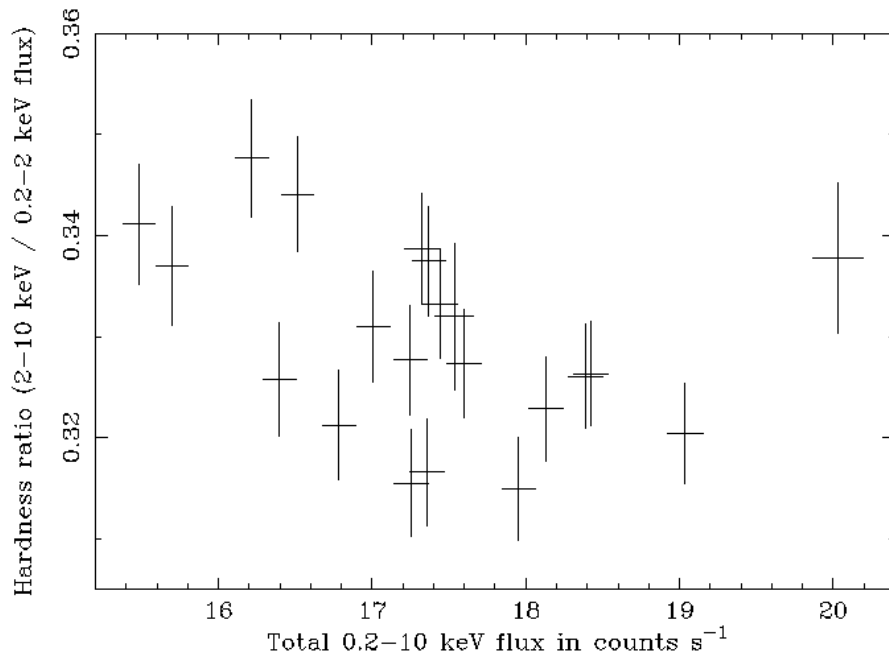


Figure 3.3: Hardness – intensity plot of NGC 3783 in 30 minute time bins. The error bars are slightly overestimated: the error on the total flux should be ± 0.08 counts s^{-1} , and the error on the hardness ratio should be ± 0.003 .

or Fe XXVI. Using the power-law of Table 3.2 as the fixed underlying continuum in the range 5.5–7.5 keV, I fitted Gaussians to these two components of $K\alpha$ as well as $K\beta$. The best fit parameters are given in Table 3.3, and the resulting model is plotted in Fig. 3.5.

The narrow $K\alpha$ line has a blueshift consistent with zero and its FWHM is unresolved by the pn. This is consistent with the findings of Kaspi et al. (2002), who are able to resolve the line and find a FWHM of 1720 ± 360 km s^{-1} . The flux of the line seen by pn is slightly greater than measured from Chandra data ($(7.1 \pm 0.9) \times 10^{-5}$ photons $cm^{-2} s^{-1}$ versus $(5.26 \pm 0.63) \times 10^{-5}$ photons $cm^{-2} s^{-1}$). The Chandra spectrum shows a low flux red wing to the line, which is identified as a Compton reflection shoulder; this is probably also seen in the pn data (see Fig. 3.5). However, the XMM-Newton spectrum shows an additional broad component, which is not seen in the Chandra spectrum. This broad line contains as much flux as the narrow component. Broad and narrow components were also observed in BeppoSAX data

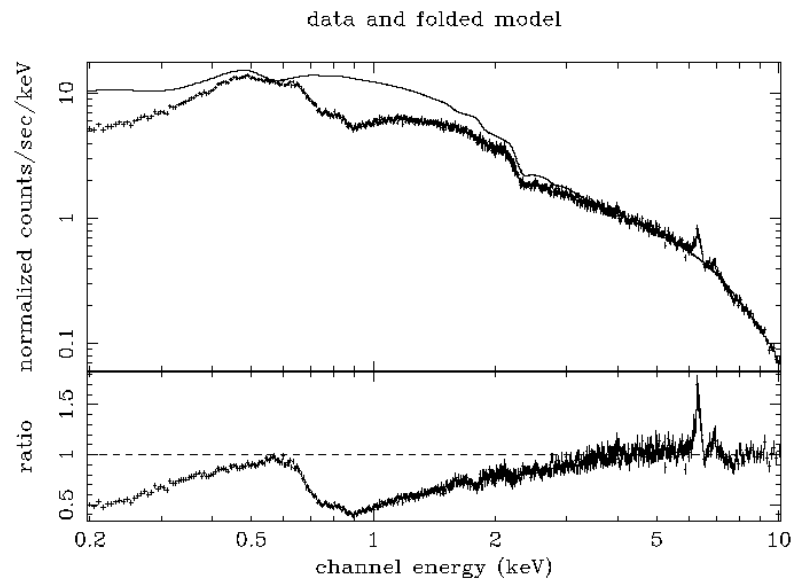


Figure 3.4: Continuum power-law fit to the 3.5–5.5 and 7.5–10 keV ranges of the pn spectrum of NGC 3783, extrapolated over 0.2–10 keV. The ratio of the data to the continuum model is shown in the bottom panel.

Table 3.3: The parameters of three Gaussians fitted to the emission lines seen in the pn spectrum of NGC 3783: E_{rest} , expected rest frame energy in keV; E_{meas} , measured rest frame energy in keV, flux in 10^{-5} photons $\text{cm}^{-2} \text{s}^{-1}$, Full Width Half Maximum (FWHM) in eV; V_{broad} , velocity broadening in km s^{-1} ; cz , Doppler shifted velocity in km s^{-1} (negative values indicate blueshifts). The fit has a χ^2_{red} of 1.1 for 70 degrees of freedom, in the range 5.5–7.5 keV.

Line	Identification	E_{rest}	E_{meas}	Flux	FWHM	V_{broad}	cz
1	broad Fe $K\alpha$	6.39	6.29 ± 0.03	7 ± 1	240 ± 80	11000 ± 4000	5000 ± 1000
2	narrow Fe $K\alpha$	6.39	6.40 ± 0.01	7.1 ± 0.9	70 ± 50	3000 ± 3000	-600 ± 600
3	Fe $K\beta$	7.06	6.98 ± 0.04	3.7 ± 0.9	200 ± 100	9000 ± 6000	3000 ± 2000
	Fe XXVI	6.96					-1000 ± 2000^a

^a if line 3 is identified with Fe XXVI

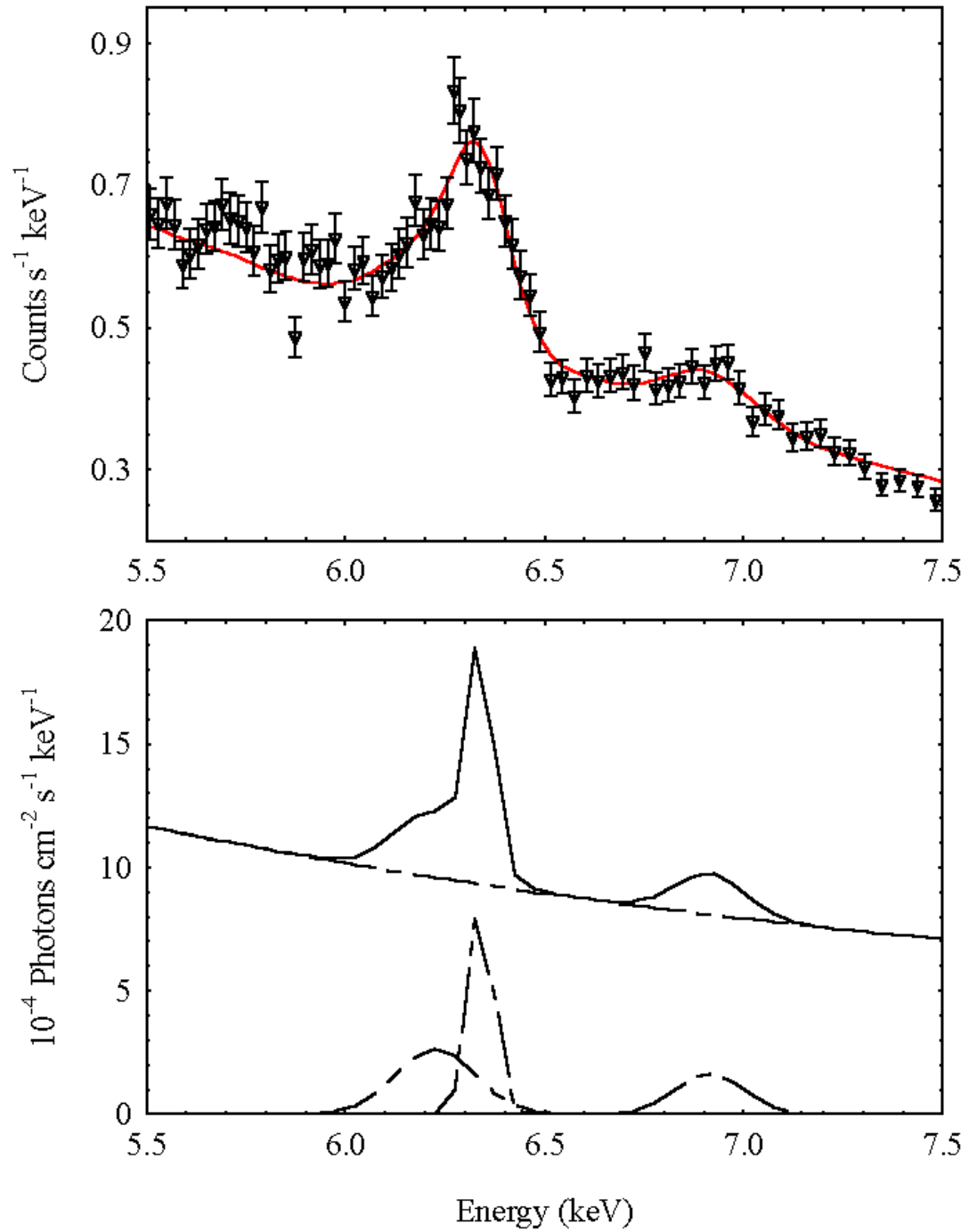


Figure 3.5: Fit to the iron emission lines in the pn spectrum of NGC 3783 (left, lines 1 and 2 (Fe $K\alpha$); right, line 3). Top panel: data (black) and model (red). Bottom panel: overall model (solid line) and model components (dotted line).

(De Rosa et al., 2002b); their broad component is a lot broader, however, than that described here ($\sigma = 0.72^{+1.28}_{-0.27}$ keV as opposed to $\sigma = 0.10 \pm 0.03$ keV), possibly due to the lower spectral resolution of BeppoSAX in this range.

A Fe K α line should be accompanied by K β emission at $\sim 14\%$ of the intensity of K α (e.g. Hölzer et al., 1997). The combined K β flux predicted from both broad and narrow K α components is about half that actually measured in the line observed at around 7 keV, which implies that the rest of the flux originates from Fe XXVI.

The significant redshift of the broad Fe K α line makes it tempting to fit a relativistically broadened disc line to it, or alternatively to the whole broad+narrow line. It is hard to determine the shape of such a line, as there is very low contrast with the continuum, although it can be fitted by this model if the disc is face-on and has an emissivity index below about 2. The shape of such a disc line is effectively Gaussian, making it hard to distinguish this possibility from the line shape being simply a Gaussian.

3.3 RGS spectrum

The continuum underlying the RGS spectrum was modelled as the power-law (with Galactic neutral absorption) that was fitted to the pn data. The power-law parameters were corrected for the relative calibration differences between the pn and the RGS as described by den Herder et al. (2002), so that the new power-law slope and normalisation were $\Gamma=1.54$ and 0.0175 photons keV $^{-1}$ cm $^{-1}$ s $^{-1}$ at 1 keV respectively.

There is a large deficit of flux under this power-law continuum below 17 Å, which in the past, with lower resolution spectra, has been fitted by an O VII edge (see e.g. George et al., 1998), and a triangular continuum feature at about 15 Å, which was interpreted as an O VIII edge. A large number of narrow absorption lines, and a small number of narrow emission lines, are visible in the spectrum. Parameters of the most important of these are listed in Table 3.4. I list the measured and rest wavelengths, blueshifts and equivalent widths of the deepest absorption lines of O,

N, C and Fe, as well as these parameters plus flux for the O VII forbidden line in emission. The corresponding values of equivalent width and flux from Kaspi et al. (2002) are quoted where applicable. Due to the re-emission accompanying Ly α and He α absorption lines, the β transitions can appear deeper than the α lines. In the case of C VI, the Ly β line is included in the table as it is in a region less affected by Galactic absorption than Ly α , and is thus easier to measure accurately. The theoretically deepest transition of O VI falls in the region of the O VII emission triplet, and is thus very hard to observe. Again, in this case, the second deepest line is listed.

The most prominent emission line is O VII (f). The signal-to-noise is too poor to distinguish the other two members of the triplet, but the fact that O VII (f) is the most prominent suggests immediately that the emission is from tenuous photoionised gas (Porquet and Dubau, 2000). The forbidden line appears to be blueshifted by $600 \pm 200 \text{ km s}^{-1}$, consistent with the blueshift of the warm absorber, whereas Kaspi et al. (2002) find that the line is not blueshifted in their spectrum.

The narrow absorption lines provide much more information. Identification of the transitions involved shows that the signatures of two main phases of gas are present in the spectrum; a high ionisation phase, characterised by L-shell transitions of iron and ‘traditional’ warm absorber ions such as O VIII, O VII, N VII and C VI, and a low ionisation phase giving rise to inner shell oxygen lines (O VI, O V and O IV) and a UTA of M-shell iron. Both regimes have the same blueshift, fitted as $-800 \pm 200 \text{ km s}^{-1}$ to each phase as a whole, which is consistent with the value of Kaspi et al. (2002) of $-590 \pm 150 \text{ km s}^{-1}$.

The pattern of iron absorption in a warm absorber spectrum is a powerful test of the ionisation structure of the absorbing medium. In a plasma with a given ionisation parameter, iron will be present in several different ionisation states. The relative importance of these states gives a good constraint on the ionisation parameter of the gas; in general, the main locus of iron absorption shifts to shorter wavelengths as the medium becomes more highly ionised.

In the RGS spectrum of NGC 3783, there are two main loci of iron absorption.

Table 3.4: The blueshifts and equivalent widths of some important spectral lines in the RGS data. Parameters: λ_{meas} , measured wavelength in Å (in rest frame of NGC 3783); λ_{rest} , rest frame wavelength in Å; v_{shift} , velocity shift in km s^{-1} ; line flux in 10^{-5} photons $\text{cm}^{-2} \text{s}^{-1}$; $\text{Flux}_{\text{chan}}$, line flux in Chandra spectrum as quoted in Kaspi et al. (2002) in 10^{-5} photons $\text{cm}^{-2} \text{s}^{-1}$; EW, measured equivalent width in mÅ; EW_{chan} , equivalent width in Chandra spectrum as quoted in Kaspi et al. (2002) in mÅ.

Line	λ_{meas}	λ_{rest}	v_{shift}	Flux	$\text{Flux}_{\text{chan}}$	EW	EW_{chan}
O IV $\text{K}\beta$	22.67 ± 0.02	22.777^{a}	-1400 ± 300			80 ± 10	–
O V $\text{K}\alpha$	22.27 ± 0.02	22.334	-900 ± 300			70 ± 20	–
O VI $\text{K}\alpha^{\text{b}}$	19.293 ± 0.006	19.341	-760 ± 90			76 ± 9	–
O VII $\text{K}\alpha^{\text{c}}$	21.5 ± 0.1	21.602	-900 ± 1000			20 ± 20	40.1 ± 34.6
O VIII $\text{Ly-}\alpha^{\text{d}}$	18.92 ± 0.01	18.969	-900 ± 200			50 ± 10	53.6 ± 15.9
N VII $\text{Ly-}\alpha$	24.67 ± 0.06	24.781	-1300 ± 700			90 ± 10	72.6 ± 34.9
C VI $\text{Ly-}\beta^{\text{e}}$	28.39 ± 0.01	28.466	-800 ± 200			100 ± 10	–
O VII (f)	22.06 ± 0.02	22.101	-600 ± 200	7 ± 2	10.13 ± 2.74	-130 ± 40	-270.4 ± 73.2
Fe XVII	14.97 ± 0.02	15.014	-800 ± 400			92 ± 6	26.2 ± 5.3
Fe XVIII	14.17 ± 0.01	14.210^{f}	-800 ± 200			148 ± 8	24.8 ± 5.5
Fe XIX	13.50 ± 0.01	13.523^{g}	-500 ± 200			164 ± 9	55.3 ± 8.1
Fe XX	12.815 ± 0.008	12.842^{h}	-600 ± 200			167 ± 8	56.7 ± 5.6

^a this value is yet to be benchmarked in the laboratory, and could be off by as much as 40 mÅ; ^b blended with a weaker absorption line of O V; ^c partially filled in by re-emission; ^d perhaps partially filled in by re-emission; ^e blended with a weaker absorption line of Si XI; ^f a blend of lines at 14.1548, 14.2042, 14.2120 and 14.2600 Å; ^g a blend of lines at 13.5070, 13.5146, 13.5210, 13.5540 and 13.5706 Å; ^h a blend of lines at 12.8130, 12.8270, 12.8319, 12.8470 and 12.9040 Å.

One is around 13–15 Å, corresponding to Fe XVII, Fe XVIII, Fe XIX and Fe XX, and the other is the M-shell UTA at 16–17 Å.

Below about 13 Å, it becomes harder to detect absorption features from the highly ionised states of iron that can absorb in this region. This defines the short wavelength end of the high ionisation phase. At around 15 Å, absorption from Fe XV and Fe XVI might be expected. It is clear that there is a very low column of these species, otherwise the short wavelength side of the 15 Å feature would be absorbed away by them. The long wavelength boundary to the Fe L-shell absorption is then defined by the 15 Å feature.

The position of the iron M-shell UTA in the spectrum is determined by the ionisation parameter of the absorbing gas. Its position is also affected by the absorber’s blueshift, so the blueshift of the low ionisation gas must first be obtained using the inner shell oxygen transitions. Having established this, the range of states in the UTA turns out to be Fe VI–Fe XIV. The long wavelength end of the 15 Å feature then defines the short wavelength boundary of iron absorption from the low ionisation phase.

I claim, then, that the 15 Å feature provides a well-defined cut-off between iron absorption from two different ionisation phases in the absorbing gas; its height and shape determines which iron states can be present in the absorbing medium. Each of these two loci of iron absorption is associated with absorption from other elements, so once the ionisation parameter has been derived from the pattern of iron absorption, we can see what other ions are expected to be present, and can test their abundance relative to iron.

3.4 Warm absorber modelling

Having shown that there are two main ionisation phases in this warm absorber, I used the ionised absorber models in SPEX 2.00 (*xabs* and *slab*) to construct, firstly, a two phase warm absorber model to give an insight into the physical conditions of the absorber, and secondly, an ion-by-ion model to provide estimates of the individual

ion columns.

3.4.1 Two-phase model

I applied a two phase absorber to the power-law continuum using the *xabs* model. The blueshift for both phases was set to 800 km s^{-1} , and the turbulent velocity was fixed at 300 km s^{-1} , similar to that used by Kaspi et al. (2001) in analysing the Chandra HETGS spectrum. The absorption lines are unresolved by the RGS.

The ionisation parameters of the two phases are set by the pattern of iron absorption, as described above. Taking the most important states in the high-ionisation phase to be Fe XVII, Fe XVIII and Fe XIX, I estimated $\log \xi$ of this phase to be 2.4. This may well be a simplification, as the presence of the higher ionisation states that are not so well fitted by this could be an indication of a range of ionisation parameters in the high ionisation phase. The low ionisation phase is well represented by a $\log \xi$ of 0.3, which reproduces the form and position of the UTA very well.

Having worked out the ionisation parameters, I fitted overall equivalent Hydrogen columns for the phases assuming Anders and Grevesse (1989) solar elemental abundances. Then the abundances of individual elements were allowed to vary. If it was impossible to establish the presence or abundance of an element, it was kept in the model but fixed at its solar relative abundance. The high ionisation phase can be well reproduced with abundances close to solar; nitrogen appears to be underabundant, contrary to what was found in IRAS 13349+2438 (Sako et al., 2001) and NGC 1068 (Kinkhabwala et al., 2002), and my value for the relative oxygen abundance, 0.7, should probably be about 0.9 (J. Kaastra, priv. comm.), as the solar oxygen abundance (Anders and Grevesse, 1989) used in SPEX has been shown by a new measurement (Allende Prieto et al., 2001) to be too high. To fit the form of the very deep UTA, the low ionisation phase needs to have an iron abundance around ten times higher relative to solar than C, N and O. Table 3.5 summarises the parameters of the two phases described here, the two phase model is shown superimposed on the data in Fig. 3.6, and the two phases of the model applied separately to the continuum are shown in Fig. 3.7.

Table 3.5: Properties of the NGC 3783 two-phase warm absorber model. $\log \xi$, v_{turb} and v_{blue} were held fixed during fitting, and N_{H} and the elemental abundances were allowed to vary.

Parameter	High-ionisation phase	Low-ionisation phase
$\log \xi^{\text{a}}$	2.4	0.3
N_{H}^{b}	$2.8^{+0.01}_{-0.3} \times 10^{22}$	$5.4^{+0.05}_{-0.5} \times 10^{20}$
$v_{\text{turb}}^{\text{c}}$	300	300
$v_{\text{blue}}^{\text{d}}$	800	800
C abundance ^e	0.8	1.0
N abundance	0.2	1.0
O abundance	0.7	1.0
Ne abundance	0.9	
Mg abundance	0.9	
Si abundance	2.5	
S abundance	1.0	
Ar abundance	0.7	
Fe abundance	0.9	10.7

^a Log of the ionisation parameter, where ξ is in erg cm s^{-1}

^b Equivalent hydrogen column of phase in cm^{-2}

^c Turbulent velocity in km s^{-1}

^d Blueshift of phase in km s^{-1}

^e Abundances relative to solar; estimated errors on abundances are about ± 0.5 . Values are only given for elements whose abundances could be directly measured; the abundance of all other elements in the model was fixed at 1.

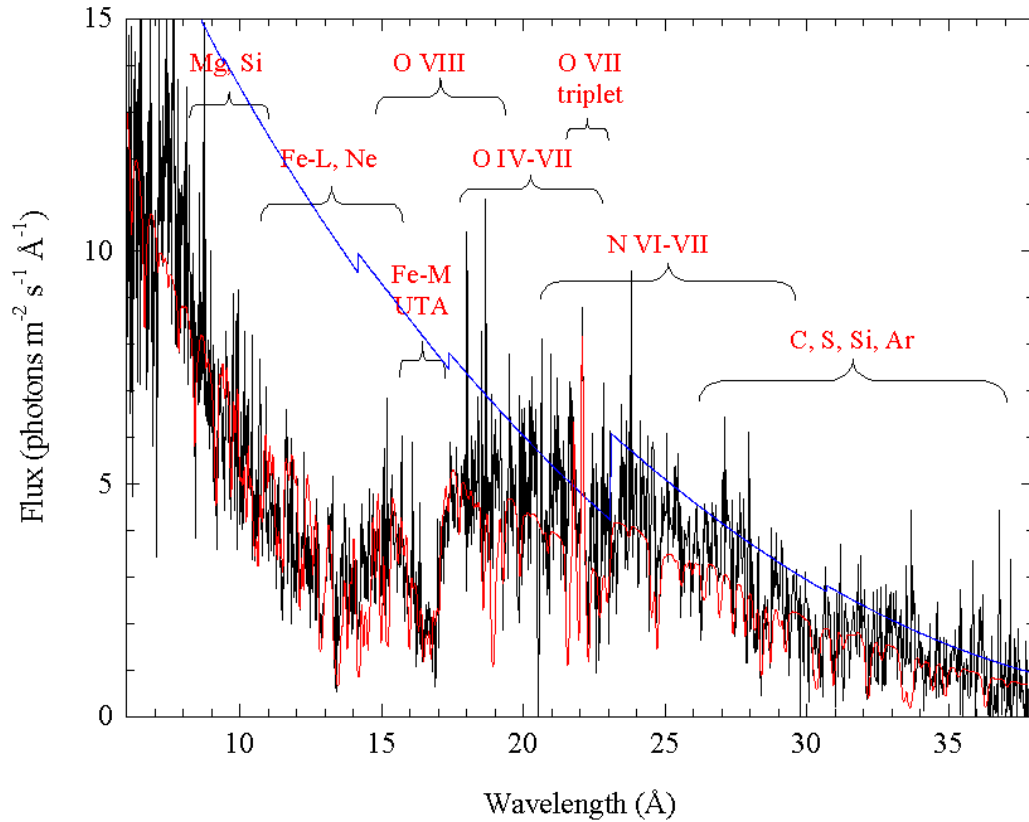


Figure 3.6: Combined RGS1 and RGS2 rest frame spectrum of NGC 3783 (black), with the power-law continuum (blue) and the power-law plus two-phase warm absorber model (red) superimposed, plotted over the range 6–38 Å. Species absorbing or emitting in various spectral ranges are indicated.

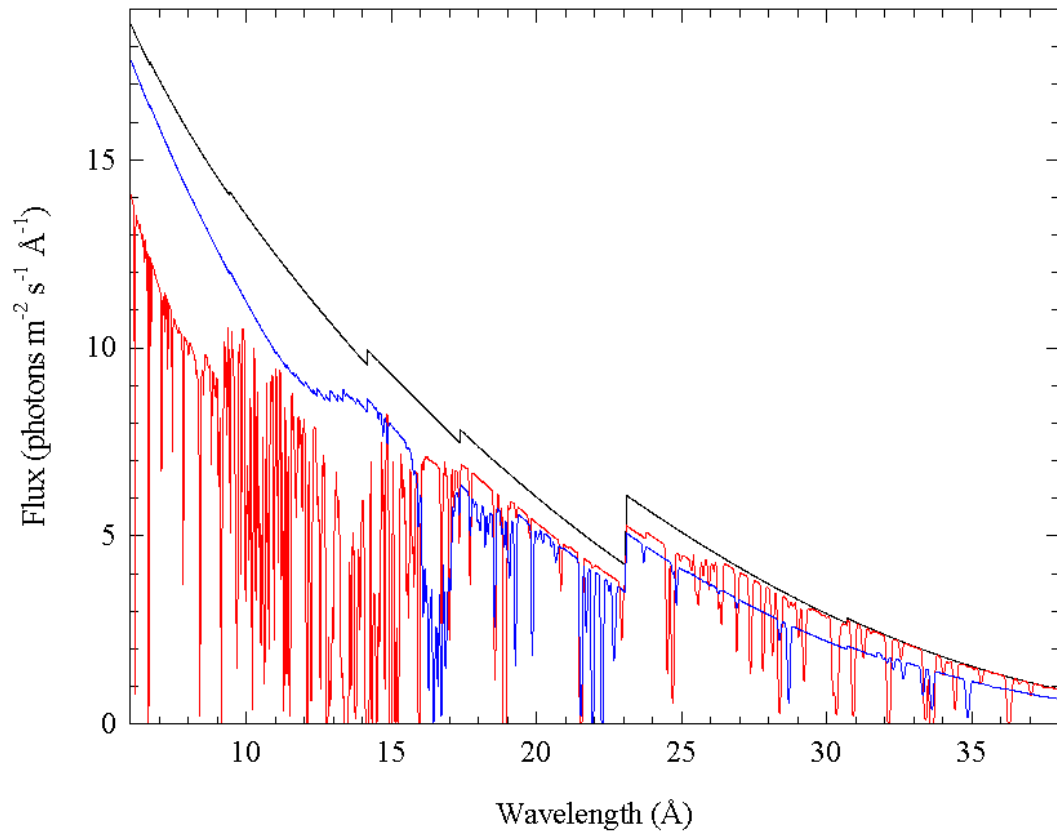


Figure 3.7: The two phases of the NGC 3783 warm absorber model applied separately to the continuum (high-ionisation phase in red, low-ionisation phase in blue, and power-law continuum in black) plotted over the range 6–38 Å (rest frame). The absorption edges in the continuum are due to neutral gas in our Galaxy.

3.4.2 Detailed model

Table 3.6 gives the estimated columns of the individual ions in the spectrum, as modelled using *slab*. This model is shown superimposed on the data in Fig. 3.8 and Fig. 3.9. The model provides a very good representation of the spectrum, especially in some regions of the L-shell iron absorption, although there are also some remaining discrepancies in this range. The ionic column of each iron state in Table 3.6 is plotted against its ionisation parameter of maximum abundance in Fig. 3.10, except for Fe XV for which only an upper limit could be obtained. The plot clearly shows the two different phases in the warm absorber, with the low ionisation gas fairly tightly centred at $\log \xi \sim 0.3$, and an indication that the high ionisation phase has a wider range of ionisation parameters (note the logarithmic scale).

3.5 Discussion

3.5.1 Broadband X-ray and UV variability

In the short 40 ks observation there is no evidence to support a connection between the X-ray and UV variability. Whilst the X-ray flux changes by 30% between its highest and lowest points, the UV is constant within its 10% errors. Although the different X-ray energy bands show the same pattern of variability, there is an indication that the spectrum is softer at higher fluxes, and that there is a gradual change in the hardness ratio over the course of the observation.

3.5.2 Emission and absorption in the Fe $K\alpha$ region.

The 0.2–10 keV EPIC-pn continuum spectrum is well-fitted by a power-law at higher energies, with the warm absorber causing a significant deficit of counts at the low energy end. There is no evidence for a soft excess, or a reflection component. It is possible that a soft excess could be hidden under the warm absorber.

The narrow component of the Fe $K\alpha$ line looks similar to the narrow line observed by Kaspi et al. (2001, 2002), although the parameters obtained from the pn spectrum

Table 3.6: The absorbing columns of individual ions in the detailed model of the warm absorber.

Ion	Log ₁₀ column ^a	Log ξ_{ma} ^b	Ion	Log ₁₀ column ^a	Log ξ_{ma} ^b
C V	16.5 ± 0.5	0.15	Fe VI	16.0 ± 0.5	-0.90
C VI	17.5 ± 0.2	1.15	Fe VII	16.1 ± 0.5	-0.35
N VI	16.9 ± 0.2	0.70	Fe VIII	17.1 ± 0.5	0.05
N VII	16.8 ± 0.2	1.50	Fe IX	16.8 ± 0.5	0.35
O IV	17.1 ± 0.2	-0.75	Fe X	16.8 ± 0.5	0.55
O V	17.5 ± 0.2	-0.05	Fe XI	16.4 ± 0.5	0.75
O VI	17.0 ± 0.5	0.45	Fe XII	16.0 ± 0.5	1.00
O VII	17.3 ± 0.2	1.15	Fe XIII	16.2 ± 0.5	1.20
O VIII	16.8 ± 0.5	1.75	Fe XIV	16.2 ± 0.5	1.40
Ne IX	18.0 ± 0.5	1.70	Fe XV	≤ 15.4	1.60
Ne X	18.2 ± 0.5	2.25	Fe XVI	16.4 ± 0.5	1.60
Mg XI	17.5 ± 0.5	2.10	Fe XVII	17.5 ± 0.2	2.10
Mg XII	17.8 ± 0.5	2.60	Fe XVIII	17.5 ± 0.2	2.30
Si XI	17.0 ± 0.2	1.70	Fe XIX	17.4 ± 0.2	2.50
Si XII	17.9 ± 0.2	2.05	Fe XX	17.5 ± 0.2	2.80
Si XIII	17.5 ± 0.2	2.40	Fe XXI	17.7 ± 0.2	3.00
Si XIV	18.0 ± 0.5	2.90	Fe XXII	17.1 ± 0.2	3.10
S XII	17.0 ± 0.2	1.70	Fe XXIII	17.5 ± 0.5	3.30
S XIII	17.5 ± 0.2	2.05	Fe XXIV	17.0 ± 0.5	3.45
S XIV	16.7 ± 0.2	2.40			
Ar XIII	16.1 ± 0.2	1.80			
Ar XIV	16.4 ± 0.5	2.10			

^a where the column is in cm⁻²

^b log ξ at which the ion is at its maximum abundance (ξ is in erg cm s⁻¹)

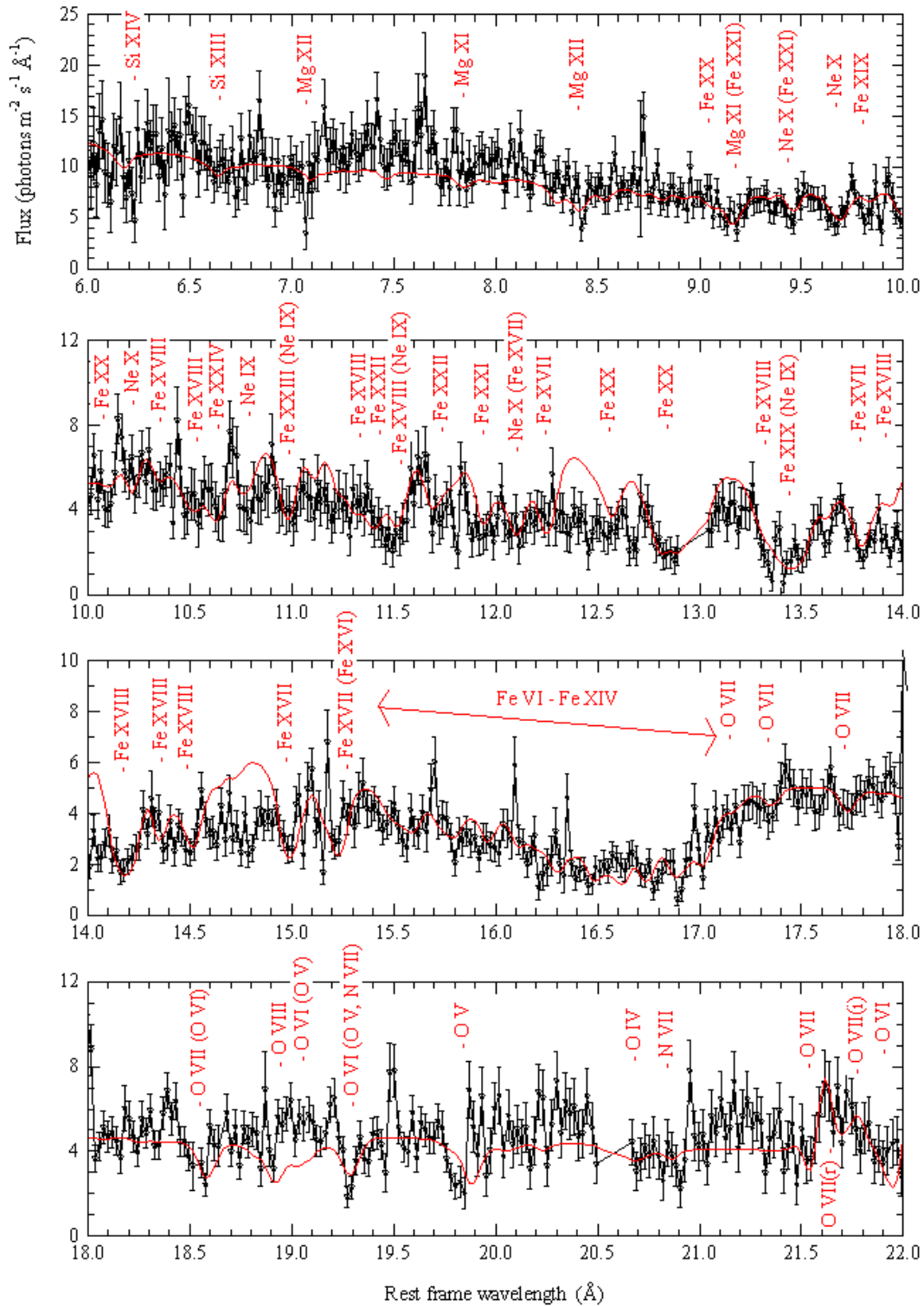


Figure 3.8: Combined RGS1 and RGS2 rest frame spectrum of NGC 3783 (black), binned into groups of two channels, with detailed warm absorber model superimposed (red), plotted over the range 6–22 \AA . The most important spectral features in the data and model are labelled.

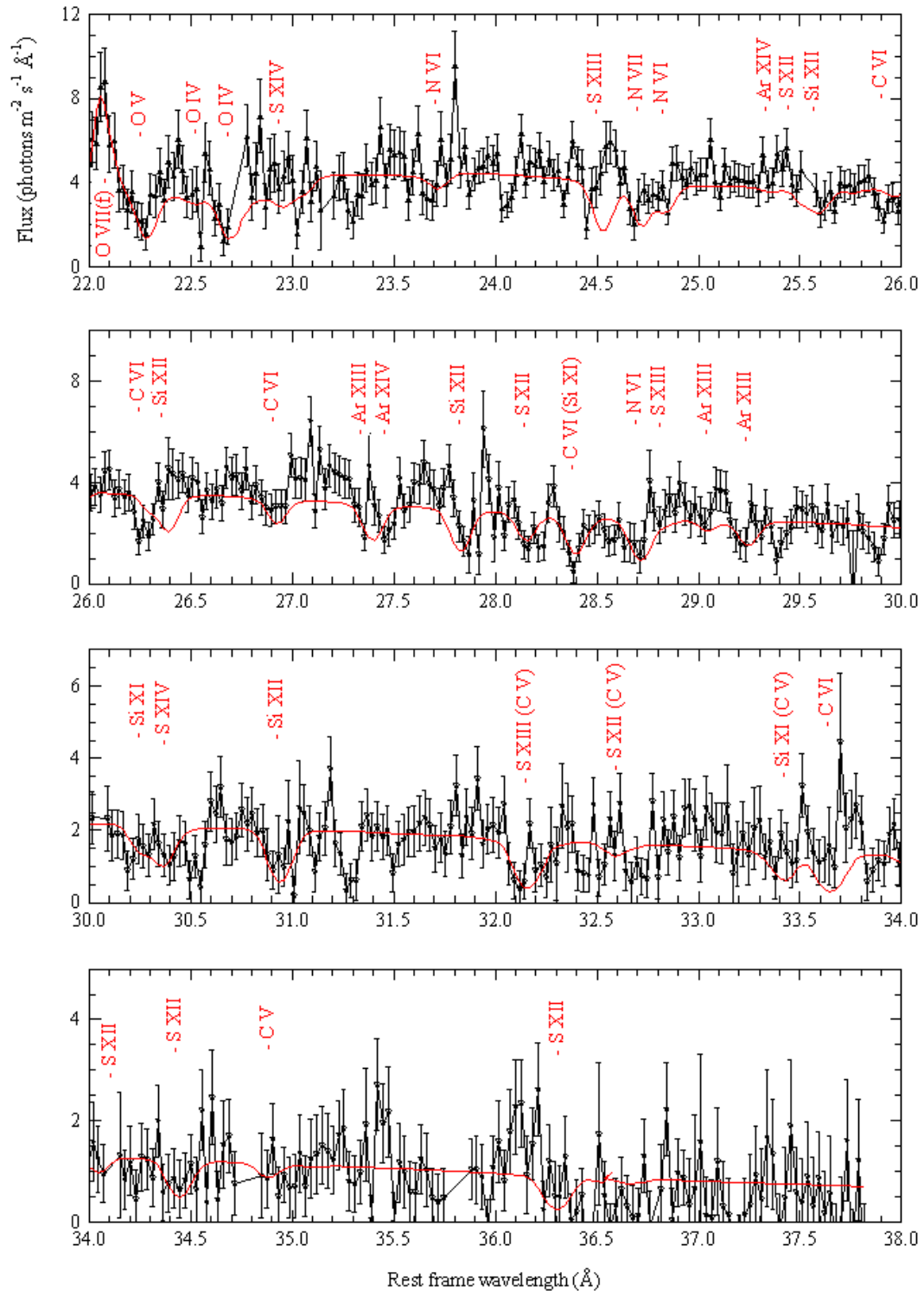


Figure 3.9: Combined RGS1 and RGS2 rest frame spectrum of NGC 3783 (black), binned into groups of two channels, with detailed warm absorber model superimposed (red), plotted over the range 22–38 \AA . The most important spectral features in the data and model are labelled.

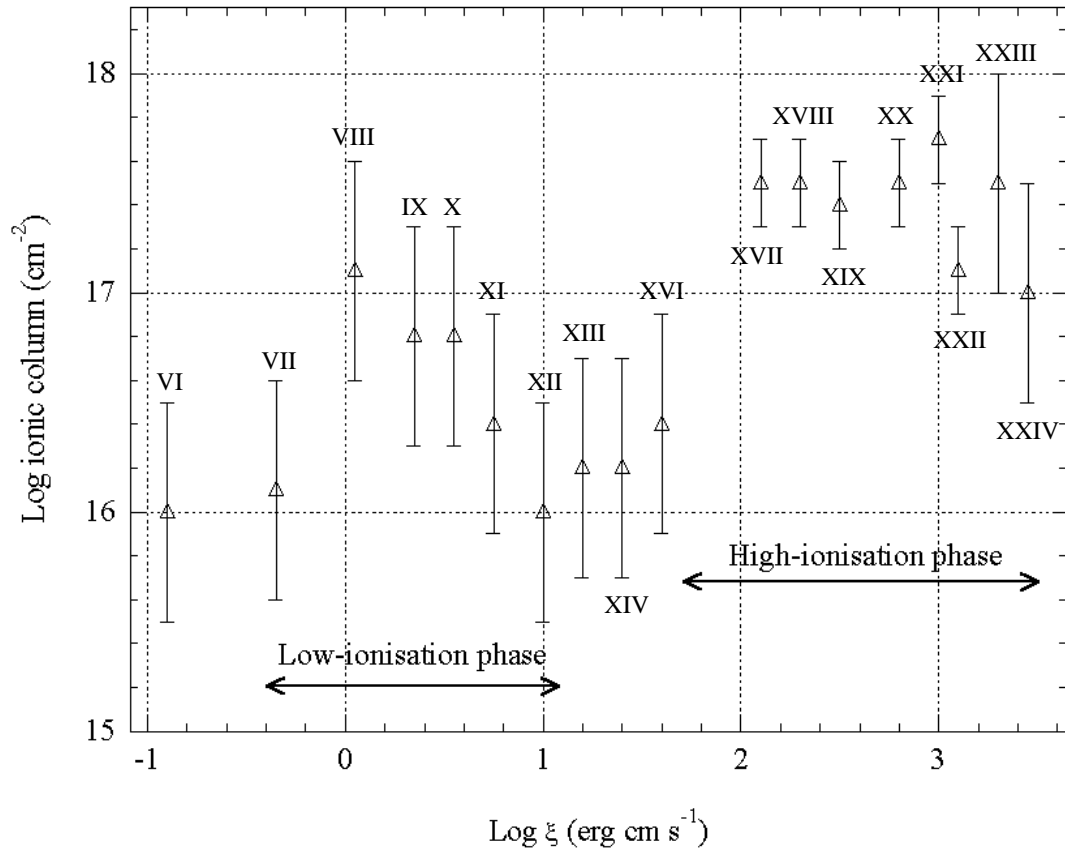


Figure 3.10: Ionic column plotted against ionisation parameter of maximum abundance for the iron states VI–XXIV (except Fe xv, for which only an upper limit could be obtained) listed in Table 3.6.

are poorly constrained. It occurs at its rest wavelength and is unresolved at the pn spectral resolution. I also find evidence for a broad component to the emission that is not discussed by Kaspi et al. (2002), although a broad component has recently been observed with BeppoSAX. The broad line in the pn spectrum is redshifted by 5000 km s^{-1} , and the overall profile is reminiscent of the NGC 3783 (1) Fe $K\alpha$ line of Nandra et al. (1997) which was interpreted as a discline; however, the pn broad component is much less broad than either that or the broad line seen in BeppoSAX data. It is therefore tempting to fit a discline model to the broad component - or the whole profile - of the pn Fe $K\alpha$ line. Because of the small amount of flux present in the broad component, though, it is not possible to obtain good constraints on such a model.

The broad line, being Fe I $K\alpha$, must originate in relatively cool gas. The broadening, then, is dynamical rather than thermal, and the width of the line ($11000 \pm 4000 \text{ km s}^{-1}$) could place it in the ‘very broad’ line region of Winge et al. (1992). The redshift is either due to the emitter falling in towards the nucleus, or it is due to gravitational effects close to the black hole. Why, though, is this broad component not visible in the 900 ks Chandra spectrum, which surely has sufficient signal-to-noise to see it? The broad line could conceivably be a transitory phenomenon. The much fainter line at higher energy is probably a combination of Fe $K\beta$ from both components of Fe I and also from Fe XXVI; the combination of these different lines will affect the apparent broadening and redshift of the observed line.

3.5.3 The soft X-ray warm absorber

The two-phase warm absorber model

The overall form of the spectrum is reproduced very well by the simple two-phase model. The strangest feature, physically, is that iron is ten times more abundant, relative to its solar value, than oxygen in the low ionisation phase. The abundances in the high ionisation phase are close to their solar values. NGC 3783 is not alone in requiring an abnormal iron abundance to explain its UTA. IRAS 13349+2438

(Sako et al., 2001) was found to require an iron abundance of 2–3 times that of oxygen, and the UTA in NGC 5548 also needs an iron overabundance (Kaastra et al., 2002b). The apparent high iron abundance in the low ionisation phase is very dependent upon the turbulent velocity, absorbing column and assumed continuum level. Other possible factors include the fit being biased by the UTA being wider than expected (because of the distribution of states being inadequately explained by a single ionisation parameter), and uncertainties in the ionisation balance calculations of M-shell iron (the dielectronic recombination rates for these ions have never been measured or calculated with modern codes; E. Behar, priv. comm.; see section 3.6.3). The high abundances could also be due to a covering factor effect (see Arav et al., 2002); since the iron abundance is measured relative to the abundances of O, N and C, and if the lines of these elements are highly saturated, then their equivalent widths will be determined by the velocity width and covering factor, and will be only weakly dependent upon the column density.

The UTA would, with the lower resolution spectra of the past, have been fitted with an O VII absorption edge (16.78 Å). It is clear from this spectrum that any edge absorption is actually concealed by the deep UTA. Both of the ionisation phases produce O VII; the relative importance of O VII from each will depend upon the relative columns of the two phases. My high ionisation phase oxygen is dominated by O VIII, and at the equivalent hydrogen column of this phase, $2.8 \times 10^{22} \text{ cm}^{-2}$, significant O VIII absorption edge opacity exists. However, as in the case of O VII, the absorption edge is heavily cut into by iron transitions - in this case, from L-shell iron. So, whilst this very deep warm absorber does give rise to edge opacity in O VII and O VIII, the superimposition of all the iron transitions, and the fact that the O VII could come from either phase, means that fitting O VII and O VIII edges is not a useful diagnostic for the physical conditions in the warm absorber.

Indeed, the O VIII column appears to be overpredicted by the model, as the very deep O VIII Ly α line (18.97 Å; see Fig. 3.6) is not consistent with the data. This may be partly because this model does not take account of O VIII narrow line emission, which has been documented by Kaspi et al. (2002) and Behar et al. (2003). The iron

absorption is also overpredicted at the short wavelength side of the 15 Å feature, as shown by Fig. 3.6, and increasingly underpredicted at shorter wavelengths. This is compensated for, as can be seen in Fig. 3.7, by the generation of a neon absorption edge at ~ 9.5 Å. This indicates that the iron absorption in the high ionisation phase may not be correctly explained by a single ionisation parameter, and may require a wider range of ionisation. The low ionisation phase is well approximated by a single $\log \xi$ of 0.3.

The detailed warm absorber model

The detailed model agrees with the data very well, particularly in parts of the L-shell iron region. There are still some significant residuals in this range, though, which are unlikely to be due to an inaccuracy in our knowledge of the Fe L-shell transitions, whose wavelengths and blends are very well known. Some contribution may come from ions not included in our model, particularly those of calcium. Another interesting possibility is that the residuals are due to higher order transitions from the saturated UTA ions (Behar et al., 2001). It is more likely that the residuals are due to an underestimation of the O VIII column and the associated continuum absorption; although increasing the column would give rise to an unacceptably deep O VIII Ly α , this could be offset by the inclusion of narrow line emission from this ion.

As shown by Fig. 3.10, the model requires a lot of gas at $\log \xi$ above 2. The high ionisation phase can be investigated further using transitions visible to the RGS in the 23–38 Å region, where the Chandra HETGS is not sensitive. Absorption lines are present from N VI, N VII, C VI and possibly C V, Si XI, Si XII, S XII, S XIII, S XIV, Ar XIII and Ar XIV. Inspecting the model superimposed on the data, in Fig 3.8 and Fig 3.9, one can clearly see where the calculated wavelengths of these lines are inaccurate. There are also further unidentified lines yet to be included in our model.

3.5.4 The structure of the warm absorber in NGC 3783

What can the modelling tell us about the structure of the warm absorber in NGC 3783? Both phases are outflowing with the same line-of-sight velocity of about 800 km s^{-1} . The high ionisation phase has an equivalent hydrogen column (in our line of sight) around fifty times that of the low ionisation phase. Whilst the high ionisation phase seems to contain gas at a wide range of ionisation parameters, the low ionisation phase seems to be concentrated around a single ionisation parameter.

When the nucleus of NGC 3783 is radiating at a given luminosity, the ionisation parameter of the warm absorber is determined by its distance from the central source and its density. ξ is proportional to $1/r^2$ and $1/n$; it is thus more sensitive to distance than it is to density. I therefore suggest that the high ionisation phase of the absorber, with its wide range of ionisation parameters, could consist of a gas at a wide range of distances and densities (to a lesser extent), as in the multi-temperature wind model of Krolik and Kriss (2001). The low ionisation phase would then consist of gas localised at a specific distance from the source, and of a specific (perhaps higher) density.

Sako et al. (2001) suggested that the UTA in IRAS 13349+2438 might have originated in the dusty torus which surrounds the active nucleus. In this picture, my low ionisation phase could consist of dense (perhaps iron-rich) material swept up off the torus into the fast moving high-ionisation phase of the warm absorber, where it would be photoionised and carried along at the same speed as the high-ionisation material.

3.6 Some recent results

Since the publication of my work on NGC 3783 (Blustin et al., 2002a), four other papers concerned with modelling the X-ray warm absorber of this AGN have appeared: Behar et al. (2003), Krongold et al. (2003), Netzer et al. (2003) and Reeves et al. (2004). Much of this work draws heavily on my methods and results. I summarise and discuss the main relevant results from each of these papers below.

3.6.1 Behar et al. (2003)

These authors deal with a 280 ks XMM-Newton RGS observation of NGC 3783, subsequent to the 40 ks one described in this chapter. They do not fit a global model, although they superimpose my ‘detailed model’ on the extremely high signal-to-noise RGS spectrum and find that it is generally a good representation of the data. Instead, this paper concentrates on the oxygen absorption and emission in the spectrum, using these transitions to attempt to derive physical properties of the warm absorber.

The first finding of Behar et al. (2003) is that although the continuum flux increases by a factor of 2 over the course of the observation, there is no apparent change in the absorption structure. This places it at least 0.5 pc (K-shell oxygen) or 2.8 pc (M-shell iron) away from the central engine. They find that the oxygen absorption and emission lines have similar velocity widths, implied columns and ionisation distributions (at least for H-like and He-like ions, as no oxygen emission is seen from states below this). This is interpreted as evidence for a biconical outflow giving rise to both the absorption and emission lines, creating the P-Cygni line profiles observed in the spectrum; such outflows have been observed in emission (and spatially resolved) in Seyfert 2 galaxies.

Behar et al. (2003) find that if the absorption and emission do indeed originate in the same medium, a localised (clumpy) geometry for the emitter is ruled out. Instead, they put forward the scenario of the warm absorber/emitter existing in ionisation cones not closer than about 10 pc from the nucleus, with gas densities of a few hundred particles per cm^3 and less. The mass loss rate in this outflow would be of the order of a few solar masses a year, which is a lot higher than the amount of mass that actually needs to be accreted in order to power the AGN luminosity. The warm absorber/emitter outflow would then be a significant part of the energy transport of the AGN.

3.6.2 Krongold et al. (2003)

Krongold et al. (2003) developed a two-phase warm absorber model for the 900 ks Chandra HETGS spectrum of NGC 3783. The models they used were very similar to the SPEX model *xabs* which I used; the one important difference was that their model allows the SED of the input spectrum to be directly specified, whereas *xabs* needs to be completely re-calculated for different SEDs. They also based their estimation of the ionisation structure on the patterns of iron absorption.

The Krongold et al. (2003) model is in general very similar to my two phase model. The two phases are, as in my model, based on the UTA and on the gas associated with L-shell iron absorption. One major difference is that they can fit the UTA with a solar abundance of iron. The other major differences are that they can fit the entire high ionisation phase with a single ionisation parameter, and the majority of their O VII absorption originates from the UTA phase. The reason why they are able to fit a UTA with solar abundances is probably to do with their low ionisation phase having an absorbing column ten times higher than that of mine. This may well be because their continuum includes a blackbody soft excess component (at a temperature of 0.1 keV), based on the findings of De Rosa et al. (2002b) from BeppoSAX data, allowing for deeper absorption in this part of the spectrum.

The dominant oxygen state in my low ionisation absorber is O VI, accompanied by significant fractions of O VII and O V which would become even more apparent at higher column densities, thus limiting the possibility of obtaining a lower iron abundance by increasing the overall column. The Krongold et al. (2003) low ionisation phase is more highly ionised than mine, with O VII having the greatest column among the oxygen ions; their model would also generate a relatively high column of O VI, but since they do not include the inner-shell oxygen ions in their model, they do not test whether the high overall column would give rise to a deep O VI edge not present in the data, or whether their low ionisation phase could reproduce the O IV or O V absorption observed in the RGS spectra.

The result of setting the ionisation parameters and columns of two *xabs* ionisation

phases to the values in the Krongold et al. (2003) model is shown in Fig. 3.11 (red line). The outflow speed and turbulent velocity of the absorber, as well as the power-law slope, are set to the Krongold et al. (2003) values, and a blackbody component of the temperature that they use (0.1 keV) is added in. I re-fitted the normalisations of the power-law and blackbody components to allow for cross-calibration differences between the RGS and HETGS and source variability between the different observations. The blue line shows what happens to the model if $\log \xi$ of the lower ionisation phase is set to the value in my two-phase model (0.3), which best represents the position of the UTA (the continuum normalisations have also been re-fitted).

Using *xabs*, a $\log \xi$ of 0.8 centres the UTA at a wavelength $\sim 0.7 \text{ \AA}$ shorter than it actually appears in the data. Clearly, the different SEDs assumed between *xabs* and the Krongold et al. (2003) *phase* model lead to different ionisation balances at a given ionisation parameter, so attempting to reproduce the Krongold et al. (2003) two-phase model using *xabs* is not a sufficient test of the effect on their fits of having left out the inner shell oxygen states. However, Fig. 3.11 does show that even at a $\log \xi$ of 0.8, there is noticeable O VI absorption between $\sim 17.5\text{--}19.5 \text{ \AA}$ (observed frame) that does not match the relatively low signal-to-noise RGS data, and which would create a very noticeable discrepancy with the 900 ks Chandra spectrum to which Krongold et al. (2003) compare their model.

3.6.3 Netzer et al. (2003)

Of the four recent papers on the ionised absorption in NGC 3783, Netzer et al. (2003) is the only one which approaches the global modelling in a significantly different way to the work described in this chapter. Whilst I (and Krongold et al., 2003) concentrated on using the iron absorption to determine the overall ionisation structure (due to the very wide range of ionisation states which iron can exhibit), Netzer et al. (2003) use Si and S lines at around 6 \AA , in the range where the signal-to-noise of the 900 ks Chandra spectrum is very high. Although these elements have a smaller range of ionisation states than iron (14 and 16 for Si and S respectively,

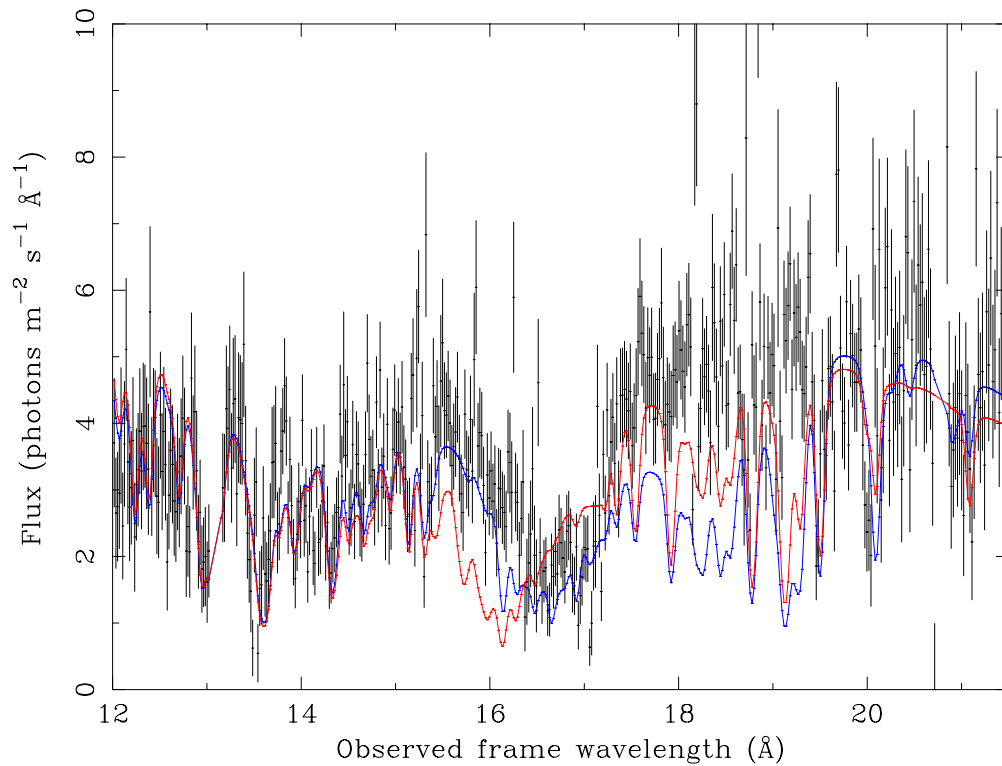


Figure 3.11: The result of constructing a two-phase warm absorber model using *xabs* with the columns and ionisation parameters of Krongold et al. (2003) (red line), compared to the 40 ks RGS spectrum of NGC 3783 (black points; plotted in the observed frame). Their power-law plus blackbody spectral continuum is used with re-fitted normalisations. The blue line shows what happens when $\log \xi$ of the low ionisation phase is set to 0.3 so that the UTA appears in the correct place for the *xabs* ionisation balance. In both cases, significant absorption from O VI, which was not included in the Krongold et al. (2003) model, is present.

as opposed to 26 for iron), and they are therefore a less sensitive diagnostic of the ionisation structure of a complex absorbing outflow, the advantage of using them is that the relevant atomic data for these transitions are very well known.

Netzer et al. (2003) found that there is a variable soft excess underlying the warm absorber, which makes a significant contribution to the soft X-ray spectral shape when the source is in what they term a ‘high state’. They found that changes in the luminosity of the soft excess did not coincide with spectral changes in the warm absorber. They modelled the absorber with three ionisation phases, basing their fits on the depths of Si and S absorption lines in the region of 5–7.1 Å. Each ionisation component is split into two velocity components, according to the findings of Kaspi et al. (2002). The combination of absorbing columns and ionisation parameters for the three phases is not a unique solution, but is described by these authors as ‘generically correct’.

Superimposing the results of their model fit on the whole spectrum, they find that their model provides an excellent representation of all parts of the warm absorber except for the UTA, which - at the ionisation parameter of their lowest ionisation phase - appears in the wrong place (their model UTA is centred at 0.7 Å lower in wavelength than it is in the observed spectrum). They put this down to an overestimation of the dielectronic recombination rates for the M-shell iron states, discussed in more detail in a further paper by Netzer (2003).

They conclude that the three phases of their absorber may be in pressure equilibrium. The three phases must be at least 3.2 pc, 0.6 pc and 0.2 pc (in increasing order of ionisation) from the source of radiation. Assuming pressure equilibrium - and that the maximum distance for the absorber must be the NLR, the distance of the absorber(s) from the central engine must be in the range ~ 3 –25 pc.

3.6.4 Reeves et al. (2004)

Whilst Behar et al. (2003), Krongold et al. (2003) and Netzer et al. (2003) concentrate on modelling the high resolution grating spectra of NGC 3783, Reeves et al. (2004) look at the CCD resolution pn spectrum from the long XMM-Newton ob-

servation of NGC 3783. They found that this band also contains evidence of the ionised absorbing outflow.

Reeves et al. (2004) modelled the underlying spectral continuum as a power-law with a small blackbody soft excess component ($kT = 0.097 \pm 0.004$ keV) and a hard X-ray reflection component similar to that observed with BeppoSAX. They found an absorption line due to L-shell iron at 6.67 ± 0.04 keV (consistent with the 1s–2p transitions of Fe XXIII, Fe XXIV and Fe XXV in the rest frame of NGC 3783). This absorption line was not explained by the two soft X-ray absorber phases (for which they initially used the physical parameters of my two-phase warm absorber model), so they added a third warm absorber phase with a very high ionisation parameter ($\log \xi = 3$). The ionisation parameters and the equivalent hydrogen columns of the three phases were then fitted, changing the parameters slightly (note that Reeves et al. 2004 use a ten times solar abundance for iron in the lowest ionisation phase, as I did, and solar abundances for the other phases).

Their most important result is that this very highly ionised phase is observed to vary over the course of the XMM-Newton observation; the 6.67 keV absorption line is seen to get significantly deeper on a timescale of $\sim 10^5$ s. The lower ionisation phases, which do not seem to vary, must be at parsec scale distances, whereas the highest ionisation phase must be much closer to the nucleus. At the ionisation parameter of this phase, and using the condition that the depth of the absorber cannot be greater than its distance from the continuum source, Reeves et al. (2004) find that it must be less than 0.1 pc from the central source (I give a derivation of the formula they use in Chapter 6, Equations 6.19–6.24). They demonstrate that the change in depth of the 6.67 keV absorption line could be caused by a change in ionisation of the absorber due to the changing continuum flux.

Reeves et al. (2004) then use the fact that the variability timescale must be greater than or equal to the ionisation timescale, so that the ionisation parameter can react to the flux changes within the variability timescale, to get an upper limit on the distance of the absorber from the source. The approximate upper limit is 0.02 pc. They estimate the density of this phase to be $\sim 10^8$ cm⁻³, and its outflow rate to be

of the order of 0.1 solar masses a year. This leads them to the same conclusion as Behar et al. (2003): the high mass outflow rate implies that a significant proportion of the matter flowing in towards the AGN is actually required for the outflow.

3.7 Conclusions

The absorbing columns and ionisation parameters of the warm absorber model phases of Kaspi et al. (2001); De Rosa et al. (2002b); Blustin et al. (2002a); Krongold et al. (2003); Netzer et al. (2003); Reeves et al. (2004) are compared in Table 3.7. The three possible phases are denoted low ionisation (Phase 1: the phase producing the UTA), mid ionisation (Phase 2, which produces the ‘typical’ H-like and He-like ions of O) and high ionisation (Phase 3, which broadly corresponds to the most highly ionised states of iron). In cases where the authors give the ionisation parameter in the form of U or U_{OX} , I have converted it to ξ using Equation 1.7 (Chapter 1), integrating over the SED given by the authors.

Although the exact numbers produced by the recent multi-phase models differ slightly, they offer the same phenomenological picture - three main ionisation phases, of which the lowest ionisation phase is associated with the UTA and the other two are responsible for the H-like and He-like transitions of astrophysically abundant elements, particularly L-shell and K-shell iron. Whether one or all of these phases could also be explained by a multi-temperature wind, with a continuous ionisation distribution, has yet to be investigated in detail. The biggest problem with the current global warm absorber models, as reported by Netzer et al. (2003) and Netzer (2003), is the uncertainty in the dielectronic recombination rates of M-shell iron, and thus the position of the UTA. Solving this problem should lead to the development of a generally agreed model for the NGC 3783 warm absorber.

There is broad agreement about the distance of the warm absorber from the central engine (Behar et al., 2003; Netzer et al., 2003), and about the significant mass outflow rate of the absorber (Behar et al., 2003; Reeves et al., 2004). The overall structure of the ionised outflow in NGC 3783 is coming into focus; the implications

Table 3.7: Comparison of the properties of recent multi-phase warm absorber models for NGC 3783; Phases 1, 2 and 3 are in order of increasing ionisation

Authors	Parameter	Phase 1	Phase 2	Phase 3
Kaspi et al. 2001	IP ^a	–	1.8	2.8
	N _H ^b	–	22.2	22.2
De Rosa et al. 2002b	IP ^a	–	2.4	–
	N _H ^b	–	22.3	–
Blustin et al. 2002a	IP ^a	0.3	2.4	–
	N _H ^b	20.7	22.5	–
Krongold et al. 2003	IP ^a	0.8	2.4	–
	N _H ^b	21.6	22.2	–
Netzer et al. 2003	IP ^a	1.1	2.3	2.9
	N _H ^b	21.9	22.0	22.3
Reeves et al. 2004	IP ^a	-0.1	2.1	3.0
	N _H ^b	21.0	22.1	22.6

^a Ionisation parameter (Log ξ , where ξ is in erg cm s⁻¹)

^b Log of the equivalent hydrogen column of the phase, where N_H is in cm⁻²

for the production of the outflow, and the energetics of the central engine, have yet to be worked out.

Chapter 4

NGC 7469

4.1 Introduction

This chapter describes my work on data from the XMM-Newton observation of NGC 7469, making comparisons and connections between this and the results of a previous FUSE observation, in order to understand the relationship between X-ray and UV ionised absorption and emission in this object.

NGC 7469 is a well-studied Seyfert 1.2 galaxy. Table 4.1 gives some basic parameters relating to this object. The primary interest from our point of view here is the reported presence of soft X-ray warm absorption in its ASCA spectra (Reynolds, 1997; George et al., 1998; Kriss et al., 2000b), although this has not been detected in more recent BeppoSAX data (De Rosa et al., 2002a). The XMM-Newton observation of NGC 7469 provides the first high resolution soft X-ray spectra of this object, and the best opportunity yet to investigate its warm absorber.

4.2 X-ray results from XMM-Newton

My preliminary results on NGC 7469 were first presented in Blustin et al. (2002b), and the full analysis, described in this chapter, is published in Blustin et al. (2003). The latter was published in conjunction with a paper by Kriss et al. (2003) which described FUSE UV spectroscopy of NGC 7469. The FUSE results are summarised

Table 4.1: Some basic information on NGC 7469 (coordinates are J2000)

Right Ascension	Declination	Redshift	Galactic column ^a
23h 03m 15.623s	+08d 52m 26.39s	0.0164 ^b	4.82

^a Galactic absorbing column in 10^{20} cm^{-2} (Elvis et al., 1989)

^b de Vaucouleurs et al. (1991)

in Section 4.3.2 below.

4.2.1 X-ray and UV Variability

The X-ray lightcurves of NGC 7469 were obtained from the pn data as the MOS data were seriously affected by pile-up. Over the course of the 40 ks observation, the total 2–10 keV X-ray flux was seen to increase by $\sim 50\%$. Looking at the lightcurves of different energy bands (Fig. 4.1), it becomes apparent that the soft 0.2–2 keV band is varying the most (there is a 55% increase in flux in the first 15 ks), whilst the 6–10 keV band changes much more slowly ($\sim 20\%$ increase over the course of the 45 ks observation). The decrease in the hardness ratio as the flux increases shows that we are dealing with either a variable soft excess, a changing spectral index or variable absorption, a conclusion which is well illustrated by the plot of hardness against total flux (Fig. 4.2). This shows a very clear correlation between increasing flux and decreasing hardness; the linear correlation coefficient of the plotted points is 0.92, with a probability of obtaining this level of correlation from a random distribution of $\sim 10^{-10}$. The UV lightcurve, obtained from the series of UVW2 filter images (Fig 4.3) from the OM shows no unambiguous variability within the 10% errors.

4.2.2 0.2–10 keV continuum and Fe $K\alpha$ line

Because of the spectral variability demonstrated by the X-ray lightcurves, I fitted models separately to pn data from the two halves of the observation (as the spec-

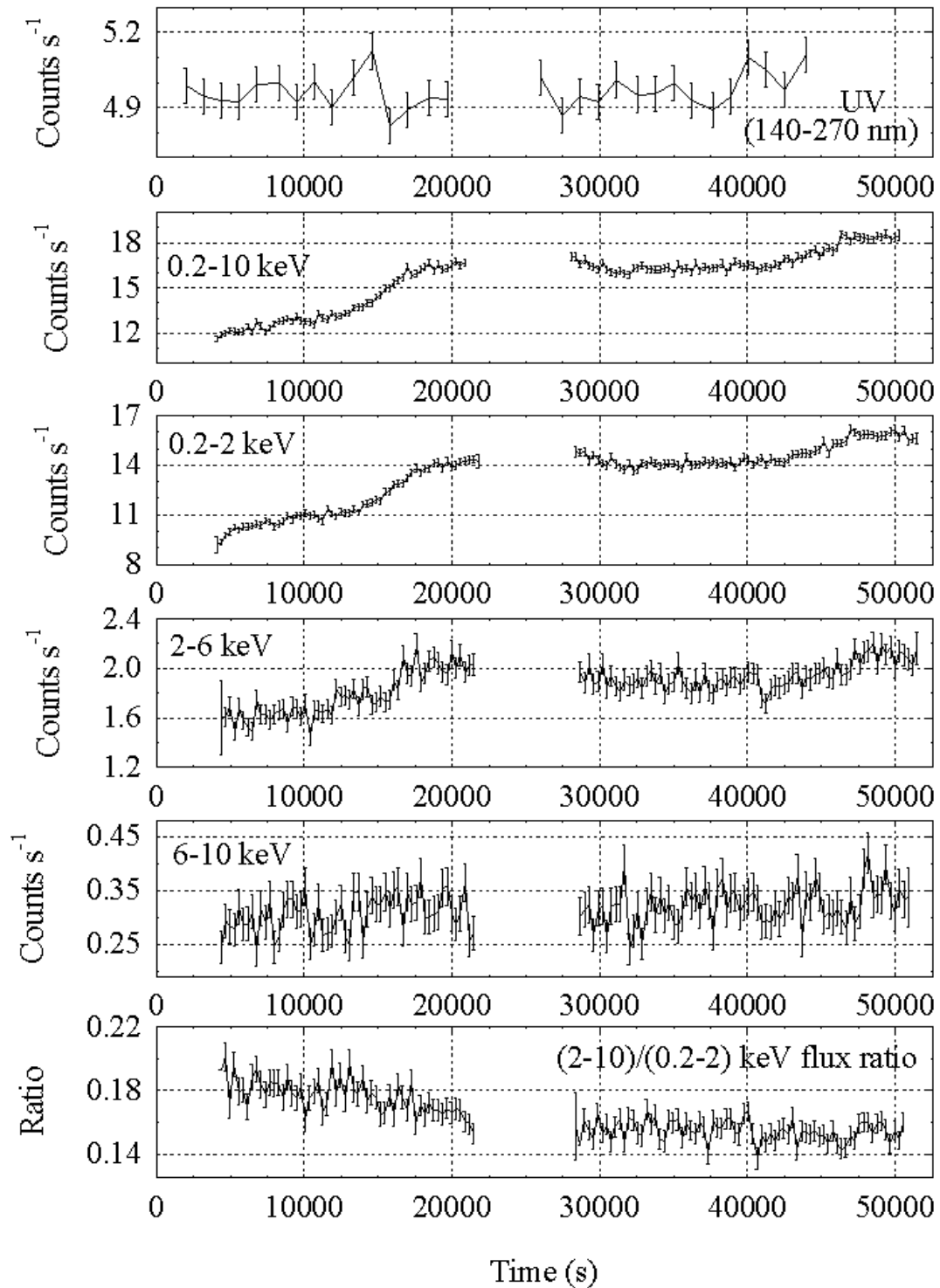


Figure 4.1: Multiwavelength background-subtracted lightcurves: top, UV (140–270 nm) lightcurve from the OM, in 1000 s time bins; middle four, pn lightcurves in the bands 0.2–10, 0.2–2, 2–6 and 6–10 keV, in 300 s time bins; bottom, the hardness ratio (2–10 keV / 0.2–2 keV flux) in 300 s time bins.

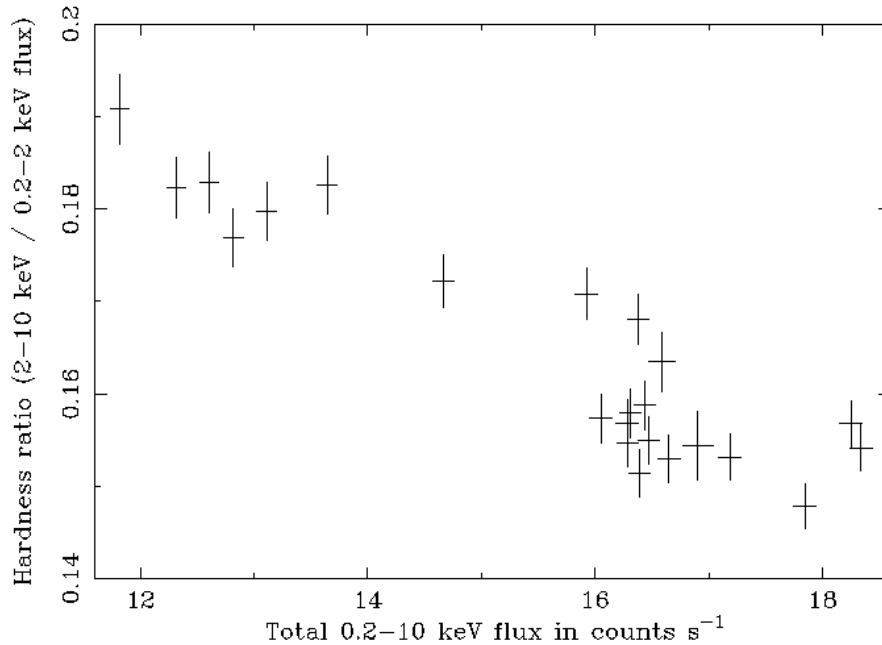


Figure 4.2: Hardness – intensity plot in 30 minute time bins.

trum was in a predominantly hard state in the first part of the observation and a predominantly soft state in the second part). The best fit model was found to be a hard X-ray power law plus two blackbodies to represent the soft excess, with a single narrow Gaussian for the Fe $K\alpha$ line and neutral absorption due to our Galaxy. Comptonisation (*compTT* in Xspec) and reflection models (*pearriv* in Xspec and *reft* in Spex) did not produce such good χ^2_{red} ; I was primarily aiming to produce a correctly shaped continuum to underly the RGS spectrum, so I continued with the (possibly unphysical) multi-blackbody soft excess. Fig. 4.4 shows the best fit model to the total (i.e. combined hard and soft state) spectra alongside the data for the individual soft and hard states. The model components are also plotted. The pn spectra were grouped to provide 125 counts per bin, giving approximately 50 eV bins in the region of the Fe $K\alpha$ line. Fig. 4.5 shows the ratios of the two datasets to this model, and the continuum fit parameters are listed in Table 4.2. Although its flux changes, the form of the soft excess does not change significantly between the two states.

To increase the signal-to-noise in the Fe $K\alpha$ line, I added the pn spectrum to those from MOS1 and MOS2. Due to the pile-up of the MOS spectra, the resulting

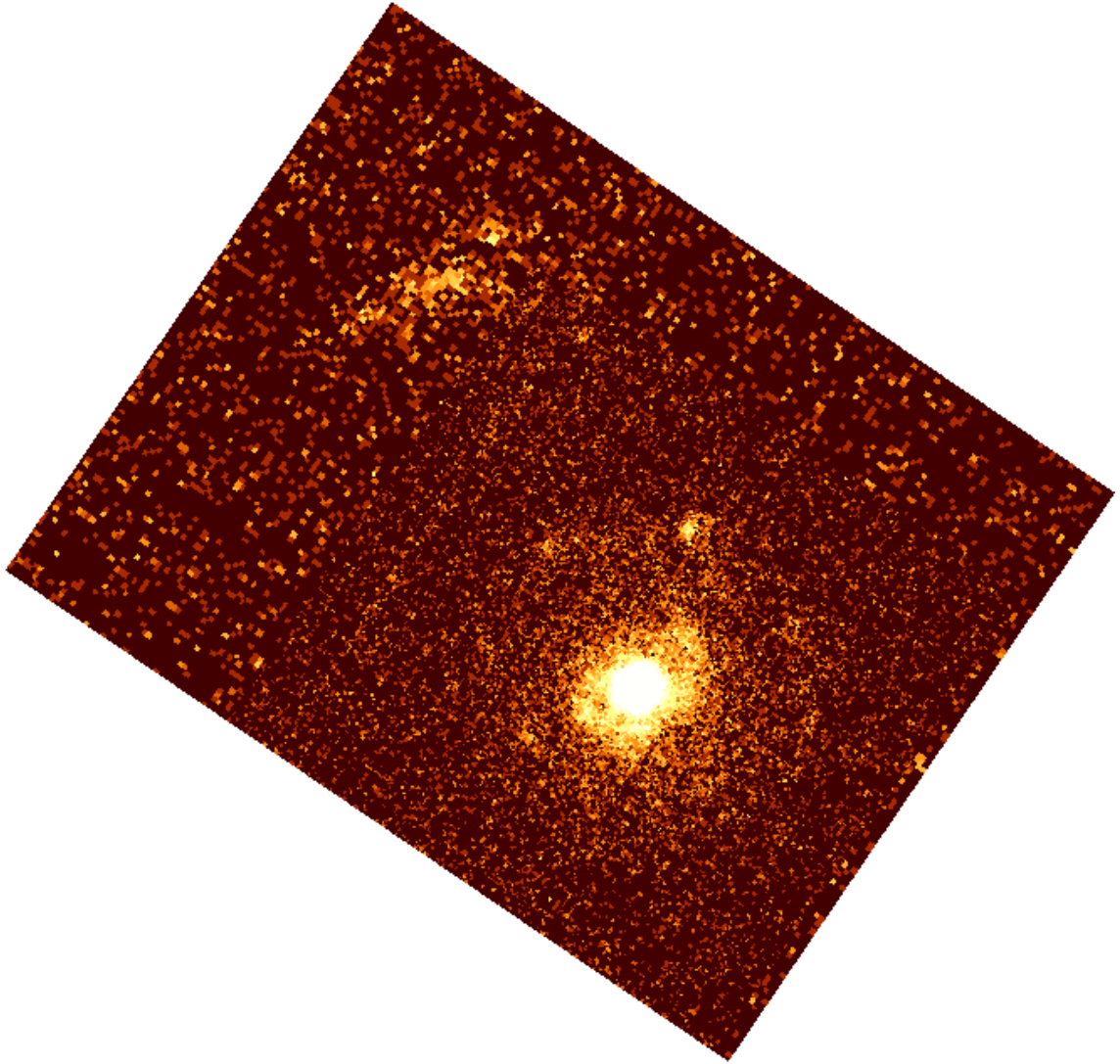


Figure 4.3: UVW2 filter image (combined from all exposures) of NGC 7469 (bottom right) and IC 5283 (top left). North is up, East to the left; image size approx. $140'' \times 110''$. NGC 7469 is within an imaging window with $0.5''$ pixels, whereas IC 5283 is in a $1''$ pixel region. The nuclear image of NGC 7469 is saturated so that the wider UV structure of the galaxy is visible.

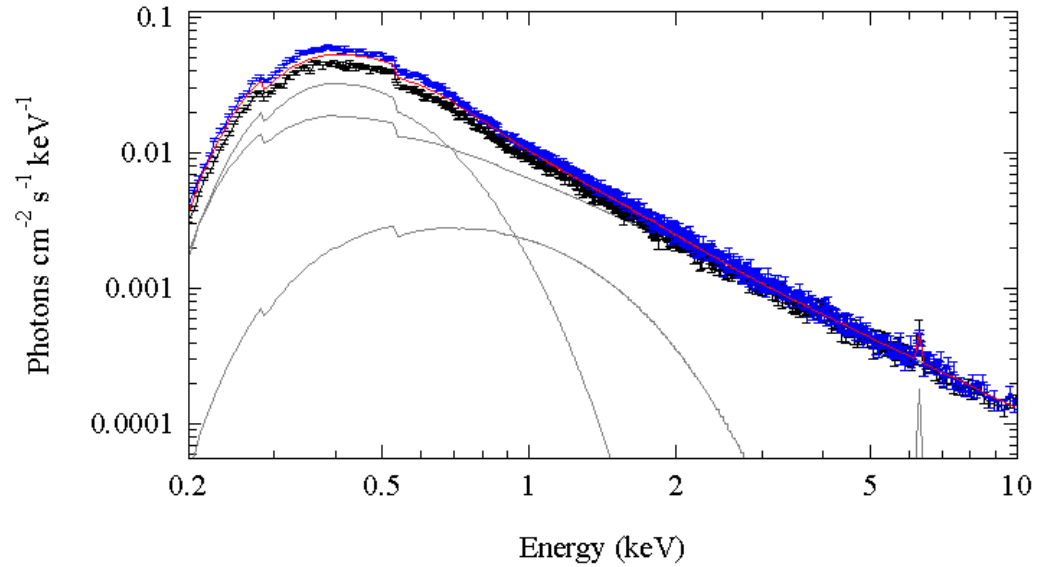


Figure 4.4: The soft (blue) and hard (black) PN spectra plotted with the best fit model for the total pn spectrum (red), with the two blackbodies, power-law and Fe $K\alpha$ line model components (all in grey).

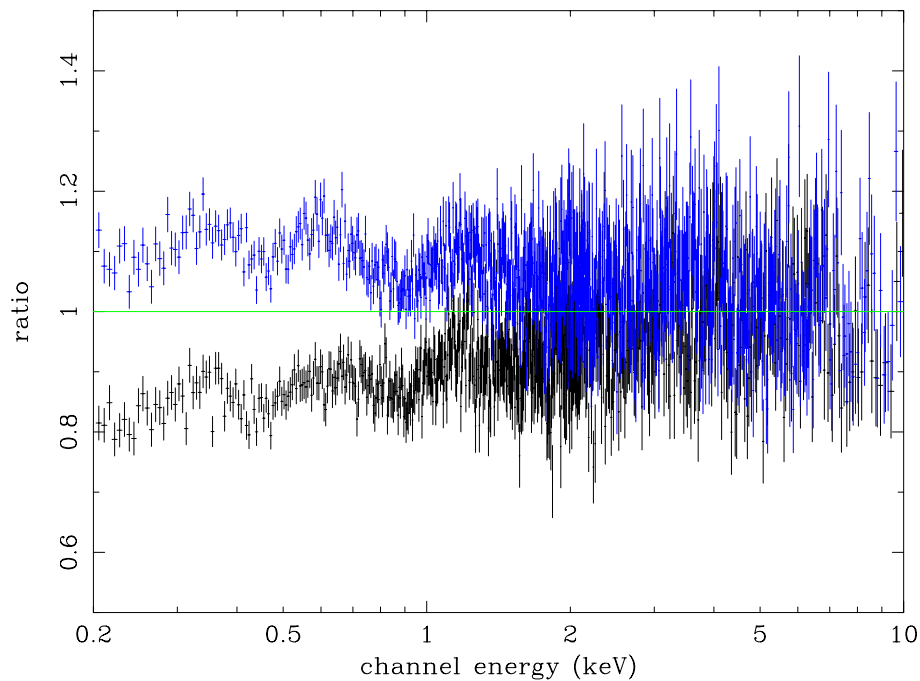


Figure 4.5: The ratio of the soft pn spectrum (blue) and the hard pn spectrum (black) to the best fit model for the total pn spectrum.

Table 4.2: Fits to the X-ray continuum and Fe $K\alpha$ emission line: N_{HGal} , Galactic absorbing column in 10^{20} cm^{-2} , fixed (Elvis et al., 1989); Γ , photon index; N_{P} , power-law normalisation in 10^{-3} photons $\text{keV}^{-1} \text{ cm}^{-2} \text{ s}^{-1}$ at 1 keV; kT_{BB1} and kT_{BB2} , temperatures of blackbody 1 and 2 in keV; N_{BB1} and N_{BB2} , normalisations of blackbody 1 and 2 in $10^{-5} L_{39}/D_{10}^2$, where L_{39} is the source luminosity in 10^{39} s^{-1} and D_{10} is the distance to the source in units of 10 kpc; rest frame energy E of Fe $K\alpha$ in keV; FWHM of Fe $K\alpha$ in eV; V_{broad} , velocity broadening (FWHM) of Fe $K\alpha$ in km s^{-1} ; cz , de-redshifted velocity of Fe $K\alpha$ in km s^{-1} (negative values are blueshifts); F , flux of Fe $K\alpha$ in 10^{-5} photons $\text{cm}^{-2} \text{ s}^{-1}$; reduced χ^2 with degrees of freedom in brackets.

Parameter	Total PN spectrum	Hard PN spectrum	Soft PN spectrum	Combined EPIC spectrum	RGS spectrum
N_{HGal}	4.82	4.82	4.82	4.82	4.82
Γ	1.749 ± 0.005	1.732 ± 0.007	1.755 ± 0.007	1.7 ± 0.1	1.749, fixed
N_{P}	7.28 ± 0.03	6.80 ± 0.04	7.52 ± 0.04	6 ± 1	6.3 ± 0.5
kT_{BB1}	0.112 ± 0.001	0.114 ± 0.001	0.111 ± 0.001	–	0.112, fixed
N_{BB1}	26.6 ± 0.2	21.4 ± 0.3	30.7 ± 0.3	–	19.5 ± 0.7
kT_{BB2}	0.303 ± 0.004	0.304 ± 0.007	0.303 ± 0.004	–	0.303, fixed
N_{BB2}	7.0 ± 0.1	5.6 ± 0.1	8.1 ± 0.1	–	8 ± 2
E	6.40 ± 0.02	6.39 ± 0.02	6.41 ± 0.03	6.40 ± 0.02	–
FWHM	130^{+80}_{-110}	60^{+100}_{-60}	150^{+2500}_{-150}	160 ± 70	–
V_{broad}	6000 ± 5000	3000^{+5000}_{-3000}	$7000^{+100000}_{-7000}$	8000 ± 3000	–
cz	-300 ± 900	100 ± 1000	-1000 ± 2000	-500 ± 800	–
F	2.7 ± 0.5	3.2 ± 0.6	2.4 ± 0.7	3.0 ± 0.4	–
χ_{red}^2	$1.80^{\text{a}} (399)$	$1.12^{\text{a}} (607)$	$1.28^{\text{a}} (692)$	$1.25^{\text{b}} (61)$	$1.17^{\text{c}} (994)$

^a in the range 0.2–10 keV, ^b in the range 5–8 keV, ^c in the range 0.32–2.07 keV.

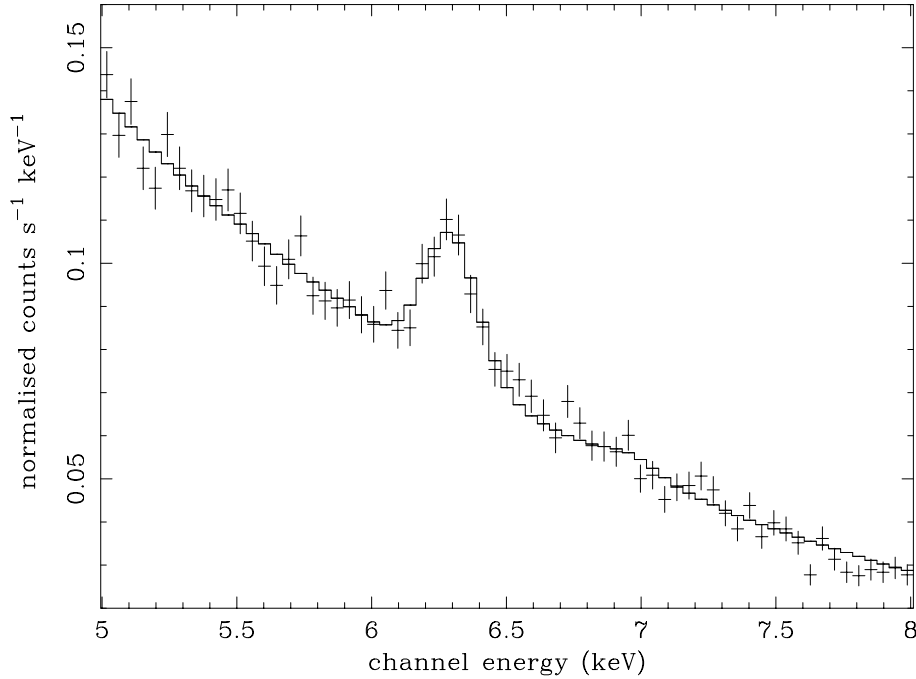


Figure 4.6: The (observer’s frame) Fe $K\alpha$ emission line (combined MOS1, MOS2 and pn data) with the model including both Fe $K\alpha$ and Fe $K\beta$.

combined spectrum was not suitable for continuum fitting. I therefore fitted a local power-law to the 5–8 keV range and used this as the underlying continuum when fitting the iron line. The line was best fitted as a Gaussian, marginally resolved, whose parameters are given in Table 4.2. I added in a Gaussian, with the same σ as $K\alpha$, to represent Fe $K\beta$, with the expected 14% of the intensity. The χ^2_{red} worsened slightly to 1.28 for 58 degrees of freedom; this final model is shown in Fig. 4.6.

4.2.3 RGS spectrum

Warm absorber

The power-law and two blackbody model (with neutral absorption due to our Galaxy) fitted to the pn data was used as the underlying continuum for the RGS spectrum. The blackbody temperatures and power-law slope were kept the same as in the best-fit pn model, but the normalisations of the three components were re-fitted to the RGS data, avoiding problems with differences in relative normalisations between the instruments. This does not take into account the known calibration difference in

power-law slopes between the RGS and pn of 0.1; the blackbody component, however, is the most important contribution to the continuum spectrum over most of the RGS range. This assumption will probably have only a small effect on the fitted normalisations. The parameters of the best fit continuum are given in Table 4.2. The presence of the warm absorber will have some effect on the fitted continuum, and this is discussed at the end of this section.

The RGS data were binned into groups of three channels, slightly below the instrument resolution, for the analysis. A number of narrow emission and absorption lines are present in the spectrum; these features are marked in Fig. 4.7 and Fig. 4.8, which show the RGS spectrum with the model superimposed. No absorption edges are visible. To estimate the statistical significance σ of the narrow features, a sliding Gaussian fit was performed over the whole RGS spectral range (see Chapter 2); the results of this are shown in Fig. 4.9, with the most important features identified. The parameters of the absorption and emission lines (identification, rest wavelength, observed wavelength, equivalent width, velocity shifts, flux, velocity width (as appropriate) and $\log \xi$ of maximum abundance) are given in Table 4.3 and Table 4.4 respectively, and the rest wavelength, velocity shifts, flux, velocity width and $\log \xi$ of maximum abundance of the broad and narrow O VI lines observed in the UV by FUSE (Kriss et al., 2003) are also listed in Table 4.4 for comparison.

The velocity shifts of the absorption lines unaffected by re-emission (thus excluding O VIII Ly α and C VI Ly α which are partially filled in by re-emission in a P-Cygni profile), with an Equivalent Width inconsistent with zero, are plotted against $\log \xi$ of maximum abundance for those ions in Fig. 4.10. This shows immediately that there is a very wide distribution of ionisation parameter in the warm absorber, and that all ionisation levels are blueshifted. Unfortunately, there are not enough measurable ions to robustly determine any variation in blueshift with ionisation; the weighted average of all the velocity shifts is $-800 \pm 100 \text{ km s}^{-1}$, whereas the weighted averages for the high-ionisation phase ($\log \xi$ clustering around 1.5) and the low ionisation phase ($\log \xi$ below 0.5) are, respectively, $-900 \pm 100 \text{ km s}^{-1}$ and $-600 \pm 200 \text{ km s}^{-1}$.

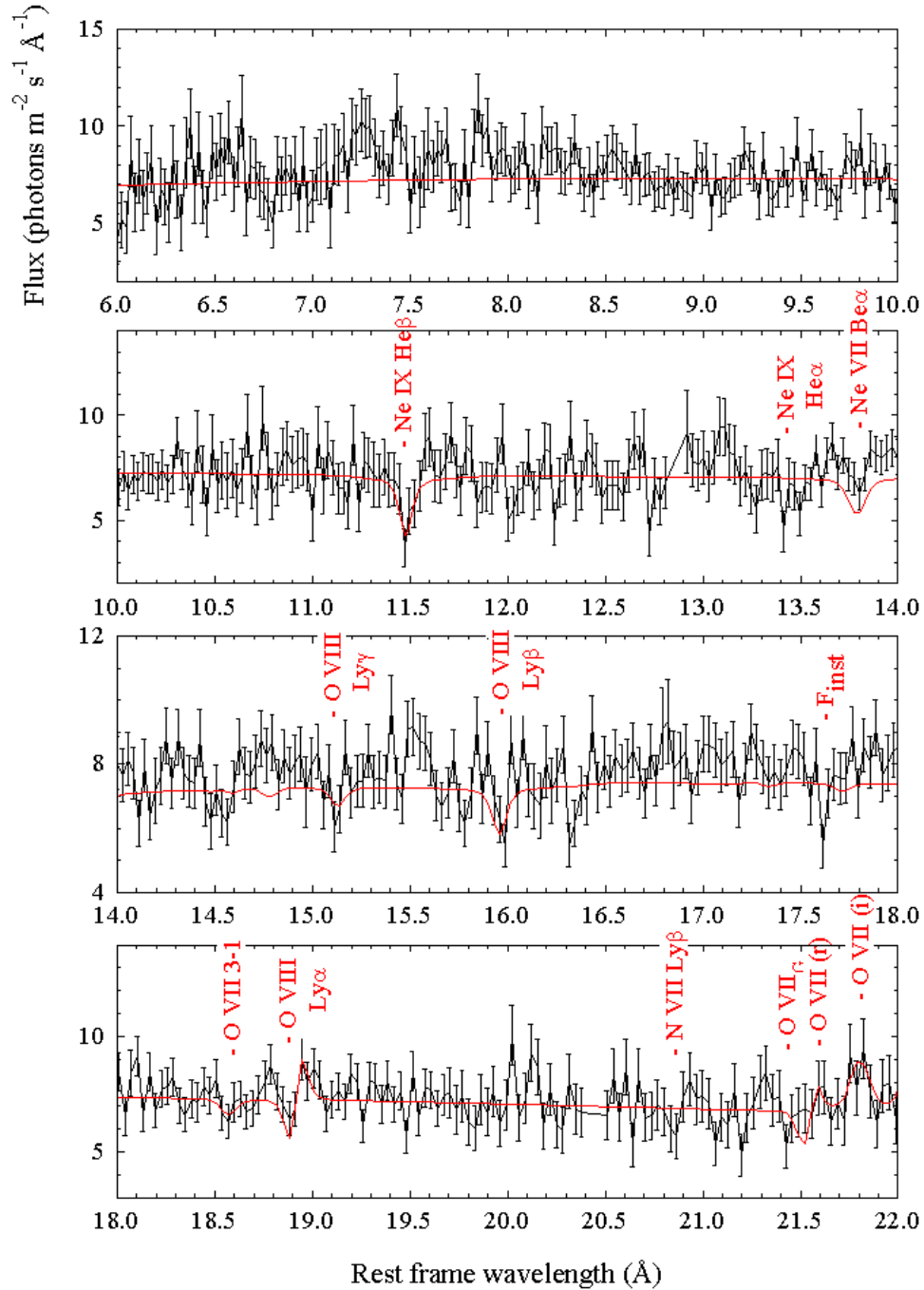


Figure 4.7: Combined RGS1 and RGS2 rest frame spectrum of NGC 7469 (black), binned into groups of three channels, with power-law plus two blackbody continuum model superimposed (red) including all lines listed in Table 4.3 and Table 4.4, plotted over the range 6–22 \AA . The positions of other possible spectral features are labelled. The G subscript refers to features originating in our galaxy, and F_{inst} is an instrumental Fluorine feature.

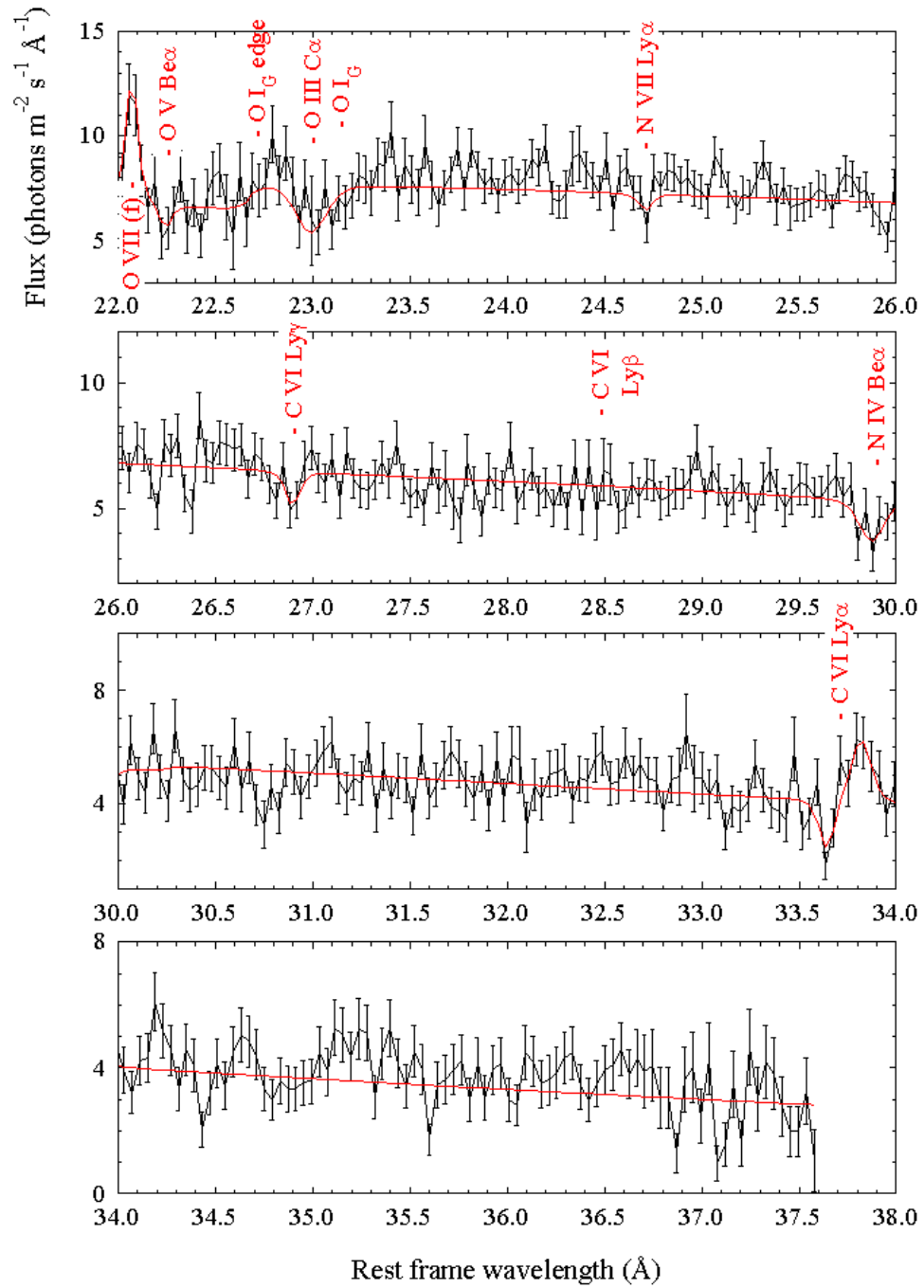


Figure 4.8: As for Fig. 4.7, plotted in the range 22–38 \AA .

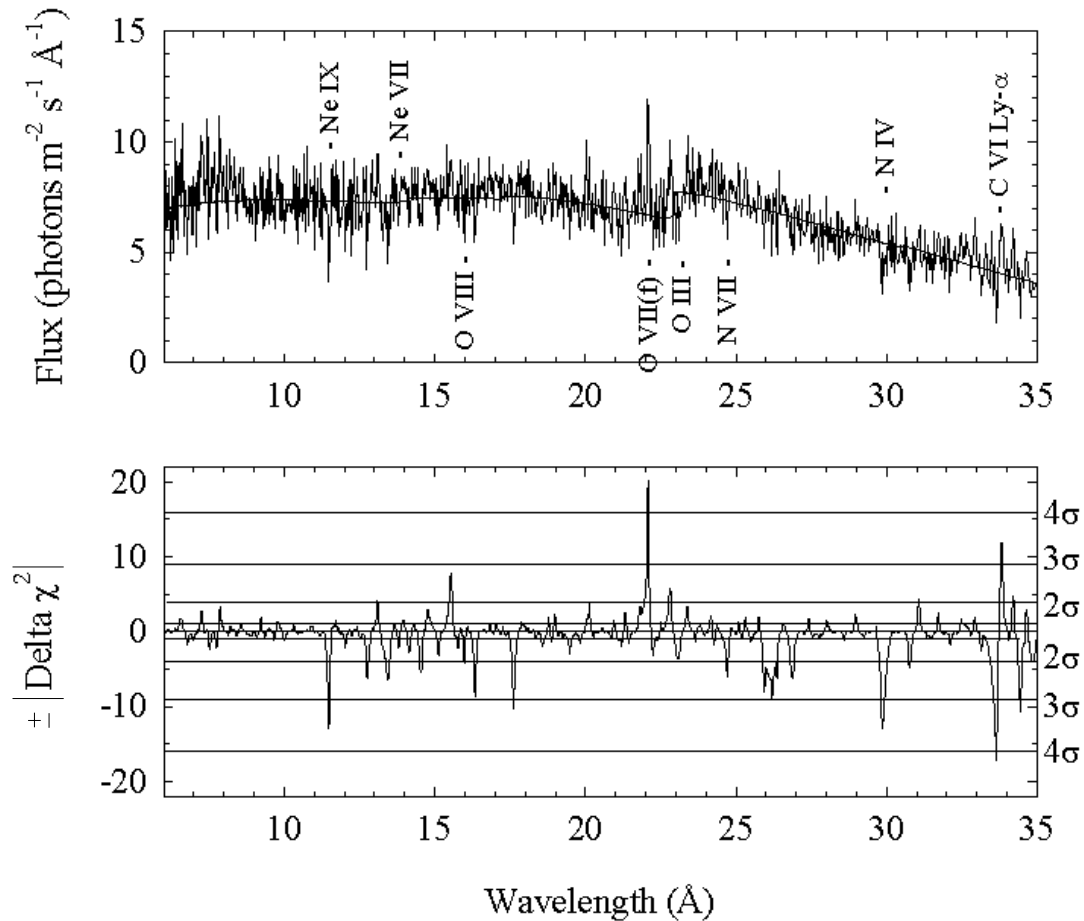


Figure 4.9: Top: combined RGS1 and RGS2 rest frame spectrum of NGC 7469 (6–38 Å) with power-law plus two blackbody continuum superimposed, and the positions of important features marked. Bottom: plot of the statistical significance of the narrow absorption and emission lines. This plot shows the absolute value of the change in χ^2 when a narrow Gaussian of variable width (up to 1000 km s⁻¹) is added to an underlying continuum which has been smoothed with a 70 channel boxcar function (see Section 2.5). Positive and negative values of $|\Delta\chi^2|$ refer to emission and absorption features respectively. The number of σ indicates the confidence level at which the spectral feature, as fitted by the Gaussian, is significant. Since the fit involves one interesting parameter, namely the equivalent width of the Gaussian, the number of σ represented by a given percentage confidence level is the square root of $|\Delta\chi^2|$.

Table 4.3: Absorption lines in the RGS spectrum of NGC 7469: rest wavelengths (λ_{rest} ; Å), observed wavelengths (λ_{obs} ; Å), equivalent widths (EW; mÅ), velocity shifts (v ; km s $^{-1}$), and $\log \xi_{\text{max}}$ (ξ is in erg cm s $^{-1}$) where the ion is most abundant; rms errors are quoted throughout, except for $\log \xi_{\text{max}}$ where the error bars give the range where the ion has a higher relative abundance than adjacent ionisation states.

Transition	λ_{rest}	λ_{obs}	EW	v	$\log \xi_{\text{max}}$
O VIII Ly α	18.969	18.89 \pm 0.05	10 \pm 10		1.8 \pm 0.3
O VIII Ly β	16.006	15.98 \pm 0.02	20 \pm 10	-600 \pm 500	1.8 \pm 0.3
O VIII Ly γ	15.176	15.12 \pm 0.05	10 \pm 10		1.8 \pm 0.3
O VII 3-1	18.629	18.57 \pm 0.04	10 \pm 10		1.1 $^{+0.4}_{-0.5}$
O V Be α	22.334	22.25 \pm 0.04	20 \pm 20		0 $^{+0.4}_{-0.3}$
O III Ca	23.058	22.99 \pm 0.04	70 \pm 20	-800 \pm 500	-1.8 \pm 0.6
N VII Ly α	24.781	24.72 \pm 0.04	10 \pm 10		1.5 \pm 0.3
N IV Be α	29.896	29.87 \pm 0.03	60 \pm 20	-300 \pm 400	-0.6 \pm 0.5
C VI Ly α	33.736	33.65 \pm 0.03	50 \pm 20	-800 \pm 200	1.1 $^{+0.4}_{-0.3}$
C VI Ly γ	26.990	26.90 \pm 0.03	20 \pm 10	-1000 \pm 300	1.1 $^{+0.4}_{-0.3}$
Ne IX He β	11.547	11.48 \pm 0.02	50 \pm 20	-1600 \pm 500	1.7 $^{+0.3}_{-0.4}$
Ne VII Be α	13.814 ^a	13.79 \pm 0.02	40 \pm 10	-500 \pm 500	0.5 \pm 0.3

^a from Behar and Netzer (2002)

Table 4.4: Emission lines in the RGS spectrum of NGC 7469: rest wavelengths (λ_{rest} ; Å), observed wavelengths (λ_{obs} ; Å), equivalent widths (EW; mÅ), velocity shifts (v ; km s $^{-1}$), fluxes (in 10^{-5} photons cm $^{-2}$ s $^{-1}$), velocity widths (v_{broad} , FWHM; km s $^{-1}$) and $\log \xi_{\text{max}}$ (ξ is in erg cm s $^{-1}$) where the ion is most abundant; rms errors are quoted throughout, except for $\log \xi_{\text{max}}$ where the error bars give the range where the ion has a higher relative abundance than adjacent ionisation states. Also listed are rest wavelengths, velocity shifts, fluxes, velocity widths and $\log \xi_{\text{max}}$ for the broad and narrow O VI emission lines observed by FUSE (Kriss et al., 2003).

Transition	λ_{rest}	λ_{obs}	EW	v	Flux	v_{broad}	$\log \xi_{\text{max}}$
O VIII Ly α	18.969	18.98 \pm 0.05	-20 \pm 10	200 \pm 700	1.4 \pm 1.0	0 $^{+3000}_{-0}$	1.8 \pm 0.3
O VII (f)	22.101	22.07 \pm 0.02	-80 \pm 20	-400 \pm 200	6.0 \pm 1.7	0 $^{+700}_{-0}$	1.1 $^{+0.4}_{-0.5}$
O VII (i)	21.807	21.80 \pm 0.04	-40 \pm 20	-100 \pm 500	2.7 \pm 1.6	700 $^{+2000}_{-700}$	1.1 $^{+0.4}_{-0.5}$
O VI ^a	1031.93			323 \pm 37	4457 \pm 223	4901 \pm 146	0.5 $^{+0.1}_{-0.2}$
O VI ^a	1037.62			323 \pm 37	2241 \pm 115	4901 \pm 146	0.5 $^{+0.1}_{-0.2}$
O VI ^b	1031.93			-163 \pm 55	1221 \pm 151	1061 \pm 82	0.5 $^{+0.1}_{-0.2}$
O VI ^b	1037.62			-163 \pm 55	616 \pm 78	1061 \pm 82	0.5 $^{+0.1}_{-0.2}$
C VI Ly α	33.736	33.82 \pm 0.03	-90 \pm 30	700 \pm 200	3.6 \pm 1.3	700 $^{+800}_{-700}$	1.1 $^{+0.4}_{-0.3}$

^a from the Broad Line Region

^b from the Narrow Line Region

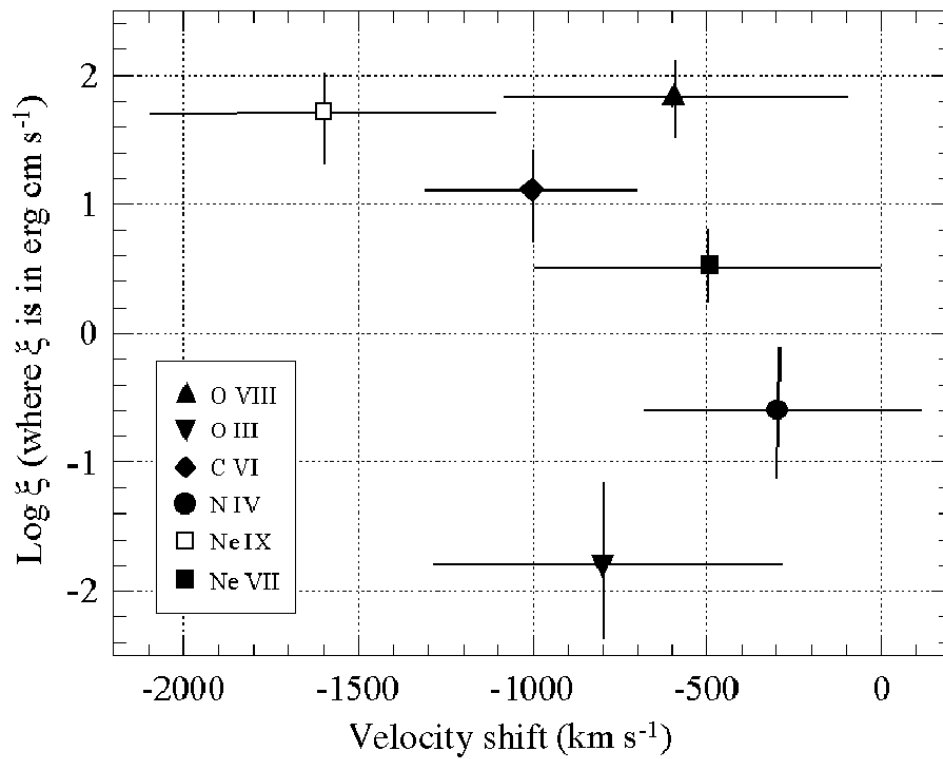


Figure 4.10: Velocity shift plotted against $\log \xi$ of maximum abundance for ions observed in the RGS spectrum of NGC 7469.

The high-ionisation phase has the largest number of measurable ions, so we can learn the most about its properties. Its average ionisation parameter can be estimated if we assume that the O VII and O VIII lines come from this phase, using the ratio of the absorbed fluxes of O VIII Ly β and the O VII 3–1 resonance line. O VIII Ly α and O VII 2–1 resonance are partially filled in by re-emission and are thus less useful for this purpose. Log ξ , estimated by this method (see Chapter 1), is $1.6_{-0.4}^{+0.7}$.

An unusual feature of the RGS spectrum of NGC 7469 is the apparent lack of iron absorption, which is such a major factor in the spectra of other warm absorber Seyferts (the most extreme example is NGC 3783; see Chapter 3). This is probably because of the low overall column of the NGC 7469 absorber; taking log ξ of the high-ionisation phase to be 1.6, the *xabs* model in SPEX 2.00 can be used to fit an overall equivalent hydrogen column of $(1.5 \pm 0.9) \times 10^{20} \text{ cm}^{-2}$. Iron absorption would not be significant, at the signal-to-noise of our spectrum, at this column. I assumed a turbulent velocity of 100 km s^{-1} in this estimation, which is much higher than the measured value for the UV absorber (25 km s^{-1} ; Kriss et al. 2003); using a value of 25 km s^{-1} for the X-ray absorber turbulent velocity, the fitted overall column is $(0.6 \pm 0.3) \times 10^{20} \text{ cm}^{-2}$. This is consistent with the value obtained using $v = 100 \text{ km s}^{-1}$, probably due to the relatively low signal-to-noise of the RGS spectrum. Construction of a full global model for the warm absorber in this source will have to wait for a much higher signal-to-noise RGS spectrum from the $\sim 150 \text{ ks}$ XMM-Newton observation of this source planned for late 2004.

Warm emitter

The measured parameters of the emission lines are given in Table 4.4. These parameters were fitted without taking absorption into account, so the blueshifts of O VIII Ly α and C VI Ly α will be affected by this, as they have P-Cygni profiles. The lines are not significantly broadened, but any broadening could be obscured by the absorption. The other two important lines in the spectrum, O VII (i) and O VII (f), are less likely to be affected.

Although O VII (i) and O VII (f) are clearly visible, the third member of the O VII triplet, O VII (r), is not seen. The presence of the O VII 3–1 resonance *absorption* line means that the 2–1 resonance absorption is cancelling out the 2–1 resonance (O VII (r)) emission. The same situation is seen with O VIII, where Ly α absorption is partially filled in by Ly α emission and so is less deep than the Ly γ and Ly β absorption lines.

If we want to use the ratio of the fluxes of the O VIII Ly α and O VII (r) emission lines to estimate the ionisation parameter of the warm emitter, then we have to find a way of modelling the O VII and O VIII absorption. I did this by fitting O VII and O VIII absorbing columns (using *slab* in SPEX 2.00, again assuming a velocity width of 100 km s⁻¹) to the O VII 3–1 resonance and O VIII Ly β and Ly γ absorption lines. Columns of $\log N_{\text{O VII}} = 16.5^{+0.4}_{-1.9}$ and $\log N_{\text{O VIII}} = 17.3 \pm 0.3$ (where N is in cm⁻²) were obtained, at a fitted blueshift of 900 ± 400 km s⁻¹. The ratio of these implies a $\log \xi$ of $2.1^{+1.6}_{-0.5}$ which is consistent with the value obtained above using a simple ratio of absorbed fluxes. At this ionisation parameter, the overall column of the absorber would be $(4 \pm 2) \times 10^{20}$ cm⁻².

O VII (f) line is the brightest line and the least absorbed. I therefore used its blueshift, and the fact that it is unresolved, to fix the blueshift of O VIII Ly α and O VII (r) to be 400 km s⁻¹ and their velocity broadening to be zero. The lines were modelled as Gaussians, with the O VII and O VIII absorption described above applied using *slab*. The fluxes obtained will be dependent on whether the absorption is applied only to the continuum or to both the continuum and emission lines; in the latter case, the emission line fluxes would need to be higher.

The resulting line fluxes are listed in Table 4.5, along with the flux ratios and derived ionisation parameters. If the warm absorber only covers the continuum (model B), $\log \xi$ would be $2.2^{+0.3}_{-0.2}$. If the absorber covers both lines and continuum (model A), $\log \xi$ would be slightly higher at 2.7 ± 0.2 . Both of these values indicate that the emission lines are produced in gas of a similar ionisation level to that of the high-ionisation warm absorber.

The ratio of the fluxes of the O VII forbidden and intercombination lines can be

Table 4.5: Estimates of the ionisation parameter of the warm emitter using the ratio of the fluxes of O VIII Ly α and O VII (r) emission lines. The fluxes were fitted assuming an O VIII absorbing column of $10^{17.3}$ cm $^{-2}$ and an O VII column of $10^{16.5}$ cm $^{-2}$, both blueshifted by 900 km s $^{-1}$. The O VIII Ly α and O VII (r) emission lines were assumed to have a blueshift of 400 km s $^{-1}$ and zero intrinsic width, for fitting purposes.

Model ^a	A	B
F _{O VII} ^b	4 \pm 2	3 \pm 1
F _{O VIII} ^b	32 \pm 6	5 \pm 1
X _{ion} ^c	7 ⁺⁸ ₋₃	2 ⁺² ₋₁
log ξ ^d	2.7 \pm 0.2	2.2 ^{+0.3} _{-0.2}

^a A: warm absorption applied to both continuum and emission lines, B: warm absorption only applied to continuum (Galactic neutral absorption applied to both)

^b model line flux in 10^{-5} photons cm $^{-2}$ s $^{-1}$, including the effects of Galactic (but not intrinsic) absorption

^c ratio of fluxes of O VIII Ly α and O VII (r)

^d implied log ξ in erg cm s $^{-1}$

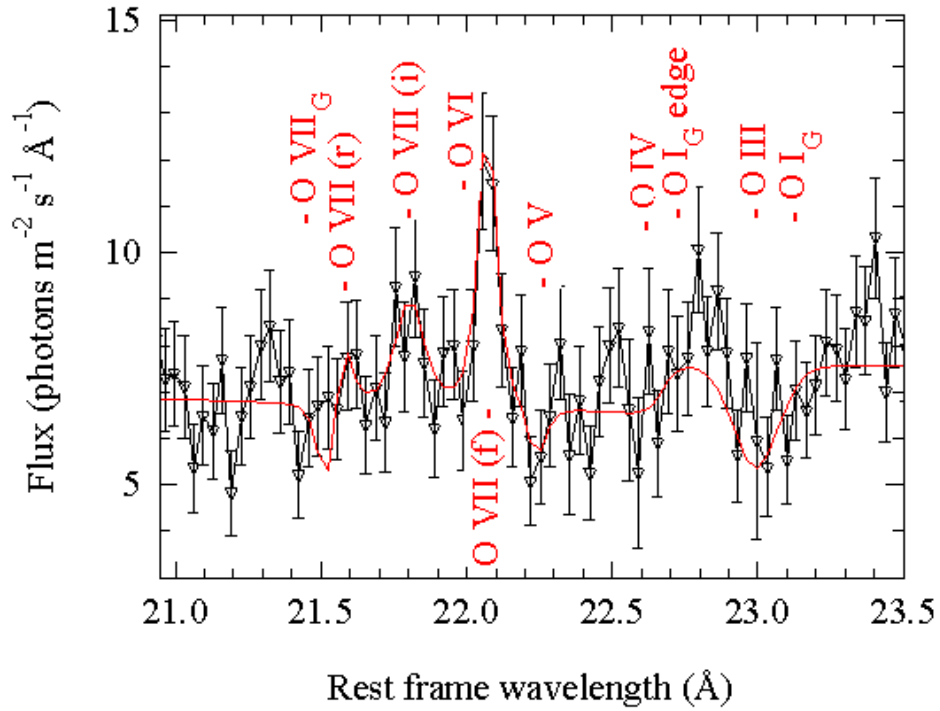


Figure 4.11: The O VII emission line triplet region with model overposed (continuum plus fitted columns of O VII and O VIII; the other absorption and emission lines are included with the parameters given in Table 4.3 and Table 4.4). Positions of other transitions not significantly detected are also shown.

used to estimate the density of the emitter (Porquet and Dubau, 2000). Care has to be taken in using these ratios, as they can be affected by photoexcitation (see Chapter 1) which is known to occur in the warm emitter of NGC 1068 (Kinkhabwala et al., 2002). However, in this case, the ratio of the lines (~ 2) gives a firm estimate of the upper limit of $\sim 10^{10} \text{ cm}^{-2}$ for the density. The oxygen line region of the spectrum with the emission lines model overposed is shown in Fig. 4.11.

Finally, I tested the effect of the warm absorption on the continuum fitting. The presence of only a few narrow lines and no absorption edges implies that the warm absorber/emitter should have little effect on the EPIC CCD resolution spectrum. Using the pn spectrum and the SPEX *slab* model, I applied absorption to the continuum from O VIII, O VII, O V, O III, N VII, Ne IX and C VI (estimated using *slab*, from

the depths of narrow lines in the RGS spectrum, as $10^{17.3}$, $10^{16.5}$, $10^{16.2}$, $10^{16.6}$, $10^{16.2}$, $10^{17.5}$ and $10^{17.0}$ cm^{-2} respectively), taking into account the normalisation difference between the RGS and pn. Absorption lines not currently included in *slab* (N IV and Ne VII) were modelled with Gaussian profiles with the parameters in Table 4.3. The emission lines were also modelled as Gaussians, and had the measured parameters given in Table 4.4 (O VII (f), O VII (i) and C VI) or were given the parameters derived from the warm absorber covering only the continuum (O VII (r) and O VIII Ly α). The warm absorber/emitter, modelled in this way, requires an increase of up to 10% in the soft excess normalisation and $\sim 2\%$ in the power-law normalisation. Adding these warm absorber components to the pn model partly accounted for some of the residuals seen in Fig. 4.5, but did not totally get rid of them. These residuals are within the 10% calibration uncertainties of the pn camera.

4.3 Discussion and conclusions

4.3.1 XMM-Newton observation

The pn spectra and lightcurves of NGC 7469 show this AGN to have a variable hardness ratio. There is no evidence of correlated X-ray and UV variability during the observation. The X-rays vary more than the UV; there is at least 20% variability in all of the X-ray bands, whilst any UV variability is within 10%. I model the X-ray soft excess with two blackbody components over a power-law continuum. This model provides a good representation of the spectrum, but the fairly rapid variability makes it seem unlikely that blackbodies are anything other than a fitting device in this case. A more physical model would involve, for example, Inverse Comptonisation of UV photons from an accretion disc in a rapidly varying accretion disc corona, with different parts of a highly dynamic corona contributing to the overall spectrum of the soft excess. It has proved hard to constrain the large number of parameters in a Comptonisation model for this object, and so, although this may be a more physical representation of the soft excess, I decided to use the blackbodies as a convenient parameterisation in order to establish an accurately shaped continuum to underly

the RGS data.

A narrow, unresolved Fe K α line is present in the pn spectrum. When the MOS and pn data are combined to increase the signal-to-noise, the line appears marginally resolved, with a FWHM and a slight intrinsic redshift consistent with O VI and Si IV UV emission lines from the Broad Line Region (Kriss et al., 2003). The apparent broadening may, however, be due to the presence of a weak Fe XXV line at 6.64 keV. The currently unpublished Chandra HETGS spectrum of NGC 7469 could shed further light on this issue.

The soft excess underlies a shallow warm absorber/emitter, characterised not by absorption edges, as previously thought (e.g. Reynolds, 1997) but by narrow absorption and emission lines. It contains gas outflowing at an average speed of $800 \pm 100 \text{ km s}^{-1}$, spread over about four decades in ionisation parameter from $\log \xi = -2$ to $\log \xi = 2$. The highest ionisation phase of the absorber is the best constrained, and is found to have an average $\log \xi$ of $1.6^{+0.7}_{-0.4}$ and an overall equivalent hydrogen column of $(1.5 \pm 0.9) \times 10^{20} \text{ cm}^{-2}$. This is about two orders of magnitude lower than that found in NGC 3783 (Blustin et al., 2002a), and is probably the reason why no iron absorption is observed in the spectrum. Not enough lines are visible from the low ionisation phase to make meaningful conclusions about its physical conditions.

Four prominent emission lines from O VII (f), O VII (i), O VIII Ly α and C VI Ly α are observed in the RGS spectrum, the latter two having P-Cygni profiles. O VII (f) has the best determined parameters, and is found to be unresolved and to be blueshifted by $400 \pm 200 \text{ km s}^{-1}$. I show that the warm emitter has a level of ionisation similar to that of the high ionisation warm absorber.

NGC 7469 possesses a very strong starburst component which dominates the bolometric luminosity of the galaxy (Genzel et al., 1995). The starburst could theoretically have an important influence on the RGS spectrum, although Perez-Olea and Colina (1996) show that it probably only accounts for 4% of the X-ray luminosity. In any case, X-ray emitting gas associated with a starburst would be collisionally ionised plasma, from which the O VII (r) emission line would be stronger than the O VII (f) line. The opposite is true in the RGS spectrum; O VII (f) is the

strongest observed feature and this remains the case even if the flux of O VII (r) is corrected for the effects of the warm absorber. The presence of dominant O VII (f) emission is a clear indication of an origin in photoionised gas (i.e. associated with an AGN) rather than in collisional plasma. The starburst, therefore, does not appear to be making a noticeable contribution to the observed soft X-ray spectrum.

4.3.2 UV results from FUSE and the X-ray/UV connection

NGC 7469 was observed about a year before XMM-Newton by FUSE. The results of this, and a comparison with the X-ray results described in this Chapter and published in Blustin et al. (2003), have been published by Kriss et al. (2003). I will briefly summarise their results here, and discuss the X-ray/UV warm absorber/emitter connection in NGC 7469. My collaboration with G. Kriss on the joint X-ray/UV analysis originated in discussions during the AGN Spectroscopy Workshop held at MPE-Garching in December 2001.

The main result from the FUSE observation is that there are two velocity components in the UV absorber (Fig 4.12). Component #1 has a blueshift of 569 km s⁻¹, and a covering factor of about 50%, consistent with coverage of the continuum only and not the broad lines. Kriss et al. (2003) argue that this places UV #1 inside the Broad Line Region (BLR), perhaps as an accretion disc wind. UV component #2 has a much higher blueshift of 1898 km s⁻¹, and a covering fraction of $\sim 90\%$ of the broad line and continuum emission, locating it exterior to the BLR.

The most obvious point of contact between the X-ray and UV ranges is the O VI ion, which has absorption lines in both. Unfortunately, there is no O VI line visible in the RGS spectrum, putting the O VI column somewhere lower than $10^{16.5}$ cm⁻². This is unsurprising as the O VI columns for both UV phases, $\sim 8 \times 10^{14}$ cm⁻², are far too low to be visible in the RGS spectrum. Kriss et al. (2003) show, however, that the O VI and H I columns observed in the UV, and the O VII and O VIII columns observed in the X-rays, are all consistent with a photoionised warm absorber model with an equivalent hydrogen column of 3.5×10^{20} cm⁻² and an ionisation parameter $U = 6$ (U is defined as the ratio of ionising photons in the Lyman continuum to

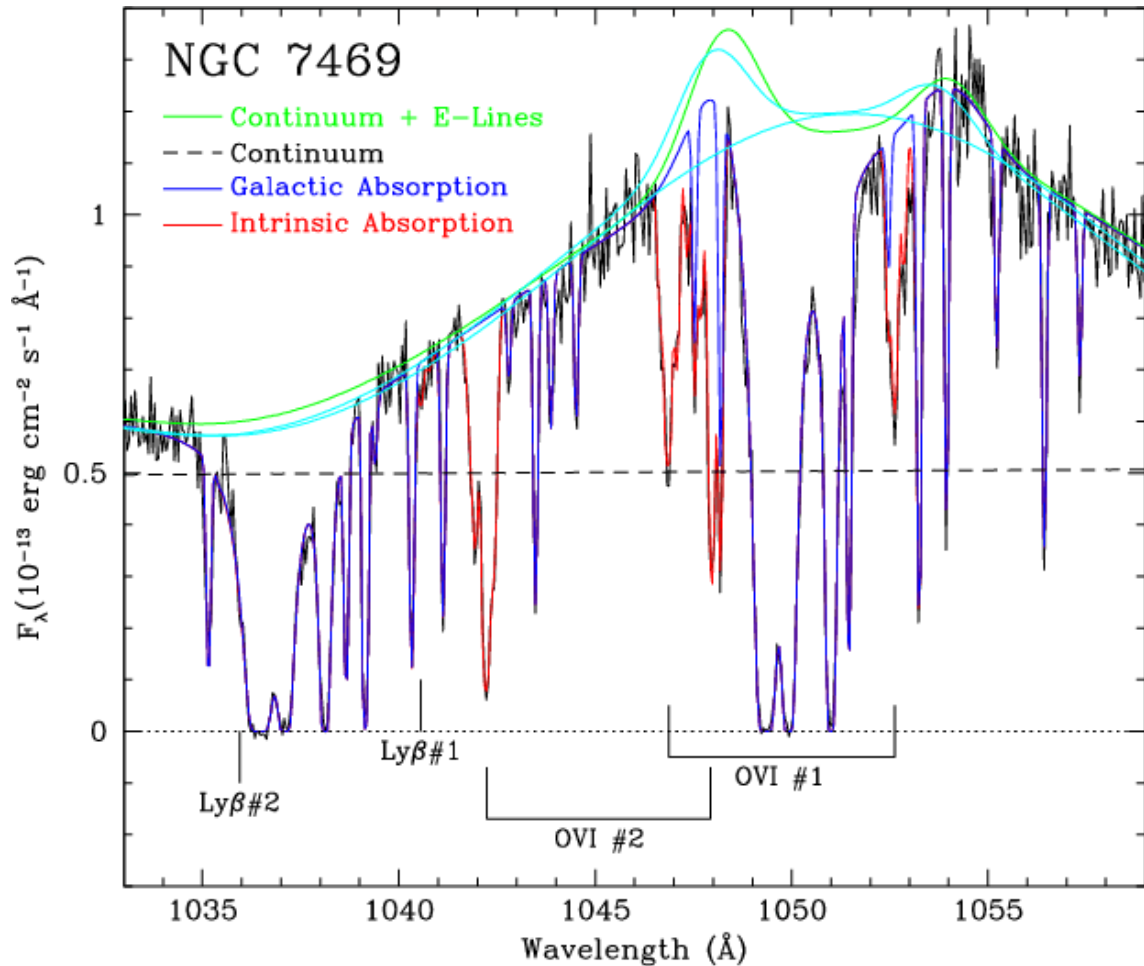


Figure 4.12: Part of the FUSE UV spectrum of NGC 7469 (Kriss et al., 2003), showing the multiple intrinsic absorption components (red), the absorption due to our Galaxy (dark blue), the continuum level (black dotted line), and the continuum plus broad and narrow emission lines (green). The light blue lines represent two extreme models, tried by Kriss et al. (2003), in which there are either no narrow emission lines, or the narrow emission lines are not obscured at all by the intrinsic absorber.

the electron density; for the best fit FUSE continuum model, $\xi = 24.05 \times U$, and thus $U = 6$ is equivalent to $\log \xi$ of 2.2). This fits in well with the parameters I derived for the high-ionisation X-ray absorber, when I fitted the columns of O VII and O VIII directly ($\log \xi = 2.1_{-0.5}^{+1.6}$, and an overall hydrogen column of $(4 \pm 2) \times 10^{20} \text{ cm}^{-2}$), and so combined with the fact that the blueshift of the high-ionisation X-ray absorber is the best match for that of UV#1, Kriss et al. (2003) identify the high-ionisation X-ray warm absorber with UV#1, placing them within the BLR.

There is, on the other hand, no X-ray counterpart for UV#2: although it has an ionisation parameter within the range seen in X-rays ($U = 0.2$; $\log \xi = 0.68$), it has a blueshift far higher than that of the X-ray absorber, and a modelled overall column of $3.8 \times 10^{18} \text{ cm}^{-2}$ which is too weak to be observable in the RGS spectrum. There is also no UV phase that seems to coincide with the low-ionisation X-ray absorber.

What are the consequences for our overall picture of the circumnuclear environment of NGC 7469? The overall Kriss et al. (2003) interpretation is that the data are consistent with a UV and X-ray absorbing accretion disc wind within the BLR, with another UV absorbing wind further out, perhaps originating in the dusty torus. They also point out that other interpretations are of course possible, in terms of a thermally-driven wind at greater distances (as in Krolik and Kriss, 2001).

If we take the disc wind plus torus wind interpretation, then it is interesting to see where the soft X-ray emission lines, and the low ionisation X-ray absorber, fit into it. Wandel et al. (1999) reverberation studies of NGC 7469 found the distance of the BLR from the nucleus to be of the order 10^{16} cm . Assuming $\log \xi$ of 2 for the high-ionisation absorber, and a 1–1000 Ryd luminosity of $\sim 10^{44} \text{ erg s}^{-1}$ (taken from the RGS continuum model), I estimate a lower limit to the absorber density of $\sim 10^{10} \text{ cm}^{-3}$.

I have shown that the soft X-ray emission lines come from gas at an ionisation parameter similar to that of the high-ionisation warm absorber. If I take the further step of identifying the emitter with this absorber, then the upper density limit of $\sim 10^{10} \text{ cm}^{-3}$ derived from the O VII triplet line ratios places the absorber/emitter at the distance of the BLR. If the overall equivalent hydrogen column of the absorber

is $4 \times 10^{20} \text{ cm}^{-2}$, and the density is 10^{10} cm^{-3} , then the depth of the absorber can be estimated as 400 000 km. This is extremely small in comparison with the distance from the nucleus, so it would imply that the absorber had a sheet-like or low filling factor structure.

If the velocity widths and blueshifts of the X-ray lines were consistent with those from the UV BLR, it would be possible to say more definitely whether the X-ray lines really do come from the high-ionisation absorber. The absorption affecting the X-ray lines makes it hard to measure their widths and blueshifts precisely enough, however. O VII (f), which is the brightest and least affected by absorption, has a width and blueshift which are closer to those of the narrow O VI UV lines, identifying it with the Narrow Line Region (NLR). This is the scenario that has recently been claimed for the soft X-ray emission lines in NGC 3783 (Behar et al., 2003). If they do come from the NLR, then either they are not coming from the high-ionisation X-ray absorber, or it was not correct to place this absorber within the BLR.

Very few ions are detected from the low ionisation X-ray absorber, so one cannot say much more than that the ionisation levels range down as far as $\log \xi \sim -2$. Placing this gas coincident with the high ionisation phase would imply a very wide range of density in the accretion disc wind absorber. It is also possible that this low ionisation gas is located much further out from the nucleus. The UV absorber seems, though, to show evidence of increasing outflow speed with distance from the nucleus, and so, since the high and low ionisation phases of X-ray gas have similar blueshifts, one could prefer the clumpy absorber interpretation. This picture is summarised in Fig 4.13.

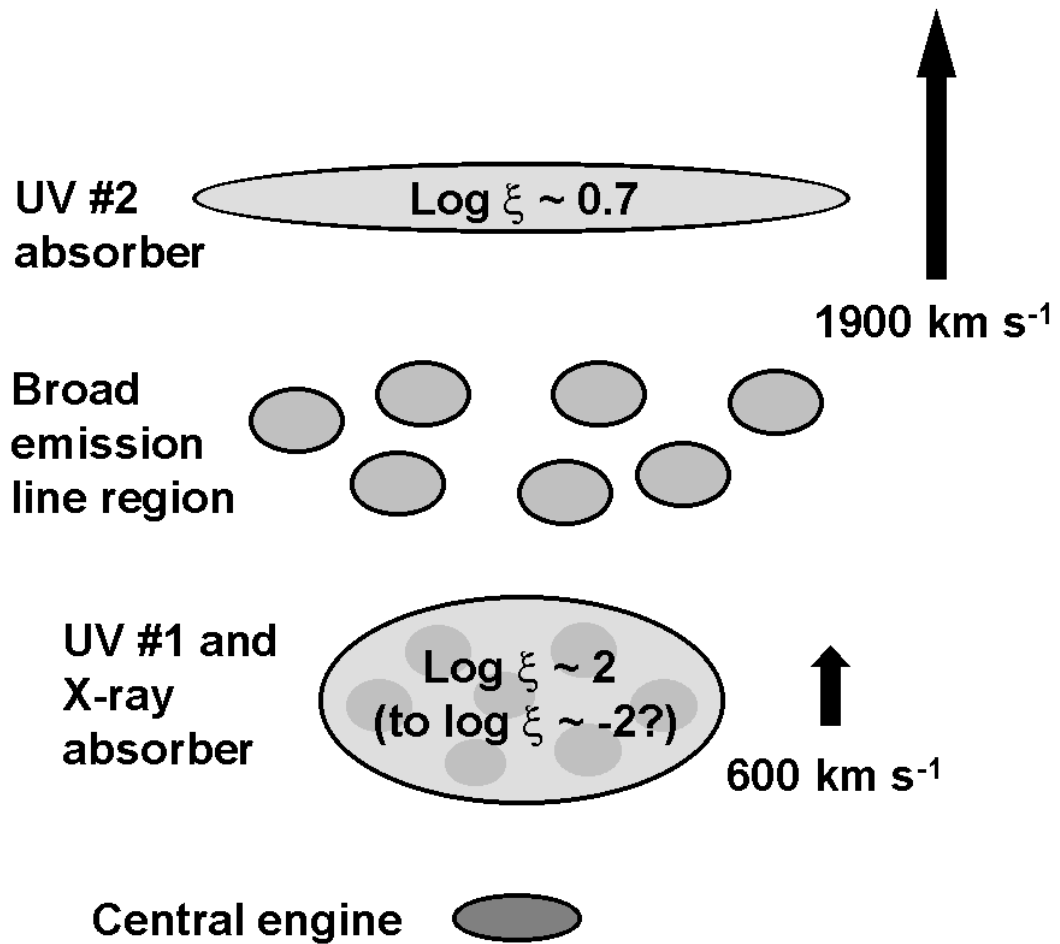


Figure 4.13: The overall picture of the circumnuclear region of NGC 7469 as inferred from X-ray and UV absorption and emission measurements.

Chapter 5

BL Lac objects

5.1 Introduction

Having worked on understanding the soft X-ray absorption structures in two Seyfert 1 galaxies, I turned my attention to another class of AGN: BL Lac objects. Although these sources are well known for their almost featureless spectra throughout the electromagnetic spectrum, certain BL Lacs have been claimed to exhibit broad, deep absorption features at soft X-ray wavelengths (see Chapter 1). In order to investigate this, I looked at data from XMM-Newton observations of four BL Lac objects for which these absorption features have been reported: 1H1219+301, H1426+428, Markarian 501 and PKS 0548-322. Some basic parameters of these sources are given in Table 5.1. The work described in this chapter is published in Blustin et al. (2004).

There is only one report of such absorption in 1H1219+301. Madejski et al. (1991) discovered a ~ 100 eV wide absorption ‘notch’ (trough) at $0.56^{+0.01}_{-0.02}$ keV in the Einstein Solid State Spectrometer (SSS) spectrum of this object (the energy is quoted in the observed frame, as are all energies in this section unless stated otherwise). H1426+428, on the other hand, has shown evidence of soft X-ray ionised absorption in spectra from three different missions, which was discovered first by Madejski et al. (1992) in a BBXRT spectrum. The BBXRT data were re-analysed in more detail by Sambruna et al. (1997), along with data from ROSAT and ASCA. Interestingly, the feature manifested itself differently in the different spectra; the

Table 5.1: Some basic parameters of the BL Lac objects discussed in this chapter (coordinates are J2000).

Target	Right Ascension	Declination	Redshift ^a	Galactic column ^b
1H1219+301	12h 21m 21.941s	+30d 10m 37.11s	0.182	1.78 ^c
H1426+428	14h 28m 32.6s	+42d 40m 21s	0.129	1.36 ^d
Markarian 501	16h 53m 52.2s	+39d 45m 37s	0.03366	1.73 ^c
PKS 0548-322	5h 50m 40.771s	-32d 16m 17.76s	0.069	2.51 ^d

^a redshift as listed by the NASA Extragalactic Database (NED)

^b Galactic absorbing column in 10^{20} cm^{-2}

^c Elvis et al. 1989

^d Costamante et al. 2001

BBXRT feature was best parameterised by a broad Gaussian absorption line at ~ 0.66 keV with a width less than or equal to 43000 km s^{-1} , whilst the ROSAT and ASCA data (fitted together due to the similar flux levels in the two observations) contained indications of two absorption edges at 0.15 keV and 0.52 keV.

An absorption feature was seen in Markarian 501 with the Einstein SSS and possibly with ROSAT. The feature in the Einstein data was first described by Urry et al. (1986) as an absorption trough at ~ 0.57 keV with a width of 80 eV, and later by Madejski et al. (1991) as a notch at 0.56 ± 0.01 keV with a width of 240 eV and covering factor of 0.52. Fink et al. (1991) reported a possible absorption line in ROSAT data at $0.37^{+0.25}_{-0.09}$ keV, with a width fixed at 100 eV, although the feature was not statistically significant.

An absorption feature in PKS 0548-322 was first detected by Madejski et al. (1991) in an Einstein SSS spectrum; they fitted the feature as an absorption trough at 0.57 ± 0.02 keV. ASCA data have since revealed an absorption edge at ~ 0.66 keV (Sambruna and Mushotzky, 1998); this feature could alternatively be explained as a notch at 0.82 keV with a width fixed at 100 eV and covering factor 0.12. These authors re-analysed the Einstein data, finding an edge at 0.487 keV. They also found two edges in a ROSAT spectrum of this source, one at 1 keV (which was probably instrumental in origin) and another at 0.553 keV, which could either have been intrinsic to the source or due to calibration uncertainties.

These broad absorption features are usually interpreted as being due to ionised oxygen in the immediate environment of the BL Lac object, following the original Canizares and Kruper (1984) identification of an absorption trough in PKS 2155-304 as O VIII Ly α . Exactly this interpretation was given by Madejski et al. (1991) for the ‘notches’ they detected in Einstein SSS data. The first reported feature in Markarian 501 was described more generally as being due to ‘highly ionised oxygen’ (Urry et al., 1986). The ~ 0.66 keV BBXRT feature of Sambruna et al. (1997) was only marginally consistent with O VIII Ly α , and was best explained by absorption edges of O V–O VII. Of the two edges reported in their combined ROSAT and ASCA fits, one (at 0.15 keV) had no physical interpretation, whilst the other, at

0.52 keV, could be identified with the K-edge of O III. The possible 0.37 keV line seen in ROSAT data by Fink et al. (1991) was not given an interpretation. Two identifications were provided by Sambruna and Mushotzky (1998) for the feature they reported in PKS 0548-322: either an O VI absorption edge or a notch from Fe XIX–Fe XX or Ne VII.

Sambruna et al. (1997) and Sambruna and Mushotzky (1998) also fit the data with photoionised absorption models. Sambruna et al. (1997) noted that the absorption feature in H1426+428 was present at a lower energy when the source flux was lower, in line with the predictions of photoionised warm absorber models; conversely, Sambruna and Mushotzky (1998) found that the feature in PKS 0548-322 was at a lower energy when the source flux was actually higher.

Prior to the launch of XMM-Newton and Chandra, that was where the understanding of BL Lac ‘warm absorbers’ stood. Since then, Chandra LETGS spectra of Markarian 421 have yielded evidence of very weak intrinsic narrow absorption lines of O VII He α (Nicastro et al., 2000, 2003), but most attention has been focussed on the discovery of narrow absorption lines from the intervening Warm-Hot Intergalactic Medium (WHIM) in PKS 2155-304 (Nicastro et al., 2002) and Markarian 421 (Nicastro et al., 2003), also observed with the XMM-Newton RGS (Rasmussen et al., 2003). Despite the many observations of these two objects as calibration sources by XMM-Newton and Chandra, deep broad absorption features have not yet been observed in either of them.

5.2 Lightcurves

The X-ray lightcurves of the four BL Lacs are plotted in Fig. 5.1. The 0.4–10 keV pn lightcurves (1H1219+301, H1426+428 and Markarian 501) are constant to within $\sim 5\%$, and the RGS lightcurve of PKS 0548-322, for which no pn data were available, was on average constant to within $\sim 10\%$ (the signal-to-noise was lower than for the pn lightcurves). The spectral fitting is therefore not likely to be seriously affected by spectral variability.

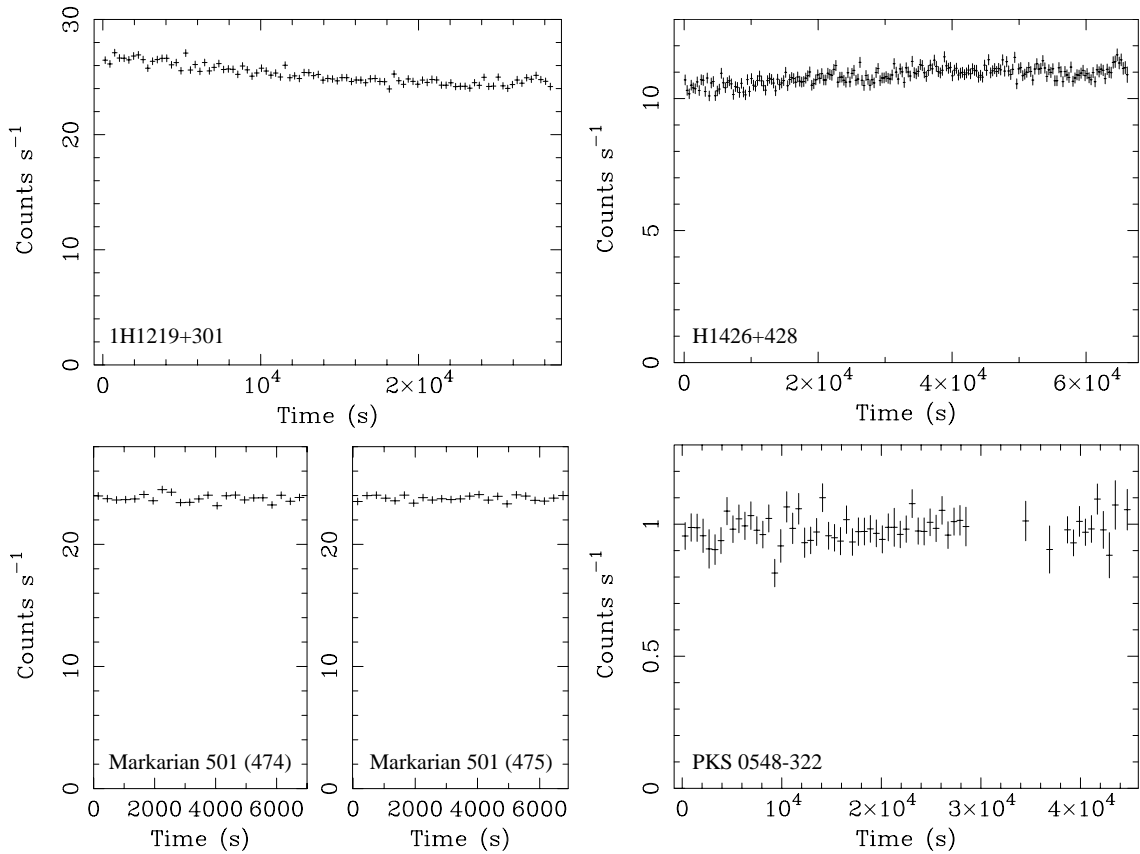


Figure 5.1: The 0.4–10 keV pn lightcurves of 1H1219+301, H1426+428 and Markarian 501 (from orbits 474 and 475), all in 300 s time bins, and the RGS lightcurve of PKS 0548-322 (0.35–2.5 keV; 600 s time bins).

5.3 EPIC spectra

I started off by looking at the EPIC-pn data of 1H1219+301, H1426+428 and Markarian 501 (there were no pn data for PKS 0548-322). In order to observe any departures from a smooth continuum, I fitted simple power-law models to the 0.4-10 keV pn spectra, with fixed neutral absorption due to our Galaxy. The ratios of these fitted power-laws to the data are shown in Fig. 5.2. Whilst there is certainly spectral curvature in excess of the power-law, these plots show no evidence for intrinsic spectral features - or excess neutral absorption in addition to the Galactic column. Motivated by the deviations of the spectra from a single power-law, I fitted them all with broken power-law models (and fixed Galactic neutral absorption). The resulting models are shown overplotted on the data in Fig. 5.2. The parameters of both single power-law and broken power-law fits are listed in Table 5.2.

5.4 RGS spectra

In order to ascertain the presence or otherwise of broad features in the RGS spectra of the four BL Lacs, I fitted first single power-laws, and then (taking the observed spectral curvature into account) broken power-laws to the data. The parameters of these models are given in Table 5.2. Figs. 5.3–5.6 show straightaway that there are no significant broad absorption features in the RGS spectra. Testing whether the narrow absorption and emission type features in the RGS spectra are real, however, is more complicated. To measure the statistical significance of these features, I fitted a Gaussian against a local smoothed continuum to all of the apparent features in the spectrum, as described in Chapter 2. The results of this are plotted above the relevant RGS spectra in Figs. 5.3–5.6.

The numbers and significance of narrow features in the RGS spectra of 1H1219+301 and Markarian 501 are entirely in line with what is to be expected from random statistical noise. The RGS spectra of H1426+428 and PKS 0548-322 each have one feature significant at 4σ and contain, respectively, five and ten features significant at 3σ - only one of which is in each case due to emission. This is not consistent

Table 5.2: Fit parameters for power-law and neutral absorption, and broken power-law with neutral absorption, fits to the EPIC-pn (0.4–10 keV) and RGS (0.35–2.5 keV) spectra of the BL Lacs observed: N_{H} , neutral absorbing column in 10^{20} cm^{-2} (fixed); Γ_1 , slope of single or soft power-law; E_{B} , break energy in keV; Γ_2 , slope of hard power-law; N , power-law normalisation in 10^{-2} photons $\text{keV}^{-1} \text{ cm}^{-2} \text{ s}^{-1}$ at 1 keV; reduced χ^2 of the total fit (degrees of freedom are given in brackets); F_{2-10} , 2–10 keV flux of preferred model in $10^{-11} \text{ erg cm}^{-2} \text{ s}^{-1}$.

Object	Instrument	N_{H}	Γ_1	E_{B}	Γ_2	N	χ^2_{red}	F_{2-10}
1H1219+301	pn	1.78 ^a	2.49 ± 0.01			2.23 ± 0.08	1.38 (714)	
	pn	1.78 ^a	2.40 ± 0.02	1.4 ± 0.2	2.61 ± 0.02	2.29 ± 0.02	0.99 (712)	2.64 ± 0.02
	RGS	1.78 ^a	2.09 ± 0.02			2.00 ± 0.02	1.08 (1038)	
	RGS	1.78 ^a	1.76 ± 0.06	0.75 ± 0.05	2.44 ± 0.07	2.5 ± 0.1	0.89 (1036)	
H1426+428	pn	1.36 ^b	1.87 ± 0.01			0.90 ± 0.01	1.61 (607)	
	pn	1.36 ^b	1.92 ± 0.01	1.5 ± 0.2	1.82 ± 0.01	0.89 ± 0.01	1.24 (605)	2.90 ± 0.01
	RGS	1.36 ^b	1.68 ± 0.02			0.78 ± 0.01	1.19 (996)	
	RGS	1.36 ^b	1.47 ± 0.07	0.79 ± 0.08	1.88 ± 0.05	0.89 ± 0.05	1.05 (994)	
Markarian 501	pn	1.73 ^a	2.31 ± 0.01			2.64 ± 0.01	1.17 (653)	
	pn	1.73 ^a	2.34 ± 0.01	1.9 ± 0.4	2.23 ± 0.03	2.62 ± 0.01	1.03 (651)	4.48 ± 0.02
	RGS	1.73 ^a	2.00 ± 0.02			2.27 ± 0.02	1.01 (1038)	
	RGS	1.73 ^a	1.70 ± 0.06	0.71 ± 0.04	2.26 ± 0.05	2.8 ± 0.1	0.84 (1036)	
PKS 0548-322	RGS	2.51 ^b	1.74 ± 0.02			0.94 ± 0.01	1.28 (1038)	
	RGS	2.51 ^b	1.38 ± 0.05	0.74 ± 0.02	2.01 ± 0.04	1.19 ± 0.04	1.03 (1036)	2.47 ± 0.08

^a Elvis et al. 1989; ^b Costamante et al. 2001

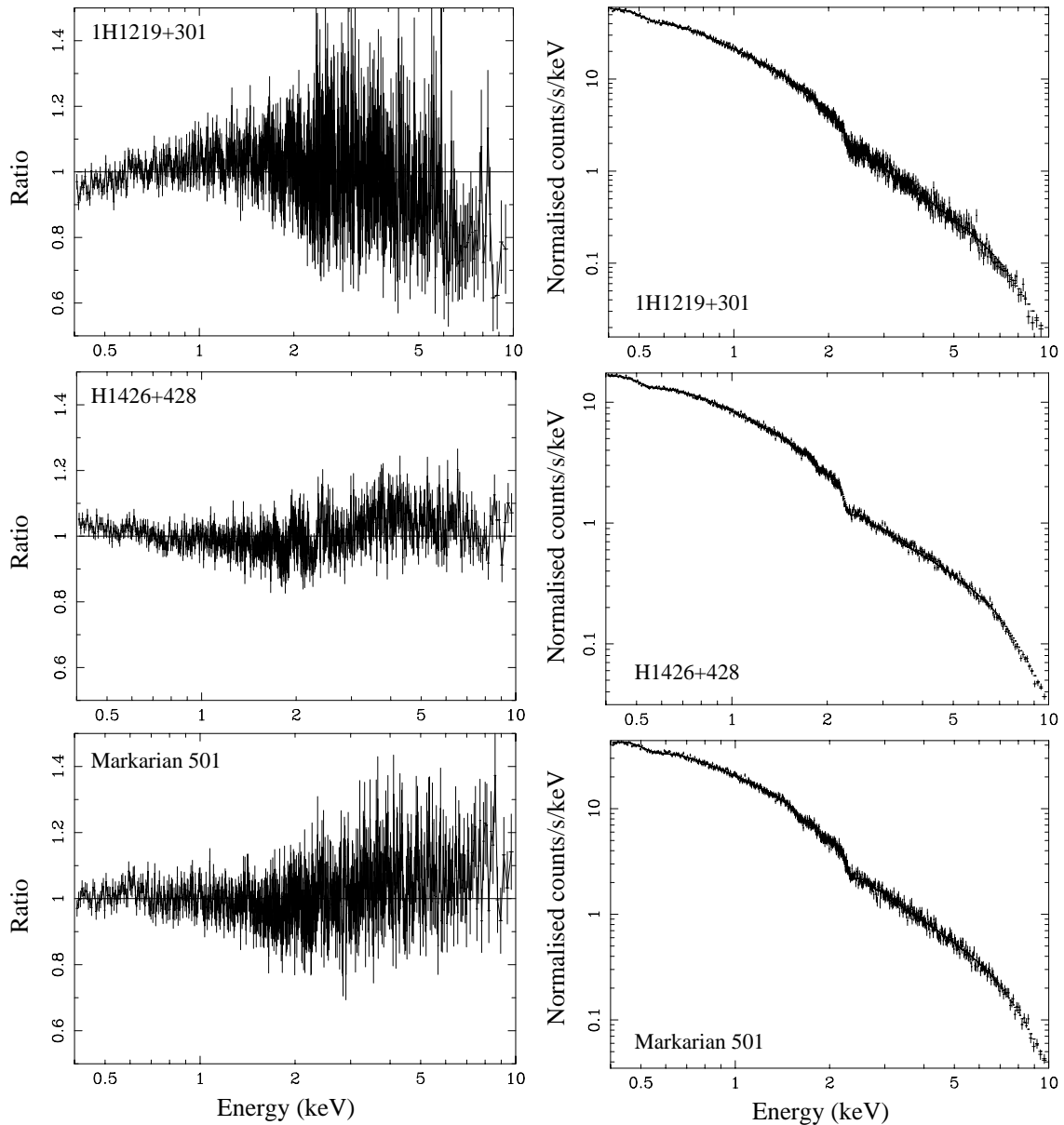


Figure 5.2: Left panels: ratios of the pn spectra of 1H1219+301, H1426+428 and Markarian 501 to fitted power-laws with fixed Galactic neutral absorption (plotted in the observed frame). Right panels: the pn spectra of 1H1219+301, H1426+428 and Markarian 501 with superimposed best-fit broken power-law models (with fixed Galactic neutral absorption; plotted in the observed frame). In all plots, the spectra are grouped to a minimum of 40, 350 and 100 counts per bin respectively.

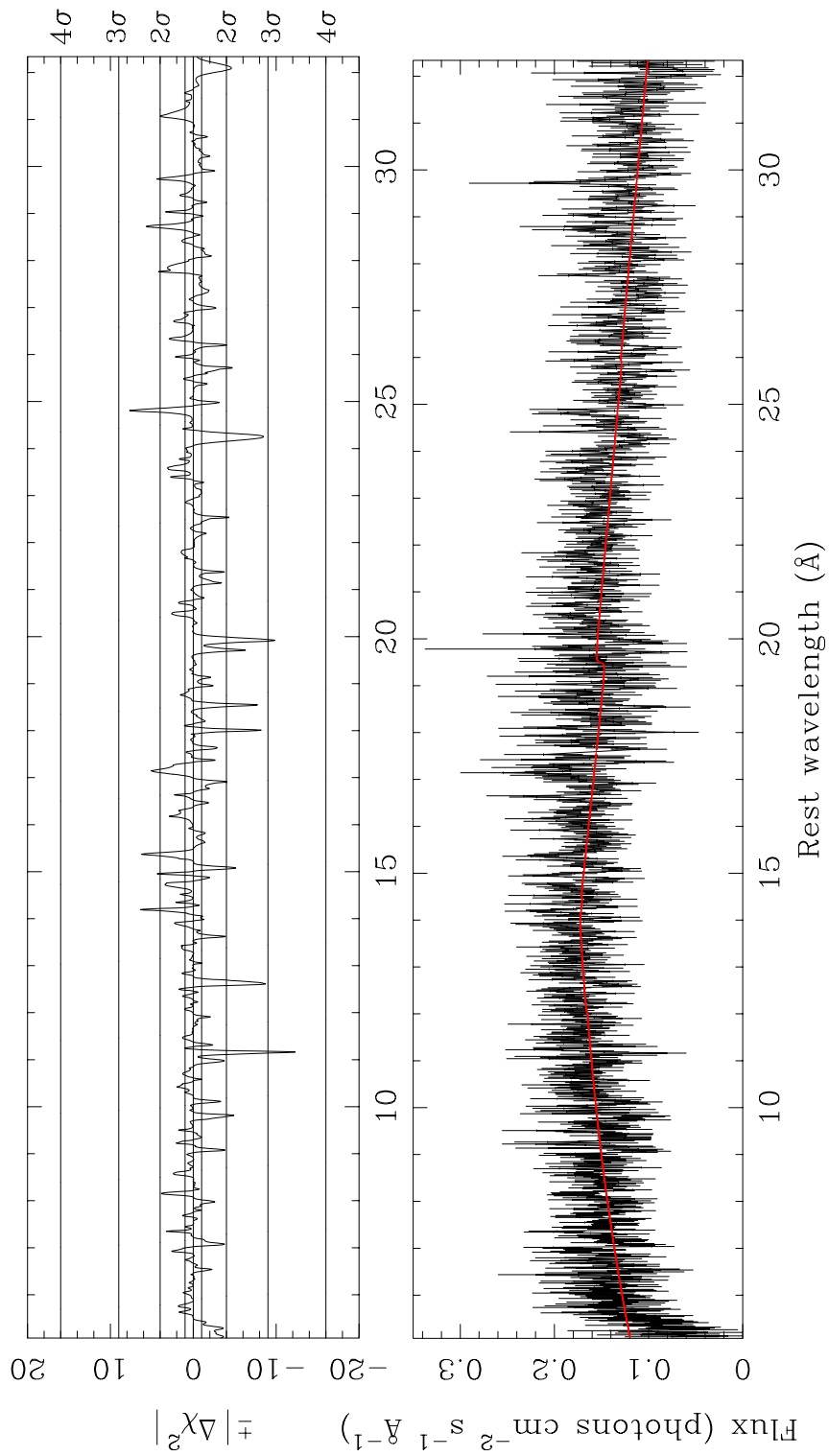


Figure 5.3: The statistical significance of narrow absorption and emission features in the RGS spectra of 1H1219+301 (top; as in Fig 4.9), and the RGS spectrum itself with best-fit broken power-law model (red) superimposed (bottom), plotted in the source rest frame.

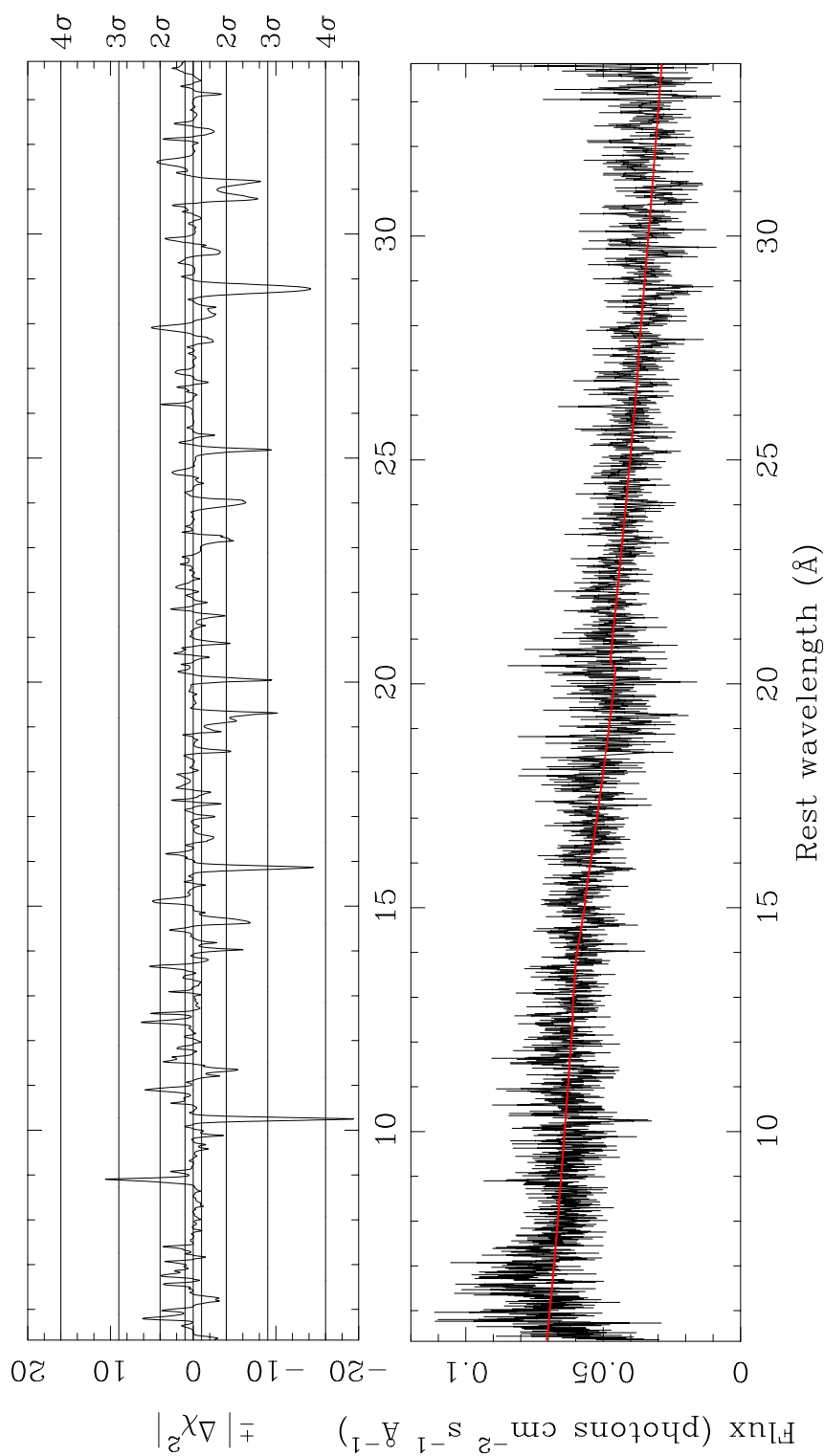


Figure 5.4: The statistical significance of narrow absorption and emission features in the RGS spectra of H1426+428 (top; as in Fig 4.9), and the RGS spectrum itself with best-fit broken power-law model (red) superimposed (bottom), plotted in the source rest frame.

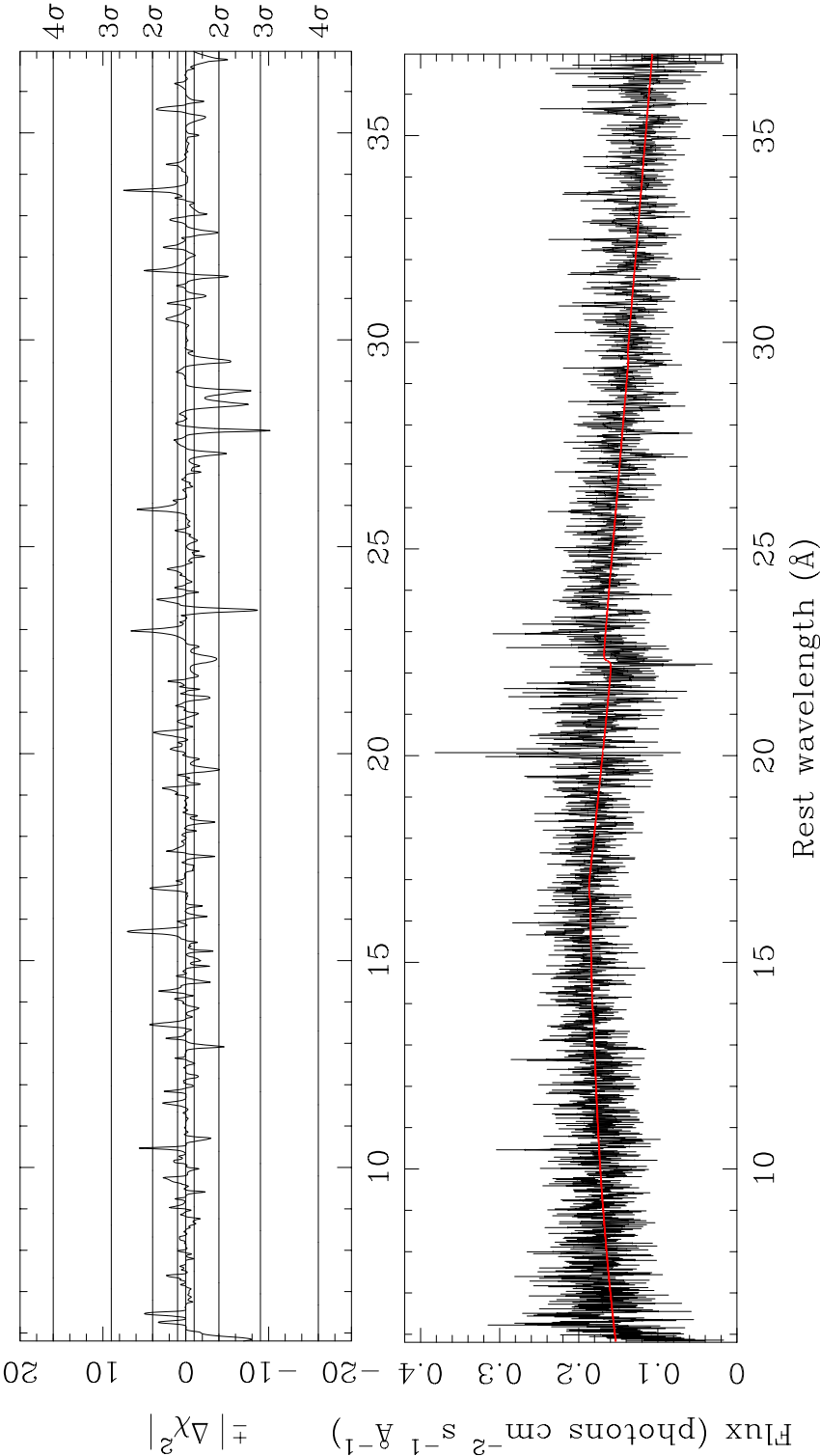


Figure 5.5: The statistical significance of narrow absorption and emission features in the RGS spectra of Markarian 501 (top; as in Fig 4.9), and the RGS spectrum itself with best-fit broken power-law model (red) superimposed (bottom), plotted in the source rest frame.

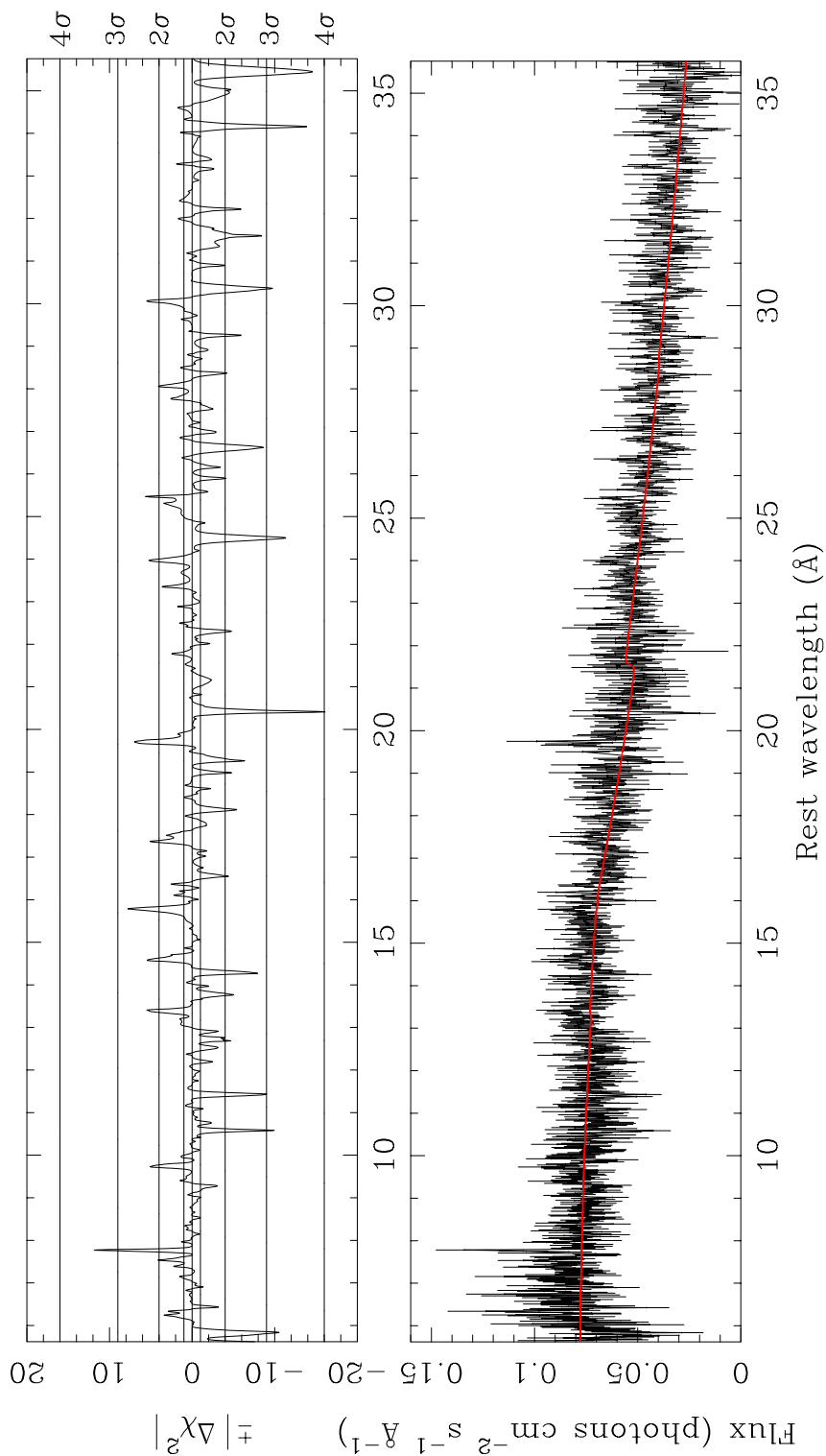


Figure 5.6: The statistical significance of narrow absorption and emission features in the RGS spectra of PKS 0548-322 (top; as in Fig 4.9), and the RGS spectrum itself with best-fit broken power-law model (red) superimposed (bottom), plotted in the source rest frame.

with what would be expected due to statistical noise. The 4σ absorption line in H1426+428 has an equivalent width of 40 ± 10 mÅ at 11.55 Å (observed frame), which is 10.23 Å in the source rest frame. It could be identified as Ne x Ly β , though the corresponding Ne x Ly α line is missing, which makes this interpretation unlikely. It could also be Ne x Ly α itself, blueshifted by ~ 47000 km s $^{-1}$; this would make sense in the context of a BL Lac jet, but I did not find any other lines which would support this pattern. The 4σ line in PKS 0548-322, at 21.82 Å in the observed frame (20.41 Å in the rest frame), has a greater equivalent width: 70 ± 20 mÅ at 21.82 Å. There is no obvious identification for it in the rest frame, but it could conceivably be O VII He α at a blueshift of ~ 17000 km s $^{-1}$. As in the case of the H1426+428 feature, this interpretation is not confirmed by the presence of further lines. Although the 3σ and 4σ lines did not appear in the vast majority to be affected by systematic errors (from, for example, anomalies in the response matrix at CCD gaps), I was unable to find a consistent interpretation for them, and thus cannot provide evidence that they are real spectral features.

5.5 Discussion and conclusions

Despite the large effective area of EPIC-pn and the high spectral resolution of the RGS, the XMM-Newton observations of 1H1219+301, H1426+428, Markarian 501 and PKS 0548-322 produced no evidence of broad, deep, ionised absorption features. Although the RGS spectra of H1426+428 and PKS 0548-322 both contain some evidence for narrow line absorption, I was unable to find any consistent interpretation for the apparent lines and cannot therefore state that these features are real. Certainly, given that Chandra LETGS spectra of Markarian 421 have shown weak narrow absorption lines intrinsic to the BL Lac (Nicastro et al., 2000, 2003), it is conceivable that the features could be real. Any confirmation of this will have to wait for future observations.

Whether or not a small number of narrow lines were present, the rather more dramatic phenomenon which I set out to investigate - the broad deep absorption

features which could have provided valuable clues to the nature of the BL Lac environment - certainly did not manifest itself. If the spectrometers on Einstein could see such features, then XMM-Newton should have been able to. Two possible explanations then present themselves: either the features are transient, or they were never there in the first place.

To see how frequently the features had actually been observed in these four objects, and whether there was any correlation between the presence of features and the source flux level, I went through the literature and collected together all X-ray flux measurements made using past X-ray missions, and made a note of whether or not a feature had been reported for each observation. I only included observations with missions which *could* have detected the feature: Einstein, ROSAT, BBXRT, ASCA, BeppoSAX and XMM-Newton. There have been no Chandra publications on these objects. EXOSAT did not have any energy resolution in the band in which the features appear. It has nevertheless been claimed (Madejski et al., 1991) that EXOSAT would have been capable of detecting the presence of deep ionised absorption features from the averaged flattening of the spectrum in the soft band. I did not find any reports in the literature of EXOSAT ever actually having been used to detect BL Lac absorption features, so I have not included data from this mission. ROSAT had very low spectral resolution in the soft band, but since there are reports of BL Lac absorption features in ROSAT data (Sambruna et al., 1997; Sambruna and Mushotzky, 1998; Fink et al., 1991), I included ROSAT fluxes. All the measured fluxes I collected are listed in Table 5.3–5.4, alongside the observation date, the reference, and an indication of whether or not an absorption feature was observed. In each case I quote the 2–10 keV flux; this was the range most often given in the literature, and so using it as standard minimised the the number of measurements which had to be converted to different energy bands (using PIMMS or Xspec with the original fit parameters), with the possibility of introducing errors in the process. The 2–10 keV band is also not seriously affected by the possible fitting degeneracy between power-law slope and excess neutral absorption in the soft band. The resulting flux points are plotted in Fig. 5.7.

Table 5.3: The history of the 2–10 keV fluxes (in 10^{-11} erg cm^{-2} s^{-1}) of 1H1219+301 and H1426+428 as observed by past and present X-ray missions.

Object	Mission	Date	$F_{(2-10)}$	Intrinsic absorption	Reference for flux value
1H1219+301	XMM-Newton	11/06/01	2.6	no	Table 5.2
	BeppoSAX	13/07/99	1.5	no	Costamante et al. (2001)
	ROSAT	18/06/92	2.7	no	Lamer et al. (1996)
	Einstein	05/06/79	1.1	yes ^a	Urry et al. (1986)
	Einstein	07/12/78	2.5	no	Urry et al. (1986)
H1426+428	XMM-Newton	16/06/01	2.9	no	Table 5.2
	BeppoSAX	08/02/99	2.0	no	Costamante et al. (2001)
	ASCA	06/02/94	1.6	yes	Sambruna et al. (1997)
	ROSAT	24/01/92	2.3	yes	Sambruna et al. (1997)
	BBXRT	09/12/90	3.5	yes	Sambruna et al. (1997)

^a Madejski et al. (1991)

Table 5.4: The history of the 2–10 keV fluxes (in 10^{-11} erg cm^{-2} s^{-1}) of Markarian 501 and PKS 0548-322 as observed by past and present X-ray missions.

Object	Mission	Date	$F_{(2-10)}$	Intrinsic absorption	Reference for flux value
Markarian 501	XMM-Newton	13/07/02	4.5	no	Table 5.2
	ASCA	26/03/96	6.6	no	Kubo et al. (1998)
	ROSAT	13/08/91	2.2	yes	Fink et al. (1991)
	ROSAT	25/02/91	1.3	no	Lamer et al. (1996)
	Einstein	22/08/79	2.7	yes	Cilieggi et al. (1993)
	Einstein	01/03/79	5.8	no	Cilieggi et al. (1993)
Einstein	25/01/79	1.8	no	Cilieggi et al. (1993)	
PKS 0548-322	XMM-Newton	03/10/01	2.5	no	Table 5.2
	BeppoSAX	07/04/99	1.5	no	Costamante et al. (2001)
	BeppoSAX	26/02/99	1.8	no	Costamante et al. (2001)
	BeppoSAX	20/02/99	2.3	no	Costamante et al. (2001)
	ASCA	30/10/93	2.8	yes	Sambruna and Mushotzky (1998)
	ROSAT	06/03/92	3.8	yes ^a	Lamer et al. (1996)
	Einstein	06/04/79	4.0	yes	Sambruna and Mushotzky (1998)
	Einstein	10/03/79	4.5	no	Cilieggi et al. (1993)

^a Sambruna and Mushotzky (1998)

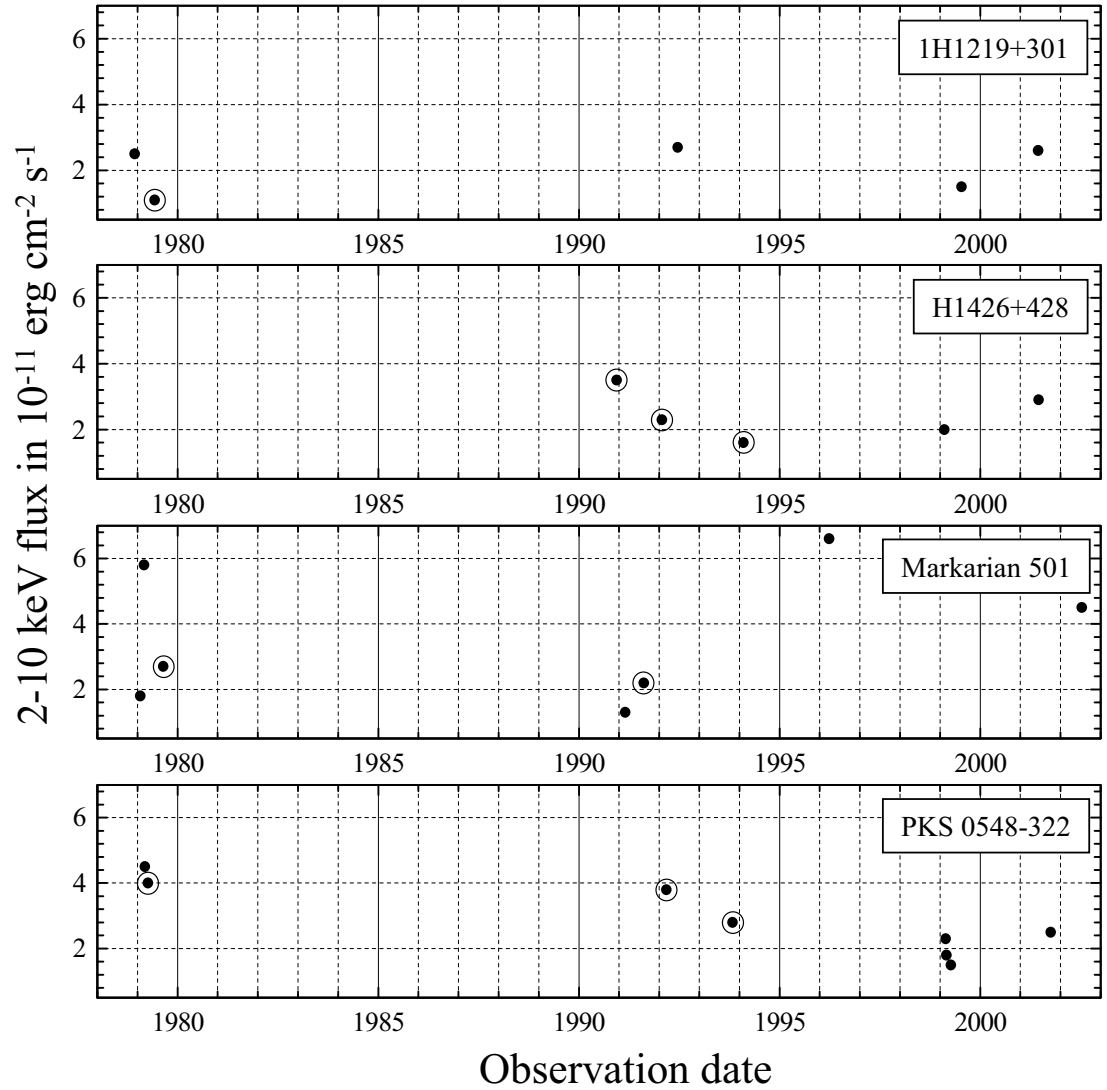


Figure 5.7: 2–10 keV fluxes of 1H1219+301, H1426+428, Markarian 501 and PKS 0548-322 observed with Einstein, ROSAT, BBXRT, ASCA, BeppoSAX and XMM-Newton. Observations where intrinsic absorption was reported are circled.

Fig. 5.7 indicates that the absorption features must be transient, if they exist. One has to take into account, though, that the features may have been present but not reported (or not detectable) during some of the pre-XMM-Newton observations, especially those of the earlier missions. Since XMM-Newton did not detect any deep broad absorption features in the objects, despite producing much higher quality datasets than the previous observations, we can definitely state that if the features are real, then they *must* be transient.

There is no clear evidence of any patterns of differing feature visibility at different flux levels. It is also hard to make any definite conclusions about the timescales over which the features might be visible; the absorption in Markarian 501 appears in a space over a few months but is no longer detected in the next observation four years hence, and the feature in H1426+428 is observed for at least three years, but is no longer detectable by the time of the next observation, eight years after the first detection.

The detection rate of the features in previous observations can be used to estimate the probability of no features being observed by XMM-Newton. The percentage of previous observations which did not yield a detection is 75%, 25%, 66% and 57% for 1H1219+301, H1426+428, Markarian 501 and PKS 0548-322 respectively. With these non-detection rates, the probability of observing no broad absorption features in any of the objects with XMM-Newton is 7%.

This means that the existence of transient deep broad intrinsic absorption features in the BL Lacs can be ruled out at 93% confidence. The failure of a further set of comparable observations to detect any features would mean that their existence can be ruled out at 99.5% confidence. Future observations with XMM-Newton and Chandra will tell whether broad absorption features in BL Lacs can be consigned to history; other classes of objects - for example Broad Line Radio Galaxies - may prove more fruitful sources of information on the circumnuclear environment of radio-loud AGN.

Chapter 6

Conclusions and new perspectives

6.1 Introduction

This dissertation has examined the evidence for intrinsic X-ray absorption in two Seyfert 1 galaxies (NGC 3783 and NGC 7469) and four BL Lac objects (1H1219+301, H1426+428, Markarian 501 and PKS 0548-322). The overall conclusion is that both Seyferts have ionised outflows with wide ranges of ionisation, giving rise to both X-ray absorption and emission, whilst the BL Lac objects showed no convincing evidence for intrinsic X-ray absorption. The lack of strong evidence for intrinsic absorption in BL Lacs is perhaps unsurprising. Assuming that the relativistic jet along our line of sight is outside the warm absorber, it probably outshines any X-ray emission from the nucleus (which might be imprinted with absorption features from the nuclear environment). As I noted in Chapter 5, Broad Line Radio Galaxies probably provide the best chance of investigating ionised gas in the nuclei of radio galaxies.

Can the new knowledge about NGC 3783 and NGC 7469, as presented in this thesis and elsewhere, take us any further in our understanding of Seyfert warm absorption? There are two levels of questions which can be asked. Firstly, the detailed phenomenology of warm absorbers: their ionisation levels, outflow speeds, and column densities - and how these factors depend on the type, orientation and luminosity of the AGN. Secondly, the big questions: where do warm absorbers come

from, where do they go, and are they important? What rôle do they play in the energetics of an active galaxy, and do they tell us something truly fundamental about the way an AGN works and the way it evolves? This question was neatly summed up by H. Netzer at the AGN Spectroscopy Workshop in MPE-Garching, December 2001: are warm absorbers weather or climate?

In order to attempt to answer a few of these questions, I have collated all available published information, at the time of writing, on Seyfert 1 type AGN (Seyfert 1.x galaxies, Narrow Line Seyfert 1s and Seyfert 1 type quasars) observed to date using the high-resolution grating spectrometers on XMM-Newton and Chandra. I found a total of 23 such objects, of which 17 show evidence of warm absorption. Sufficiently detailed spectral modelling has been applied to the warm absorbers of 14 objects for them to be usable for comparative purposes. Tables 6.1 and 6.2 give some basic information about the whole group. Fig. 6.1 shows the distribution of the sources in redshift and bolometric luminosity, and whether or not a warm absorber has been detected in each individual source. The work reported in this Chapter is being prepared for publication (Blustin et al., in preparation).

6.2 Phenomenology of X-ray warm absorbers

High resolution X-ray grating spectroscopy has allowed us to gain a much clearer view of the detailed phenomenology of warm absorbers. It is therefore worth asking, now that relatively advanced spectral models have been constructed for a number of AGN observed with such instruments, whether any interesting new patterns are emerging. For the comparisons in this section I have relied upon the published spectral models for the 14 Seyfert 1 type objects for which sufficiently detailed warm absorber models have been developed. I summarise the main parameters of these models in Table 6.3. For NGC 3783 I use the model of Netzer et al. (2003) rather than my own, as these authors had the benefit of a higher signal-to-noise spectrum, and as a result were able to construct a more sophisticated model.

The ionisation state of warm absorbers is a good place to begin. It is now

Table 6.1: Basic properties of Seyfert-type warm absorbers observed with XMM-Newton and Chandra: object name, morphological type, redshift, $\log L_{\text{bol}}$ (erg s^{-1}), whether the X-ray spectrum is dominated by emission lines (EM), whether the source has a warm absorber (WA), whether a detailed spectral model has been published (Mod), whether the warm absorber is outflowing (Outflow), and reference for the warm absorber model (or non-detection of a warm absorber).

Object	Type	z	$\log L_{\text{bol}}$	EM	WA	Mod	Outflow	Reference
MR2251-178	Sy1 RQQ	0.06398	45.7 ^a	•	•	•	•	Kaspi et al. 2003
PG0844+349	Sy1 RQQ	0.064	45.5	•	•	•	•	Pounds et al. 2003a
PG1211+143	Sy1 RQQ	0.0809	45.6	•	•	•	•	Pounds et al. 2003b
PKS 0558-504	NLSy1 RLQ	0.137	~ 46					O'Brien et al. 2001b
IRAS 13349+2438	NLSy1 RQQ	0.10764	46.4 ^b	•	•	•	•	Sako et al. 2001
ESO 141-G55	Sy1	0.036	~ 45					Gondoin et al. 2003
NGC 4593	Sy1	0.0084	43.5 ^c	•	•	•	•	Steenbrugge et al. 2003a
NGC 3783	Sy1	0.00973	44.7 ^d	•	•	•	•	Netzer et al. 2003
Markarian 509	Sy1.2	0.0344	$\geq 45.5^e$	•	•	•	•	Yaqoob et al. 2003
NGC 7469	Sy1.2	0.0164	44.4 ^f	•	•	•	•	Chapter 4
Markarian 279	Sy1.5	0.0305	$\sim 45^g$					Scott et al. 2004

^a Monier et al. 2001; ^b Beichman et al. 1986; ^c Santos-Lleo et al. 1995; ^d Markowitz et al. 2003; ^e Kriss et al. 2000a; ^f Petrucci et al. 2004; ^g Bachev and Strigachev 2003

Table 6.2: Table 6.1 continued.

Object	Type	z	log L _{bol}	EM	WA	Mod	Outflow	Reference
NGC 3516	Sy1.5	0.009	~ 44	•	•	•	•	Netzer et al. 2002
NGC 5548	Sy1.5	0.01676	44.7 ^a	•	•	•	•	Steenbrugge et al. 2003b
NGC 4151	Sy1.5	0.00332	~ 44 ^b	•				Schurch et al. 2004
NGC 5506	Sy1.9	0.00618	~ 44	•				Bianchi et al. 2003
NGC 4258	Sy1.9 LINER	0.00149	~ 42 ^c	•	•			Young and Wilson 2004
Markarian 478	NLSy1	0.079 ^d	45.2 ^d					Marshall et al. 2003
Ton S180	NLSy1	0.06198	~ 46 ^e	•				Rózańska et al. 2004
MCG -6-30-15	NLSy1	0.00775	~ 44 ^f	•	•	•	•	Sako et al. 2003
Markarian 766	NLSy1	0.012929	~ 44 ^g	•	•	•		Mason et al. 2003b
NGC 4051	NLSy1	0.00234	43.4	•	•	•	•	Ogle et al. 2004
Markarian 359	NLSy1	0.0174	~ 44	•	•		?	O'Brien et al. 2001a
Ark 564	NLSy1	0.02468	44.4 ^h	•	•	•	•	Matsumoto et al. 2004

^a Pounds et al. 2003c; ^b Swain et al. 2003; ^c Yuan et al. 2002; ^d Gondhalekar et al. 1994; ^e Turner et al. 2002; ^f Reynolds 2000; ^g Pounds et al. 2003d; ^h Romano et al. 2002

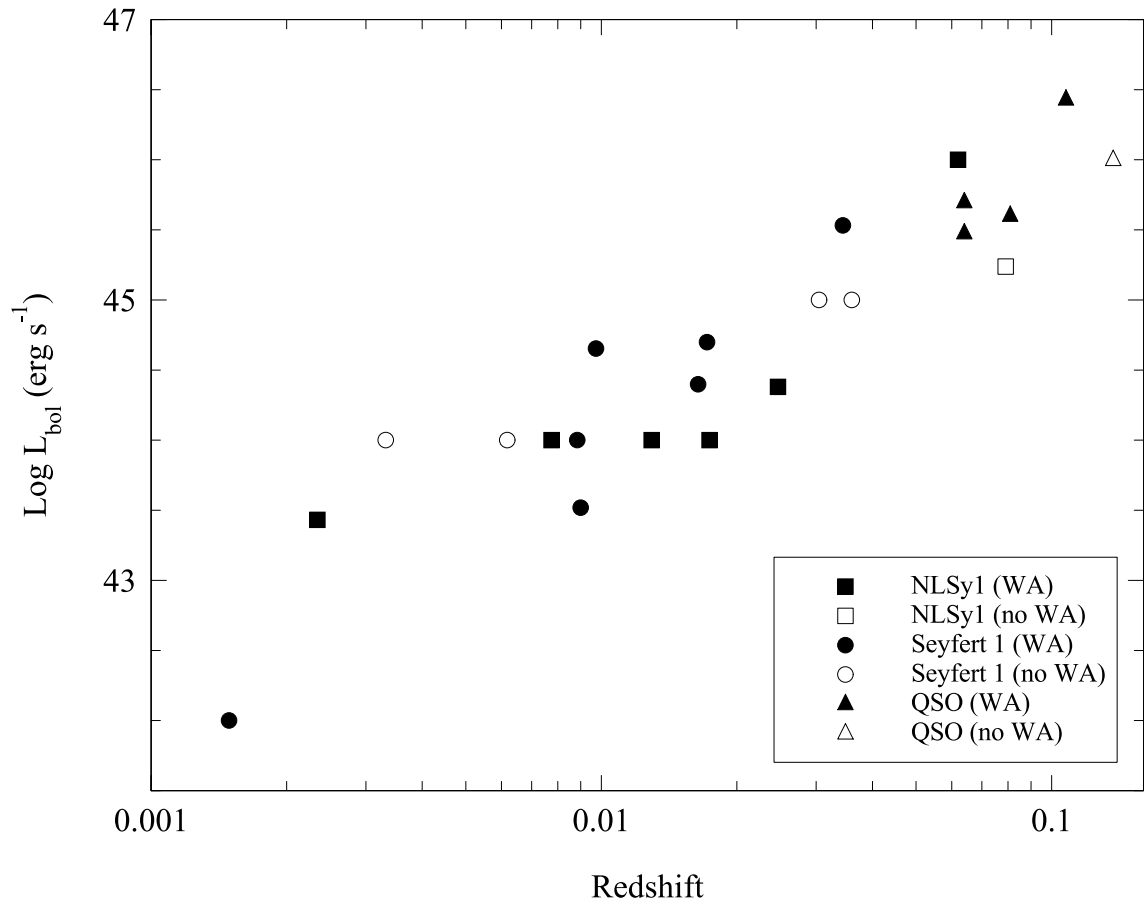


Figure 6.1: The distribution in redshift and bolometric luminosity of Seyfert 1 type AGN observed with the high-resolution spectrometers on XMM-Newton and Chandra: filled shapes indicate that the presence of a warm absorber has been reported.

Table 6.3: Equivalent hydrogen columns ($\log N_{\text{H}}$; cm^{-2}), ionisation parameters ($\log \xi$; erg cm s^{-1}) and outflow velocities (v_{out} ; km s^{-1}) of the modelled warm absorber phases of objects listed in Tables 6.1 and 6.2.

Object	$\log N_{\text{H}}$	$\log \xi$	v_{out}
MR2251-178	21.51	2.9	250 ^a
	20.3	0.68	250 ^a
PG0844+349	23.6	3.7	63000
PG1211+143	23.7	3.4	24000
	21.8	1.7	24000
	22.9	-0.9	not given
IRAS 13349+2438	22.3	2.25	0
	21.25	0	420
NGC 4593	21.2	2.61	400
	19.8	0.5	380
NGC 3783	21.9	1.1	750 ^b
	22.0	2.3	750 ^b
	22.3	2.9	750 ^b
Markarian 509	21.3	1.76	200
NGC 7469	20.6	2.1	800
NGC 3516	21.9	0.78	200 ^a
NGC 5548	21.68	2.69	311
	21.52	1.98	440
	20.15	0.4	290
MCG -6-30-15	21.3	1.25	150
	21.3	2.5	1900
Markarian 766	21.2	0.7	0
NGC 4051	21	1.4	402
Ark 564	21	0	150 ^a
	21	2	150 ^a

^a Estimated from the blueshift of the UV absorber; ^b Average of two velocity phases at 1000 and 500 km s^{-1} .

apparent that warm absorbers can contain a range of ionisation levels. There is currently no consensus as to whether this takes the form of discrete ionisation phases (i.e. Krongold et al., 2003), a continuous ionisation parameter distribution (Behar and Netzer, 2002), or some combination of these (c.f. Chapter 3). All spectral modelling of warm absorbers, to date, has assumed that the gas contains discrete ionisation phases; for the 14 objects I am looking at here, the average number of modelled ionisation phases is two.

I contend that the number of modelled phases does not tell us anything fundamental about the ionisation structure, as it is more likely to be a function of the quality of the data, and of the spectroscopic knowledge and techniques of the investigator. Indeed, two of the highest statistical quality spectra - those of NGC 3783 (Netzer et al., 2003) and NGC 5548 (Steenbrugge et al., 2003a) - require three ionisation phases, and it is quite possible that better quality spectra of other objects would also require a larger number of phases.

Perhaps a more interesting quantity is the range of ionisation parameters in the absorber, which I estimate here as the difference between $\log \xi$ of the highest and lowest modelled ionisation phases. I list these values in Table 6.4, alongside other averaged properties of the warm absorber for each object as discussed below. Naively, one might expect that - if all warm absorbers had the same ionisation structure - increasing the overall total column N_{Htot} of the absorber would bring a greater range of ionisation states into view. In reality, the objects in my sample show no such correlation, which either implies a wide variation in the ionisation structures, or, very probably, significant differences in the analysis methods and statistical quality of the spectra used by different authors. In particular, observers may be looking mainly for ‘traditional’ warm absorber ions such as O VIII and O VII, and others at a similar ionisation level, and may not be expecting to find much more lowly ionised species for which atomic data are harder to obtain.

The average ionisation parameter of an absorber, though a rather crude measure, is probably less open to interpretation than its ionisation range, and may be more useful for comparative purposes. I have estimated average values of ξ for the sources,

Table 6.4: Averaged warm absorber parameters for the sources in Table 6.3: object name, log 1–1000 Ryd ionising luminosity ($\log L_{\text{ion}}$; erg s^{-1}), log range in ionisation parameter ($\Delta \log \xi$; erg cm s^{-1}), log total equivalent hydrogen column ($\log N_{\text{Htot}}$; cm^{-2}), log weighted average ionisation parameter ($\log \xi_{\text{avg}}$; erg cm s^{-1}), weighted average outflow velocity (v_{avg} ; km s^{-1}).

Object	$\log L_{\text{ion}}$	$\Delta \log \xi$	$\log N_{\text{Htot}}$	$\log \xi_{\text{avg}}$	v_{avg}
MR2251-178	44.9 ^a	2.22	21.54	2.87	250
PG0844+349	44.2 ^a	0	23.6	3.7	63000
PG1211+143	43.9 ^a	4.3	23.77	3.39	24000
IRAS 13349+2438	44.6 ^a	2.25	22.34	2.21	30
NGC 4593	43.5 ^a	2.11	21.82	2.54	204
NGC 3783	44.0 ^a	1.8	22.58	2.68	750
Markarian 509	44.5 ^a	0	21.3	1.76	200
NGC 7469	44.0 ^b	4	20.60	2.1	800
NGC 3516	43.1 ^a	0	21.9	0.78	200
NGC 5548	44.6 ^c	2.29	21.92	2.51	362
MCG -6-30-15	43.2 ^a	1.25	21.60	2.22	1025
Markarian 766	43.4 ^a	unknown	21.2	0.7	0
NGC 4051	42.6 ^d	no info	21	1.4	402
Ark 564	44.9 ^{a, e}	2	21.30	1.70	150

^a Estimated with PIMMS using the extension of the fitted X-ray power-law (as given in the reference listed in Tables 6.1 and 6.2) over the 1–1000 Ryd range.

^b Estimated using the continuum model in Chapter 4.

^c Kaastra et al. 2002b

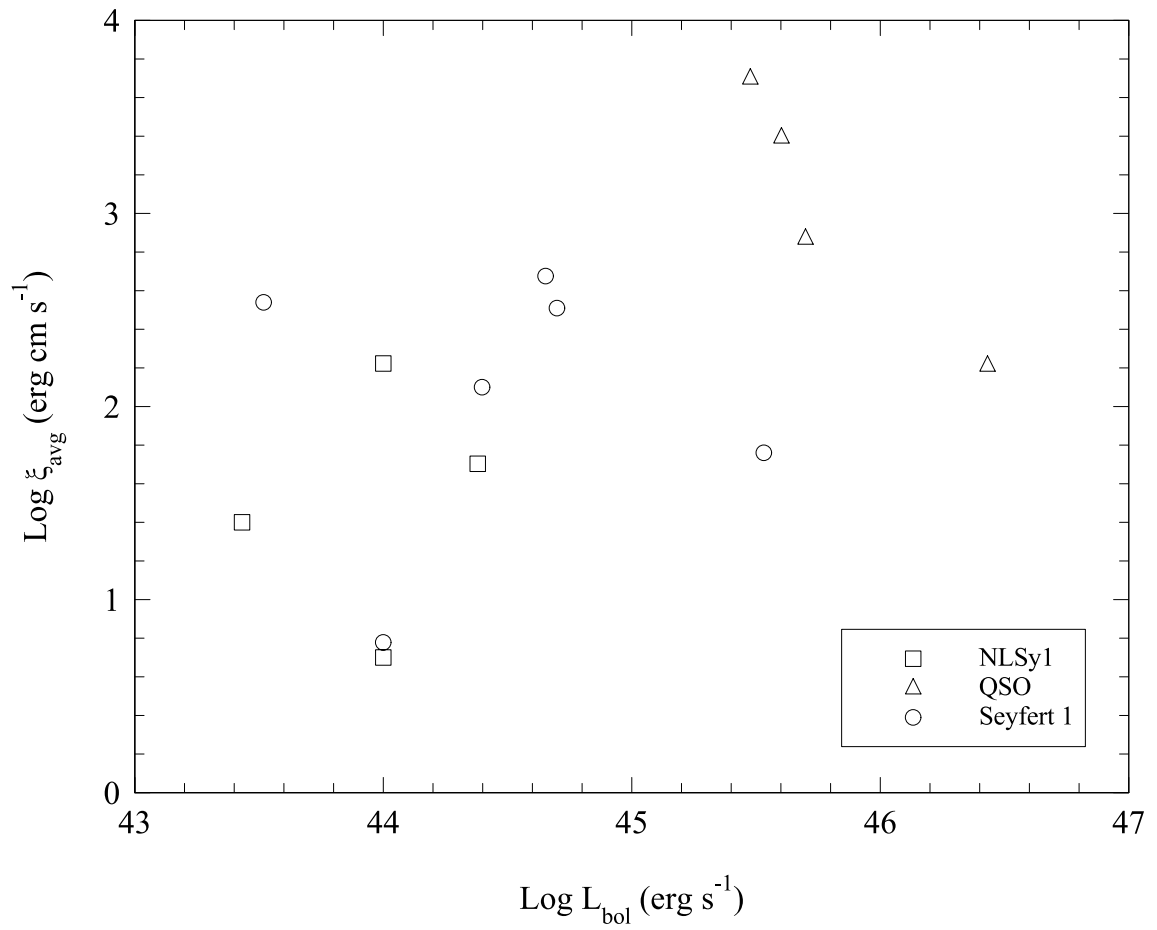
^d Ogle et al. 2004

^e L_{ion} estimated from the extrapolation of the measured power-law of Matsumoto et al. (2004) is actually larger than the value of L_{bol} estimated by Romano et al. (2002); either the source has become brighter, or the Romano et al. (2002) estimate was incorrect.

weighting the ξ of individual phases according to their absorbing columns. The distance scales of an AGN environment are expected to be roughly proportional to the square root of the bolometric luminosity of the central engine (see e.g. Netzer and Laor, 1993), and so since (according to the definition of the ionisation parameter) ξ decreases faster with distance than it increases with luminosity, one might expect the average ionisation parameter of warm absorbers to decrease with increasing source luminosity. In fact, there is no significant correlation between average ionisation and log bolometric luminosity (linear correlation coefficient $C = 0.52$, probability p of getting C greater than or equal to this from a random distribution = 0.3). There are slight differences between $\log \xi_{\text{avg}}$ for each class of AGN; for the quasars, $\log \xi_{\text{avg}} = 3.0 \pm 0.6$, for the Seyferts $\log \xi_{\text{avg}} = 2.1 \pm 0.7$ and for the NLSy1s $\log \xi_{\text{avg}} = 1.5 \pm 0.6$, where the errors are given as the standard deviation. The overall $\log \xi_{\text{avg}}$ for all types is 2.2 ± 0.8 . $\log \xi_{\text{avg}}$ is plotted versus $\log L_{\text{bol}}$ in Fig. 6.2.

There is also no significant correlation between log total column and log bolometric luminosity ($C = 0.50$, $p = 0.3$; see Fig. 6.3), but again, the three classes of object have slightly different average log columns: 22.8 ± 0.9 , 21.7 ± 0.6 and $21.3 \pm 0.2 \text{ cm}^{-2}$ for quasars, Seyferts and NLSy1s respectively. The average column for all objects was $21.9 \pm 0.9 \text{ cm}^{-2}$. There is, however a significant correlation between $\log \xi_{\text{avg}}$ and $\log N_{\text{Htot}}$: $C = 0.70$, $p = 0.05$. The significance decreases to $C = 0.44$ and $p = 0.2$ for $\log \xi$ and $\log N_{\text{H}}$ of the individual phases. This correlation is simply an observational bias, since the more highly ionised the warm absorber, the greater the column required for it to be observable.

Apart from the ionisation parameter and column, a warm absorber is also characterised by its outflow velocity. It is immediately obvious from Table 6.4 that we are dealing with two rather different orders of outflow speed. The Seyferts and NLSy1s have average warm absorber outflow speeds (with the contribution of each warm absorber phase weighted by column as before) of a few hundred km s^{-1} ; the two PG quasars have outflow speeds of tens of thousands of km s^{-1} . If the PG quasars are excluded from the analysis, the average outflow speeds are not significantly correlated with bolometric luminosity (Fig. 6.4), absorbing column (Fig. 6.5)

Figure 6.2: $\text{Log } \xi_{\text{avg}}$ versus $\text{log } L_{\text{bol}}$ for the objects in Table 6.4.

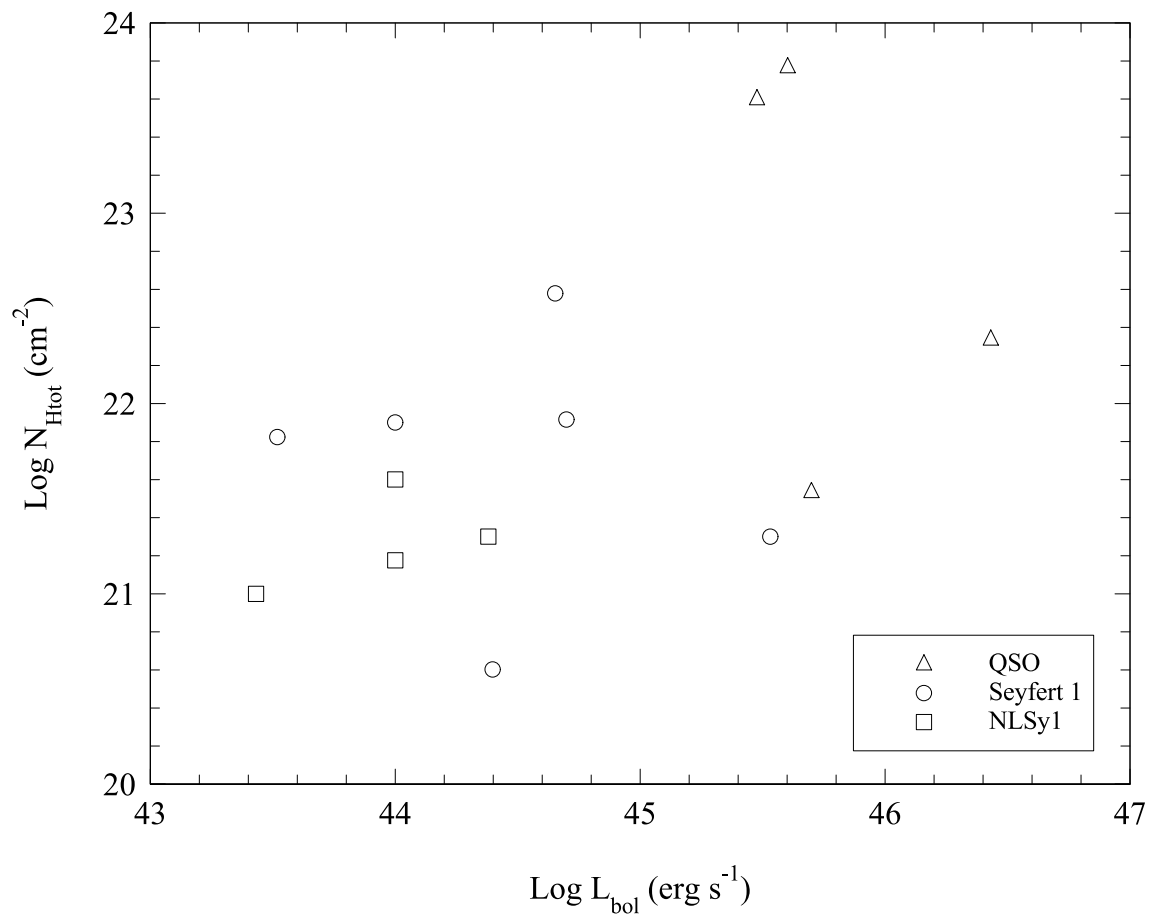


Figure 6.3: $\text{Log } N_{\text{Htot}}$ versus $\text{log } L_{\text{bol}}$ for the objects in Table 6.4.

or average ionisation parameter (Fig. 6.6).

In a radiatively accelerated wind, the density of the outflow decreases with increasing velocity, so we expect more highly ionised gas to be outflowing faster. It is therefore, perhaps, surprising that there is no correlation between the average ionisation parameters and velocities. Even the individual phases for each object, although their ionisations may vary, are outflowing at the same or similar speeds. The one exception is MCG -6-30-15 in which the high-ionisation phase is outflowing much faster.

Realistically, it might be hard to observe an increasing velocity with ionisation parameter due to the rapid fall-off with density in such winds. Also, the two outflow phases in MCG -6-30-15 might not be part of the same accelerating wind - the high velocity, high ionisation component might originate from closer in to the nucleus where the escape velocity is very high, and the low velocity component could be launched from much further away.

The relativistic velocities of the PG quasar outflows are not simply due to the high luminosities of the sources - IRAS 13349+2438 and MR2251-178 are both quasars with even higher bolometric luminosities, but they have low velocity ionised outflows very much like those seen in nearby Seyferts. There has to be some other fundamental difference in the origin of the outflow.

6.3 The nature of warm absorbers

A fundamental question about warm absorbers is whether their presence is somehow essential to an AGN - or put another way, are there Seyferts which do not have them? Previous work (e.g. Reynolds 1997) found that only about half of AGN have warm absorbers (or at least ones observable by instrumentation prior to XMM-Newton and Chandra). The group of AGN I am looking at here is not an ideal sample to answer this question, since many of them were selected to be observed precisely because they were known to exhibit ionised soft X-ray absorption from previous studies. There are, however, certain objects in the group which do not show evidence of

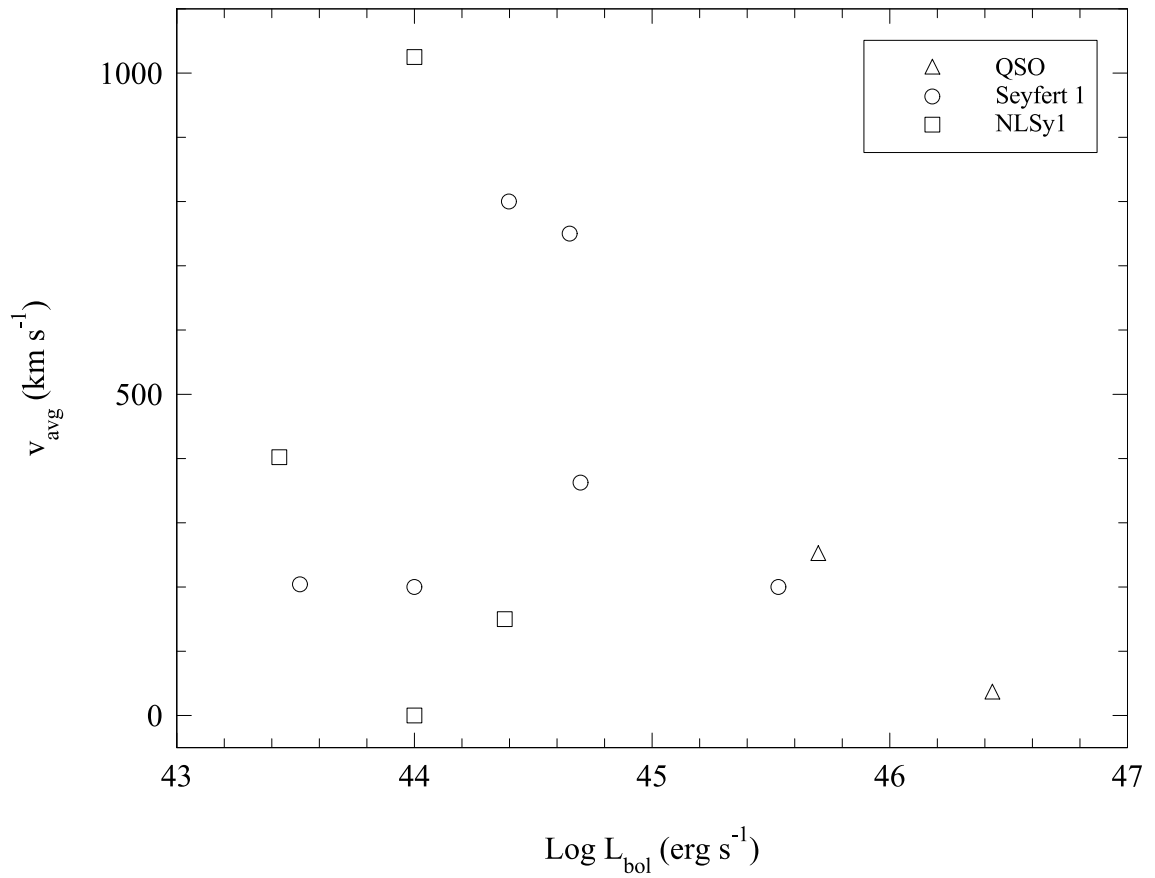


Figure 6.4: Average outflow velocity, v_{avg} , versus $\text{log } L_{\text{bol}}$ for the objects in Table 6.4, excluding PG0844+349 and PG1211+143.

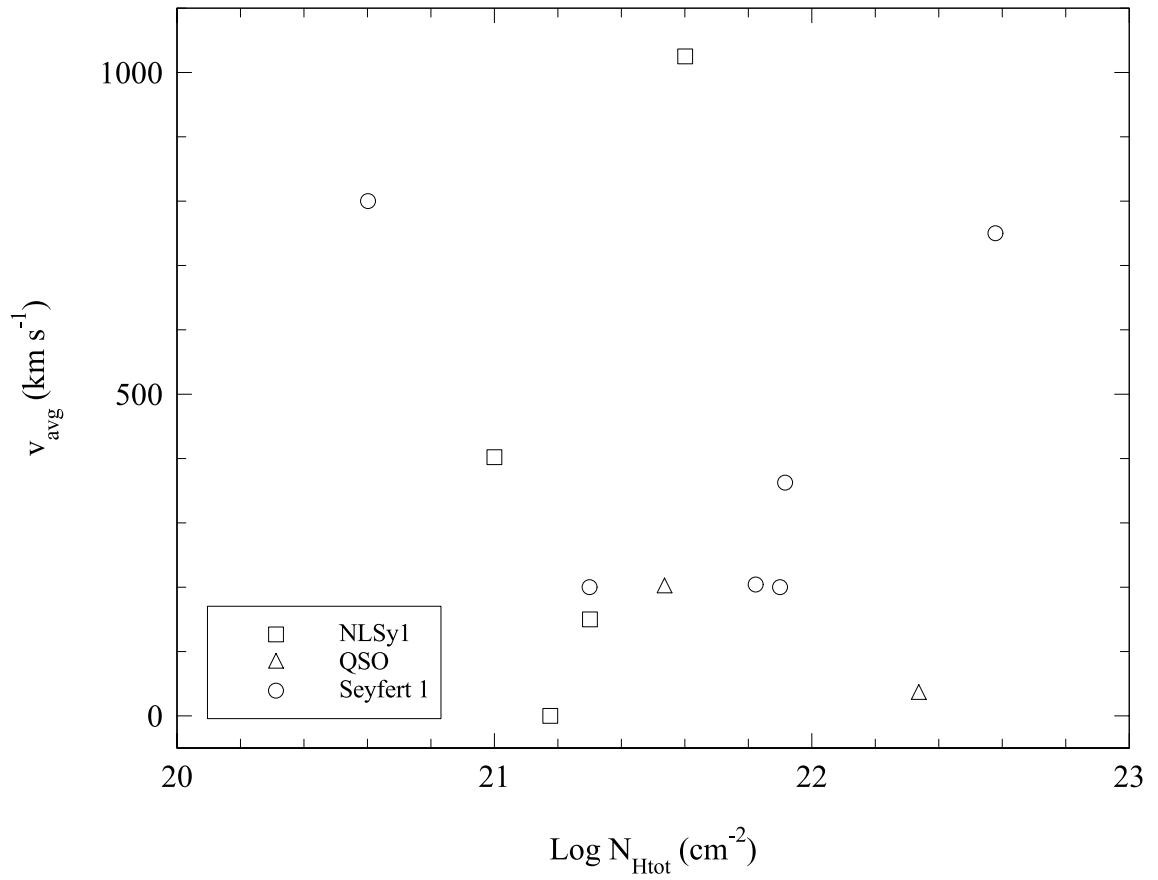


Figure 6.5: Average outflow velocity, v_{avg} , versus $\text{log } N_{\text{Htot}}$ for the objects in Table 6.4, excluding PG0844+349 and PG1211+143.

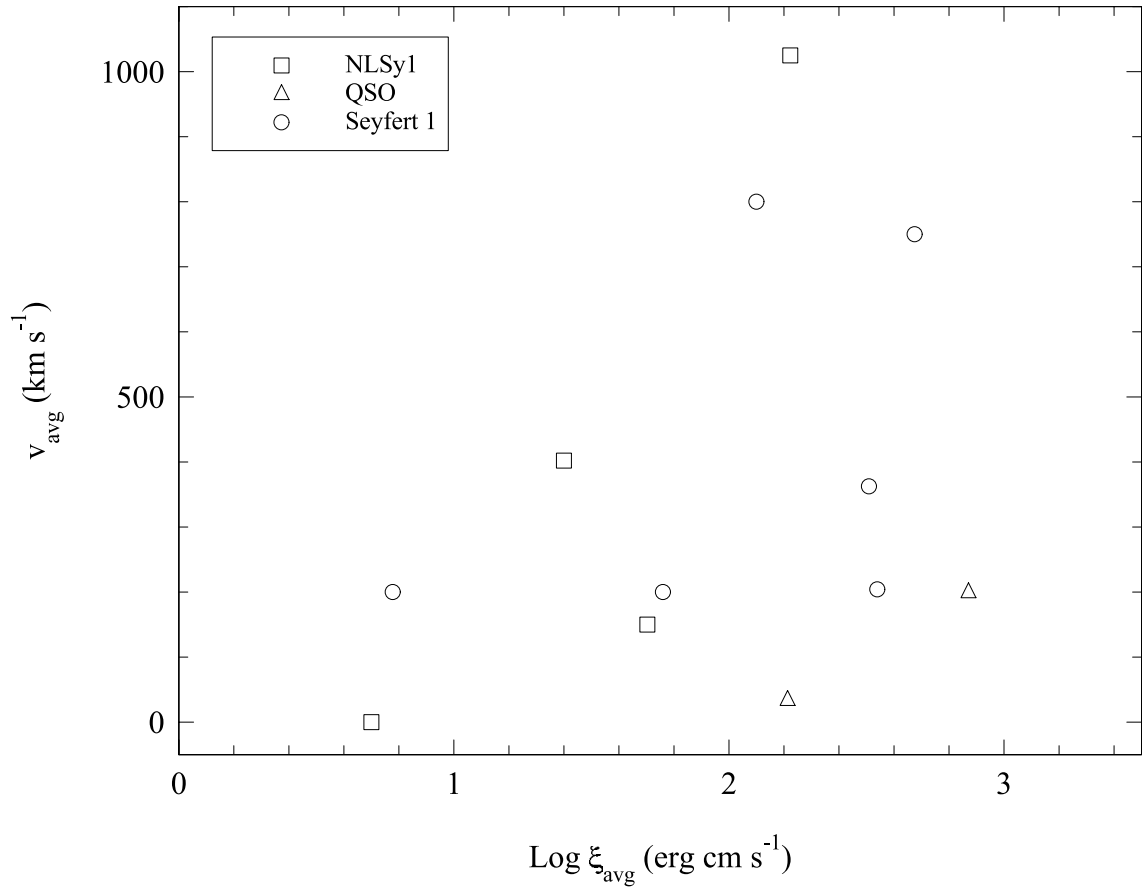


Figure 6.6: Average outflow velocity, v_{avg} , versus $\log \xi_{\text{avg}}$ for the objects in Table 6.4, excluding PG0844+349 and PG1211+143.

warm absorption.

Of a total of 23 objects in Tables 6.1 and 6.2, eleven are ordinary Seyferts (as classified by the authors referenced in the table, or otherwise by NED), seven are NLSy1s, and five are quasars. Four of the Seyferts lack a warm absorber. Two of these, NGC 4151 and NGC 5506, are emission line sources with an obscured central engine. The presence of the narrow X-ray emission lines probably implies that NGC 4151, at least, would appear to have a warm absorber if viewed from a different angle. The Chandra observation of Markarian 279 (Scott et al., 2004) was very short, and the source was in a low state, so the signal-to-noise of the spectrum is poor. Although Scott et al. (2004) found no significant evidence of X-ray warm absorption, this source does have an intrinsic UV absorber, making it very likely that an X-ray absorber will be found in better quality data in future; Crenshaw et al. (1999) found that objects in their sample with UV absorption always showed evidence of an X-ray absorber. The one remaining object without a warm absorber, ESO 141-G55 (Gondoin et al., 2003) is towards the high end of the L_{bol} -redshift distribution, but there does not seem to be anything significantly unusual about it with respect to the other sources. NGC 4258 is basically a Seyfert 2-type object, without a soft X-ray absorber; it has however been claimed to exhibit absorption lines above 6 keV (Young and Wilson, 2004).

Of the NLSy1s, only Markarian 478 lacks a warm absorber. Like ESO 141-G55, it has a fairly high luminosity, but does not seem to have very different properties from other sources which do have warm absorbers. One of the quasars (PKS 0558-504, O'Brien et al. 2001b) does not show evidence of warm absorption. It is a radio loud quasar, though, and radio-loud objects might be particularly problematic in terms of finding observational evidence for ionised outflows (c.f. Chapter 5). Disregarding the emission line and radio loud objects in the sample, as well as Markarian 279 since it has a UV absorber, I find that 2 out of 18 (11%) of the Seyfert 1-type objects in the sample show no evidence of an ionised outflow. If this was representative of the population as a whole, it would imply a global covering factor of almost 90% for X-ray warm absorbers.

It is as well to be careful of reading too much into the non-detection of warm absorption in ESO 141-G55 and Markarian 478. An absorber might be present, but with a turbulent velocity and column density too low to be observed with today's instrumentation. If indeed there are AGN which genuinely lack warm absorbers, then we know that AGN are able to do without them and they must be a side-effect - rather than an essential feature - of the AGN process.

6.3.1 The energetics of warm absorbers

How much mass is carried out of the AGN by the outflow? How does this compare to the amount of matter being accreted? Do ionised outflows carry a significant fraction of the energy output of an AGN? The answers depend upon the way one models the outflow. The most straightforward assumption is that the warm absorber contains a gas with uniform filling factor and density smoothly decreasing with $1/r^2$. This is unlikely to be a realistic scenario, though; observations (e.g. Kinkhabwala et al., 2002) have shown that a range of densities and ionisation parameters is likely to exist at any given radius, and therefore that the warm absorber/emitter is more likely to consist of filaments or clouds with a low overall filling factor. We have to bear this in mind when estimating the mass outflow rate and energy output of the AGN.

For a spherical outflow, the mass contained within a segment of a thin spherical shell of radius r , thickness δr , solid angle Ω and mass density $\rho(r)$ is

$$M = r^2 \rho(r) \delta r \Omega. \quad (6.1)$$

If matter is moving through this shell at a speed $\delta r / \delta t = v(r)$, then the mass outflow rate through the shell is

$$\dot{M}_{out} = r^2 \rho(r) v(r) \Omega. \quad (6.2)$$

Now assuming that the outflow has cosmic elemental abundances (i.e. $\sim 75\%$ by mass of hydrogen and $\sim 25\%$ by mass of helium), $\rho(r) \sim 1.23 m_p \bar{n}(r)$ where m_p is

the mass of a proton and $\bar{n}(r)$ is the average gas number density at radius r , giving

$$\dot{M}_{out} \sim 1.23r^2 m_p \bar{n}(r) v(r) \Omega. \quad (6.3)$$

In a spherical outflow at constant velocity (i.e. no acceleration or deceleration is taking place in the gas that we observe), $\bar{n}(r)$ must fall off as $1/r^2$, giving the relationship

$$\bar{n}(r) = \frac{k}{r^2}. \quad (6.4)$$

where k is a constant.

Let us say that the base of outflow is at $r = R$, where

$$\bar{n}(R) = \frac{k}{R^2}, \quad (6.5)$$

which gives

$$k = \bar{n}(R) R^2 \quad (6.6)$$

and so

$$\bar{n}(r) = \frac{\bar{n}(R) R^2}{r^2}. \quad (6.7)$$

Substituting this into Eqn. 6.3, and noting that $v(r)$ is simply v for the constant density outflow we are assuming, we get

$$\dot{M}_{out} \sim 1.23r^2 m_p v \Omega \frac{\bar{n}(R) R^2}{r^2} \quad (6.8)$$

and therefore

$$\dot{M}_{out} \sim 1.23R^2 m_p \bar{n}(R) v \Omega. \quad (6.9)$$

We need to relate $\bar{n}(r)$ to a measurable quantity. The ionisation parameter is given by

$$\xi = \frac{L_{ion}}{n(R) R^2}. \quad (6.10)$$

Now, the density in the ionisation parameter expression refers to the ‘microscopic’ electron density in the gas where the physical absorption is taking place. I assume here that the electron and ion number densities are similar, i.e. that hydrogen is fully ionised. The density in the mass outflow expression $\bar{n}(R)$ refers to a macroscopic ion number density averaged across the segment of shell. It is therefore a function of

both the number density of the gas that is actually absorbing at ionisation parameter ξ , and also the volume filling factor of this gas $C_v(R)$, so that

$$\bar{n}(R) = n(R)C_v(R). \quad (6.11)$$

This then gives us

$$\dot{M}_{out} \sim 1.23R^2m_p n(R)C_v(R)v\Omega, \quad (6.12)$$

and substituting in the expression for ionisation parameter,

$$\dot{M}_{out} \sim 1.23R^2m_p C_v(R)v\Omega \frac{L_{ion}}{\xi R^2}, \quad (6.13)$$

giving a final expression for the mass outflow rate of

$$\dot{M}_{out} \sim \frac{1.23m_p L_{ion} C_v(R)v\Omega}{\xi}. \quad (6.14)$$

I can then use this expression to estimate the mass outflow rate for the warm absorbers of the 14 AGN in my sample. ξ and v are directly measurable, and L_{ion} can be estimated from the continuum model fitted in the X-ray band (Table 6.4). I estimate the solid angle of the outflow using the information that $\sim 25\%$ of nearby AGN are type 1 (Maiolino and Rieke, 1995), and that the covering factor of these outflows seems to be at least 50% (Reynolds, 1997). This gives $\Omega \sim 1.6$ sr. The volume filling factor $C_v(R)$ is harder to estimate, especially since it very probably has some radial dependence. I cannot therefore take the same value for each AGN, as their warm absorbers could be at a wide range of radii with different (unknown) morphologies. $C_v(R)$ of the X-ray NLR could in principle be estimated from the ratio of the density derived from the emission measure (which is a macroscopic density) to the density derived from He-like triplet diagnostics, a microscopic density; we are seeing the bulk of the warm absorber near the base of the outflow however, where $C_v(R)$ could be rather different. One can however say with certainty that, since $C_v(R)$ must be less than or equal to 1, I can use $C_v(R) = 1$ and take the calculated mass outflow rate to be an upper limit.

The calculated values of the mass outflow rate upper limits are given in Table 6.5 for the ‘averaged’ warm absorbers. They vary between ~ 0.09 and $\sim 6 M_\odot \text{ yr}^{-1}$,

and there appear to be no particular patterns or differences between the different classes of AGN. It is interesting to compare the outflow rates with the accretion rate of the black hole in each case; I calculate this with the formula

$$\dot{M}_{acc} = \frac{L_{bol}}{c^2 \eta}, \quad (6.15)$$

where η is the accretion efficiency. I assume $\eta = 0.1$ for each object. The values of \dot{M}_{acc} , and of the ratio $\dot{M}_{out}/\dot{M}_{acc}$, are listed in Table 6.5. In all but one case (IRAS 13349+2438), the upper limit outflow rate is greater than the accretion rate, in one case up to 130 times greater.

Are these outflows significant in energetic terms? The upper limit of the kinetic energy carried via the outflow per unit time, i.e. the kinetic luminosity, can be estimated as

$$L_{KE} = \frac{1}{2} \dot{M}_{out} v^2 \quad (6.16)$$

where we assume that the observed velocity v is representative of the main mass of the outflow. I list values for L_{KE} in Table 6.5 alongside the percentage of L_{bol} that L_{KE} represents.

For all of the Seyferts, NLSy1s and the two quasars with low velocity absorbers, the upper limit to kinetic luminosity of the outflow is well below 1% of the bolometric luminosity of the AGN, and so cannot be playing any major rôle in the energetics of the system. The kinetic luminosities of the two high velocity quasar outflows, however, are predicted to be up to $\sim 20\%$ and an unphysical 500% of L_{bol} for PG1211+143 and PG0844+349 respectively. Since this kinetic luminosity is an upper limit, and depends on C_v , this must be telling us that C_v is really much less than 1 for the warm absorber of PG0844+349. If - improbably - the acceleration of this phase actually accounted for 100% of the bolometric luminosity of the AGN, the upper limit to C_v would need to be about 0.2.

Table 6.6 gives values of \dot{M}_{out} , \dot{M}_{acc} , $\dot{M}_{out}/\dot{M}_{acc}$, L_{KE} and the percentage of L_{bol} represented by L_{KE} calculated for the individual warm absorber phases. For these individual phases, it is clear that - assuming a volume filling factor of one - the lower ionisation phases can potentially carry the most mass. Again, the fraction of the

Table 6.5: Mass outflow rates calculated using the averaged warm absorber parameters quoted in Table 6.4: object name, mass outflow rate (\dot{M}_{out} ; $M_{\odot} \text{ yr}^{-1}$), mass accretion rate (\dot{M}_{acc} ; $M_{\odot} \text{ yr}^{-1}$), ratio of mass outflow rate to mass accretion rate ($\dot{M}_{\text{out}}/\dot{M}_{\text{acc}}$), kinetic luminosity of outflow ($\log L_{\text{KE}}$; erg s^{-1}), percentage of L_{bol} represented by L_{KE} (% of L_{bol}).

Object	\dot{M}_{out}	\dot{M}_{acc}	$\dot{M}_{\text{out}}/\dot{M}_{\text{acc}}$	$\log L_{\text{KE}}$	% of L_{bol}
MR2251-178	≤ 1.3	0.88	≤ 1.5	≤ 40	$\leq 5 \times 10^{-4}$
PG0844+349	≤ 11	0.53	≤ 21	≤ 46	≤ 500
PG1211+143	≤ 4.4	0.70	≤ 6.3	≤ 45	≤ 20
IRAS 13349+2438	≤ 0.40	4.7	≤ 0.085	≤ 38	$\leq 6 \times 10^{-7}$
NGC 4593	≤ 0.092	0.0057	≤ 16	≤ 39	≤ 0.004
NGC 3783	≤ 0.83	0.079	≤ 11	≤ 41	≤ 0.03
Markarian 509	≤ 5.6	0.60	≤ 9.4	≤ 41	≤ 0.002
NGC 7469	≤ 3.3	0.044	≤ 75	≤ 42	≤ 0.3
NGC 3516	≤ 2.3	0.018	≤ 130	≤ 40	≤ 0.03
NGC 5548	≤ 2.2	0.088	≤ 25	≤ 41	≤ 0.02
MCG -6-30-15	≤ 0.48	0.018	≤ 27	≤ 41	≤ 0.2
Markarian 766	–	0.018	–	–	–
NGC 4051	≤ 0.34	0.0047	≤ 72	≤ 40	≤ 0.06
Ark 564	≤ 12	0.042	≤ 280	≤ 41	≤ 0.03

bolometric luminosity that can be carried by each phase is generally of the order of or less than about 1%. However, the kinetic luminosity of the middle ionisation phase (no velocity information was available for the lowest ionisation phase) of PG1211+143 is up to $\sim 1000\%$ of the bolometric luminosity. Using the previous argument, the volume filling factor of this phase has to be less than 0.1, remembering also that the other ionisation phases will also be associated with finite, and different, values of C_v .

If we assume that the outflow is radiatively driven, we can get a better estimate for C_v from the percentage of the bolometric luminosity that the outflow is observed to absorb. I obtained the flux of a power-law model before and after applying absorption (with the *xabs* model in *spex*) from the ‘averaged’ warm absorbers of PG0844+349 and PG1211+143 (I used these objects as they are the ones with the highest upper limits to the percentage of L_{bol} represented by L_{KE}), and used the resulting 0.3–10 keV fluxes to estimate the fractions of the 0.3–10 keV flux, and thus luminosity, that the absorbers intercept. This fraction was multiplied by the observed 0.3–10 keV luminosity to estimate the actual luminosity absorbed by the outflows in each case. The column densities of these warm absorbers are high enough for Thomson scattering to be important; τ_t , the optical depth for Thomson scattering, is ~ 0.3 and 0.4 for PG0844+349 and PG1211+143 respectively. I used this to estimate the 0.3–10 keV luminosity lost to scattering. The percentages of L_{bol} represented by the total luminosity lost to absorption and scattering were then calculated. For PG0844+349 this percentage was 1.3%, as opposed to the 500% upper limit from \dot{M}_{out} , and for PG1211+143 it was 1.6% as compared to the 20% upper limit. This gives estimates of the volume filling factor of the two averaged absorbers as ~ 0.003 and ~ 0.08 respectively.

So do ionised outflows play a significant role in the energetics of AGN? Given that the upper limit to the fraction of L_{bol} represented by the kinetic luminosity of Seyfert and NLSy1 warm absorbers is much less than 1%, the answer has to be no. Even in the case of the high velocity outflows seen in the two PG quasars, although the upper limits to their kinetic luminosities are very high, the volume filling factors

of the ionised material are probably low enough to put their energetic importance more in line with that seen in the other objects.

6.3.2 Where do warm absorbers come from?

The outflow speed can give us a useful clue to the origins of warm absorbers. If we assume that the outflow has to obtain a speed greater than or equal to the escape velocity v_{esc} , where

$$v_{esc} = \sqrt{\frac{2GM}{R}} \quad (6.17)$$

and G is the gravitational constant, M is the mass of the black hole and R is the distance of the bulk of the gas from the black hole, then we can estimate a minimum distance of the warm absorber from the central engine using the measured outflow speeds:

$$R \geq \frac{2GM}{v_{out}^2}. \quad (6.18)$$

The maximum distance of the base of the warm absorber can also be estimated. Assuming that most of the mass of the absorber with ionisation parameter ξ is concentrated in a relatively thin layer of depth Δr (since the density falls off rapidly with radius), Δr has to be less than or equal to the distance R from the central engine:

$$\frac{\Delta r}{R} \leq 1. \quad (6.19)$$

The observed line-of-sight absorbing column N_H is a function of the density $n(R)$ of the material at ionisation parameter ξ , its volume filling factor $C_v(R)$ and Δr ;

$$N_H \sim n(R)C_v(R)\Delta r, \quad (6.20)$$

which can be combined with the expression for the ionisation parameter of the shell

$$\xi = \frac{L_{ion}}{n(R)R^2} \quad (6.21)$$

to give

$$\frac{\Delta r}{R} \sim \frac{\xi RN_H}{L_{ion}C_v(R)}. \quad (6.22)$$

Table 6.6: Mass outflow rates calculated for each *outflowing* warm absorber phase using the parameters quoted in Table 6.3: object name, $\log \xi$ of phase (erg cm s^{-1}), mass outflow rate ($\dot{M}_{\text{out}}; M_{\odot} \text{ yr}^{-1}$), mass accretion rate ($\dot{M}_{\text{acc}}; M_{\odot} \text{ yr}^{-1}$), ratio of mass outflow rate to mass accretion rate ($\dot{M}_{\text{out}}/\dot{M}_{\text{acc}}$), kinetic luminosity of outflow ($\log L_{\text{KE}}; \text{erg s}^{-1}$), percentage of L_{bol} represented by L_{KE} (% of L_{bol}).

Object	$\log \xi$	\dot{M}_{out}	\dot{M}_{acc}	$\dot{M}_{\text{out}}/\dot{M}_{\text{acc}}$	$\log L_{\text{KE}}$	% of L_{bol}
MR2251-178	2.9	≤ 1.3	0.88	≤ 1.4	≤ 40	$\leq 5 \times 10^{-4}$
	0.68	≤ 210	0.88	≤ 240	≤ 43	≤ 0.08
PG0844+349	3.7	≤ 11	0.52	≤ 21	≤ 46	≤ 500
PG1211+143	3.4	≤ 4.4	0.70	≤ 6.3	≤ 45	≤ 20
	1.7	≤ 220	0.70	≤ 310	≤ 47	≤ 1000
IRAS 13349+2438	0	≤ 810	4.7	≤ 170	≤ 44	≤ 0.2
NGC 4593	2.61	≤ 0.15	0.0058	≤ 26	≤ 40	≤ 0.02
	0.5	≤ 19	0.0058	≤ 3200	≤ 42	≤ 3
NGC 3783	1.1	≤ 31	0.079	≤ 400	≤ 43	≤ 1
	2.3	≤ 2.0	0.079	≤ 25	≤ 42	≤ 0.08
	2.9	≤ 0.50	0.079	≤ 6.4	≤ 41	≤ 0.02
Markarian 509	1.76	≤ 5.6	0.60	≤ 9.4	≤ 41	≤ 0.002
NGC 7469	2.1	≤ 3.3	0.044	≤ 75	≤ 42	≤ 0.3
NGC 3516	0.78	≤ 2.3	0.018	≤ 130	≤ 40	≤ 0.03
NGC 5548	2.69	≤ 1.2	0.088	≤ 14	≤ 41	≤ 0.008
	1.98	≤ 9.0	0.088	≤ 100	≤ 42	≤ 0.1
	0.4	≤ 230	0.088	≤ 2600	≤ 43	≤ 1
MCG -6-30-15	1.25	≤ 0.66	0.018	≤ 37	≤ 40	≤ 0.005
	2.5	≤ 0.47	0.018	≤ 27	≤ 42	≤ 0.5
Markarian 766	0.7	–	0.018	–	–	–
NGC 4051	1.4	≤ 0.34	0.0047	≤ 72	≤ 40	≤ 0.06
Ark 564	0	≤ 590	0.042	≤ 14000	≤ 43	≤ 2
	2	≤ 5.9	0.042	≤ 140	≤ 41	≤ 0.02

Applying the condition that $\Delta r/R \leq 1$, one then gets

$$R \leq \frac{L_{ion} C_v(R)}{\xi N_H}, \quad (6.23)$$

and since $C_v(R) \leq 1$,

$$R \leq \frac{L_{ion}}{\xi N_H}. \quad (6.24)$$

The resulting minimum and maximum distances are listed in Tables 6.7 and 6.8 alongside the distances of the BLR and torus for each object. The BLR distances were taken from the literature, except in the cases of IRAS 13349+2438, MCG -6-30-15 and Markarian 766 where they were estimated using $r_{BLR} \propto L_{Bol}^{0.5}$ (Netzer and Laor, 1993), with the BLR distance of NGC 5548 (a reverberation measurement; Wandel et al. 1999) used to normalise the proportionality. Torus distances were estimated using the approximate relation given in Krolik and Kriss (2001) that the inner edge of the torus is $\sim 1 \times L_{ion,44}^{0.5}$ pc, where $L_{ion,44}$ is the 1–1000 Ryd luminosity L_{ion} in units of 10^{44} erg s $^{-1}$.

The results of this comparison are that the minimum warm absorber distances for the Seyferts and NLSy1s are all further out than the BLR. In all but four cases they are also closer in than the torus. Placing the base of the warm absorber outflow at around the distance of the torus immediately rules out an origin in an accretion disc wind for these absorbers; it lends support instead to the idea that the outflows originate in a radiation driven wind from the torus (e.g. Krolik and Kriss, 2001).

But what about the Kriss et al. (2003) result, in collaboration with my own work discussed in Chapter 4, that at least one phase of the warm absorber in NGC 7469 was actually within the BLR? If the Kriss et al. (2003) suggestion is correct, it could imply that we are seeing the warm absorber in the object (and perhaps others) before it has been accelerated to the full escape speed, and therefore the gas can be closer to the central engine than I predict. This may be a reasonable suggestion, since we are seeing the bulk of the gas very close to the base of the outflow, and it will obviously take a finite distance to accelerate the outflow to escape velocity.

The situation is a little different with the quasars. Of the two objects with ‘normal’ Seyfert-type outflows, MR2251-178 fits into the same pattern as the Seyferts,

Table 6.7: Comparison of distances within the AGN environment: object name, black hole mass (M_{BH} ; $10^7 M_{\odot}$), minimum distance of warm absorber from central engine (r_{min} ; pc), maximum distance of warm absorber from central engine (r_{max} ; pc), distance of BLR from central engine (r_{BLR} ; pc), distance of torus from central engine (r_{torus} ; pc), the ratios of the minimum and maximum distances to the BLR and torus distances respectively ($r_{\text{min}}/r_{\text{BLR}}$, $r_{\text{min}}/r_{\text{torus}}$, $r_{\text{max}}/r_{\text{BLR}}$, $r_{\text{max}}/r_{\text{torus}}$).

Object	M_{BH}	r_{min}	r_{max}	r_{BLR}	r_{torus}	$r_{\text{min}}/r_{\text{BLR}}$	$r_{\text{min}}/r_{\text{torus}}$	$r_{\text{max}}/r_{\text{BLR}}$	$r_{\text{max}}/r_{\text{torus}}$
MR2251-178	0.83 ^a	1.1	97	0.027 ^b	2.8	43	0.41	3600	35
PG0844+349	2.7 ^c	0.000059	0.027	0.020 ^c	1.3	0.000045	0.00012	1.3	0.021
PG1211+143	2.36 ^c	0.00035	0.020	0.085 ^c	0.94	0.0042	0.00037	0.23	0.021
IRAS 13349+2438	80 ^d	5800	34	0.11 ^e	1.92	52000	3000	300	18
NGC 4593	0.2 ^f	0.41	4.2	0.0076 ^f	0.55	55	0.75	560	7.7
NGC 3783	1.1 ^g	0.17	1.8	0.0038 ^g	1.0	45	0.17	490	1.8
Markarian 509	9.5 ^g	20	880	0.067 ^g	1.8	310	12	13000	500

^a Morales and Fabian 2002; ^b Monier et al. 2001; ^c Kaspi et al. 2000b; ^d Brandt et al. 1997; ^e calculated from L_{Bol} as described in text; ^f Santos-Lleo et al. 1995; ^g Wandel et al. 1999.

Table 6.8: Table 6.7 continued.

Object	M_{BH}	Γ_{min}	Γ_{max}	Γ_{BLR}	Γ_{torus}	$\Gamma_{\text{min}}/\Gamma_{\text{BLR}}$	$\Gamma_{\text{min}}/\Gamma_{\text{torus}}$	$\Gamma_{\text{max}}/\Gamma_{\text{BLR}}$	$\Gamma_{\text{max}}/\Gamma_{\text{torus}}$
NGC 7469	0.76 ^a	0.10	640	0.0042 ^a	1.0	24	0.10	150000	640
NGC 3516	2.3 ^b	4.9	88	0.0088 ^c	0.36	560	14	10000	250
NGC 5548	6.8 ^a	4.5	46	0.015 ^a	1.9	290	2.3	3000	24
MCG -6-30-15	1.5 ^d	0.12	7.3	0.0068 ^e	0.39	18	0.32	1100	19
Markarian 766	1.9 ^f	–	1000	0.0068 ^e	0.49	–	–	150000	2100
NGC 4051	0.14 ^a	0.075	53	0.0054 ^a	0.20	14	0.37	9800	260
Ark 564	3.7 ^g	14	2400	$\leq 0.0025^{\text{h}}$	2.8	5600	5.1	970000	880

^a Wandel et al. 1999; ^b Gebhardt et al. 2000; ^c Wanders et al. 1993; ^d Reynolds 2000; ^e calculated from L_{Bol} as described in the text; ^f Mathur et al. 2001; ^g Matsumoto et al. 2004; ^h Shemmer et al. 2001.

whereas IRAS 13349+2438 has a minimum radius far out beyond the torus. The minimum radius for the absorber in IRAS 13349+2438 actually comes out much greater than the maximum radius: this is due to the very low average outflow speed. The two PG quasars, on the other hand, have minimum and maximum radii much closer to the central engine due to their extremely high outflow speeds, high columns and high average ionisation: the warm absorber of PG0844+349 is placed between about 2 light-hours and 30 light-days from the continuum source, and the corresponding limits for PG1211+143 are around 10 light-hours to 20 light-days. This makes an origin in an accretion disc wind more likely.

There is evidence that these inner outflows also occur in nearby Seyferts. In NGC 3783, Reeves et al. (2004) found evidence for a highly ionised phase of the warm absorber whose variability put it very close to the central engine. Crucially, the main spectral evidence for this phase were absorption lines in the 6–7 keV band, where resolution and signal-to-noise are much lower than in the soft X-rays. This very highly ionised gas is hard to observe in soft X-ray spectra, and this may be why it has not been reported in more objects. There could therefore be significant columns of such gas which have previously been unobserved.

So where does this take our understanding of the origins of warm absorbers? We seem to be dealing with two different basic types of warm absorber - the type we see in nearby Seyferts, which appears to be most consistent with a torus wind, and the rather more extreme variety observed in the two PG quasars and in the hard X-ray spectrum of NGC 3783, which could correspond to an accretion disc wind.

One interesting thing about the extreme outflows is that their presence is not a simple function of luminosity, as the two most luminous quasars I look at here have low velocity, low column Seyfert-type outflows. There must be some difference either in the availability of matter for the outflow, or in the process which can drive it. Within the unified model of AGN, this must mean either that there is some difference in the structure of the inner regions of the AGN environment, or that there is something different about the accretion process which can drive an accretion disc wind.

Having reached this point, it is now worth asking how this relates to the knowledge gained about AGN outflows from studies of UV absorbers and emitters. The higher resolution of current astronomical UV spectrometers allows us to gain quite a detailed view of the kinematics of UV absorbers. The first problem to solve, before making a comparison between outflows in the two wavebands, is the precise relationship between UV and X-ray absorption. Different conclusions have been reached about different sources: at least some of the components of the X-ray and UV absorbers have been claimed to have a common origin in NGC 3783 (Kaspi et al., 2002; Gabel et al., 2003), NGC 3516 (Kraemer et al., 2002), NGC 7469 (Kriss et al., 2003 and Chapter 4) and Ark 564 (Romano et al., 2002). Conversely, the UV and X-ray absorption apparently originate in different phases of gas (albeit at similar velocities) in Markarian 509 (Kraemer et al., 2003).

The emerging picture is that some but not all of the UV velocity phases can be seen in the X-ray absorber, and some but not all of the X-ray absorber phases can be seen in the UV; the deciding factors are the column density and ionisation parameters of the phases. Plasma which absorbs in the UV will contain ions that are observable in the soft X-ray band, although the line-of-sight column of the plasma may not be high enough for the X-ray transitions to be visible to current instrumentation. Plasma absorbing in the X-rays, so long as it is not too highly ionised, can contain ions with transitions in the UV. Working out exactly which of the UV and X-ray phases observed in any given object coincide ideally requires simultaneous high resolution spectroscopic observations in both bands.

UV absorbers generally have more than one discrete velocity component (Crenshaw et al., 1999). It can be hard to work out whether the gas phases giving rise to these components actually have different ionisation parameters, due to the limited number of spectral lines visible in certain observable wavebands. Nevertheless, two basic interpretations are possible; either we are seeing different velocity streams with different origins, or we are seeing a single accelerating (or decelerating) outflow with a multiply-peaked density profile. This latter case could imply that the ionised absorber is not a single time-steady outflow, but is the result of a series of ejection

events. If the UV wind originated from the torus, for example, then this could be due to major variations over time in the AGN luminosity (i.e. high and low states, or flares) giving rise to peaks and troughs in the amounts of material ablated from the torus. The multiple phases would thus contain an imprint of the accretion history of the AGN.

Kraemer et al. (2002) note that there is a lack of evidence of radial acceleration in AGN absorbers. Their analysis of UV absorbers in NGC 3516 does find that the different kinematic phases are moving faster the further they are from the nucleus (the X-ray absorber appears to be associated with the slowest moving phases closest to the nucleus), but they remark that this is not necessarily the sign of an accelerating outflow as the phases could have originated at different distances from the nucleus. As I discussed earlier, faster moving gas in a radiatively accelerated outflow would be expected to be more highly ionised - so are the X-ray absorbers moving faster than the UV absorbers? The observational evidence tends to favour the opposite scenario, with (at least some) of the UV phases moving faster than the X-ray phases, for instance in NGC 3516 (Kraemer et al., 2002) and NGC 7469 (Kriss et al., 2003). This may, again, be due to the decreasing column problem; UV spectrometers are able to detect much lower columns of gas than current X-ray instruments.

There is evidence of increasing velocity with distance from the nucleus in the UV NLR, interpreted as the result of radiative acceleration, in the emission line dominated objects NGC 1068 and NGC 4151. The ionisation cones forming the NLRs can be modelled as outflowing bicones at least partially evacuated along their axes (Crenshaw and Kraemer, 2000; Crenshaw et al., 2000). By measuring the velocities of individual knots or clouds in the ionisation cones, higher speeds were observed at greater distances from the nucleus, and then a decrease in speed further out interpreted as being due to interactions with a patchy ambient medium. In the case of NGC 4151 the acceleration of emission line knots continued up to 160 pc away from the nucleus, with decelerated clouds approaching the systemic velocity at 290 pc. In NGC 1068, UV continuum radiation has been observed from an

apparent shock front where an emission line knot is being decelerated (Kraemer and Crenshaw, 2000).

So, the gas in the UV NLR (which has been associated with the X-ray NLR, e.g. Kinkhabwala et al. 2002) does appear to be an outflow, plausibly accelerated by radiation from the central engine. Crenshaw et al. (2000) interpret the apparent evacuation of the NLR ionisation cone along its axis as possibly being due to the radio jet in NGC 4151; interestingly, a hollow bicone is the geometry one would expect from a torus wind.

Can the ‘inner’ outflow, which could be an accretion disc wind or an outflowing BLR, be seen in UV? As discussed in Chapter 4, Kriss et al. (2003) find that one of the UV absorber phases in NGC 7469 could originate at the distance of the BLR. Hutchings et al. (2001) found that the P-Cygni profile of O VI observed whilst NGC 3516 was in a low state was evidence that the BLR was actually an outflowing wind. If the BLR is outflowing, where is the matter being replaced from? Is the BLR a manifestation of the accretion disc wind?

The general picture that I get from the X-ray warm absorbers in Seyfert-type objects - namely that there appear to be two types of AGN outflow with different origins - is reflected in the findings of a recent survey of intrinsic UV absorption in 56 PG quasars. Laor and Brandt (2002) compared UV absorption in Soft X-ray Weak Quasars (SXWQs) and non-SXWQs. SXWQ UV outflows have a very high column (the more luminous SXWQs are Broad Absorption Line (BAL) Quasars) and presumably cause the soft X-ray spectra to be highly absorbed. Non-SXWQs, on the other hand, have UV absorbers which resemble those in nearby Seyferts. They concluded that the non-SXWQ outflows are launched at ten times the distance from which SXWQ outflows originate.

6.3.3 Where do warm absorbers end up?

The mass carried in the warm absorber must be ending up somewhere. Does it have an important effect on the host galaxy? One firstly needs to know if the ionised outflow is a short-lived phenomenon, or whether it exists for long enough to have a

significant influence on the mass budget of the AGN.

In the absence of replenishment of warm absorber material, how long would the observed columns of gas last? If one approximates the warm absorber as a slab of gas of thickness Δr lying a distance r from the absorber, with a mass density ρ and subtending a solid angle Ω , the mass M_{WA} of the absorber is given by:

$$M_{WA} = r^2 \rho \Delta r \Omega. \quad (6.25)$$

Since the mass density $\rho \sim 1.23 m_p \bar{n}$, where \bar{n} is the average number density of the column and m_p is the proton mass (as before, the factor of 1.23 corrects for a $\sim 25\%$ He, 75% H by mass elemental composition),

$$M_{WA} \sim 1.23 m_p \bar{n} r^2 \Delta r \Omega, \quad (6.26)$$

and using the fact that the equivalent hydrogen column N_H is given by

$$N_H = \bar{n} \Delta r, \quad (6.27)$$

the mass of the absorber can be estimated as

$$M_{WA} \sim 1.23 m_p N_H r^2 \Omega. \quad (6.28)$$

Assuming a solid angle of 1.6, as before, using the average N_H for the Seyfert 1 galaxies in my sample ($10^{21.7} \text{ cm}^{-2}$), and assuming that the warm absorber slab is at the distance of the torus ($\sim 1 \text{ pc}$ from the central engine), I estimate a Seyfert warm absorber mass of approximately $80 M_\odot$. If the mass outflow rate was of the order of a solar mass per year (Table 6.5), the warm absorber gas would not last out a century; even if the mass outflow rates are two or three orders of magnitude smaller than the upper limits that I calculate, due to a low volume filling factor, the warm absorber would still be extremely short-lived compared to the AGN itself. This would have implications for the observability of ionised outflows; if they only lasted $10^2 - 10^5$ years, there would be a low probability of observing them during the total AGN lifetime of perhaps 10^8 years. This means that the warm absorber column must be fed constantly by some long-lived source of matter - presumably, in the case of nearby Seyferts, the torus.

Assuming an outflow rate of $\sim 1 M_{\odot} \text{ yr}^{-1}$, and an AGN lifetime of order 10^8 years, gives the approximate estimate that the warm absorber could be pushing out up to $10^8 M_{\odot}$ of matter through its ionisation cones over the course of its existence. At the same time, the AGN will be accreting mass (which has presumably passed through the torus) via the accretion disc; taking the average accretion rate of the Seyferts in my sample, $\sim 0.14 M_{\odot} \text{ yr}^{-1}$, and assuming that a similar rate is sustained throughout the AGN lifetime of 10^8 years, the total mass accreted by the black hole is then of order $1.4 \times 10^7 M_{\odot}$. Even taking into account the uncertainty in the outflow rates, it is clear that there is a potential competition for the mass reservoir in the central regions of the AGN. Could the removal of mass through the ionised outflow be shortening the lifetime of the AGN?

Having established that the outflow is likely to be a long-lived phenomenon in the life and evolution of an AGN, and that it could potentially be returning up to $\sim 10^8 M_{\odot}$ of material into the surrounding galaxy, we have to ask what effect it might have. Firstly, does it stay in the galaxy itself, or does it escape into the IGM? The Crenshaw et al. (2000) study of the UV NLR outflow in NGC 4151 showed that the outflow had decelerated to a standstill by the time it had got about 290 pc away from the central engine; this distance is of the order of half the vertical thickness of a nearby spiral galaxy. This implies that the outflow material, in this case, is reaching the ‘top’ of the galaxy but may not be moving out into the IGM. So, the outflow could certainly be adding to the density of the host galaxy ISM, but is it doing anything else?

Kauffmann et al. (2003) find, using data from the Sloan Digital Sky Survey (SDSS), that AGN tend to show evidence for recent bursts of star formation. For ionised outflows to contribute to this, they would have to contain or encounter regions of sufficiently high density, perhaps through shocks of the type observed in NGC 1068 (Crenshaw and Kraemer, 2000). This is certainly an area which deserves more attention.

6.3.4 Are warm absorbers important?

So after all of this, should we actually be spending time thinking about warm absorbers? Are they, in Netzer's words, 'weather' or 'climate'?

Firstly, are the origins of warm absorbers telling us anything fundamental about the energetics or structure of the central engine? For nearby Seyferts, the evidence I have presented implies that the soft X-ray warm absorber we observe is more likely to reflect events around the torus area, and is not directly connected to the energy generation process in the central engine. Given that the upper limit of the kinetic luminosity of Seyfert warm absorbers is less than 1% of the bolometric luminosities of these objects, the warm absorbers cannot be playing any significant rôle in the energetics of the system anyway.

It is, however, possible that the highly ionised absorption seen above 6 keV could originate much closer to the nucleus, and this may be the best place to look if one is interested in searching for accretion disc winds in Seyfert galaxies.

Unlike in the case of the nearby Seyferts, there is good evidence that the extremely fast outflows in certain quasars really could originate in accretion disc winds. If this is the case, then they could be of great interest in understanding the energetics of the central engine. If matter is actually outflowing at or close to the upper limits that I calculate, this would imply that the accreting black hole was operating like a leaky blender, with material being drawn in towards the black hole and then ejected, with only a small amount of matter being lost to accretion. This relationship between inflow and outflow would be consistent with an ion-supported thick accretion disc, which is radiatively inefficient and loses most of the accretion energy via a massive wind, only actually accreting a small fraction of its total mass supply (e.g. Blandford and Begelman, 1999). As I have shown, though, the real mass outflow rates and kinetic luminosities are probably much lower than the upper limits I calculate. Before it is possible to draw out any accretion disc wind physics from these observations - if these outflows really are accretion disc winds - we will need some accurate estimates of the volume filling factors of the outflows.

Weather or climate? As far as the fundamental physics in the central engine is

concerned, very possibly just weather, for nearby Seyferts, although extreme quasar outflows could potentially be a window into the workings of accretion discs. But in terms of understanding the environment of the central engine, and the processes by which the AGN (and especially quasars during their evolution) interact with their host galaxies, warm absorbers remain - in my opinion - scientifically promising.

6.4 Future work

We are only just beginning to realise that the X-ray spectrum above 6 keV shows evidence of high ionisation absorption features, which could potentially be more revealing of the properties of the central engine than the soft X-ray absorbers. These need to be searched for in a much wider group of objects - Astro-E2 could find this area fertile ground.

In terms of understanding the wider environment of the AGN, namely the structure of the BLR and torus and their relation to the warm absorber outflow, simultaneous multi-wavelength spectroscopy has been shown to be extremely useful. The use of X-ray and UV spectra for this purpose was discussed in Chapter 4. I think that future studies of warm absorbers are likely to become more reliant upon this technique as X-ray astronomers move into high resolution spectroscopy and begin to finally understand what their UV colleagues have been going on about all these years.

If the torus genuinely is the source of (many) warm absorbers, and radio-loud galaxies also have an obscuring torus, then this implies that radio-loud AGN should show similar soft X-ray warm absorbers. This prediction needs to be tested. Similarly, if the torus is present in all Seyferts, why are there some Seyfert 1 galaxies which do not appear to have warm absorbers? Could this be because the ring-shaped source of the material gives rise to a hollow biconical outflow, as inferred in NGC 4151 and NGC 1068 (Crenshaw et al., 2000; Crenshaw and Kraemer, 2000), and certain viewing angles do not intersect it?

Much more work can be done on finding and modelling quasar warm absorbers,

including those in objects which are too faint for high resolution X-ray spectroscopy with current instruments. Of particular interest is the range of redshifts at which these absorbers are visible, and any links with the evolution of the quasars and their host galaxies. The potential influence of AGN outflows on star formation in nearby (and more distant) AGN could also be a fruitful area for further work.

Bibliography

- Allende Prieto, C., Lambert, D. L., and Asplund, M.: 2001, *ApJL* **556**, L63
- Alloin, D., Santos-Lleo, M., Peterson, B. M., Wamsteker, W., Altieri, B., Brinkmann, W., Clavel, J., Crenshaw, D. M., George, I. M., Glass, I. S., Johnson, W. N., Kriss, G. A., Malkan, M. A., Polidan, R. S., Reichert, G. A., Rodriguez-Pascual, P. M., Romanishin, W., Starr, C. H., Stirpe, G. M., Taylor, M., Turner, T. J., Vega, H., Winge, C., and Wood, D. O. S.: 1995, *A&A* **293**, 293
- Anders, E. and Grevesse, N.: 1989, *Geochimica et Cosmochimica Acta* **53**, 197
- Antonucci, R. R. J. and Miller, J. S.: 1985 *ApJ* **297**, 621
- Arav, N., Korista, K. T., and de Kool, M.: 2002, *ApJ* **566**, 699
- Arnaud, K. A.: 1996, in *ASP Conf. Ser. 101: Astronomical Data Analysis Software and Systems V*, p. 17
- Bachev, R. and Strigachev, A.: 2003, *astro-ph/0310647*
- Bar-Shalom, A., Klapisch, M., and Oreg, J.: 2001, *Journal of Quantitative Spectroscopy and Radiative Transfer* **71**, 169
- Barvainis, R.: 1987, *ApJ* **320**, 537
- Bassani, L., Dadina, M., Maiolino, R., Salvati, M., Risaliti, G., della Ceca, R., Matt, G. and Zamorani, G.: 1999, *ApJS* **121**, 473
- Behar, E. and Netzer, H.: 2002, *ApJ* **570**, 165

- Behar, E., Rasmussen, A. P., Blustin, A. J., Sako, M., Kahn, S. M., Kaastra, J. S., Branduardi-Raymont, G., and Steenbrugge, K. C.: 2003, *ApJ* **598**, 232
- Behar, E., Sako, M., and Kahn, S. M.: 2001, *ApJ* **563**, 497
- Beichman, C. A., Soifer, B. T., Helou, G., Chester, T. J., Neugebauer, G., Gillett, F. C., and Low, F. J.: 1986, *ApJL* **308**, L1
- Bianchi, S., Balestra, I., Matt, G., Guainazzi, M., and Perola, G. C.: 2003, *A&A* **402**, 141
- Blandford, R. D. and Begelman, M. C.: 1999, *MNRAS* **303**, L1
- Blustin, A. J., Branduardi-Raymont, G., Behar, E., Kaastra, J. S., Kahn, S. M., Page, M. J., Sako, M., and Steenbrugge, K. C.: 2002a, *A&A* **392**, 453
- Blustin, A. J., Branduardi-Raymont, G., Behar, E., Kaastra, J. S., Kriss, G. A., Page, M. J., Kahn, S. M., Sako, M., and Steenbrugge, K. C.: 2003, *A&A* **403**, 481
- Blustin, A. J., Branduardi-Raymont, G., Behar, E., Kaastra, J. S., Page, M. J., Kahn, S. M., Sako, M., and Steenbrugge, K. C.: 2002b, *Adv. Space Res.* in press
- Blustin, A. J., Page, M. J., and Branduardi-Raymont, G.: 2004, *A&A* **417**, 61
- Brandt, W. N., Mathur, S., Reynolds, C. S., and Elvis, M.: 1997, *MNRAS* **292**, 407
- Branduardi-Raymont, G., Blustin, A. J., Wu, K., Kaastra, J. S., Kahn, S. M., and Deluit, S.: 2002, in *High Resolution X-ray Spectroscopy with XMM-Newton and Chandra*
- Branduardi-Raymont, G., Sako, M., Kahn, S. M., Brinkman, A. C., Kaastra, J. S., and Page, M. J.: 2001, *A&A* **365**, L140
- Canizares, C. R. and Kruper, J.: 1984, *ApJL* **278**, L99
- Chandra Team: 2003, *The Chandra Proposers' Observatory Guide*, version 6.0

- Ciliegi, P., Bassani, L., and Caroli, E.: 1993, *ApJS* **85**, 111
- Costamante, L., Ghisellini, G., Giommi, P., Tagliaferri, G., Celotti, A., Chiaberge, M., Fossati, G., Maraschi, L., Tavecchio, F., Treves, A., and Wolter, A.: 2001, *A&A* **371**, 512
- Crenshaw, D. M. and Kraemer, S. B.: 2000, *ApJL* **532**, L101
- Crenshaw, D. M., Kraemer, S. B., Boggess, A., Maran, S. P., Mushotzky, R. F., and Wu, C.: 1999, *ApJ* **516**, 750
- Crenshaw, D. M., Kraemer, S. B., Hutchings, J. B., Bradley, L. D., Gull, T. R., Kaiser, M. E., Nelson, C. H., Ruiz, J. R., and Weistrop, D.: 2000, *AJ* **120**, 1731
- Davidson, K. and Netzer, H.: 1979, *Reviews of Modern Physics* **51**, 715
- De Rosa, A., Fabian, A. C., and Piro, L.: 2002a, *MNRAS* **334**, L21
- De Rosa, A., Piro, L., Fiore, F., Grandi, P., Maraschi, L., Matt, G., Nicastro, F., and Petrucci, P. O.: 2002b, *A&A* **387**, 838
- de Vaucouleurs, G., de Vaucouleurs, A., Corwin, H. G., Buta, R. J., Paturel, G., and Fouque, P.: 1991, *Third Reference Catalogue of Bright Galaxies*, Volume 1-3, XII, Springer-Verlag Berlin Heidelberg New York
- den Herder, J. W.: 2002, in *High Resolution X-ray Spectroscopy with XMM-Newton and Chandra*
- den Herder, J. W., Brinkman, A. C., and Kahn, S. M.: 2002, in *ESA SP-488: New visions of the X-ray Universe in the XMM-Newton and Chandra Era*, in press
- den Herder, J. W., Brinkman, A. C., Kahn, S. M., Branduardi-Raymont, G., Audard, M., Behar, E., Blustin, A., den Boggende, A. J. F., Cottam, J., Erd, C., Gabriel, C., Guedel, M., van der Heyden, K., Kaastra, J. S., Kinkhabwala, A., Leutenegger, M. A., Mewe, R., Paerels, F. B. S., Raassen, A. J. J., Peterson, J. R., Pollock, A., Rasmussen, A. P., Sako, M., Santos-Lleo, M., Steenbrugge,

- K., Tamura, T., and de Vries, C. P.: 2003, in *X-Ray and Gamma-Ray Telescopes and Instruments for Astronomy. Edited by Joachim E. Truemper, Harvey D. Tananbaum. Proceedings of the SPIE, Volume 4851, pp. 196-207 (2003).*
- den Herder, J. W., Brinkman, A. C., Kahn, S. M., Branduardi-Raymont, G., Thomsen, K., Aarts, H., Audard, M., Bixler, J. V., den Boggende, A. J., Cottam, J., Decker, T., Dubbeldam, L., Erd, C., Goulooze, H., Güdel, M., Guttridge, P., Hailley, C. J., Janabi, K. A., Kaastra, J. S., de Korte, P. A. J., van Leeuwen, B. J., Mauche, C., McCalden, A. J., Mewe, R., Naber, A., Paerels, F. B., Peterson, J. R., Rasmussen, A. P., Rees, K., Sakelliou, I., Sako, M., Spodek, J., Stern, M., Tamura, T., Tandy, J., de Vries, C. P., Welch, S., and Zehnder, A.: 2001, *A&A* **365**, L7
- Dewey, D.: 2002, in *High Resolution X-ray Spectroscopy with XMM-Newton and Chandra*
- Dubau, J. and Porquet, D.: 2002, in *ESA SP-488: New visions of the X-ray Universe in the XMM-Newton and Chandra Era*, in press
- Dunlop, J. S., McLure, R. J., Kukula, M. J., Baum, S. A., O'Dea, C. P., and Hughes, D. H.: 2003, *MNRAS* **340**, 1095
- Ehle, M., Breittellner, M., Gonzales Riestra, R., Guainazzi, M., Rodriguez, P., Santos-Lleo, M., Schartel, N., Tomas, L., Verdugo, E., and Dahlem, M.: 2003, *XMM-Newton Users' Handbook*, version 2.1
- Elvis, M., Wilkes, B. J., and Lockman, F. J.: 1989, *AJ* **97**, 777
- Ferland, G. J., Korista, K. T., Verner, D. A., Ferguson, J. W., Kingdon, J. B., and Verner, E. M.: 1998, *PASP* **110**, 761
- Fink, H. H., Thomas, H.-C., Hasinger, G., Predehl, P., Schaeidt, S., Makino, F., and Warwick, R. S.: 1991, *A&A* **246**, L6
- Gabel, J. R., Crenshaw, D. M., Kraemer, S. B., Brandt, W. N., George, I. M., Hamann, F. W., Kaiser, M. E., Kaspi, S., Kriss, G. A., Mathur, S., Mushotzky,

- R. F., Nandra, K., Netzer, H., Peterson, B. M., Shields, J. C., Turner, T. J., and Zheng, W.: 2003, *ApJ* **595**, 120
- Gallimore, J. F., Baum, S. A. and O'Dea, C. P.: 1987, *Nature* **388**, 852
- Gebhardt, K., Kormendy, J., Ho, L. C., Bender, R., Bower, G., Dressler, A., Faber, S. M., Filippenko, A. V., Green, R., Grillmair, C., Lauer, T. R., Magorrian, J., Pinkney, J., Richstone, D., and Tremaine, S.: 2000, *ApJL* **543**, L5
- Genzel, R. and Weitzel, L. and Tacconi-Garman, L. E. and Blietz, M. and Cameron, M. and Krabbe, A. and Lutz, D. and Sternberg, A. *ApJ* **444**, 129
- George, I. M. and Fabian, A. C.: 1991, *MNRAS* **249**, 352
- George, I. M., Turner, T. J., Mushotzky, R., Nandra, K., and Netzer, H.: 1998, *ApJ* **503**, 174
- Ghisellini, G., Celotti, A., Fossati, G., Maraschi, L., and Comastri, A.: 1998, *MNRAS* **301**, 451
- Ghosh, K. K., Soundararajaperumal, S., Kalai Selvi, M., and Sivarani, T.: 1992, *A&A* **255**, 119
- Gondhalekar, P. M., Kellett, B. J., Pounds, K. A., Matthews, L., and Quenby, J. J.: 1994, *MNRAS* **268**, 973
- Gondoin, P., Orr, A., and Lumb, D.: 2003, *A&A* **398**, 967
- Greenhill, L. J., Gwinn, C. R., Antonucci, R. and Barvainis, R.: 1996, *ApJL* **472**, L21
- Haardt, F. and Maraschi, L.: 1991, *ApJL* **380**, L51
- Haardt, F. and Maraschi, L.: 1993, *ApJ* **413**, 507
- Halpern, J. P.: 1984, *ApJ* **281**, 90
- HEASARC website: 2004, <http://heasarc.gsfc.nasa.gov/>

- Hölzer, G., Fritsch, M., Deutsch, M., Härtwig, J., Förster, E.: 1997, *Phys. Rev. A* **56**, 4554
- Hutchings, J. B., Kriss, G. A., Green, R. F., Brotherton, M., Kaiser, M. E., Koratkar, A. P., and Zheng, W.: 2001, *ApJ* **559**, 173
- Jaffe, W., Ford, H. C., Ferrarese, L., van den Bosch, F. and O'Connell, R. W.: 1993 *Nature* **364**, 213
- James, C. H.: 2003, http://www.mssl.ucl.ac.uk/www_astro/xmm/grisms/grism_tool.html
- Jansen, F., Lumb, D., Altieri, B., Clavel, J., Ehle, M., Erd, C., Gabriel, C., Guainazzi, M., Gondoin, P., Much, R., Munoz, R., Santos, M., Schartel, N., Texier, D., and Vacanti, G.: 2001, *A&A* **365**, L1
- Kaastra, J. S., Mewe, R., Liedahl, D. A., Komossa, S., and Brinkman, A. C.: 2000, *A&A* **354**, L83
- Kaastra, J. S., Mewe, R., and Raassen, A. J. J.: 2002a, in *ESA SP-488: New visions of the X-ray Universe in the XMM-Newton and Chandra Era*, in press
- Kaastra, J. S., Steenbrugge, K. C., Raassen, A. J. J., van der Meer, R. L. J., Brinkman, A. C., Liedahl, D. A., Behar, E., and de Rosa, A.: 2002b, *A&A* **386**, 427
- Kahn, S. M., Behar, E., Kinkhabwala, A., and Savin, D. W.: 2002, *Royal Society of London Philosophical Transactions Series A* **360**, 1923
- Kallman, T. R. and McCray, R.: 1982, *ApJS* **50**, 263
- Kaspi, S., Brandt, W. N., George, I. M., Netzer, H., Crenshaw, D. M., Gabel, J. R., Hamann, F. W., Kaiser, M. E., Koratkar, A., Kraemer, S. B., Kriss, G. A., Mathur, S., Mushotzky, R. F., Nandra, K., Peterson, B. M., Shields, J. C., Turner, T. J., and Zheng, W.: 2002, *ApJ* **574**, 643
- Kaspi, S., Brandt, W. N., Netzer, H., George, I. M., Chartas, G., Behar, E., Sambruna, R. M., Garmire, G. P., and Nousek, J. A.: 2001, *ApJ* **554**, 216

- Kaspi, S., Brandt, W. N., Netzer, H., Sambruna, R., Chartas, G., Garmire, G. P., and Nousek, J. A.: 2000a, *ApJL* **535**, L17
- Kaspi, S., Netzer, H., Chelouche, D., George, I. M., Turner, T. J., and Nandra, K.: 2003, *astro-ph/0311017*
- Kaspi, S., Smith, P. S., Netzer, H., Maoz, D., Jannuzi, B. T., and Giveon, U.: 2000b, *ApJ* **533**, 631
- Kauffmann, G., Heckman, T. M., Tremonti, C., Brinchmann, J., Charlot, S., White, S. D. M., Ridgway, S. E., Brinkmann, J., Fukugita, M., Hall, P. B., Ivezić, Ž., Richards, G. T., and Schneider, D. P.: 2003, *MNRAS* **346**, 1055
- Kinkhabwala, A., Sako, M., Behar, E., Kahn, S. M., Paerels, F., Brinkman, A. C., Kaastra, J. S., Gu, M. F., and Liedahl, D. A.: 2002, *ApJ* **575**, 732
- Klößner, H., Baan, W. A. and Garrett, M. A.: 2003, *Nature* **421**, 821
- Kraemer, S. B. and Crenshaw, D. M.: 2000, *ApJ* **544**, 763
- Kraemer, S. B., Crenshaw, D. M., George, I. M., Netzer, H., Turner, T. J., and Gabel, J. R.: 2002, *ApJ* **577**, 98
- Kraemer, S. B., Crenshaw, D. M., Yaqoob, T., McKernan, B., Gabel, J. R., George, I. M., Turner, T. J., and Dunn, J. P.: 2003, *ApJ* **582**, 125
- Kriss, G. A., Blustin, A., Branduardi-Raymont, G., Green, R. F., Hutchings, J., and Kaiser, M. E.: 2003, *A&A* **403**, 473
- Kriss, G. A., Green, R. F., Brotherton, M., Oegerle, W., Sembach, K. R., Davidsen, A. F., Friedman, S. D., Kaiser, M. E., Zheng, W., Woodgate, B., Hutchings, J., Shull, J. M., and York, D. G.: 2000a, *ApJL* **538**, L17
- Kriss, G. A., Peterson, B. M., Crenshaw, D. M., and Zheng, W.: 2000b, *ApJ* **535**,

- Krolik, J. H.: 1999, *Active Galactic Nuclei: From the Central Black Hole to the Galactic Environment*, Princeton University Press
- Krolik, J. H. and Kriss, G. A.: 2001, *ApJ* **561**, 684
- Krongold, Y., Nicastro, F., Brickhouse, N. S., Elvis, M., Liedahl, D. A., and Mathur, S.: 2003, *ApJ* **597**, 832
- Kubo, H., Takahashi, T., Madejski, G., Tashiro, M., Makino, F., Inoue, S., and Takahara, F.: 1998, *ApJ* **504**, 693
- Lamer, G., Brunner, H., and Staubert, R.: 1996, *A&A* **311**, 384
- Laor, A. and Brandt, W. N.: 2002, *ApJ* **569**, 641
- Lightman, A. P. and White, T. R.: 1988, *ApJ* **335**, 57
- Madejski, G., Serlemitsos, P., Marshall, F., Kallman, T., Mushotzky, R., Turner, J., Done, C., Arnaud, K., Boldt, E., Holt, S., Jahoda, K., Kelley, R., Petre, R., Smale, A., Swank, J., Szymkowiak, A., and Weaver, K.: 1992, in *Frontiers Science Series*, p. 583
- Madejski, G. M., Mushotzky, R. F., Weaver, K. A., Arnaud, K. A., and Urry, C. M.: 1991, *ApJ* **370**, 198
- Maiolino, R. and Rieke, G. H.: 1995, *ApJ* **454**, 95
- Malkan, M. A. and Sargent, W. L. W.: 1982, *ApJ* **254**, 22
- Maran, S. P., Crenshaw, D. M., Mushotzky, R. F., Reichert, G. A., Carpenter, K. G., Smith, A. M., Hutchings, J. B., and Weymann, R. J.: 1996, *ApJ* **465**, 733
- Maraschi, L., Ghisellini, G., and Celotti, A.: 1992, *ApJL* **397**, L5
- Markowitz, A., Edelson, R., Vaughan, S., Uttley, P., George, I. M., Griffiths, R. E., Kaspi, S., Lawrence, A., McHardy, I., Nandra, K., Pounds, K., Reeves, J., Schurch, N., and Warwick, R.: 2003, *ApJ* **593**, 96

- Marshall, H. L., Edelson, R. A., Vaughan, S., Malkan, M., O'Brien, P., and Warwick, R.: 2003, *AJ* **125**, 459
- Mason, K. O., Branduardi-Raymont, G., Ogle, P. M., Page, M. J., Puchnarewicz, E. M., Behar, E., Córdoba, F. A., Davis, S., Maraschi, L., McHardy, I. M., O'Brien, P. T., Priedhorsky, W. C., and Sasseen, T. P.: 2003a, *ApJ* **582**, 95
- Mason, K. O., Branduardi-Raymont, G., Ogle, P. M., Page, M. J., Puchnarewicz, E. M., Behar, E., Córdoba, F. A., Davis, S., Maraschi, L., McHardy, I. M., O'Brien, P. T., Priedhorsky, W. C., and Sasseen, T. P.: 2003b, *ApJ* **582**, 95
- Mason, K. O., Breeveld, A., Much, R., Carter, M., Cordova, F. A., Cropper, M. S., Fordham, J., Huckle, H., Ho, C., Kawakami, H., Kennea, J., Kennedy, T., Mittaz, J., Pandel, D., Priedhorsky, W. C., Sasseen, T., Shirey, R., Smith, P., and Vreux, J.-M.: 2001, *A&A* **365**, L36
- Mathur, S., Kuraszkiewicz, J., and Czerny, B.: 2001, *New Astronomy* **6**, 321
- Matsumoto, C., Leighly, K. M., and Marshall, H. L.: 2004, *ApJ* **603**, 456
- Monier, E. M., Mathur, S., Wilkes, B., and Elvis, M.: 2001, *ApJ* **559**, 675
- Morales, R. and Fabian, A. C.: 2002, *MNRAS* **329**, 209
- Mushotzky, R. F.: 1984, *Advances in Space Research* **3**, 157
- Nandra, K., George, I. M., Mushotzky, R. F., Turner, T. J., and Yaqoob, T.: 1997, *ApJ* **477**, 602
- Nandra, K. and Pounds, K. A.: 1994, *MNRAS* **268**, 405
- Nayakshin, S., Kazanas, D., and Kallman, T. R.: 2000, *ApJ* **537**, 833
- Netzer, H.: 1996, *ApJ* **473**, 781
- Netzer, H.: 2003, *astro-ph/0311604*

- Netzer, H., Chelouche, D., George, I. M., Turner, T. J., Crenshaw, D. M., Kraemer, S. B., and Nandra, K.: 2002, *ApJ* **571**, 256
- Netzer, H., Kaspi, S., Behar, E., Brandt, W. N., Chelouche, D., George, I. M., Crenshaw, D. M., Gabel, J. R., Hamann, F. W., Kraemer, S. B., Kriss, G. A., Nandra, K., Peterson, B. M., Shields, J. C., and Turner, T. J.: 2003, *ApJ* **599**, 933
- Netzer, H. and Laor, A.: 1993, *ApJL* **404**, L51
- Nicastro, F., Elvis, M., Fang, T., Mathur, S., Siemiginowska, A., and Zezas, A.: 2003, *AAS/High Energy Astrophysics Division* 35
- Nicastro, F., Elvis, M., and Fruscione, A.: 2000, *Bulletin of the American Astronomical Society* **32**, 1185
- Nicastro, F., Zezas, A., Drake, J., Elvis, M., Fiore, F., Fruscione, A., Marengo, M., Mathur, S., and Bianchi, S.: 2002, *ApJ* **573**, 157
- O'Brien, P. T., Page, K., Reeves, J. N., Pounds, K., Turner, M. J. L., and Puchnarewicz, E. M.: 2001a, *MNRAS* **327**, L37
- O'Brien, P. T., Reeves, J. N., Turner, M. J. L., Pounds, K. A., Page, M., Gliozzi, M., Brinkmann, W., Stephen, J. B., and Dadina, M.: 2001b, *A&A* **365**, L122
- Ogle, P. M., Brookings, T., Canizares, C. R., Lee, J. C., and Marshall, H. L.: 2003, *A&A* **402**, 849
- Ogle, P. M., Mason, K. O., Page, M. J., Salvi, N. J., Cordova, F. A., McHardy, I. M., and Priedhorsky, W. C.: 2004, *astro-ph/0401173*
- Padovani, P. and Giommi, P.: 1995, *ApJ* **444**, 567
- Paerels, F. B. S. and Kahn, S. M.: 2003, *ARA&A* **41**, 291
- Page, M. J., Davis, S. W., and Salvi, N. J.: 2003, *MNRAS* **343**, 1241
- Perez-Olea, D. E. and Colina, L.: 1996, *ApJ* **468**, 191

Petrucci, P. O., Maraschi, L., Haardt, F., and Nandra, K.: 2004, *A&A* **413**, 477

Pogge, R. W.: 1988, *ApJ* **328**, 519

Porquet, D. and Dubau, J.: 2000, *A&AS* **143**, 495

Pounds, K. A., King, A. R., Page, K. L., and O'Brien, P. T.: 2003a, *MNRAS* **346**, 1025

Pounds, K. A., Reeves, J. N., King, A. R., Page, K. L., O'Brien, P. T., and Turner, M. J. L.: 2003b, *MNRAS* **345**, 705

Pounds, K. A., Reeves, J. N., Page, K. L., Edelson, R., Matt, G., and Perola, G. C.: 2003c, *MNRAS* **341**, 953

Pounds, K. A., Reeves, J. N., Page, K. L., Wynn, G. A., and O'Brien, P. T.: 2003d, *MNRAS* **342**, 1147

Rózańska, A., Czerny, B., Siemiginowska, A., Dumont, A.-M., and Kawaguchi, T.: 2004, *ApJ* **600**, 96

Rasmussen, A., Kahn, S. M., and Paerels, F.: 2003, in *ASSL Vol. 281: The IGM/Galaxy Connection. The Distribution of Baryons at $z=0$* , p. 109

Rees, M. J.: 1984, *ARA&A* **22**, 471

Reeves, J. N., Nandra, K., George, I. M., Pounds, K. A., Turner, T. J., and Yaqoob, T.: 2004, *ApJ* **602**, 648

Reynolds, C. S.: 1996, *Ph.D. thesis*, University of Cambridge

Reynolds, C. S.: 1997, *MNRAS* **286**, 513

Reynolds, C. S.: 2000, *ApJ* **533**, 811

Reynolds, C. S. and Nowak, M. A.: 2003, *Physics Reports* **377**, 389

Romano, P., Mathur, S., Pogge, R. W., Peterson, B. M., and Kuraszkiewicz, J.: 2002, *ApJ* **578**, 64

- Sako, M., Kahn, S. M., Behar, E., Kaastra, J. S., Brinkman, A. C., Boller, T., Puchnarewicz, E. M., Starling, R., Liedahl, D. A., Clavel, J., and Santos-Lleo, M.: 2001, *A&A* **365**, L168
- Sako, M., Kahn, S. M., Branduardi-Raymont, G., Kaastra, J. S., Brinkman, A. C., Page, M. J., Behar, E., Paerels, F., Kinkhabwala, A., Liedahl, D. A., and Herder, J. W. d.: 2003, *ApJ* **596**, 114
- Salvi, N. J.: 2003, *Ph.D. thesis*, University of London
- Salvi, N. J., Page, M. J., Stevens, J. A., Wu, K., Mason, K. O., Aller, M. F., Aller, H. D., Teräsranta, H., Romero-Colmenero, E., Cordova, F. A., and Priedhorsky, W. C.: 2002, *MNRAS* **335**, 177
- Sambruna, R. M., George, I. M., Madejski, G., Urry, C. M., Turner, T. J., Weaver, K. A., Maraschi, L., and Treves, A.: 1997, *ApJ* **483**, 774
- Sambruna, R. M. and Mushotzky, R. F.: 1998, *ApJ* **502**, 630
- Santos-Lleo, M., Clavel, J., Barr, P., Glass, I. S., Pelat, D., Peterson, B. M., and Reichert, G.: 1995, *MNRAS* **274**, 1
- Savage, B. D. and Mathis, J. S.: 1979, *Ann. Rev. Astron. Astrophys.* **17**, 73
- Schurch, N. J., Warwick, R. S., Griffiths, R. E., and Kahn, S. M.: 2004, *astro-ph/0401550*
- Schurch, N. J., Warwick, R. S., Griffiths, R. E., and Sembay, S.: 2003, *MNRAS* **345**, 423
- Scott, J. E., Kriss, G. A., Lee, J. C., Arav, N., Ogle, P., Roraback, K., Weaver, K., Alexander, T., Brotherton, M., Green, R. F., Hutchings, J., Kaiser, M. E., Marshall, H., Oegerle, W., and Zheng, W.: 2004, *astro-ph/0401226*
- Shemmer, O., Romano, P., Bertram, R., Brinkmann, W., Collier, S., Crowley, K. A., Detsis, E., Filippenko, A. V., Gaskell, C. M., George, T. A., Gliozzi, M., Hiller,

- M. E., Jewell, T. L., Kaspi, S., Klimek, E. S., Lannon, M. H., Li, W., Martini, P., Mathur, S., Negoro, H., Netzer, H., Papadakis, I., Papamastorakis, I., Peterson, B. M., Peterson, B. W., Pogge, R. W., Pronik, V. I., Rumstay, K. S., Sergeev, S. G., Sergeeva, E. A., Stirpe, G. M., Taylor, C. J., Treffers, R. R., Turner, T. J., Uttley, P., Vestergaard, M., von Braun, K., Wagner, R. M., and Zheng, Z.: 2001, *ApJ* **561**, 162
- Shields, G. A.: 1978, *Nature* **272**, 706
- Shields, J. C. and Hamann, F.: 1997, *ApJ* **481**, 752
- Steenbrugge, K. C., Kaastra, J. S., Blustin, A. J., Branduardi-Raymont, G., Sako, M., Behar, E., Kahn, S. M., Paerels, F. B. S., and Walter, R.: 2003a, *A&A* **408**, 921
- Steenbrugge, K. C., Kaastra, J. S., de Vries, C. P., and Edelson, R.: 2003b, *A&A* **402**, 477
- Strüder, L., Briel, U., Dennerl, K., Hartmann, R., Kendziorra, E., Meidinger, N., Pfeffermann, E., Reppin, C., Aschenbach, B., Bornemann, W., Bräuninger, H., Burkert, W., Elender, M., Freyberg, M., Haberl, F., Hartner, G., Heuschmann, F., Hippmann, H., Kastelic, E., Kemmer, S., Kettenring, G., Kink, W., Krause, N., Müller, S., Oppitz, A., Pietsch, W., Popp, M., Predehl, P., Read, A., Stephan, K. H., Stötter, D., Trümper, J., Holl, P., Kemmer, J., Soltau, H., Stötter, R., Weber, U., Weichert, U., von Zanthier, C., Carathanassis, D., Lutz, G., Richter, R. H., Solc, P., Böttcher, H., Kuster, M., Staubert, R., Abbey, A., Holland, A., Turner, M., Balasini, M., Bignami, G. F., La Palombara, N., Villa, G., Buttler, W., Gianini, F., Lainé, R., Lumb, D., and Dhez, P.: 2001, *A&A* **365**, L18
- Swain, M., Vasisht, G., Akeson, R., Monnier, J., Millan-Gabet, R., Serabyn, E., Creech-Eakman, M., van Belle, G., Beletic, J., Beichman, C., Boden, A., Booth, A., Colavita, M., Gathright, J., Hrynevych, M., Koresko, C., Le Mignant, D., Ligon, R., Mennesson, B., Neyman, C., Sargent, A., Shao, M., Thompson, R., Unwin, S., and Wizinowich, P.: 2003, *ApJL* **596**, L163

- Tarter, C. B., Tucker, W. H., and Salpeter, E. E.: 1969, *ApJ* **156**, 943
- Tatum, J. B.: 2003, <http://orca.phys.uvic.ca/~tatum/stellatm.html>
- Theureau, G., Bottinelli, L., Coudreau-Durand, N., Gouguenheim, L., Hallet, N., Loulergue, M., Paturel, G., and Teerikorpi, P.: 1998, *A&AS* **130**, 333
- Turner, M. J. L., Abbey, A., Arnaud, M., Balasini, M., Barbera, M., Belsole, E., Bennie, P. J., Bernard, J. P., Bignami, G. F., Boer, M., Briel, U., Butler, I., Cara, C., Chabaud, C., Cole, R., Collura, A., Conte, M., Cros, A., Denby, M., Dhez, P., Di Coco, G., Dowson, J., Ferrando, P., Ghizzardi, S., Gianotti, F., Goodall, C. V., Gretton, L., Griffiths, R. G., Hainaut, O., Hochedez, J. F., Holland, A. D., Jourdain, E., Kendziorra, E., Lagostina, A., Laine, R., La Palombara, N., Lortholary, M., Lumb, D., Marty, P., Molendi, S., Pigot, C., Poindron, E., Pounds, K. A., Reeves, J. N., Reppin, C., Rothenflug, R., Salvétat, P., Sauvageot, J. L., Schmitt, D., Sembay, S., Short, A. D. T., Spragg, J., Stephen, J., Strüder, L., Tiengo, A., Trifoglio, M., Trümper, J., Vercellone, S., Vigroux, L., Villa, G., Ward, M. J., Whitehead, S., and Zonca, E.: 2001, *A&A* **365**, L27
- Turner, T. J. and Pounds, K. A.: 1989, *MNRAS* **240**, 833
- Turner, T. J., Romano, P., Kraemer, S. B., George, I. M., Yaqoob, T., Crenshaw, D. M., Storm, J., Alloin, D., Lazzaro, D., Da Silva, L., Pritchard, J. D., Kriss, G., Zheng, W., Mathur, S., Wang, J., Dobbie, P., and Collins, N. R.: 2002, *ApJ* **568**, 120
- Urry, C. M., Mushotzky, R. F., and Holt, S. S.: 1986, *ApJ* **305**, 369
- Urry, C. M., Scarpa, R., O'Dowd, M., Falomo, R., Pesce, J. E., and Treves, A.: 2000, *ApJ* **532**, 816
- Vaughan, S. and Fabian, A. C.: 2004, *MNRAS* **348**, 1415
- Véron-Cetty, M.-P. and Véron, P.: 2003, *A&A* **412**, 399
- Wandel, A., Peterson, B. M., and Malkan, M. A.: 1999, *ApJ* **526**, 579

- Wanders, I., van Groningen, E., Alloin, D., Aretxaga, I., Axon, D., de Bruyn, A. G., Clavel, J., Dietrich, M., Goad, M. R., Gondhalekar, P., Horne, K., Jackson, N., Kollatschny, W., Laurikainen, E., Lawrence, A., Masegosa, J., O'Brien, P. T., del Olmo, A., Penston, M. V., Perea, J., Perez, E., Perez-Fournon, I., Perry, J. J., Robinson, A., Rodriguez Espinosa, J. M., Stirpe, G. M., Tadhunter, C., Terlevich, R., Unger, S., Wagner, S. J., and Williams, R.: 1993, *A&A* **269**, 39
- Winge, C., Pastoriza, M. G., Storchi-Bergmann, T., and Lipari, S.: 1992, *ApJ* **393**, 98
- Yaqoob, T., McKernan, B., Kraemer, S. B., Crenshaw, D. M., Gabel, J. R., George, I. M., and Turner, T. J.: 2003, *ApJ* **582**, 105
- Young, A. J. and Wilson, A. S.: 2004, *ApJ* **601**, 133
- Young, A. J., Wilson, A. S., and Shopbell, P. L.: 2001, *ApJ* **556**, 6
- Yuan, F., Markoff, S., Falcke, H., and Biermann, P. L.: 2002, *A&A* **391**, 139